MATHEMATICAL MODELLING OF THE FORMATION OF URANIUM HYDRIDE BLISTERS

A THESIS SUBMITTED TO THE UNIVERSITY OF MANCHESTER
FOR THE DEGREE OF DOCTOR OF PHILOSOPHY
IN THE FACULTY OF SCIENCE AND ENGINEERING

2022

Holly Barker

Department of Mathematics
School of Natural Sciences

Contents

List of Tables

List of Figures

Abstract

MATHEMATICAL MODELLING OF THE FORMATION OF
URANIUM HYDRIDE BLISTERS
Holly Barker
A thesis submitted to The University of Manchester
for the degree of Doctor of Philosophy, 2022

Uranium metal is used in the nuclear power and defence sectors. After use, it is extremely important to store uranium safely to prevent adverse effects on the environment. If uranium comes into contact with hydrogen, they react to form uranium hydride UH_3. Uranium hydride is brittle and tends to crumble away from the metal as a powder [1]. It is also pyrophoric [2–5] and presents an issue in terms of safe storage. The metal often has a surface passivation layer (SPL) predominantly made of uranium dioxide UO_2 which does not react with hydrogen and protects the metal from hydriding to an extent [6]. Eventually hydride will form beneath the SPL. Hydride nucleates at distinct sites and grows into blisters or pits [7–9]. After some time, some blisters cease to grow and some break through the SPL, exposing the surroundings to UH_3.

In this thesis, one- and two-dimensional multi-physics continuum models for the uranium-hydrogen system are developed and solved. The models incorporate hydrogen diffusion, hydriding reaction, and the effects of stress, deformation, temperature and the oxide layer. Simulated finite element method results for a one-dimensional model allow for comparisons between two different boundary conditions controlling hydrogen in-flux and instantaneous and time-dependent reaction kinetics with varying Damköhler values. Sensitivity analysis reveals that the parameters controlling hydrogen in-flux

are highly influential on the extent to which the metal is hydrided. Results for two-dimensional finite element method models of hydriding are presented in two groups: reaction-diffusion-only models with and without an SPL, and thermoelastic models. An analysis of a reaction-diffusion-only model with no SPL reveals the evolution of a quasi-steady state that is a potential mechanism for the cessation of hydride growth. The introduction of an SPL shows that hydride is preferentially produced below regions where diffusivity in the SPL is higher. The results of the thermoelastic models reveal that restricting the non-uniform deformation of uranium induces large stresses in the metal. Difficulties encountered when combining the reaction-diffusion and thermoelastic models into a multi-physics model in two dimensions are discussed.

Declaration

No portion of the work referred to in this thesis has been submitted in support of an application for another degree or qualification of this or any other university or other institute of learning.

Copyright

Acknowledgements

I would firstly like to thank my supervisor, Prof. Andrew L. Hazel for his guidance over the last four years, both in person and more recently through video calls. Andrew has patiently helped me to grow from an undergraduate student into a researcher, to be confident in my abilities, and to see the big picture (both mathematically and in general) on numerous occasions when I couldn't. I also thank Dr. Phil D.D. Monks, my industrial supervisor from AWE, for lending his materials science knowledge, guiding the project's aims, and answering my often jumbled questions about uranium and sensitivity analysis. Also from AWE I thank Dr. J. Petherbridge and Dr. R.M. Harker for their helpful discussions and emails. For providing the funding to make this project possible, I thank AWE plc. and the Engineering and Physical Sciences Research Council (EPSRC).

To the members of office 1.134 in the Alan Turing Building past and present: thank you for providing four years of welcome (and unwelcome) distractions, being there to celebrate when things (rarely) went well and convincing me to keep trying when I (repeatedly) said I was never going to manage to write this thesis.

Next, to Dr. Puneet Matharu — Puneet, I categorically would not have been able to complete this PhD without you. You taught me every single thing I know about computers, gave literal days of your own time over to helping me with coding problems I thought were insurmountable, and were kind and patient throughout. We even had fun doing it! I will never be able to thank you enough.

My family — Mum, Dad, Hannah and Grandma — I want to thank you for your constant support and encouragement. Hannah, you've worked so hard to get this degree, and you did it with a level head and good humour. Even though I'm the big sister, you're the one setting the example. Mum, thank you for being on the other end of the phone every single time I called for the last four years, ready to listen my overblown worries and stress. Thank you for telling me when it's time to get a good night's sleep and encouraging me when I need to **just keep going**.

To the girls of Wensley Drive — Hannah, Laura, Eleanor and Alice — thank you so much for welcoming me into your spare room and your friendship group when I had no income and nowhere to live in Manchester. I loved every minute of watching TV, listening to MNEK, and having very silly fun.

To my greatest friends, Bella, Jes and Natalie. Bella, you are hilariously funny and your crazy stories liven up my day every time I see you. Thank you for showing me that it's best to take life a little less seriously and to have fun whenever I can. Jes, you have taught me so much about how to be a friend. Where would I have been in lockdown without your karaoke, your DVT avoidance walks, your sofa pits, and your other stubborn attempts to cheer me up? I appreciated all of it, even when I couldn't say it. I will always fondly remember living through a global pandemic in our little flat with my **unbelievably** annoying best friend. And Natalie — what can I say? I can't believe we've done everything we said we'd do. Thank you for your kindness, calming influence, humour, warmth, and generosity of time and attention. Your friendship has shaped so much of the person I am today — thank you for being my best friend for all these years.

And finally to Owen — you've been a constant source of emotional support, fun and brilliant company, even when you've been equally as stressed as me, even when you had work to do, even when you were tired, even when we had to communicate online in lockdown, even when you lived on a different continent. You've made me see the bright side by looking forward to future adventures. You've listened to every panicked outburst and told me hundreds of times that things are really **not** that bad. And when things really **were** that bad, you reminded me that it's never the end of the world. Thank you so much.

Chapter 1

Introduction and literature review

Uranium is most widely known for its use as a fuel in the nuclear power and defence industries which harness its power as a radioactive element. After use, nuclear waste remains, which contains not only uranium, but uranium compounds, lighter fission products and heavier trans-uranic elements. This waste must be kept in storage for a long time to reduce the probability of adverse effects on the environment. In the nuclear power industry, nuclear material is in the form of cylindrical pellets, which are stacked and encased in cladding material to form fuel rods. After use, the rods are stored standing in water tanks or in air inside sealed concrete containers to keep them from irradiating their environment.

By the time uranium reaches storage, its surface is covered with a layer of uranium compounds, notably oxides, hydroxides and carbides [10]. This layer passivates the metal, making it less susceptible to further reaction with the environment [9], and in the context of corrosion is therefore referred to as a surface passivation layer (SPL). It is well-documented that uranium and oxygen are highly reactive [11, 12], and the main component of the SPL is uranium oxide, UO_2. Though the SPL works as a protective layer [12], it can be penetrated by hydrogen from the atmosphere [7, 9, 10, 13]. Hydrogen diffuses through the SPL. Once hydrogen comes into contact with the uranium metal, they react to form uranium hydride, UH_3. Hydrides are observed to nucleate at discrete sites and grow to form small hydride blisters, as observed by many authors including early observations by Owen and Scudamore [14], among many others [7, 9, 10, 15]. Figure 1.1 shows four stages of the growth of hydride blisters on uranium. Since $UH_3$is less dense than uranium metal, the material undergoes deformation local to the blister which generates stress [16, 17]. Some of these small blisters stop growing and are contained below the protective oxide layer, while others burst through or

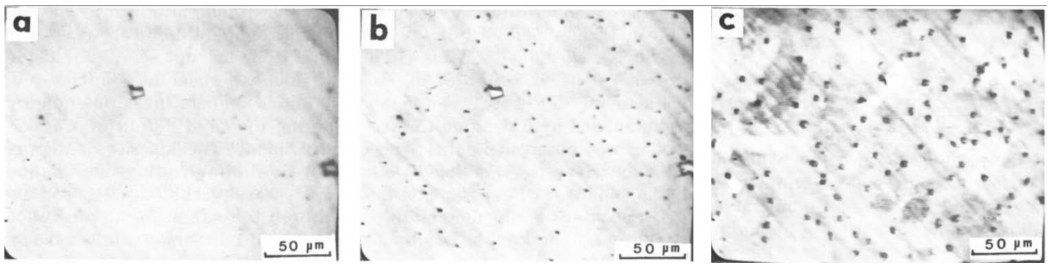

Figure 1.1: Three stages of uranium hydride blister growth on uranium metal in the first few minutes of hydrogen exposure: (a) the metal surface before exposure to hydrogen, (b)-(c) hydride blisters forming on the metal. Images taken from Bloch et al. (1984) [15].

'breach' the oxide layer. An example of this breach may be seen in Figure 1.2. Once the oxide is breached, the underlying uranium hydride is exposed.

The presence of exposed uranium hydride is extremely detrimental to safe storage. UH_3 is pyrophoric [2–4] — it spontaneously ignites when in contact with air — and the reaction is fast and highly exothermic [19]. Like many metal hydrides, UH_3 is hard but brittle [1]. Its brittleness means that exposed hydride will crumble away from the bulk metal as a powder, also called spalling. The hydride's tendency to spall combines with its flammability for potentially disastrous results [19]: a mechanism for the escape of radioactive waste into the environment. Heat produced from burning hydride can also affect the structural integrity of the cladding material in which it is stored [20].

A better understanding of how nuclear waste degrades over time will help with cleaner, safer long-term storage solutions which is a matter of utmost importance in the nuclear industries. The aim of this PhD project is to develop and solve continuum multi-physics models for the initiation and growth of hydride blisters on both pure uranium metal and uranium with a pre-existing SPL, including the effects of deformation and stress.

The ordered structure of this thesis is as follows:

- A review of the literature is presented. This review is in two parts; one describing experimental results and observations and one showing existing reaction-diffusion continuum models
- The multi-physics continuum model for the hydriding of uranium which is solved in this thesis is derived
- The finite element method is described in the context of solving reaction-diffusion models on one- and two-dimensional domains

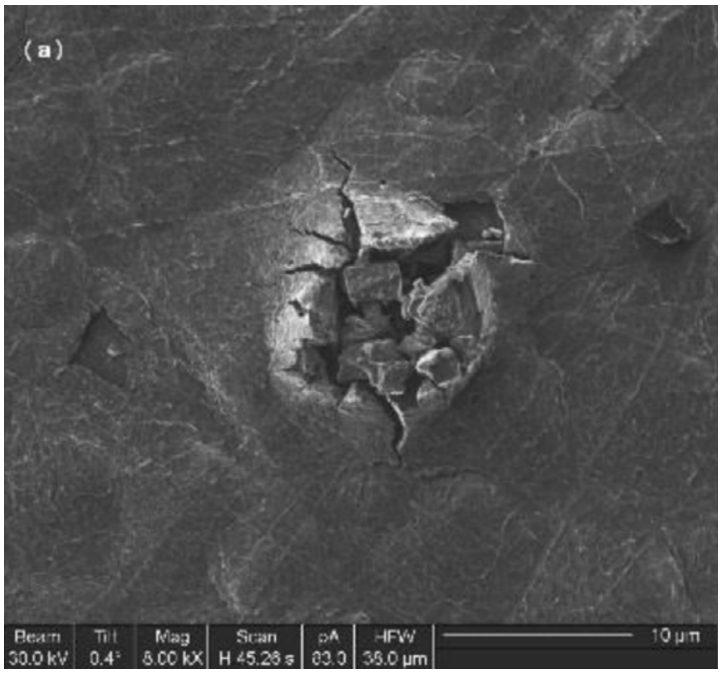

Figure 1.2: Uranium hydride blister which has breached the oxide layer. Image taken from Banos et al. (2016) [18].

- The method of sensitivity analysis is described in the context of distinguishing parameters in a model which significantly influence the model results

- Various one- and two-dimensional models are solved using the finite element method and sensitivity analysis is used to determine influential parameters

We proceed to a review of the literature. Firstly, we discuss relevant experimental results and models of physical parameters which inform the models in this project. Secondly, previous works on mathematical modelling using reaction-diffusion are presented.

1.1 Experimental results

A 2018 review by Banos, Harker and Scott [8], concentrates on the small nucleation and blistering before bulk hydriding begins. This reflects an understanding in the literature of the importance of these mechanisms in modelling the full hydriding process. In the review, uranium hydriding is discussed in distinct stages; induction, nucleation and growth, coalescence, and bulk reaction.

Induction describes the processes which occur before the commencement of reaction. This includes the traversal of hydrogen across the SPL to reach the metal and build-up of hydrogen on the metal-SPL interface. The next stage is nucleation, where certain regions of the metal begin to form hydride. Imperfections in the metal and oxide can influence the location of these sites. Some of these blisters remain small after a short period of growth and some keep growing until they merge, beyond which bulk reaction ensues.

Here, we discuss physical features which have been observed in uranium-hydrogen systems (and other metal-hydrogen systems) that are important to consider when building models.

1.1.1 Surface passivation layer

A surface passivation layer (SPL) is observed to grow on the surface of massive uranium metal when exposed to dry air, water vapour, or liquid water [21]. To some extent, the SPL passivates, or prevents the metal from reacting further [6]. The SPL mainly consists of oxide, but also includes hydroxides, carbides and other compounds, and is often referred to as 'the oxide layer'. H_2 molecules are adsorbed onto the oxide surface and penetrate the SPL to reach the metal-oxide interface. It is disputed whether hydrogen diffuses through the oxide as molecular H_2, atomic H or ionic H [8]. Provided hydrogen transport to the metal-oxide interface is larger than that from the interface into the bulk metal, hydrogen will begin to concentrate just below the SPL [22]. Hydrogen and uranium react to form uranium hydride UH_3 in the metal, below the SPL [5, 9]. Regions of metal which have thin SPL coverage have been shown to exhibit preferential hydride nucleation [5–7, 14]. Many metals such as copper [23], nickel [24], and various uranium alloys [25] exhibit different oxide thicknesses on different orientations of metal grain, and it can be expected that the same will be true for uranium metal.

It is possible for uranium hydride to be formed as a direct product of the uranium-water reaction. In this case, hydride and oxide are formed simultaneously. A thin $3-5$nm layer of hydride is produced below the SPL [26]. At a later stage, the hydride-metal interface becomes a moving reaction front for bulk hydriding. This system does not experience the nucleation and growth of hydride blisters [8], and is not the focus of this project. Rather, it focusses on the growth of hydrides in the case of a pre-existing SPL.

1.1.2 Effect of stress and the terminal solid solubility limit

Appel et al. performed experiments on the effect of pre-existing stress on hydride precipitation [27]. They used apparatus to bend uranium bars, generating tensile stresses up to 7.5×10^8Pa, and then exposed the bars to hydrogen. It was shown that in pre-stressed uranium samples, regions of metal with higher tensile stress showed faster rates of hydride precipitation.

Hydrides are observed to preferentially grow at grain boundaries [9, 10, 15], across which there is a change in the direction of metal lattice orientation. As previously stated, the thickness of the SPL can depend on the grain orientation of the metal it is grown on. The mismatch in oxide growth rate causes the induction of stress at grain boundaries, which is theorised to be the reason preferential growth is observed [18, 25].

The hydriding process itself generates stresses. The hydride, UH_3, is less dense than uranium metal [28], which causes local expansion, and therefore stresses are induced [29] which affect the future hydriding process.

When subject to stress, uranium hydride is brittle and tends to crack. On a pure uranium substrate, cracks appear on the top of large blisters [9]. A major effect which has been observed in zirconium studies is that hydriding is preferential near the tips of existing cracks due to the stress fields [30].

The reason why stress influences hydriding is linked to the terminal solid solubility limit (TSS). The TSS is the lowest hydrogen concentration in metal at which hydride will begin to form. The TSS of hydrogen in metals is observed to increase exponentially with temperature [10], so more hydrogen must be present in order to form hydride at higher temperatures. Since UH_3 is less dense than uranium, if compressive stresses exist in the material, hydrogen concentration will need to be higher for reaction to be energetically preferable [31]. It has been suggested that the TSS in hydride-forming metals depends on stress [31, 32].

The 1996 paper by Lufrano et al. [32] uses an equation for the TSS for hydride-forming metals under stress which was derived by Puls [33]:

$$C_{TSS}^{Puls} = A \exp\left[\frac{\Delta\bar{H}}{\chi RT}\right] \exp\left[\frac{\bar{w}_{acc}}{\chi RT}\right] \exp\left[\frac{\bar{w}_{int}}{\chi RT}\right] \exp\left[\frac{\bar{V}_H}{RT}\left(\frac{\sigma_k^k}{3}\right)\right] \tag{1.1}$$

where T is the temperature of the metal, A is a material-dependent factor, $\Delta\bar{H}$ is the molar enthalpy of formation of hydride, R is the ideal gas constant, $\bar{w}_{acc}$ is the molar

Gibbs Free Energy (GFE) to accommodate the strain caused by forming hydride from the solid solution, $\bar{w}_{int}$ is the molar GFE of the interaction between this strain and externally applied stresses and $\bar{V}_H$ is the partial molal volume of hydrogen dissolved in uranium. The variable σ_k^k is the trace of the stress. The constant, χ describes the stoichiometry of the hydride; for example $\chi = 3$ for UH_3. This equation for the TSS shows how it is affected by the heat release and expansion of hydride formation.

This is in contrast with the equation presented by Varias [34] in a model for zirconium hydriding:

$$C_{TSS}^{Varias} = C_{TSS}^{Puls} \exp\left[\frac{\bar{V}_H}{RT}\left(-\frac{1}{2}S^{ijkl}\sigma_{ij}\sigma_{kl}\right)\right] \tag{1.2}$$

where S^{ijkl} is the elastic compliance tensor. The author states that this exponential factor arises when deriving the solubility limit, but is usually neglected since the elastic compliance of metals is very small [34].

Lufrano, Sofronis and Birnbaum provide a two-fold explanation of why areas of tensile stress are subject to preferential hydride precipitation in niobium [32]. They state that areas of higher tensile stress within the metal experience more inward hydrogen diffusion. Additionally, in such regions, it is energetically preferable for the reaction to proceed. In the 2015 review on hydride degradation in zirconium by Bair et al. [35], the causal relation between the two effects is explored. Two models are presented: the precipitation-first model [36] and the diffusion-first model [37]. The precipitation first model describes that stresses at crack tips ease the constraints for precipitation and thus lower the TSS. Hydride is formed, removing diffusing hydrogen from the system. This induces a hydrogen concentration gradient and so hydrogen diffuses towards the crack. It is the diffusion first model, however, which is now regarded to be correct [38]. This states that it is the stress field near a crack tip that directly causes hydrogen to diffuse in. Once hydrogen concentration reaches the TSS, more hydride is formed. This hydride may in turn crack easily, and as such the crack propagates.

Literature on the importance of the effect of temperature and stress on TSS specific to uranium could not be found, so the extent to which they affect the model overall is thus far unclear. In this report, the solubility limit is assumed to not depend directly on these quantities.

Stress also affects the SPL; some of the blisters on the metal-oxide interface generate a high enough stress field to crack the SPL. If the crack is large enough, the hydride may breach the SPL and be exposed to the atmosphere [14].

As a further note on TSS, in zirconium [39], zircaloy-2 [40], zircaloy-4 [40] and titanium [41], there have been found to be two distinct solubility limits. One is the concentration limit above which hydride precipitates, C^p_{TSS}). The other is the concentration limit below which hydride can re-dissolve, C^d_{TSS}. The difference between the two is significant [40]. No discussion of C^p_{TSS} and C^d_{TSS} for uranium has been found in the literature over the course of this work. It is unclear whether there has just been little work done in the area so far - until recently, most of the literature has been concerned solely with hydriding, but the advent of uranium as a possible hydrogen storage mechanism has opened up more interest in uranium de-hydriding. For this reason, a single C_{TSS} value was used in the model used in this report.

1.1.3 Diffusion coefficient

An increased diffusion coefficient means hydrogen diffuses more readily into the metal. However, it is also quicker to diffuse away from the metal-oxide interface into the bulk. Both have an effect on the rate at which hydrogen concentrates close to the interface. It has been shown that the diffusion coefficient (or diffusivity), D_U, for hydrogen in uranium increases with temperature as an Arrhenius relation [17].

Arrhenius relations are classically used to obtain the rate constant, k, of a reaction

$$k = A\exp\left(-E_A/RT\right) \tag{1.3}$$

where E_A is the activation energy of the reaction and A is a constant. This means we may consider the numerator of the exponent in the Arrhenius diffusion coefficient to be the activation energy of diffusion. Condon found the diffusivity to be [17]

$$D_U = 1.9\times10^{-6}\exp(-5820/T)\mathrm{m}^2\mathrm{s}^{-1}. \tag{1.4}$$

Mallett and Trzeciak derived a different expression for the diffusivity [42], which can also be converted into the Arrhenius form,

$$D_U = 1.9\times10^{-6}\exp(-5570/T)\mathrm{m}^2\mathrm{s}^{-1}. \tag{1.5}$$

This is the expression used in this report, as suggested by my industrial supervisor.

Some models, including that by Lufrano et al. [32] use an effective diffusion coefficient which is equal to an average between that of metal and hydride, weighted by their relative abundance. Another model of hydriding by Condon [17], assumes that

the diffusivity is constant and equal to the value in pure metal. This is due to the tendency of hydride to readily disintegrate into powder - diffusion through hydride cannot affect processes in the metal once it has spalled. Again further models [43, 44] assume that the diffusion in the hydride is significantly slower and neglect hydrogen flux in the hydride altogether. Diffusion of hydrogen has been shown to be slower in hydride than in uranium metal [10].

1.1.4 Blister nucleation

As mentioned previously, hydrides form preferentially below regions of thin SPL and on metal grain boundaries. They also grow at inclusions of other compounds and imperfections such as scratches on the metal.

Hydride begins to form on uranium as blisters or pits [7–9]. In uranium, the cause of the preferential hydriding influences the behaviour of the blister during the growth phase [10]. Blisters are segregated into two distinct families - large, fast-growing blisters which eventually coalesce to form a layer of hydride [15], and small blisters, which exhibit slow growth.

Arkush et al. observed small blisters growing on scratches caused by the pretreatment of the metal [9]. They were observed to cease growth at around $5\mu m$. It has been suggested [8] that these hydrides cease to grow because of the large compressive stress imposed by the oxide layer. If the stress field is not large enough to cause a breach of the oxide, they simply stop growing.

Larger hydride blisters have been observed to form in the vicinity of carbide inclusions [9, 14, 45]. Owen and Scudamore suggested that this is because the inclusion provides a route through the SPL which is easier for the hydrogen to traverse [14]. These blisters are less densely populated than the hydride blister patterns seen elsewhere.

1.2 Existing reaction-diffusion models

In this section, we discuss previous uses of reaction-diffusion and advection-reaction-diffusion equations to model gas diffusion through metals where the lattice and solute react to form a compound.

Dutton and Puls [37] studied hydrogen diffusion in zirconium using a steady-state

equation for the hydrogen flux $\mathbf{J}$,

$$\nabla \cdot \mathbf{J} = 0. \tag{1.6}$$

This is cited as one of the first efforts to model a hydriding process with a diffusion equation, though it doesn't capture any of the time dependent behaviour.

A 2000 paper by Tanski et al. [46] uses an advection-reaction-diffusion system to describe the reaction. Their central equation is

$$\frac{\partial C}{\partial t} = \nabla \cdot (D_U \nabla C) - Da\, C_{UH} \left(C - \frac{1}{K_e} \right), \tag{1.7}$$

with two more to describe the depletion of pure uranium metal and pure hydrogen. C and C_{UH} are the concentrations of hydrogen and hydride, K_e is an equilibrium constant and Da is the ratio of reaction rate to diffusivity (the Damköhler number). The authors state that the reaction term exhibits a dependence on the hydride concentration because the expansion of the matrix feeds the reaction rate. They also include SPL breach and some stress effects in the modelling. If the local concentration of hydride is higher than the concentration required for rupture, then the metal is assumed to be in direct contact with the hydrogen gas. Also, if hydride reaction occurs in one region, due to its expansion, the neighbouring regions will be affected by work-hardening. The effect of the work-hardening is incorporated by changing the hydride concentration for rupture.

In their simulations, they start with a randomly distributed hydrogen concentration and they observe the formation of hydride pits. These pits grow until they reach the surface, when they begin to spread across the surface. They do not make comparisons with experiment, but they do see nucleation and growth of hydrides. However, the model they use predicts sub-surface hydride nucleation when experimentally, it is observed at the metal-oxide interface. They do not take into account the effect of temperature or stress on the hydrogen diffusion.

J. Condon also produced a reaction-diffusion system model [17];

$$\frac{\partial C}{\partial t} = D_U \frac{\partial^2 C}{\partial x^2} + \chi \frac{\partial U}{\partial t} \tag{1.8}$$

$$\frac{\partial U}{\partial t} = -k_1 C U \tag{1.9}$$

where again $\chi = 3$ for UH_3, k_1 is a reaction rate constant, and U is the molar fraction of unreacted uranium. D_U and k_1 are functions of temperature. The author includes the spalling of the hydride layer by the use of a moving boundary. To calculate the

moving boundary location, they find the stress due to expansion. If the stress is above a critical value for fracture, the material has spalled. So the boundary is set to be the outermost point for which stress is less than critical. Typical experimental reaction rates for this reaction produce s-shaped curves, where the central region shows that the reaction progresses linearly outside of the initial and final stages. The Condon results showed good correlation with measured values for reaction rate. However, the effects of stress and temperature have not been thoroughly explored - stress is not considered to affect hydrogen flux.

In neither of the above models is the possibility of de-hydriding discussed. However, this can be seen in a further similar model by Kirkpatrick and Condon [47]. The key equations are

$$\frac{\partial C}{\partial t} = \frac{\partial}{\partial x}\left(\frac{D_U C_{sat}}{C_{sat} - C}\frac{\partial C}{\partial x}\right) + \chi\frac{\partial U}{\partial t} \tag{1.10}$$

$$\frac{\partial U}{\partial t} = -k_1 C U + k_2(1-U)^{1/3} \tag{1.11}$$

where the final term in the second equation contains the de-hydriding reaction rate constant k_2. Apart from the addition of the de-hydriding term, we also see the spatial derivative of concentration is pre-factored by $\frac{D_U C_{sat}}{C_{sat}-C}$. C_{sat} is the concentration at which the matrix is saturated with free diffusing hydrogen, the maximum possible concentration.

This model achieved good comparison with experiments to determine the velocity of the spall front by Galkin et al. [48] for low temperatures, but poor comparison at higher temperatures. They also compared their work on the depletion rate of U with the experiments of Bloch and Mintz [16] but were "dissatisfied" with the results.

A 1996 paper by Lufrano, Sofronis and Birnbaum uses a continuum mechanics model to predict the hydride growth which includes the effect of stress [32]. The equation used for diffusion is

$$q\frac{\partial C}{\partial t} = \frac{\partial}{\partial x}\left(D_U\frac{\partial C}{\partial x} + \frac{DC}{RT}\frac{\partial \mu}{\partial x}\right) \tag{1.12}$$

where the chemical potential of the diffusing hydrogen in the stressed solid, $\mu = \mu|_{\sigma=0} - \bar{V}_H\sigma_k^k/3$, (with $\mu|_{\sigma=0}$ is the chemical potential in the same unstressed solid).

The parameter q is given by

$$q = \begin{cases} 1-f, & \text{if} \quad 0 \leq f < 1 \\ 1, & \text{if} \quad f = 1 \end{cases} \tag{1.13}$$

and f is the volume fraction of hydride which depends on the local hydrogen concentration. For the stress-strain constitutive law, a linear, homogeneous, isotropic elastic relation is used:

$$\sigma^{ij} = 2G\varepsilon^{ij} + \lambda\left(\varepsilon^k_k - \varepsilon^{k\,H}_k\right)\delta^{ij} \tag{1.14}$$

where $\varepsilon^{ij} = \frac{1}{2}\left(\frac{\partial u^i}{\partial x_j} + \frac{\partial u^j}{\partial x_i}\right)$ is the strain, with u^i the displacement of a material particle in the x^i direction. The superscript H denotes strain due to hydrogen effects and λ and G are the first and second Lamé coefficients respectively. Dilational strains are considered for calculation of the strain rate tensor $\dot{\varepsilon}$ caused by hydride production:

$$\dot{\varepsilon}^H = \frac{1}{3}\frac{d}{dt}\left[\frac{\bar{V}_{Hr}}{\bar{V}_U}f + (1-f)\bar{V}_H C\right]. \tag{1.15}$$

The ratio of partial molar volume of hydride to uranium, $\bar{V}_{Hr}/\bar{V}_U$, is the factor by which the volume is increased when uranium forms hydride. Again, the model does not explore the effects of all factors that drive diffusion - here the temperature is not considered. It is well-documented that temperature gradients affect hydrogen diffusion in metals [49, 50].

The models in the literature which are closest to this work are discussed thoroughly in the next section. To obtain a model in which temperature, stress, expansion, and concentrations of hydrogen and hydride are not fixed, a highly coupled system of equations is required, with these quantities as independent variables. This has not been exhausted in the models detailed above. The first part of this thesis will aim to investigate such a model to produce a description of the hydriding process within the reaction-diffusion framework.

The model comprises a reaction-diffusion problem to conserve mass of diffusing hydrogen, an equation to describe the chemical reaction between uranium and hydrogen, the equations of linear thermoelasticity and an equation to describe thermal conduction. There are five independent variables: concentrations of uranium U and diffusing hydrogen C, temperature T, stress σ and displacement $\mathbf{u}$ describing material deformation.

Chapter 2

Model Derivation

The system we will model is a block of uranium metal with a pre-existing surface passivation layer (SPL) on its surface in the presence of atmospheric hydrogen. Figure 2.1(a) shows the proposed set-up — in each image, a cross section taken perpendicular to the material surface is shown, with the atmosphere at the top of the images and the bulk of uranium metal at the bottom. In this case, we see the SPL (shown in pink) is of non-uniform thickness. As described in Chapter 1, we expect to see uranium hydride forming preferentially in areas where the SPL is thin. In figure 2.1(b) we see hydride initiation below the region of thin SPL, and fig. 2.1(c) shows the hydride growing. As the hydride grows, the SPL deforms. Finally, in fig. 2.1(d), the hydride breaches the SPL and hydride is exposed to the atmosphere.

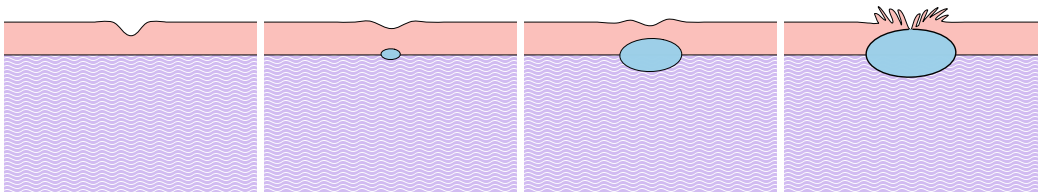

(a) Pre-hydriding (b) Hydride initiation (c) Hydride growth (d) Blister breach

Figure 2.1: Schematic to show four sequential stages of uranium hydriding (a-d). In each sub-figure, purple indicates uranium metal, pink is the SPL and the blue blister is uranium hydride. In (a), a block of uranium is shown with an SPL of non-uniform thickness on its surface, (b) and (c) show the initiation and growth of a hydride blister at the metal-SPL interface and (d) shows blister breach.

There are many physical features that would need to be accommodated into a model for it to completely adhere to the observed process, as discussed in Chapter 1. The model used in this project will encompass the following processes:

- Firstly, hydrogen in the atmosphere is absorbed by the material, as shown in figure 2.2. Martin et al. [51], describe this process as physisorption of a H_2 molecule on the surface, followed by chemisorption whereby the molecule dissociates into two atoms, and surface penetration of those atoms.

- Then, in the case where an SPL is present, hydrogen diffuses through the SPL as shown in figure 2.2(a). Whether there is an SPL present or not (as in the case of figure 2.2(b)), hydrogen will reach the uranium surface.

- If the local concentration of hydrogen in uranium is above the terminal solid solubility (TSS) at any point, the hydriding reaction proceeds.

- Hydriding is exothermic, so reaction can increase the temperature of the system. These changes in temperature induce thermal expansion of the material.

- The material experiences lattice expansion through two mechanisms: the inclusion of hydrogen in the uranium as a solute, and the expansion when hydride is formed.

- In cases where material deformation is localised, or some condition restricts the expansion, the material experiences stresses.

- Stress affects the chemical potential.

- Non-uniform changes in temperature and chemical potential in turn affect hydrogen flux.

This makes for a potentially highly-coupled model. Most models that currently exist in the literature, some of which are detailed in the previous chapter, do not include all of these effects. Many consider a less complex model; sometimes just the concentration of hydrogen is modelled, sometimes temperature effects are neglected and some authors do not consider the effect of stress. To fully model the behaviour of a real system, all of the above will need to be included.

The model presented in this work is a multi-physics continuum mechanics model, guided by the description above. It is made up of:

- A mass conservation equation for the concentration of solute hydrogen, C, present at each point in the material. The equation should describe hydrogen diffusion, depletion of solute hydrogen as hydride is formed, and the effect of stress and temperature on the hydrogen flux. Concentration is in units of mol m^{-3}.

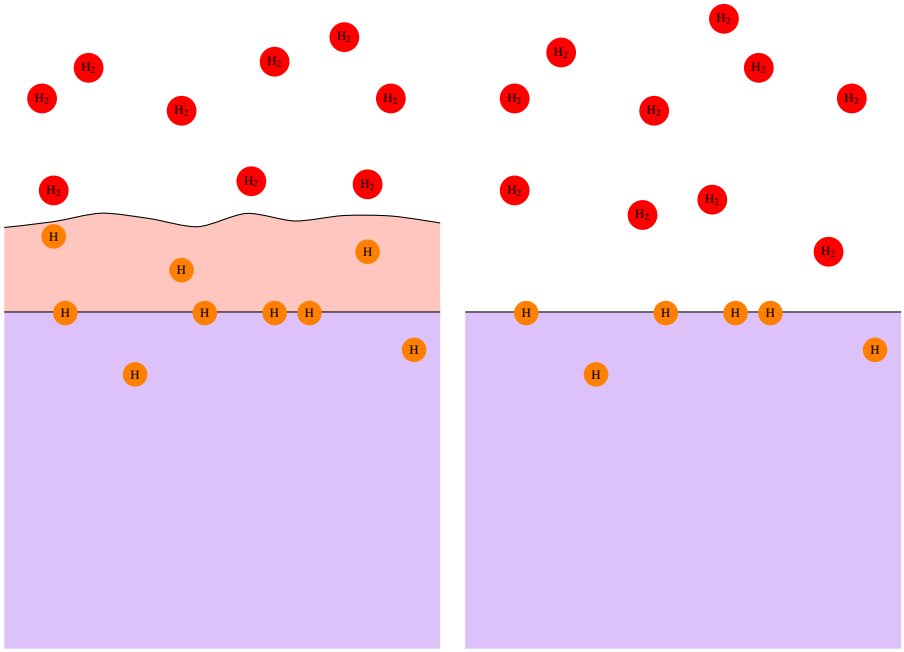

(a) With SPL (b) Without SPL

Figure 2.2: Schematic to show hydrogen absorption from the atmosphere and diffusion into the material. Purple indicates uranium metal, pink is the SPL, the red circles are H_2 molecules present in the atmosphere and the orange circles are the H atoms dissolved in the solid material.

- An energy conservation equation, which should describe heat conduction in the solid material, the exothermic effect of hydride production, and any changes in temperature associated with the flow of hydrogen in the material. This equation is solved for temperature of the material, T, in units of K.
- An equation for the conservation of linear momentum and a stress-displacement relation to describe how the material deforms. They should encode material deformations due to thermal expansion, the presence of diffusing hydrogen, and expansion as hydride is formed. These equations are solved for stress σ in Nm^{-2} and displacement u in m.
- An equation to describe the hydriding reaction, which will only proceed when hydrogen concentration is above the TSS. Two different quantities are used in this report to measure the extent of reaction: the volume fraction of hydride, f, a dimensionless quantity which takes a value between 0 and 1 and the remaining concentration of uranium, U, in units of mol m^{-3}.

To summarise, the model will consist of five field equations which can be solved

for the five field variables, C, T, σ, u and f or U. The remainder of this chapter focuses on building such a model. Regarding the (many) physical parameters in this problem, a comprehensive list of the values used in this report are found in Appendix F, alongside sources. Some of the parameters could not be found for the uranium-hydrogen binary system and have instead been approximated by their values for other metals.

2.1 Conservation of mass

The first equation we consider ensures the total mass of hydrogen in the system is conserved. Total mass of hydrogen includes diffusing hydrogen and hydrogen bound in hydride. As in the treatment by Varias [52], we first look at the rate of change of the number of moles of hydrogen in some volume Ω_0 with respect to the Lagrangian coordinate system. This rate is balanced by the flow of hydrogen out of the volume. The boundary of the volume Ω_0 is the surface $\partial\Omega_0$, which has an outer unit normal $\mathbf{n}$. All quantities are measured on the undeformed configuration. We obtain a continuity equation

$$\frac{d}{dt}\int_{\Omega_0} c_{TOT}\,dV_0 + \int_{\partial\Omega_0} \mathbf{j}\cdot\mathbf{n}\,dS_0 = 0. \tag{2.1}$$

The total concentration of hydrogen, c_{TOT}, is measured in moles per unit volume of the undeformed configuration. The concentration flux across the boundary $\mathbf{j}$ is measured in moles per unit area of the undeformed configuration per second. Moving the time derivative inside the integral, and using the divergence theorem gives

$$\int_{\Omega_0}\left(\frac{dc_{TOT}}{dt} + \nabla_{\mathbf{x}}\cdot\mathbf{j}\right)dV_0 = 0. \tag{2.2}$$

The spatial derivative is taken with respect to the Lagrangian coordinate system. We now use that the time derivative of any quantity measured on the undeformed configuration is equivalent to its partial time derivative. Also, since Equation (2.2) is valid on an arbitrary volume, we have the differential equation

$$\frac{\partial c_{TOT}}{\partial t} + \nabla_{\mathbf{x}}\cdot\mathbf{j} = 0, \tag{2.3}$$

which is Fick's second law on the Lagrangian configuration [50].

Repeating this argument for a deforming volume, Ω_t bounded by the surface $\partial\Omega_t$

which has outer unit normal $\mathbf{N}$, we begin with

$$\frac{d}{dt}\int_{\Omega_t} C_{TOT}\,dV_t + \int_{d\Omega_t} \mathbf{J}\cdot\mathbf{N}\,d\Omega_t = 0. \tag{2.4}$$

C_{TOT} and $\mathbf{J}$ are the total concentration and flux of hydrogen measured per unit volume and per unit surface area of the deformed configuration respectively. If $\mathbf{X}$ is the Eulerian coordinate system, the deformation gradient tensor $\mathbf{F}$ is defined by $F_j^{\bar{i}} = \frac{\partial X^{\bar{i}}}{\partial x^j}$, and we have $c_{TOT} = |\mathbf{F}|C_{TOT}$ and $\mathbf{j} = |\mathbf{F}|\mathbf{F}^{-1}\mathbf{J}$.

In Equation (2.4), the volume Ω_t is time-dependent, and we must use the Reynolds Transport Theorem to move the time derivative inside the integral:

$$\int_{\Omega_t}\left(\frac{DC_{TOT}}{Dt} + C_{TOT}\nabla_{\mathbf{X}}\cdot\mathbf{V}\right)dV_t + \int_{d\Omega_t}\mathbf{J}\cdot\mathbf{N}\,d\Omega_t = 0. \tag{2.5}$$

The time derivative of C_{TOT} is the material derivative $\frac{D}{Dt}$ and the spatial derivative is taken with respect to the Eulerian coordinate system $\mathbf{X}$. The Eulerian velocity of a material particle $\mathbf{V}$ is the velocity of each point in the moving domain and encodes the deformation from Ω_0 to Ω_t. Application of the divergence theorem and expansion of the material derivative gives

$$\int_{\Omega_t}\left(\frac{\partial C_{TOT}}{\partial t} + \nabla_{\mathbf{X}}\cdot(C_{TOT}\mathbf{V}) + \nabla_{\mathbf{X}}\cdot\mathbf{J}\right)dV_t = 0. \tag{2.6}$$

Again we argue that this equation is true on an arbitrary volume Ω_t to obtain Fick's second law in the Eulerian configuration

$$\frac{\partial C_{TOT}}{\partial t} + \nabla_{\mathbf{X}}\cdot(C_{TOT}\mathbf{V} + \mathbf{J}) = 0. \tag{2.7}$$

We have $\mathbf{V} = \frac{\partial \mathbf{U}(\mathbf{R},t)}{\partial t}|_{\mathbf{r}}$, the velocity of a given material particle. The displacement $\mathbf{U}(\mathbf{R},t)$ describes the deformation of this material point from the original position $\mathbf{r}$, to its current position $\mathbf{R}$ and is defined by

$$\mathbf{U}(\mathbf{R},t) = \mathbf{R} - \mathbf{r}(\mathbf{R},t). \tag{2.8}$$

Equations (2.3) and (2.7) are Fick's second law in the Lagrangian and Eulerian representations respectively. The method of solution employed in this work is the finite element method, in which solving Eulerian equations is more complicated and requires the calculation of the moving domain. By assuming that deformations are sufficiently

small, we will now show that the Lagrangian equation may be used to approximate the Eulerian equation, and we will apply similar logic to other equations throughout this chapter.

We assume that for all material points in the domain, the displacement remains small, giving the current position

$$\mathbf{R} = \mathbf{r}(\mathbf{R},t) + \mathbf{U}(\mathbf{R},t) = \mathbf{r}(\mathbf{R},t) + \varepsilon\hat{\mathbf{U}}(\mathbf{R},t) \tag{2.9}$$

in the Eulerian frame, or

$$\mathbf{R}(\mathbf{r},t) = \mathbf{r} + \mathbf{u}(\mathbf{r},t) = \mathbf{r} + \varepsilon\hat{\mathbf{u}}(\mathbf{r},t) \tag{2.10}$$

in the Lagrangian frame. All components of $\hat{\mathbf{U}}(\mathbf{R},t)$ and $\hat{\mathbf{u}}(\mathbf{r},t)$ are $O(1)$ and $\varepsilon << 1$. We now turn our attention to the case of a one-dimensional problem for brevity.

The one-dimensional Eulerian and Lagrangian coordinates are related by $X(x,t) = x + \varepsilon\hat{u}(x,t)$. Using equation (2.10), performing a derivative in the X-direction becomes

$$\frac{\partial}{\partial X} = \left(\frac{\partial X}{\partial x}\right)^{-1}\frac{\partial}{\partial x} = \left(1+\varepsilon\frac{\partial \hat{u}}{\partial x}\right)^{-1}\frac{\partial}{\partial x} = \left(1-\varepsilon\frac{\partial \hat{u}}{\partial x} + O(\varepsilon^2)\right)\frac{\partial}{\partial x}. \tag{2.11}$$

We also have that the Eulerian velocity is of $O(\varepsilon)$

$$V(X,t) = \left.\frac{\partial U(X,t)}{\partial t}\right|_x = \varepsilon\frac{\partial \hat{U}(X,t)}{\partial t}. \tag{2.12}$$

We substitute these into a one-dimensional version of Equation (2.7)

$$\begin{aligned}\frac{\partial C_{TOT}}{\partial t} &+ \frac{\partial}{\partial X}(C_{TOT}V + J) \\ &= \frac{\partial C_{TOT}}{\partial t} + \left(1-\varepsilon\frac{\partial \hat{u}}{\partial x} + O(\varepsilon^2)\right)\frac{\partial}{\partial x}\left(C_{TOT}\varepsilon\frac{\partial \hat{U}(X,t)}{\partial t} + J\right) \\ &= 0\end{aligned} \tag{2.13}$$

To leading order,

$$\frac{\partial C_{TOT}}{\partial t} + \frac{\partial J}{\partial x} = 0 \tag{2.14}$$

and we have that for sufficiently small deformations, the Eulerian Fick's law is equivalent to Equation (2.3), the Lagrangian Fick's law in one dimension. Extending this

idea to three dimensions, we have

$$\frac{\partial C_{TOT}}{\partial t} + \nabla_{\mathbf{x}} \cdot \mathbf{J} = 0. \tag{2.15}$$

We can use the Lagrangian Fick's Law to approximate the relationship between Eulerian concentration and flux. This small deformation approximation will be revisited when discussing other equations.

2.2 Hydrogen flux

Hydrogen diffusion into the system initiates the process of hydriding. The speed of hydrogen diffusion through a solid depends on gradients of temperature, concentration and stress within the system.

Many authors who have investigated models for this behaviour, including Varias and Massih [43], have used modified versions of Fick's first law to model hydrogen diffusion in metals. One such equation is derived by Shewmon in Diffusion in Solids [50] as described below. It is observed that when considering mass diffusion in isolation, it is governed by the tendency of matter to move to reduce concentration gradients. This is Fick's first law

$$\mathbf{J} = -D\nabla_{\mathbf{x}} C \tag{2.16}$$

where D is called the diffusion coefficient or the diffusivity. $\mathbf{J}$ is the Eulerian mass flux of hydrogen and again we use that Eulerian and Lagrangian spatial derivatives are equivalent to leading order for small deformations (see Equation (2.11)). Diffusion is assumed to be isotropic.

Temperature gradient is also observed to affect mass flux. Including this in our flux equation gives

$$\mathbf{J} = -D\nabla_{\mathbf{x}} C - \beta\nabla_{\mathbf{x}} T \tag{2.17}$$

where the sign of the constant β depends on whether the solute is more likely to move up or down a temperature gradient. The applied temperature gradient doesn't change the mechanism by which the solute molecules move, it serves to alter the probability with which they move in either direction. Shewmon argues that this implies that β is proportional to D [50] and gives the relationship between them as $\beta = \frac{DQC}{RT^2}$ where Q is called the heat of transport, which is determined experimentally, and R is the ideal gas

constant. Our modified Fick's law is

$$\mathbf{J} = -D\nabla_{\mathbf{x}}C - \frac{DQC}{RT^2}\nabla_{\mathbf{x}}T. \tag{2.18}$$

In the model we are considering, we wish to include the effect of deformation and stress. Stress-driven diffusion is important to include here because we hope to build a model which can look at hydride blister formation and growth - localised processes which induce stresses in the metal.

For a stressed solid, the effects of stress and concentration gradients on diffusion are encoded in the chemical potential, μ. Chemical potential is the partial molar free energy; the amount of free energy which is added to the system when one mole of the chemical species is added at a constant temperature. It is measured in $J\ mol^{-1}$. By the argument described by Shewmon [50], $\mathbf{F}_D = -\nabla_{\mathbf{x}}\mu$ is considered to be a 'driving force' of the mass flux since solute tends to flow down gradients of chemical potential. The associated drift velocity of a diffusing solute particle due to that force is $\mathbf{v} = M\mathbf{F}_D = -M\nabla_{\mathbf{x}}\mu$ where M is a coefficient which describes the mobility of the substance. Einstein's equation for the solute mobility is given by $M = \frac{D}{k_B T}$,where k_B is Boltzmann's constant. To obtain the driving force of a single particle, we must also divide by Avogadro's number N_A [53].

Substituting M into the drift velocity in the case of a single particle, we have an equation for the particle velocity [50, 53]

$$\mathbf{v} = -\frac{D}{k_B N_A T}\nabla_{\mathbf{x}}\mu = -\frac{D}{RT}\nabla_{\mathbf{x}}\mu \tag{2.19}$$

where $R = k_B N_A$ has been substituted. The mass flux associated with the chemical potential gradient is

$$\mathbf{J} = C\mathbf{v} = -\frac{DC}{RT}\nabla_{\mathbf{x}}\mu \tag{2.20}$$

This is added to the mass flux associated with the temperature gradient $-\frac{DQC}{RT^2}\nabla_{\mathbf{x}}T$ as in Equation (2.18) to give the mass flux of diffusing solute driven by gradients of chemical potential and temperature

$$\mathbf{J} = -\frac{DC}{RT}\left(\nabla_{\mathbf{x}}\mu + \frac{Q}{T}\nabla_{\mathbf{x}}T\right). \tag{2.21}$$

2.3 Chemical potential

For the chemical potential of a stress-free solid with a diffusing substance, we have Raoult's law [54]

$$\mu = \mu_0 + RT\ln(C) \tag{2.22}$$

where μ_0 is the chemical potential of the unstressed solid with zero solute concentration. We assume the metal is homogeneous when there is no hydrogen diffusion or stress, so $\nabla_{\mathbf{x}}\mu_0 = 0$. The chemical potential only appears in the equations as $\nabla_{\mathbf{x}}\mu$, so we are not required to know the value of μ_0: $\nabla_{\mathbf{x}}\mu_0 = 0$ is sufficient.

The equation for chemical potential of a stressed solid with a diffusing substance is derived from thermodynamic arguments laid out by Li [55] and is shown in full in Appendix A. The result is

$$\mu = \mu_0 + RT\ln(C) + \frac{\partial w}{\partial n} - W. \tag{2.23}$$

The term $\frac{\partial w}{\partial n}$ is the partial molal strain energy (the increase in strain energy, w, per number of moles of solute added, n). W is the work done by external stresses when one mole of the diffusing substance is added to the system.

Varias' 1998 paper [34] showed how these final two terms should be written in terms of the Cauchy stress, σ, and we finally have

$$\mu = \mu_0 + RT\ln(C) - \frac{\sigma_k^k}{3}\bar{V}_H \tag{2.24}$$

where σ_k^k is the trace of the Cauchy stress tensor and $\bar{V}_H$ is the partial molar volume of diffusing hydrogen in the metal (the increase in volume when one mole of hydrogen is diffused into the metal matrix). The details of this calculation are also shown in Appendix A.

2.4 Conservation of energy

The conservation of energy equation is derived from the material derivative of the internal energy and entropy per unit mass following the arguments by Varias [34, 56]. It is included in its entirety in Appendix B, with references to terms that are specific to

hydriding. The resulting equation is

$$\rho c_p \frac{DT}{Dt} + \frac{\Delta \bar{H}}{\bar{V}_{Hr}} \frac{Df}{Dt} = \nabla_{\mathbf{X}} \cdot (\kappa \nabla_{\mathbf{X}} T) - \mathbf{J} \cdot \nabla_{\mathbf{X}} \mu, \tag{2.25}$$

where ρ is the density of uranium, c_p is the specific heat capacity at constant pressure, $\Delta \bar{H}$ is the change in molar enthalpy due to the formation of UH_3, $\bar{V}_{Hr}$ is the partial molar volume of UH_3, f is the volume fraction of UH_3 (which is described in more detail in section 2.8.1) and κ is the thermal conductivity of uranium. The spatial derivatives are taken with respect to the Eulerian coordinates, $\mathbf{X}$, and the derivatives $\frac{DT}{Dt}$ and $\frac{Df}{Dt}$ are material derivatives.

We look at the one-dimensional equivalent of equation (2.25) and expand the material derivatives

$$\rho c_p \left(\frac{\partial T}{\partial t} + V \frac{\partial T}{\partial X} \right) + \frac{\Delta \bar{H}}{\bar{V}_{Hr}} \left(\frac{\partial f}{\partial t} + V \frac{\partial f}{\partial X} \right) = \frac{\partial}{\partial X} \left(\kappa \frac{\partial T}{\partial X} \right) - J \frac{\partial \mu}{\partial X}. \tag{2.26}$$

Using equations (2.11) and (2.12) to replace the Eulerian velocity V and Eulerian derivative, we have to leading order,

$$\rho c_p \frac{\partial T}{\partial t} + \frac{\Delta \bar{H}}{\bar{V}_{Hr}} \frac{\partial f}{\partial t} = \frac{\partial}{\partial x} \left(\kappa \frac{\partial T}{\partial x} \right) - J \frac{\partial \mu}{\partial x}. \tag{2.27}$$

The equivalent three-dimensional equation is

$$\rho c_p \frac{\partial T}{\partial t} + \frac{\Delta \bar{H}}{\bar{V}_{Hr}} \frac{\partial f}{\partial t} = \nabla_{\mathbf{x}} \cdot (\kappa \nabla_{\mathbf{x}} T) - \mathbf{J} \cdot \nabla_{\mathbf{x}} \mu, \tag{2.28}$$

and we again have an equation where the derivatives are with respect to the Lagrangian coordinate system, $\mathbf{x}$.

2.5 Conservation of momentum

Cauchy's equation of motion is

$$\rho \frac{D\mathbf{V}}{Dt} = \nabla_{\mathbf{X}} \cdot \sigma + \rho \mathbf{F}_B \tag{2.29}$$

where $\mathbf{F}_B$ represents any body forces acting. This equation is a representation of Newton's second law in a continuum. We can simplify it by considering the different timescales present. The timescale of interest in this problem is that of diffusion. On

the diffusion timescale, the solid is always in approximate equilibrium, so the acceleration term is zero. We consider a system with no body forces acting and a Cartesian coordinate system, so we have

$$\frac{\partial \sigma_{ij}}{\partial X_j} = 0. \tag{2.30}$$

Alternatively, using the small-deformation approximation in equation (2.10), we may write to leading order

$$\frac{\partial \sigma_{ij}}{\partial x_j} = 0 \tag{2.31}$$

where the derivative is with respect to the Lagrangian coordinates.

2.6 Strain tensors

The material modelled in this work undergoes deformation due to elastic effects, changes in temperature, hydrogen diffusion and the reaction to form hydride. To describe this deformation, we define three infinitesimal (or Cauchy) strain tensors, ε, ε^{Th} and ε^{H}, which describe strain due to elastic, thermal and hydrogen effects respectively. The strains are infinitesimal since we assume all deformations are small.

The infinitesimal strain tensor

$$\varepsilon_{ij} = \frac{1}{2}\left(\frac{\partial u_i}{\partial x^j} + \frac{\partial u_j}{\partial x^i}\right) \tag{2.32}$$

describes the deformation of a material, where u_i is the displacement in the x_i direction. The tensor is defined on the Lagrangian Cartesian coordinate system, but we can argue, as usual, that differentiation with respect to Lagrangian and Eulerian coordinates is equivalent for small deformations. The thermal strain is

$$\varepsilon^{Th}{}_{kl} = \alpha \Delta T \delta_{kl} \tag{2.33}$$

where δ_{kl} is the Kronecker delta and α is the coefficient of thermal expansion, which describes change in volume with respect to temperature change, ΔT.

The strain measure ε^{H} includes expansion caused by hydrogen diffusing into the metal and the expansion during hydride formation. In his 1961 work on solute diffusion in semiconductors [57], Prussin states a one-dimensional equation for the effect of solute concentration on strain in a material. The relation was extended to three

dimensions by Yang [58] to give a volumetric expansion

$$\varepsilon^{H1}{}_{kl} = \frac{1}{3} C \bar{V}_H \delta_{kl}. \tag{2.34}$$

We assume that hydride and metal experience the same expansion when hydrogen diffuses though: partial molar volume of hydrogen in hydride is equal to that in uranium metal.

We also wish to incorporate the isotropic expansion due to hydride formation. We use [32, 59]

$$\varepsilon^{H2}{}_{kl} = \frac{1}{3} f \frac{\bar{V}_{Hr}}{\bar{V}_U} \delta_{kl} \tag{2.35}$$

where $\bar{V}_{Hr}$ and $\bar{V}_U$ are the partial molar volumes of hydride and uranium respectively. Their ratio is the multiple by which the volume of the metal lattice grows when hydride is formed. We have [43]

$$\varepsilon^H = \varepsilon^{H1} + \varepsilon^{H2} \tag{2.36}$$

Note that δ^k_k is equal to the dimension of the system: in one dimension $\delta^k_k = 1$, in two dimensions $\delta^k_k = 2$ and in three dimensions $\delta^k_k = 3$. This equation for the strain due to hydrogen effects is similar to the one derived by Lufrano, Sofronis and Birnbaum [32] that was described in chapter 1 but differs since we also allow for hydrogen to diffuse through hydride.

2.7 Stress-strain relation

The second Piola-Kirchoff stress, s^{ij} is the force per unit undeformed area. For a linear thermoelastic material, s^{ij} is defined by

$$\sigma^{ij} = \tilde{J} s^{ij} \tag{2.37}$$

where σ^{ij} is the Cauchy stress and $\tilde{J}$ is the Jacobian of the deformation gradient tensor, given by

$$\tilde{J} = \frac{\left| \frac{\partial \mathbf{R}}{\partial x^i} \cdot \frac{\partial \mathbf{R}}{\partial x^j} \right|}{\left| \frac{\partial \mathbf{r}}{\partial x^i} \cdot \frac{\partial \mathbf{r}}{\partial x^j} \right|}. \tag{2.38}$$

Using the small deformation approximation in equation (2.10), we can write

$$\tilde{J} = \frac{\left| \frac{\partial(\mathbf{r}+\varepsilon\hat{\mathbf{u}})}{\partial x^i} \cdot \frac{\partial(\mathbf{r}+\varepsilon\hat{\mathbf{u}})}{\partial x^j} \right|}{\left| \frac{\partial \mathbf{r}}{\partial x^i} \cdot \frac{\partial \mathbf{r}}{\partial x^j} \right|} = 1 + O(\varepsilon) \tag{2.39}$$

so to leading order, $\sigma^{ij} = s^{ij}$. The linear thermoelastic constitutive law which relates s^{ij} to the strain is [43, 60]

$$s^{ij} = s_0^{ij} + C^{ijkl}(\varepsilon_{kl} - \varepsilon_{kl}^{Th}), \tag{2.40}$$

under the assumption that changes in displacement and temperature are small. The constant tensor s_0 refers to some pre-stress in the system and the fourth-order tensor C^{ijkl} is the elasticity tensor. The measures ε and ε^{Th} are the infinitesimal strains described in section 2.6. As stated, we may replace s^{ij} with the Cauchy stress, giving

$$\sigma^{ij} = \sigma_0^{ij} + C^{ijkl}(\varepsilon_{kl} - \varepsilon_{kl}^{Th}). \tag{2.41}$$

We assume the system is not pre-stressed and that in addition to elastic and thermal deformation, it also experiences strain due to hydrogen effects ε^H. By including these assumptions, we have the equation

$$\sigma^{ij} = C^{ijkl}\left(\varepsilon_{kl} - \varepsilon^{Th}{}_{kl} - \varepsilon^{H}{}_{kl}\right). \tag{2.42}$$

The elasticity tensor is given by [43]

$$C^{ijkl} = \lambda\delta^{ij}\delta^{kl} + G(\delta^{ik}\delta^{jl} + \delta^{il}\delta^{jk}), \tag{2.43}$$

where λ and G are the first and second Lamé coefficients of the material respectively. Equation (2.43) and the strain tensors from the previous section are substituted into the constitutive law (2.42), giving

$$\sigma^{ij} = \lambda\delta^{ij}\varepsilon_k^k + 2G\varepsilon^{ij} - \delta^{ij}(\delta_k^k\lambda + 2G))\left[\alpha(T - T_0) + \frac{1}{3}\left(C\bar{V}_H + \frac{\bar{V}_{Hr}}{\bar{V}_U}f\right)\right]. \tag{2.44}$$

This is a linear stress-strain relation for a thermoelastic, isotropic material which is experiencing isotropic expansion due to solute diffusion and density change during reaction.

2.8 Hydriding reaction equation

The extent of reaction is measured using two different field variables — in the earlier stages of this project, the volume fraction of hydride f was used, and in the later stages, we use U, the remaining concentration of uranium in mol m^{-3}. The resulting equations for both cases are presented here.

2.8.1 Extent of reaction by lever rule

In the first instance, the equation to calculate the rate of reaction for hydride precipitation and dissolution follows the treatment by Jernkvist and Massih [61]. Figure 2.3 shows the phase diagrams used in their work. The plots show the observed temperature- and concentration-dependent phases of hydrogen-zirconium and hydrogen-titanium systems. Referring to the low temperature region of each plot (below 823K in the case of zirconium and below 573K in the case of titanium) where hydride is observed to form, there are three distinct regions. Labelled on each plot are the temperature-dependent curves C_{LB} and C_{UB} which demarcate these regions. The region to the left of C_{LB} is purely metal, and the region to the right of C_{UB} is purely metal hydride, while the grey region bounded between them has coexisting metal and hydride. Therefore C_{LB} is the low bound, the concentration below which no hydride is observed and C_{UB} is the upper bound, above which no metal is observed. We note that this description of C_{LB} matches with the definition of the solubility limit: the minimum concentration at which hydride precipitates. We thus re-label C_{LB} as C_{TSS}.

We define an equilibrium volume fraction of hydride, f_e. This is the amount of hydride which would be produced if the system were to remain in its current state indefinitely (all other quantities such as temperature and stress were held constant). The value of f_e depends on where the system state is in phase space. The equilibrium volume fraction is defined by the current hydrogen concentration relative to these bounds, using a lever rule [61]:

$$f_e = \begin{cases} 0 & \text{if } C_{TOT} \leq C_{TSS} \\ \dfrac{C_{TOT} - C_{TSS}}{C_{UB} - C_{TSS}} & \text{if } C_{TSS} < C_{TOT} < C_{UB} \\ 1 & \text{if } C_{TOT} \geq C_{UB} \end{cases} \tag{2.45}$$

We assume that the volume fraction will proceed towards this equilibrium value f_e

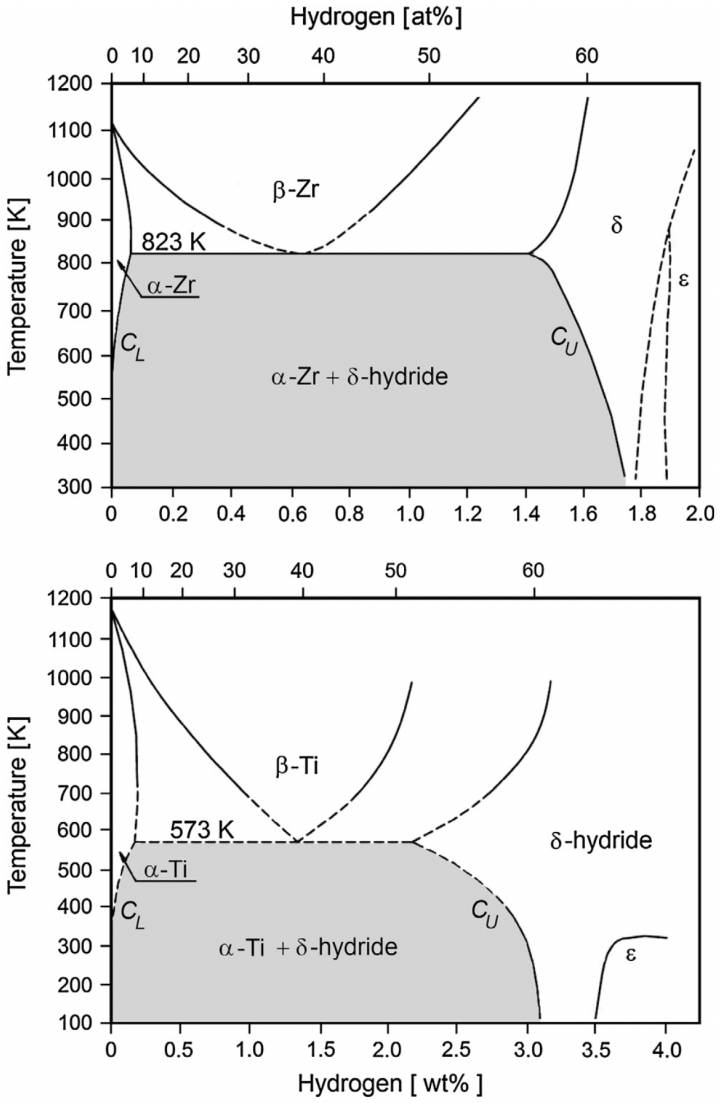

Figure 2.3: Phase diagrams of the Zr-H and Ti-H binary systems in the temperature-hydrogen content plane. The hydrogen content is measured both in weight percentage on the bottom axis and atomic percentage on the top axis. Lines in the phase-space demarcate regions where there is pure metal, pure hydride, and a mixture of the two. The grey region in each case indicates the region in which hydriding is taking place; where both metal and hydride are present. To the left of the grey region, when the hydrogen content is below the lower limit C_{LB}, there is a white region where the Zr/Ti is in the purely metal phase. To the right of the grey region, when the hydrogen content is above the upper limit C_U, there is a white region where the Zr/Ti is in the purely hydride phase. At higher temperatures, above the grey region there is another white region where the Zr/Ti is in the purely metal phase. The phase space is also separated into the most likely crystal structures of the metal and hydride at that temperature and hydrogen content. The different crystal structures are represented by the letters α, β, δ and ε. Since this work describes a continuum model, we have no need to distinguish between the different crystal structures. Image taken from Jernkvist and Massih 2014 [61].

with some rate, k_f, giving the rate equation [61]

$$\frac{\partial f}{\partial t} = k_f(f_e - f). \tag{2.46}$$

Since the rate of reaction depends linearly on the concentration of hydrogen only, this is first-order reaction kinetics.

We now use these defined reaction kinetics to replace reaction terms in the model. Firstly, the total hydrogen concentration C_{TOT} is made up of diffusing hydrogen and hydrogen which has reacted to form hydride. We use the volume fraction of hydride f to write the total hydrogen concentration

$$C_{TOT} = C + fC_b \tag{2.47}$$

where C is the concentration of dissolving hydrogen, a quantity that has been defined previously in this chapter. Note that hydrogen can diffuse through the metal, oxide and hydride, so there is no f-dependent factor multiplying C. The concentration C_b is the concentration of hydrogen bound in hydride; the number of moles of hydrogen which is present per m^3 of hydride. Thus C_b is given by $\frac{3}{\bar{V}_{Hr}}$, where $\bar{V}_{Hr}$ is the volume taken up by one mole of uranium hydride. We multiply by 3 to account for the stoichiometry of UH_3; three times as many moles of hydrogen atoms are present as moles of UH_3. We note that C_{UB}, the upper bound, must be greater than or equal to C_b. No definition of C_{UB} could be found for the uranium-hydrogen binary system in the literature, so it has been taken to be some constant value larger than C_b.

Using the definition of C_{TOT} in equation (2.47) our Fick's law, equation (2.15) becomes

$$\frac{\partial C}{\partial t} + \nabla_{\mathbf{x}} \cdot \mathbf{J} = -\frac{\partial f}{\partial t} C_b. \tag{2.48}$$

We note that increase in the volume fraction of hydride acts as a sink of free hydrogen C in the system as we would expect.

We have derived the conservation of mass and an equation to describe the hydriding reaction using f. The equations describing energy conservation and the stress-strain relation have already been derived using f, and Cauchy's momentum equation does not have terms relating to hydride content. Thus, when modelling extent of reaction by the lever rule, the full set of governing equations is given by equations (2.28), (2.31), (2.44), (2.46) and (2.48), with definitions of J, μ and f_e given by equations (2.21), (2.24) and (2.45) respectively.

2.8.2 Extent of reaction by rate law

The second equation used to model the hydride precipitation reaction is derived from the law of mass action and is given by

$$\frac{\partial U}{\partial t} = -k_{Hr} C^3 U \tag{2.49}$$

where k_{hr} is the reaction rate constant, U is the uranium concentration and as before, C is hydrogen concentration. In Condon's paper [17], the reaction is described as first order in both C and U, whereas this equation gives the reaction is first order in U and third order in C. This change is as a result of a suggestion by my industrial supervisor.

As a consequence of using this reaction equation, the terms containing $\frac{\partial f}{\partial t}$ should be replaced in the conservation of mass and conservation of energy equations. To do this, we take the time derivative of C_{TOT}

$$\frac{\partial C_{TOT}}{\partial t} = \frac{\partial C}{\partial t} + C_b \frac{\partial f}{\partial t}. \tag{2.50}$$

Using that uranium hydride is composed of three hydrogen atoms for every one uranium atom, we could also write

$$\frac{\partial C_{TOT}}{\partial t} = \frac{\partial C}{\partial t} - 3\frac{\partial U}{\partial t}, \tag{2.51}$$

so that

$$\frac{\partial f}{\partial t} = -\frac{3}{C_b}\frac{\partial U}{\partial t}. \tag{2.52}$$

Thus equations (2.15) and (2.28) are replaced by the equations

$$\begin{aligned} \frac{\partial C}{\partial t} &= -\nabla_{\mathbf{x}} \cdot \mathbf{J} + 3\frac{\partial U}{\partial t} \\ \rho c_p \frac{dT}{dt} - \Delta\bar{H}\frac{dU}{dt} &= \nabla_{\mathbf{x}} \cdot (\kappa \nabla_{\mathbf{x}} T) - \mathbf{J} \cdot \nabla_{\mathbf{x}} \mu. \end{aligned} \tag{2.53}$$

where the definition $C_b = \frac{3}{\bar{V}_{Hr}}$ from section 2.8.1 was used in the energy equation. The term containing f must also be replaced in the constitutive law. Integrating equation (2.52) in time, and using that when $f = 0$, U is equal to its initial value, U_0 we have that

$$f = \frac{3}{C_b}\Delta U \tag{2.54}$$

where $\Delta U = U_0 - U$. Thus, and again using $C_b = \frac{3}{\bar{V}_{Hr}}$, .5the constitutive law (2.44) is

replaced by

$$\sigma^{ij} = \lambda\delta^{ij}\varepsilon^k_k + 2G\varepsilon^{ij} - \delta^{ij}(\delta^k_k\lambda + 2G))\left[\alpha(T-T_0) + \frac{1}{3}\left(C\bar{V}_H + \frac{\bar{V}^2_{Hr}}{\bar{V}_U}\Delta U\right)\right]. \quad (2.55)$$

We have derived the conservations of mass and energy, an equation to describe the hydriding reaction and a constitutive law using U. Cauchy's momentum equation does not have terms relating to hydride content. Thus, when modelling extent of reaction by the rate law, the full set of governing equations is given by equations (2.31), (2.49), (2.53) and (2.55), with definitions of J and μ given by equations (2.21) and (2.24) respectively.

2.9 Sieverts' law

Sieverts' law [62] states that the concentration of a diatomic gas dissolved in a metal is proportional to the square root of the partial pressure of the diatomic gas in the atmosphere. In G.L. Powell's chapter of the book Uranium Processing and Properties [63], he writes an equation for C^U_S, the number of moles of hydrogen dissolved per mole of uranium as

$$C^U_S = K(T)\sqrt{P_{atm}} \quad (2.56)$$

where P_{atm} is the partial pressure of the gas in the atmosphere, $K(T)$ is the constant of proportionality which depends on properties of the metal and the gas, as well as the temperature T. For the uranium-hydrogen system, Powell gives the constant as [64]

$$K(T) = \frac{A(1+Be^{-L/T})e^{(E-25997.5)/T}\left(1-e^{-5986/T}\right)}{0.02072T^{1.75}\left(1-e^{-1680/T}\right)^3}\text{mol H(mol U)}^{-1}bar^{-0.5} \quad (2.57)$$

where the temperature T is in Kelvin and A, B, L and E are constants which depend on whether the metal is in α, β, or γ phase [1]. The phases α, β, and γ describe the crystal structure of the metal. Uranium exists mostly in the α phase below $668°C$ [65], and we have $A = 1$, $B = 1550$, $L = 6000$ and $E = 24850$ for α-uranium [63]. Since C^U_S is the number of moles of hydrogen dissolved per mole of uranium, we must divide by the constant $\bar{V}_U$, the volume of one mole of uranium, to obtain a concentration of hydrogen

[1] Note that in the book Uranium Processing and Properties the equation is different, though the earlier paper by Powell [64] is cited as the source. Using the constants to match data to the graphs given in the book, Dr. Phil D.D. Monks and Dr, J. Petherbridge from AWE plc. advised that the formulation given in the paper is correct and the book is incorrect.

in moles per unit volume. We label the resultant quantity the Sieverts' concentration, C^S, given by

$$C^S = \frac{K(T)\sqrt{P_{atm}}}{\bar{V}_U}. \tag{2.58}$$

This value is used as a condition on the hydrogen concentration at any boundary where uranium metal is incident on the atmosphere. In the models where the Sieverts' concentration is used, the experimental conditions (temperature and hydrogen pressure) are taken from the work in A. Chohollo's thesis [66]. The temperature is $80°C$ $(353.15K)$ and the hydrogen pressure is 10mbar (0.01bar). This gives the value $C^S = 0.534\text{mol m}^{-3}$.

2.10 Variational functionals for linear thermoelasticity

Finally, we look at using the calculus of variations to derive field equations for physical systems by taking derivatives of invariant quantities. In theory, it should be possible to start with a number of invariant quantities, for example mass and energy, and derive a complete set of governing equations to describe any physical system. If this method works, it can provide an extremely mathematically elegant way to derive complicated systems of equations.

After many unsuccessful attempts to derive, or find in the literature, a complete set of invariants for the uranium hydriding system which incorporate diffusing and reacting substances, this must be left as future work. However, it is possible to derive the equations of linear thermoelasticity this way, so we present that argument here as a partial derivation of our model.

To begin, we introduce two invariants, Π_1 and Π_2. We first look at Π_1, the 'thermoelastic potential' [67],

$$\Pi_1 = \int_\Omega \left(W - \mathbf{F}_B \cdot \mathbf{u} + \frac{1}{2}\frac{c_V}{T_0}(\Delta T)^2 \right) \, d\Omega \tag{2.59}$$

where W is the isothermal mechanical energy, c_V is the specific heat per unit volume and ΔT is the temperature change from T_0, the reference temperature for the unstressed, undeformed state and again $\mathbf{F}_B$ is the body force. The volume, Ω is enclosed by the surface $\partial\Omega$, on which tractions and displacements are prescribed; these are the boundary conditions for the solid mechanics problem.

The isothermal mechanical energy

$$W = \sigma_{ij}\varepsilon_{ij} - \frac{1}{2}C_{ijkl}\sigma_{ij}\sigma_{kl}, \tag{2.60}$$

where σ and

$$\varepsilon = \frac{1}{2}\left((\boldsymbol{\nabla}\otimes\mathbf{u}) + (\boldsymbol{\nabla}\otimes\mathbf{u})^{\intercal}\right) \tag{2.61}$$

are the components of stress and strain respectively. The tensor C_{ijkl} is the elastic flexibility tensor. From thermodynamics arguments, we have [67]

$$\Delta T = -\frac{T_0}{c_V}\left(\boldsymbol{\nabla}\cdot\mathbf{S} + \alpha\sigma_{ij}\delta_{ij}\right) \tag{2.62}$$

where α is the coefficient of thermal expansion, δ_{ij} is the Kronecker delta and $\mathbf{S}$ is the vector of heat flow divided by temperature — the so-called entropy flow.

Substituting W and ΔT into the invariant Π_1, we have

$$\begin{aligned}\Pi_1(\sigma_{ij},u_i,S_i) = \int_\Omega \Bigg(&\sigma_{ij}\varepsilon_{ij} - \frac{1}{2}C_{ijkl}\sigma_{ij}\sigma_{kl} - \mathbf{F}_B\cdot\mathbf{u} \\ &+ \frac{1}{2}\frac{c_V}{T_0}\left(-\frac{T_0}{c_V}\left(\boldsymbol{\nabla}\cdot\mathbf{S} + \alpha\sigma_{ij}\delta_{ij}\right)\right)^2\Bigg)\, d\Omega.\end{aligned} \tag{2.63}$$

The second invariant Π_2 is defined [67]

$$\Pi_2 = \frac{1}{2}\frac{\partial}{\partial t}\int_\Omega \frac{T_0}{\kappa}\mathbf{S}\cdot\mathbf{S}\, d\Omega \tag{2.64}$$

where κ is the coefficient of thermal conduction.

The total variation of $\Pi_1 + \Pi_2$ is equal to the energy transferred to Ω by work done on and heat flow over the boundary $\partial\Omega$

$$\begin{aligned}\delta\left(\Pi_1(\sigma_{ij},u_i,S_i) + \Pi_2(S_i)\right) &= \delta\Pi_1(\sigma_{ij},u_i,S_i) + \delta\Pi_2(S_i) \\ &= \int_{\partial\Omega}\mathbf{T}\cdot\delta\mathbf{u}\, dS + \int_{\partial\Omega}\Delta T\mathbf{n}\cdot\delta\mathbf{S}\, dS\end{aligned} \tag{2.65}$$

where $\mathbf{T}$ is the traction on the boundary, which has outward normal $\mathbf{n}$. Boundary conditions for the solid mechanics problem can either prescribe a traction or displacement. The boundary is partitioned into two: $\partial\Omega^\sigma$ with the prescribed traction $\bar{\mathbf{T}}$ and

$\partial\Omega^u (= \partial\Omega - \partial\Omega^\sigma)$ with prescribed displacement $\bar{\mathbf{u}}$. The boundary condition imposing $\bar{\mathbf{u}}$ means that $\delta\mathbf{u} = 0$ on $\partial\Omega^u$ [68]. We are left with

$$\begin{aligned}\delta\left(\Pi_1(\sigma_{ij}, u_i, S_i) + \Pi_2(S_i)\right) &= \delta\Pi_1(\sigma_{ij}, u_i, S_i) + \delta\Pi_2(S_i) \\ &= \int_{\partial\Omega^\sigma} \bar{\mathbf{T}} \cdot \delta\mathbf{u}\, dS + \int_{\partial\Omega} \Delta T \mathbf{n} \cdot \delta\mathbf{S}\, dS.\end{aligned} \tag{2.66}$$

The expression (2.66) is known as the variational principle. Using definitions of Π_1 and Π_2 from equations (2.63) and (2.64), and grouping together like terms, we have

$$\begin{aligned}\delta\left(\Pi_1(\sigma_{ij}, u_i, S_i) + \Pi_2(S_i)\right) = &\int_\Omega \sigma_{ij}\delta\varepsilon_{ij}\, d\Omega - \int_\Omega \mathbf{F}_B \cdot \delta\mathbf{u}\, d\Omega \\ &- \int_\Omega \Delta T \delta\left(\boldsymbol{\nabla}\cdot\mathbf{S}\right)\, d\Omega + \frac{\partial}{\partial t}\int_\Omega \frac{T_0}{\kappa}\mathbf{S}\cdot\delta\mathbf{S}\, d\Omega \\ &+ \int_\Omega \left(\varepsilon_{ij} - C_{ijkl}\sigma_{kl} - \alpha\Delta T\delta_{ij}\right)\delta\sigma_{ij}\, d\Omega\end{aligned} \tag{2.67}$$

We can use the divergence theorem (and the symmetry property of the stress tensor) on the first and third terms on the right hand side, giving

$$\begin{aligned}\int_\Omega \sigma_{ij}\delta\varepsilon_{ij}\, d\Omega &= \int_\Omega \boldsymbol{\sigma}\colon \delta\left(\frac{1}{2}\left((\boldsymbol{\nabla}\otimes\mathbf{u}) + (\boldsymbol{\nabla}\otimes\mathbf{u})^\intercal\right)\right)\, d\Omega \\ &= \frac{1}{2}\int_\Omega \left(\boldsymbol{\sigma}\colon \delta(\boldsymbol{\nabla}\otimes\mathbf{u}) + \boldsymbol{\sigma}\colon \delta\left((\boldsymbol{\nabla}\otimes\mathbf{u})^\intercal\right)\right)\, d\Omega \\ &= -\frac{1}{2}\int_\Omega \left((\boldsymbol{\nabla}\cdot\boldsymbol{\sigma})\cdot\delta\mathbf{u} + (\boldsymbol{\nabla}\cdot\boldsymbol{\sigma}^\intercal)\cdot\delta\mathbf{u}\right)\, d\Omega \\ &\qquad + \frac{1}{2}\int_{\partial\Omega}\left((\boldsymbol{\sigma}\cdot\mathbf{n})\cdot\delta\mathbf{u} + (\boldsymbol{\sigma}^\intercal\cdot\mathbf{n})\cdot\delta\mathbf{u}\right)\, dS \\ &= -\int_\Omega (\boldsymbol{\nabla}\cdot\boldsymbol{\sigma})\cdot\delta\mathbf{u}\, d\Omega + \int_{\partial\Omega}(\boldsymbol{\sigma}\cdot\mathbf{n})\cdot\delta\mathbf{u}\, dS,\end{aligned} \tag{2.68}$$

and

$$\int_\Omega \Delta T\delta\left(\boldsymbol{\nabla}\cdot\mathbf{S}\right)\, d\Omega = -\int_\Omega \boldsymbol{\nabla}T\cdot\delta\mathbf{S}\, d\Omega + \int_{\partial\Omega}\Delta T\mathbf{n}\cdot\delta\mathbf{S}\, dS, \tag{2.69}$$

where the notation $A : B = A_{ij}B_{ij}$ is used for two tensors A and B. Using these substitutions in equation (2.67) and again grouping like terms results in the expression

$$\begin{aligned}\delta(\Pi_1(\sigma_{ij},u_i)+\Pi_2(S_i)) = &-\int_\Omega (\nabla\cdot\sigma+\mathbf{F}_B)\cdot\delta\mathbf{u}\,d\Omega+\int_\Omega\left(\frac{T_0}{\kappa}\frac{\partial\mathbf{S}}{\partial t}+\nabla T\right)\cdot\delta\mathbf{S}\,d\Omega\\ &+\int_\Omega(\varepsilon_{ij}-C_{ijkl}\sigma_{kl}-\alpha\Delta T\delta_{ij})\delta\sigma_{ij}\,d\Omega+\int_{\partial\Omega^\sigma}(\sigma\cdot\mathbf{n})\cdot\delta\mathbf{u}\,dS+\int_{\partial\Omega}\Delta T\mathbf{n}\cdot\delta\mathbf{S}\,dS.\end{aligned} \tag{2.70}$$

Finally, equating the variational principle (2.66) with our definition (2.70), we have

$$\begin{aligned}&\int_\Omega(\varepsilon_{ij}-C_{ijkl}\sigma_{kl}-\alpha\Delta T\delta_{ij})\delta\sigma_{ij}\,d\Omega-\int_\Omega(\nabla\cdot\sigma+\mathbf{F}_B)\cdot\delta\mathbf{u}\,d\Omega\\ &+\int_\Omega\left(\frac{T_0}{\kappa}\frac{\partial\mathbf{S}}{\partial t}+\nabla T\right)\cdot\delta\mathbf{S}\,d\Omega+\int_{\partial\Omega^\sigma}(\sigma\cdot\mathbf{n}-\bar{\mathbf{T}})\cdot\delta\mathbf{u}\,dS=0.\end{aligned} \tag{2.71}$$

Since the variations of the variables σ_{ij}, u_i and S_i are arbitrary, we have that all the integrands must separately equal zero:

$$\begin{aligned}\varepsilon_{ij}-C_{ijkl}\sigma_{kl}-\alpha\Delta T\delta_{ij}&=0\\ \nabla\cdot\sigma+\mathbf{F}_B&=0\\ \frac{T_0}{\kappa}\frac{\partial\mathbf{S}}{\partial t}+\nabla T&=0\\ \sigma\cdot\mathbf{n}-\bar{\mathbf{T}}&=0.\end{aligned} \tag{2.72}$$

The first equation is the thermoelastic constitutive law. The second is Cauchy's quasi-static conservation of momentum. The fourth is the condition for stress continuity across the boundary $\partial\Omega^\sigma$. The third requires some rearranging; taking its divergence and using equation (2.62) to replace the entropy flow term gives the heat equation with a stress-heating term

$$\kappa\nabla\cdot\nabla T = c_V\frac{\partial T}{\partial t}+\alpha T_0\frac{\partial\sigma_{ij}}{\partial t}\delta_{ij}. \tag{2.73}$$

We use the Hookean elastic flexibility tensor for isotropic materials in the constitutive law,

$$C_{ijkl}=\frac{1+\nu}{E}\left[\frac{1}{2}(\delta_{ik}\delta_{jl}+\delta_{il}\delta_{jk})-\frac{\nu}{1+\nu}\delta_{ij}\delta_{kl}\right] \tag{2.74}$$

where ν is Poisson's ratio and E is the Young's modulus for the material. This gives

the constitutive law

$$\varepsilon_{ij} = \frac{1+\nu}{2E}(\sigma_{ij}+\sigma_{ji}) - \frac{\nu}{E}\delta_{ij}\sigma_{kk} + \alpha\Delta T\delta_{ij}. \tag{2.75}$$

2.10.1 Importance of equation ordering in the finite element method

From equation (2.71), we gain an important insight: each field equation is associated with variation in a specific field variable. For example, the constitutive law indexed by ij is associated with variations in σ_{ij}.

The models presented in this work consist of differential equations and boundary and initial conditions which are imposed to give a unique solution. The finite element method (FEM) is used throughout to solve these models. In FEM, the governing equations are solved at discrete positions, called 'nodes', and a node which is on a domain boundary is called a 'boundary node'. A boundary condition on a given field variable is imposed by replacing the equation at the boundary node which is associated with that variable with an equation for the boundary condition. So, for example we look at imposing a boundary condition on the first component of displacement, u_1. Since the associated field equation is the first component of Cauchy's conservation of momentum,

$$\frac{\partial\sigma_{11}}{\partial x_1} + \frac{\partial\sigma_{12}}{\partial x_2} = 0, \tag{2.76}$$

on the boundary node, this equation should be replaced with a boundary condition for u_1. As was discovered over the course of this project, if the wrong field equation is edited for the boundary condition, then the problem has been constructed incorrectly and a viable solution cannot be found. The fact that this important idea drops out of the variational formulation compounds with its mathematical elegance to make it a highly attractive way to construct systems of field equations.

Chapter 3

Computing solutions

3.1 oomph-lib

The finite element method (FEM), which is presented in this chapter, has been used throughout this PhD project to solve systems of PDEs. The software used is oomph-lib [69], an open-source FEM solver developed at the University of Manchester.

3.2 Finite element method implementation

The N coupled differential equations are to be solved for the N independent variables on the domain Ω. In this chapter alone, $\mathbf{u}$ is redefined as the vector (length N) of independent variables, the solution to the system of equations. We write the governing differential equations as the so-called 'residual equations',

$$\mathcal{R}_j\left(x_m, t, u_l(x_m,t), \frac{\partial u_l}{\partial x_m}, \frac{\partial^2 u_l}{\partial x_m \partial x_n}, \ldots, \frac{\partial u_l}{\partial t}, \frac{\partial^2 u_l}{\partial t^2}, \ldots\right) = 0, \tag{3.1}$$

where $j, l = 0, 1, \ldots N-1$ and the indices m and n loop over the dimensions of Ω. The system is solved when $\mathbf{u}$ is computed for which the residuals, $\mathcal{R}_j$, are equal to zero. The dependence of $\mathcal{R}_j$ on the derivatives is suppressed and the dependence of the residuals on each independent variable and spatial coordinate is condensed to

$$\mathcal{R}_j\left(\mathbf{x}, t, \mathbf{u}(\mathbf{x},t)\right) = 0, \qquad j = 0, 1, \ldots N-1, \tag{3.2}$$

bearing in mind that each $\mathcal{R}_j$ depends on the components of the vectors $\mathbf{x}$ and $\mathbf{u}$, and is not itself vector-valued.

Solutions which solve these equations on the domain and satisfy the initial and boundary conditions are the problem's 'strong' solutions. Here, we instead look for its 'weak' solutions. Multiplying equation (3.2) by a 'test' function $\phi(\mathbf{x})$ and integrating over Ω obtains the 'weak form' of the residual equations

$$\int_{\Omega} \mathcal{R}_j\left(\mathbf{x},t,\mathbf{u}_w(\mathbf{x},t)\right)\phi(\mathbf{x})d\mathbf{x} = 0 \tag{3.3}$$

for the weak solutions $\mathbf{u}_w$, which must also satisfy the boundary and initial conditions. By imposing that the above integral must be zero for any $\phi(\mathbf{x})$ we have that the weak solutions will be strong solutions, and we can drop the subscript to give

$$\int_{\Omega} \mathcal{R}_j\left(\mathbf{x},t,\mathbf{u}(\mathbf{x},t)\right)\phi(\mathbf{x})d\mathbf{x} = 0. \tag{3.4}$$

The general form of the diffusion-reaction equations used in this report is

$$\mathcal{R}_j\left(\mathbf{x},t,\mathbf{u}(\mathbf{x},t)\right) = \frac{\partial u_j}{\partial t} + R(\mathbf{x},t,u_l,\nabla u_l) - \tilde{D}\nabla\cdot\nabla u_j - \nabla\cdot\mathbf{F}(\mathbf{x},t,u_l,\nabla u_l) = 0, \tag{3.5}$$

where $R(\mathbf{x},t,u_l,\nabla u_l)$ and $\nabla\cdot\mathbf{F}(\mathbf{x},t,u_l,\nabla u_l)$ are the reaction terms and $\tilde{D}$ is a constant. We note that second spatial derivatives of the independent variables appear only in the terms $\tilde{D}\nabla\cdot\nabla u_j$ and $\nabla\cdot\mathbf{F}(\mathbf{x},t,u_l,\nabla u_l)$ of equation (3.5). The weak form of this residual equation is given by

$$\int_{\Omega}\left(\frac{\partial u_j}{\partial t} + R\left(\mathbf{x},t,u_l,\nabla u_l\right) - \tilde{D}\nabla\cdot\nabla u_j - \nabla\cdot\mathbf{F}\left(\mathbf{x},t,u_l,\nabla u_l\right)\right)\phi(\mathbf{x})d\mathbf{x} = 0. \tag{3.6}$$

The divergence theorem is applied to give

$$\begin{aligned}\int_{\Omega}\left(\frac{\partial u_j}{\partial t} + R\left(\mathbf{x},t,u_l,\nabla u_l\right)\right)\phi(\mathbf{x})d\mathbf{x} + \int_{\Omega}\left(\tilde{D}\nabla u_j + \mathbf{F}\left(\mathbf{x},t,u_l,\nabla u_l\right)\right)\cdot\nabla\phi(\mathbf{x})d\mathbf{x} \\ = \int_{\partial\Omega}\phi(\mathbf{x})\left(\tilde{D}\nabla u_j + \mathbf{F}\left(\mathbf{x},t,u_l,\nabla u_l\right)\right)\cdot\mathbf{n}dS.\end{aligned} \tag{3.7}$$

where the vector $\mathbf{n}$ is the outward-pointing normal of the boundary $\partial\Omega$ of Ω. Note that the second derivatives of the independent variables no longer appear in the weak form. Neumann boundary conditions are applied by substituting imposed flux values in the boundary term.

We see that for the integral in equation (3.7) to be finite, we must restrict the allowed set of functions from which the $u_l(\mathbf{x},t)$, $\nabla u_l(\mathbf{x},t)$, $\phi(\mathbf{x})$ and $\nabla\phi(\mathbf{x})$ can be taken.

To proceed, we first define ζ, a tuple of non-negative integers

$$\zeta = (\zeta_1 \dots \zeta_n), \qquad \zeta_i \in \mathbb{N} \cup \{0\} \tag{3.8}$$

with the 'length' of ζ defined by

$$|\zeta| = \sum_{i=1}^{n} \zeta_i. \tag{3.9}$$

We now look at a function f which is integrable on Ω, and define the expression

$$D^{\zeta} f = \left(\frac{\partial}{\partial x_1}\right)^{\zeta_1} \dots \left(\frac{\partial}{\partial x_n}\right)^{\zeta_n} f \tag{3.10}$$

to be the ζ spatial derivative of f[1]. The Sobolev norm of a function f which is integrable on Ω is defined as

$$||f||_{W_p^k(\Omega)} = \left(\sum_{|\zeta| \leq k} \int_{\Omega} |D^{\zeta} f|^p dx\right)^{\frac{1}{p}} \tag{3.11}$$

where all $D^{\zeta} f$ must exist for all $|\zeta| \leq k$, where k is some non-negative integer, and p takes some real value $p \in [1, \infty)$. The Sobolev space, in turn, is defined as the space of integrable functions for which this norm is finite

$$W_p^k(\Omega) = \{f : ||f||_{W_p^k(\Omega)} < \infty\}. \tag{3.12}$$

Specifically, we look at the space $W_p^1(\Omega)$, where the zeroth and first derivatives of f to the power p are integrable

$$\begin{aligned} W_p^1(\Omega) &= \{f : ||f||_{W_p^1(\Omega)} < \infty\} \\ ||f||_{W_p^1(\Omega)} &= \left(\int_{\Omega} |f|^p dx + \sum_{i=1}^{n} \left(\int_{\Omega} \left|\frac{\partial f}{\partial x_i}\right|^p dx\right)\right)^{\frac{1}{p}} \end{aligned} \tag{3.13}$$

[1] Strictly speaking, to define Sobolev spaces, only the existence of the 'weak' derivative of f is required. All functions for which the ordinary derivative exists also have a weak derivative, so we continue with sufficiently differentiable functions in the strong sense. Also, the function f is only required to be from the set of functions which are locally integrable on Ω, a superset of the set of functions which are integrable on Ω

where n is the dimension of Ω. Using this definition, if we restrict

$$u_l(\mathbf{x},t) \in W_p^1(\Omega) \quad l = 0,1,\ldots,N-1 \quad \text{and} \quad \phi(\mathbf{x}) \in W_p^1(\Omega) \tag{3.14}$$

then the integral in equation (3.7) will be finite if we consider the (possibly non-linear) form of the functions $R(\mathbf{x},t,u_l,\nabla u_l)$ and $\mathbf{F}(\mathbf{x},t,u_l,\nabla u_l)$ in our choice of p. It is noted that if the divergence theorem were not applied to go from equation (3.6) to equation (3.7), stricter conditions would be imposed on the function space for u_l, i.e. $u_l(\mathbf{x},t) \in W_p^2(\Omega)$.

Next, each u_l is written as an infinite expansion

$$u_l(\mathbf{x},t) = \sum_{q=1}^{\infty} U_{lq}(t)\psi_q(\mathbf{x}) \tag{3.15}$$

where $U_{lq}(t)$ are coefficients to be found and the 'shape' functions $\psi_q(\mathbf{x})$ are an infinite set of complete basis functions for the function space of the homogeneous solution. Using the restriction (3.14) that functions $u_l(\mathbf{x},t)$ reside in the space $W_p^1(\Omega)$ we have

$$\sum_{q=1}^{\infty} U_{lq}(t)\psi_q(\mathbf{x}) \in W_p^1(\Omega). \tag{3.16}$$

Thus the set of functions $\psi_q(\mathbf{x})$ are specifically a complete basis for $W_p^1(\Omega)$. Since the test functions $\phi(\mathbf{x})$ inhabit this space, they may be written

$$\phi(\mathbf{x}) = \sum_{k=1}^{\infty} \Phi_k \psi_k(\mathbf{x}). \tag{3.17}$$

This means the residual equation (3.4) now reads

$$\sum_{k=1}^{\infty} \Phi_k \int_{\Omega} \mathcal{R}_j(\mathbf{x},t,\mathbf{u}(\mathbf{x},t))\,\psi_k(\mathbf{x})d\mathbf{x} = 0, \tag{3.18}$$

which we write

$$\sum_{k=1}^{\infty} \Phi_k r_{jk} = 0 \tag{3.19}$$

where $r_{jk} = \int_{\Omega} \mathcal{R}_j(\mathbf{x},t,\mathbf{u}(\mathbf{x},t))\,\psi_k(\mathbf{x})d\mathbf{x}$. The residual equations must equal zero for any test function $\phi(\mathbf{x})$, or equivalently for any values of the coefficients Φ_k. This

means that we have the infinitely many equations

$$r_{jk} = 0 \qquad \forall j = 0,1,\ldots,N-1 \quad \text{and} \quad \forall k \in \mathbb{N}. \tag{3.20}$$

The residuals r_{jk} depend on the unknown coefficients U_{jq}, of which there are also infinitely many. If we take equations (3.19) and (3.15), and truncate the infinite sums in each to M terms

$$\sum_{k=1}^{M} \Phi_k r_{jk} = 0 \tag{3.21}$$

$$u_l(\mathbf{x},t) = \sum_{q=1}^{M} U_{lq}(t)\psi_q(\mathbf{x}), \tag{3.22}$$

then, writing the explicit dependence of r_{jk} on the U_{lq}, equation (3.20) becomes

$$\begin{aligned} r_{jk}(U_{01},U_{02},\ldots,U_{0M},\ldots,U_{N-1\,1},U_{N-1\,2},\ldots,U_{N-1\,M}) = 0 \\ \forall j = 0,1,\ldots,N-1 \quad \text{and} \quad \forall k = 1,2\ldots M. \end{aligned} \tag{3.23}$$

This is $N \times M$ coupled equations for $N \times M$ unknown coefficients. Truncation of the first sum, equation (3.21), is equivalent to weakening the condition 'the integral (3.3) (also in equations (3.4), (3.6), (3.7)) is zero for any $\phi(\mathbf{x})$', to 'the integral is zero for the functions $\phi(\mathbf{x})$ which it is possible to make from the finite, (incomplete) basis of $W_p^1(\Omega)$, $\psi_k(\mathbf{x})$ with $k = 1,2,\ldots,M$'. We say these functions form a complete basis of the space $\tilde{W}_p^1(\Omega)$.

Returning to the specific problem of diffusion-reaction, and using the residual equations in equation (3.7), equation (3.23) becomes

$$\begin{aligned} 0 = r_{jk} = \Bigg[& \int_\Omega \left(\frac{\partial u_j}{\partial t} + R(\mathbf{x},t,u_l,\nabla u_l) \right) \psi_k(\mathbf{x}) d\mathbf{x} \\ & + \int_\Omega \left(\tilde{D}\nabla u_j + \mathbf{F}(\mathbf{x},t,u_l,\nabla u_l) \right) \cdot \nabla \psi_k(\mathbf{x}) d\mathbf{x} \\ & - \int_{\partial\Omega} \psi_k(\mathbf{x}) \left(\tilde{D}\nabla u_j + \mathbf{F}(\mathbf{x},t,u_l,\nabla u_l) \right) \cdot \mathbf{n} dS \Bigg]. \end{aligned} \tag{3.24}$$

From the truncated summation expression for u_l, given in equation (3.22), we have that

the temporal and spatial derivatives of u_l are

$$\begin{aligned}\frac{\partial u_l}{\partial t} &= \frac{\partial}{\partial t}\left(\sum_{q=1}^{M} U_{lq}(t)\psi_q(\mathbf{x})\right) = \sum_{q=1}^{M}\frac{dU_{lq}(t)}{dt}\psi_q(\mathbf{x}),\\ \nabla u_l &= \frac{\partial}{\partial x_m}\left(\sum_{q=1}^{M} U_{lq}(t)\psi_q(\mathbf{x})\right) = \sum_{q=1}^{M} U_{lq}(t)\nabla\psi_q(\mathbf{x}).\end{aligned} \tag{3.25}$$

Replacing u_l and it's derivatives with these expansions in equation (3.24), we have the equation [2]

$$\begin{aligned}0 = r_{jk}(U_{01},\ldots,U_{N-1\,M}) &= \int_\Omega \mathcal{R}_j(\mathbf{x},U_{01},\ldots,U_{N-1\,M})\psi_k(\mathbf{x})d\mathbf{x}\\
&= \Bigg[\int_\Omega\left(\sum_{q=1}^{M}\frac{dU_{jq}(t)}{dt}\psi_q(\mathbf{x}) + R\left(\mathbf{x},t,\sum_{q=1}^{M}U_{lq}(t)\psi_q(\mathbf{x}),\sum_{q=1}^{M}U_{lq}(t)\nabla\psi_q(\mathbf{x})\right)\right)\psi_k(\mathbf{x})d\mathbf{x}\\
&+ \int_\Omega\left(\tilde{D}\sum_{q=1}^{M}U_{jq}(t)\nabla\psi_q(\mathbf{x}) + \mathbf{F}\left(\mathbf{x},t,\sum_{q=1}^{M}U_{lq}(t)\psi_q(\mathbf{x}),\sum_{q=1}^{M}U_{lq}(t)\nabla\psi_q(\mathbf{x})\right)\right)\cdot\nabla\psi_k(\mathbf{x})d\mathbf{x}\\
&- \int_{\partial\Omega}\psi_k(\mathbf{x})\left(\tilde{D}\sum_{q=1}^{M}U_{jq}(t)\nabla\psi_q(\mathbf{x}) + \mathbf{F}\left(\mathbf{x},t,\sum_{q=1}^{M}U_{lq}(t)\psi_q(\mathbf{x}),\sum_{q=1}^{M}U_{lq}(t)\nabla\psi_q(\mathbf{x})\right)\right)\cdot\mathbf{n}dS\Bigg].\end{aligned} \tag{3.26}$$

We need to approximate the time-derivative of the unknowns $U_{jq}(t)$. In this project, the second-order backward differentiation formula (BDF2) is used. For a differential equation of the form

$$\frac{d\mathbf{u}}{dt} = \mathbf{f}(t,\mathbf{u}), \tag{3.27}$$

the timestepper BDF2 approximates the derivative at time T using

$$\frac{\frac{3}{2}\mathbf{u}^{(T)} - 2\mathbf{u}^{(T-\Delta t)} + \frac{1}{2}\mathbf{u}^{(T-2\Delta t)}}{\Delta t} = \mathbf{f}(T,\mathbf{u}^T) \tag{3.28}$$

where Δt is the timestep size, and the superscripts on $\mathbf{u}$ indicate the time — $\mathbf{u}^{(T-\Delta t)}$ and $\mathbf{u}^{(T-2\Delta t)}$ are the known solution vectors at the previous timestep and the timestep

[2] When the equation is written in the form of (3.26), we see that the restriction that the functions $\psi_k(\mathbf{x})$ and $\nabla\psi_k(\mathbf{x})$ be from the space $\tilde{W}_p^1$ is not sufficient to ensure the existence of these integrals. The integrability of $\psi_k(\mathbf{x})\nabla\psi_k(\mathbf{x})$ and other such products is also required. It can be seen from the choice of basis functions that such products are integrable.

before that respectively. Using this to substitute for the time derivative in equation (3.26), we obtain

$$
\begin{aligned}
0 = r_{jk}(U_{01},\ldots,U_{N-1\,M}) &= \int_\Omega \mathcal{R}_j(\mathbf{x},U_{01},\ldots,U_{N-1\,M})\psi_k(\mathbf{x})d\mathbf{x} \\
&= \Bigg[\int_\Omega \Bigg(\sum_{q=1}^{M}\frac{\frac{3}{2}U_{jq}-2U_{jq}^{(T-\Delta t)}+\frac{1}{2}U_{jq}^{(T-2\Delta t)}}{\Delta t}\psi_q(\mathbf{x}) \\
&+ R\left(\mathbf{x},t,\sum_{q=1}^{M}U_{lq}(t)\psi_q(\mathbf{x}),\sum_{q=1}^{M}U_{lq}(t)\nabla\psi_q(\mathbf{x})\right)\Bigg)\psi_k(\mathbf{x})d\mathbf{x} \\
&+ \int_\Omega\left(\tilde{D}\sum_{q=1}^{M}U_{jq}(t)\nabla\psi_q(\mathbf{x})+\mathbf{F}\left(\mathbf{x},t,\sum_{q=1}^{M}U_{lq}(t)\psi_q(\mathbf{x}),\sum_{q=1}^{M}U_{lq}(t)\nabla\psi_q(\mathbf{x})\right)\right)\cdot\nabla\psi_k(\mathbf{x})d\mathbf{x} \\
&- \int_{\partial\Omega}\psi_k(\mathbf{x})\left(\tilde{D}\sum_{q=1}^{M}U_{jq}(t)\nabla\psi_q(\mathbf{x})+\mathbf{F}\left(\mathbf{x},t,\sum_{q=1}^{M}U_{lq}(t)\psi_q(\mathbf{x}),\sum_{q=1}^{M}U_{lq}(t)\nabla\psi_q(\mathbf{x})\right)\right)\cdot\mathbf{n}dS\Bigg].
\end{aligned}
\tag{3.29}
$$

When finding the solution at $t = T$, the solutions at the previous two timesteps will already be known and their value can be substituted into the residual equation [3].

To look for a solution to equation (3.29) we employ Newton's method — an iterative root-finding procedure. In Newton's method, the residual values $r_{jk}(U_{01},\ldots,U_{N-1\,M})$ are calculated for an initial 'guess' of the set of unknown values U_{lq}. The initial guess for the unknowns and the associated residuals is labelled by the superscript (0), $r_{jk}^{(0)}(U_{01}^{(0)},\ldots,U_{N-1\,M}^{(0)})$. The values at the a-th iteration are labelled

$$
r_{jk}^{(a)}\left(U_{01}^{(a)}\ldots U_{N-1\,M}^{(a)}\right). \tag{3.30}
$$

The U_{lq} at the $(a+1)$-th iteration are calculated by solving the system

$$
\left(\left.\frac{\partial r_{jk}}{\partial U_{lq}}\right|_{U_{lq}^{(a)}}\right)\left(U_{lq}^{(a+1)}-U_{lq}^{(a)}\right) = -r_{jk}^{(a)} \tag{3.31}
$$

[3] To use this second-order timestepping approximation, when calculating the solution at $t = \Delta t$, the previous solutions needed will be from $t = 0$ (where the initial condition is applied) and $t = -\Delta t$ (prior to the initial condition). To circumvent this problem, we assume that the system was stationary and at the initial condition prior to $t = 0$. This is not an unreasonable assumption, since in our simulations, $t = 0$ is when the material is first exposed to hydrogen.

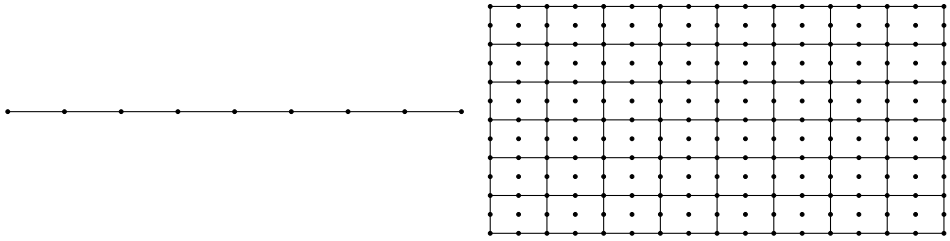

(a) A one-dimensional mesh.

(b) A two-dimensional quadrilateral mesh (with quadratic interpolation).

Figure 3.1: Examples of meshes in one dimension and two dimensions. The dots represent node locations $\mathbf{x}_i$, and the lines demarcate separate elements.

for $U_{lq}^{(a+1)}$ where $\left(\left.\frac{\partial r_{jk}}{\partial U_{lq}}\right|_{U_{lq}^{(a)}}\right)$ is the $(N\times M)\times(N\times M)$ Jacobian matrix. A root (or zero) of the residual equation is found when the residuals are sufficiently small with respect to some pre-defined metric:

$$\left| r_{jk}^{(a)}\left(U_{01}^{(a)}\ldots U_{N-1\,M}^{(a)}\right)\right| < \varepsilon. \tag{3.32}$$

For time-dependent problems (like the diffusion-reaction equations of this project) the solution at the previous timestep is used as the initial guess for the next timestep.

It remains to discuss how this system of equations is solved using the finite element method (FEM), and the choice of shape and test functions. The FEM is a method for numerically solving differential equations on discretised domains. The domain is split into elements, and the equations are solved on each element. Each element has 'nodes' — points at which the solution is calculated — which are located at $\mathbf{x}_i$. Examples of a one-dimensional mesh and a two-dimensional quadrilateral mesh are shown in Figure 3.1.

For this work, consider specifically line elements in one-dimension and rectangular quadrilateral elements in two dimensions (the examples in Figure 3.1 illustrate these cases). At each node location $\mathbf{x}_i$, the solution is evaluated as $\mathbf{u}(\mathbf{x}_i,t)$. The approximate solution at all points in the element is $\tilde{\mathbf{u}}(\mathbf{x},t)$, given by interpolation between the nodes. The shape functions are defined based on the required order of this interpolation and conditions on both their specified value at certain nodes and specified domain of finite support.

Each shape function has a value of 1 at one node and 0 at all other nodes. As discussed previously, these shape functions $\psi_k(\mathbf{x})$ will form a basis of the space $\tilde{W}_p^1$,

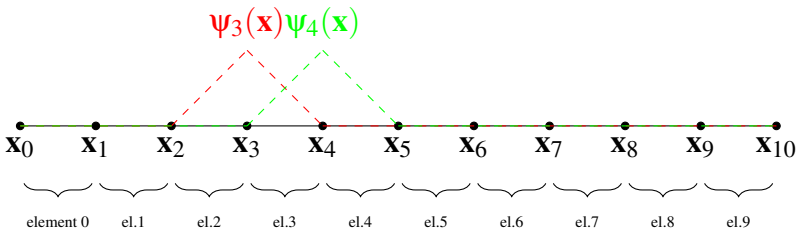

(a) Linear shape functions in one dimension.

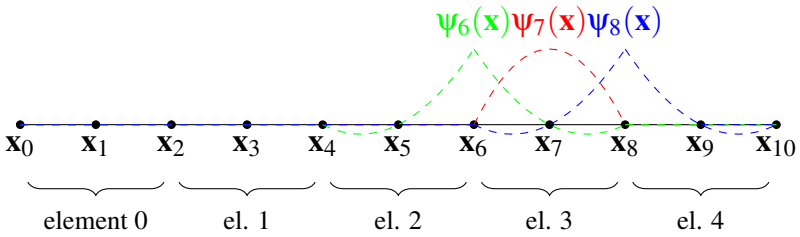

(b) Quadratic shape functions in one dimension.

Figure 3.2: Linear and quadratic shape functions for the third element on a one-dimensional domain with ten nodes. Shape functions are shown by red, green and blue dashed lines.

and we choose to label each with the index of the node it is associated with. To be clear, if we look at the value of the shape function $\psi_i(\mathbf{x})$ at each node $\mathbf{x}_j$, we have

$$\psi_i(\mathbf{x}_j) = \delta_{ij} = \begin{cases} 1 & \text{if} \quad i = j \\ 0 & \text{if} \quad i \neq j. \end{cases} \tag{3.33}$$

The shape function has finite support such that it is non-zero only in the vicinity of its associated node. The definition of 'vicinity' depends on the order of interpolation and is easiest to explain with diagrams like Figure 3.2.

For linear interpolation, the shape functions are piecewise linear, as shown in Figure 3.2(a). The two shape functions which have support over element 3 have been plotted. In higher dimensions, the shape functions are piecewise bi- or tri-linear and have support in the vicinity of one node. A two-dimensional quadrilateral linear element has four nodes (the four vertices of the element) and a 3D quadrilateral linear element has a node at each of its eight vertices.

An example of one-dimensional quadratic shape functions is shown in Figure 3.2(b). For each element, there are three piecewise quadratic shape functions that take non-zero values over the element. The one-dimensional elements shown have three nodes; in the two-dimensional case, this increases to nine nodes (as seen on the example mesh

in Figure 3.1(b)) and the shape functions are quadratic in both spatial coordinates.

The choice of interpolation depends on the pay-off between two factors. Say we have a one-dimensional domain with nine equally sized elements. If linear interpolation is used, there are ten nodes, ten shape functions, and therefore ten residual equations to solve (for each distinct variable). However, if the interpolation is quadratic, there are nineteen nodes, and nineteen residual equations, but the FEM solution can more closely approximate higher order polynomials in the true solution.

For a node where there is a Dirichlet boundary condition on u_l (u_l is said to be 'pinned'), it is not required to solve a residual equation at that node. For example, if there is a boundary condition $u_l(\mathbf{x} = \mathbf{x}_0) = 0$, then there is no need to update $u_l(\mathbf{x} = \mathbf{x}_0)$ and therefore its associated entries do not appear in the Jacobian for the Newton method.

Using the finite support of the shape functions leads us to the final elemental decomposition of the equations. Each residual r_{jk} is associated with one node at $\mathbf{x}_k$ and one shape function $\psi_k(\mathbf{x})$ (for each variable, indexed by j). Using the example of the one-dimensional domain in Figure 3.2(a), that shape function is zero-valued and has zero spatial derivatives everywhere except in element $k-1$ and element k. This means that, from the definition of r_{jk} in equation (3.29), the integrand is zero over almost all of the domain. For our one-dimensional linear element example, we have

$$\begin{aligned} r_{jk}(U_{01},\ldots,U_{N-1\,M}) &= \int_\Omega \mathcal{R}_j(\mathbf{x},U_{01},\ldots,U_{N-1\,M})\psi_k(\mathbf{x})d\mathbf{x} \\ &= \int_{\text{element k}-1} \mathcal{R}_j(\mathbf{x},U_{01},\ldots,U_{N-1\,M})\psi_k(\mathbf{x})d\mathbf{x} \\ &\quad + \int_{\text{element k}} \mathcal{R}_j(\mathbf{x},U_{01},\ldots,U_{N-1\,M})\psi_k(\mathbf{x})d\mathbf{x}. \end{aligned} \tag{3.34}$$

This means that to assemble the residual equations, the integral can be calculated over each element once, and then each residual is composed of a sum over the relevant elements. Take one term in (3.29), for example the diffusion term:

$$\int_{\text{el. k}-1} \tilde{D}\sum_{q=1}^{M} U_{jq}(t)\nabla\psi_q(\mathbf{x})\cdot\nabla\psi_k(\mathbf{x})d\mathbf{x} + \int_{\text{el. k}} \tilde{D}\sum_{q=1}^{M} U_{jq}(t)\nabla\psi_q(\mathbf{x})\cdot\nabla\psi_k(\mathbf{x})d\mathbf{x}. \tag{3.35}$$

We see that many of the terms in the sum over q are zero, unless the support of $\psi_q(\mathbf{x})$ overlaps with that of $\psi_k(\mathbf{x})$ — if $\mathbf{x}_q$ and $\mathbf{x}_k$ are in the same vicinity. This is used when calculating the Jacobian matrix $\left(\left.\frac{\partial r_{jk}}{\partial U_{lq}}\right|_{U_{lq}^{(a)}}\right)$. The contribution of the diffusion term to

the Jacobian is

$$\frac{\partial}{\partial U_{lq}}\left(\int_{\text{el. k}-1}\tilde{D}\sum_{q=1}^{M}U_{jq}(t)\nabla\psi_q(\mathbf{x})\cdot\nabla\psi_k(\mathbf{x})d\mathbf{x}+\int_{\text{el. k}}\tilde{D}\sum_{q=1}^{M}U_{jq}(t)\nabla\psi_q(\mathbf{x})\cdot\nabla\psi_k(\mathbf{x})d\mathbf{x}\right)\Bigg|_{U_{lq}^{(a)}}$$
$$=\left(\int_{\text{el. k}-1}\tilde{D}\sum_{q=1}^{M}\delta_{lj}\nabla\psi_q(\mathbf{x})\cdot\nabla\psi_k(\mathbf{x})d\mathbf{x}+\int_{\text{el. k}}\tilde{D}\sum_{q=1}^{M}\delta_{lj}\nabla\psi_q(\mathbf{x})\cdot\nabla\psi_k(\mathbf{x})d\mathbf{x}\right)\Bigg|_{U_{lq}^{(a)}} \tag{3.36}$$

which is only non-zero if $\mathbf{x}_q$ is in the vicinity of $\mathbf{x}_k$. This means that the Jacobian matrix is sparse which can be exploited in solving the Newton method (3.31).

In practice, the integrals for the finite element method are approximated using numerical integration methods, such as a Gauss integration rule. To facilitate this, each element and its shape functions are mapped to the space $[-1,1]^n$ where n is the dimension of Ω.

To summarise, the method is as follows:

- Put the residual equations into their weak form.
- Define a mesh, shape functions and a timestepping method. Use these to discretize the equations.
- Pin the variables where they are imposed by Dirichlet conditions.
- Calculate the residual values for some initial guess of the unknowns.
- Calculate the Jacobian and use it to solve for the set of unknown values for the next iteration.
- Iterate the Newton method until the residuals are suitably small.
- This is the solution of the problem for this timestep. Use this solution as the initial guess for the Newton method for the next timestep.

All of the equations derived in Chapter 2 are of the form of the diffusion-reaction equations given by equation (3.5). Thus, they can be solved by FEM following the procedure detailed above.

3.3 Strong and weak form of reaction-diffusion equations on different domains

Choice of the domain Ω and its boundary $\partial\Omega$ affect the strong and weak forms shown in equations (3.5) and (3.7). In this section, strong and weak forms are presented for one- and two-dimensional Cartesian domains. The derivation of the weak form in a three-dimensional cylindrical co-ordinate system is presented in Appendix C. The hydriding model has not yet been solved on a cylindrical domain, but since obtaining the weak form for general orthogonal co-ordinate systems is non-trivial, the derivation is presented for use in future work.

The general strong form of the reaction-diffusion equations are repeated here with function dependencies suppressed for clarity:

$$\frac{\partial u_j}{\partial t} + R_j - \tilde{D}_{(j)} \boldsymbol{\nabla} \cdot \boldsymbol{\nabla} u_j - \boldsymbol{\nabla} \cdot \mathbf{F}_j = 0$$

$$\int_\Omega \left(\frac{\partial u_j}{\partial t} + R_j \right) \phi d\mathbf{x} + \int_\Omega \left(\tilde{D}_{(j)} \boldsymbol{\nabla} u_j + \mathbf{F}_j \right) \cdot \boldsymbol{\nabla} \phi d\mathbf{x} = \int_{\partial\Omega} \phi \left(\tilde{D}_{(j)} \boldsymbol{\nabla} u_j + \mathbf{F}_j \right) \cdot \mathbf{n} dS. \tag{3.37}$$

Before using oomph-lib to solve the more complicated equations of the hydriding model, a test equation was used to check the code implementation. In changing the header files for the reaction-diffusion equations in oomph-lib, two new types of term were added. The first allows for the reaction terms R, to be dependent on the gradients of the independent variables, as well as the variables themselves. The second type of term is labelled F, which prevents second spatial derivatives from appearing in the weak form of the equations. Appendix D describes the procedure to check this new code implementation works as expected.

3.3.1 One-dimensional domain

In the case where Ω is a one-dimensional domain and $\partial\Omega$ comprises the boundary points $x = x_1$ and $x = x_2$, as shown in Figure 3.3, the strong and weak form equations become

$$\frac{\partial u_j}{\partial t} + R_j - \tilde{D}_{(j)} \frac{\partial^2 u_j}{\partial x^2} - \frac{\partial F_j}{\partial x} = 0 \tag{3.38}$$

and

$$\int_{x_1}^{x_2}\left(\frac{\partial u_j}{\partial t}+R_j\right)\phi(x)dx+\int_{x_1}^{x_2}\left(\tilde{D}_{(j)}\frac{\partial u_j}{\partial x}+F_j\right)dx=\left[\phi(x)\left(\tilde{D}_{(j)}\frac{\partial u_j}{\partial x}+F_j\right)\right]_{x=x_1}^{x=x_2} \tag{3.39}$$

respectively, where

$$u_j=u_j(x,t),\ R_j=R_j\left(x,t,u_l,\frac{\partial u_l}{\partial x},\frac{\partial u_l}{\partial t}\right)\ \text{and}\ F_j=F_j\left(x,t,u_l,\frac{\partial u_l}{\partial x}\right). \tag{3.40}$$

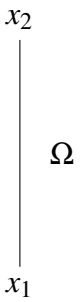

Figure 3.3: One-dimensional domain.

3.3.2 Two-dimensional Cartesian domain

In the case where Ω is a two-dimensional Cartesian domain and $\partial\Omega$ is its rectangular boundary, as shown in Figure 3.4, the strong and weak form equations become

$$\frac{\partial u_j}{\partial t}+R_j-\tilde{D}_{(j)}\left(\frac{\partial^2 u_j}{\partial x^2}+\frac{\partial^2 u_j}{\partial y^2}\right)-\left(\frac{\partial F_{j1}}{\partial x}+\frac{\partial F_{j2}}{\partial y}\right)=0 \tag{3.41}$$

and

$$\begin{aligned}
&\int_{y_1}^{y_2}\int_{x_1}^{x_2}\left\{\left(\frac{\partial u_j}{\partial t}+R_j\right)\phi(x,y)\right.\\
&\quad\left.+\left(\tilde{D}_{(j)}\frac{\partial u_j}{\partial x}+F_{j1}\right)\frac{\partial\phi(x,y)}{\partial x}+\left(\tilde{D}_{(j)}\frac{\partial u_j}{\partial y}+F_{j2}\right)\frac{\partial\phi(x,y)}{\partial y}\right\}dxdy\\
&=\int_{y_1}^{y_2}\phi(x,y)\left(\tilde{D}_{(j)}\frac{\partial u_j}{\partial x}+F_{j1}\right)\Big|_{x=x_2}dy-\int_{x_1}^{x_2}\phi(x,y)\left(\tilde{D}_{(j)}\frac{\partial u_j}{\partial y}+F_{j2}\right)\Big|_{y=y_1}dx\\
&\quad+\int_{x_2}^{x_1}\phi(x,y)\left(\tilde{D}_{(j)}\frac{\partial u_j}{\partial y}+F_{j2}\right)\Big|_{y=y_2}dx-\int_{y_2}^{y_1}\phi(x,y)\left(\tilde{D}_{(j)}\frac{\partial u_j}{\partial x}+F_{j1}\right)\Big|_{x=x_1}dy
\end{aligned}\tag{3.42}$$

respectively, where

$$\begin{aligned}
u_j &= u_j(x,y,t)\\
R_j &= R_j\left(x,y,t,u_l,\frac{\partial u_l}{\partial x},\frac{\partial u_l}{\partial y},\frac{\partial u_l}{\partial t}\right)\\
F_{jk} &= F_{jk}\left(x,y,t,u_l,\frac{\partial u_l}{\partial x},\frac{\partial u_l}{\partial y}\right).
\end{aligned}\tag{3.43}$$

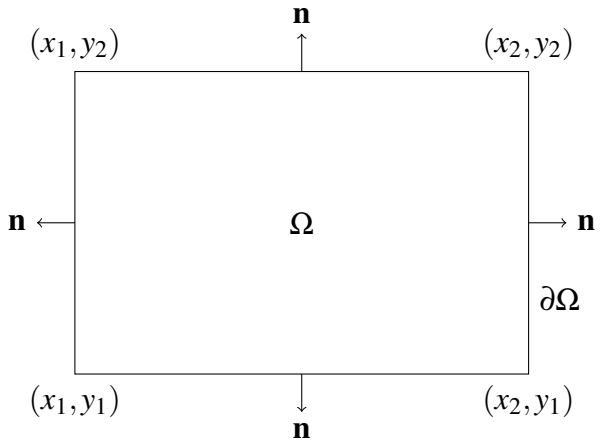

Figure 3.4: Two-dimensional Cartesian domain.

Chapter 4

Introduction to sensitivity analysis

Sensitivity analysis measures how sensitive a system is to changes in each of its inputs. More specifically, it investigates a mathematical model $u = f(\{\bar{x}_i\}_{i=1}^n)$ where the inputs $\{\bar{x}_i\}_{i=1}^n$ are random and the function f is, in general, highly non-linear. The variables u, and f redefined in these terms of a general mathematical model for the purposes of this chapter alone. It may be difficult to quantify the dependence of u on its inputs, as is the case in our highly-coupled finite element model. Introducing randomness into the input parameters makes for a stochastic output, and we can quantify change in u with respect to changes in each $\bar{x}_i$. Sensitivity analysis can be used to fix parameters which do not affect the output to some nominal value, or to indicate that more precise experimental measurements of the coefficients should be made. In this project, sensitivity to change has been quantified through variance-based decomposition (VBD). VBD calculates what proportion of the output variance can be attributed to variance in each of the inputs or groups of inputs. The result of this calculation is the set of Sobol indices.

4.1 Sobol indices

Sobol indices were initially developed by I.M. Sobol. Their derivation is described here, mostly following two papers authored by Sobol [70, 71]. We begin by describing the method for ANOVA (ANalysis Of VAriances) decomposition of a function.

4.1.1 ANOVA decomposition

We define a mathematical model $u = f(\bar{x})$ where $\bar{x} = (\bar{x}_1, \ldots, \bar{x}_n)$ the vector of unknown parameters is defined on the unit hypercube. We expand f by

$$\begin{aligned} f(\bar{x}) &= f_0 + \sum_{i=1}^{n} f_i(\bar{x}_i) + \sum_{j=1}^{n} \sum_{i=1}^{j-1} f_{ij}(\bar{x}_i, \bar{x}_j) + \cdots + f_{12\ldots n}(\bar{x}_1, \ldots, \bar{x}_n) \\ &= f_0 + \sum_{s=1}^{n} \sum_{i_1 < \cdots < i_s} f_{i_1 \ldots i_s}(\bar{x}_{i_1}, \ldots, \bar{x}_{i_s}) \end{aligned} \tag{4.1}$$

for $1 \leq i_1 < \cdots < i_s \leq n$. This expansion is defined by Sobol as an expansion into 'summands of different dimensions' [70] or its ANOVA-representation if

- f_0 is constant (Condition 1), and
- $\int_0^1 f_{i_1 \ldots i_s}(\bar{x}_{i_1}, \ldots, \bar{x}_{i_s}) d\bar{x}_k = 0$ for $k = i_1, \ldots, i_s$ (Condition 2).

For example, take one of the 'second dimension' functions, $s = 2$, and the specific function $f_{24}(\bar{x}_2, \bar{x}_4)$ which has $i_1 = 2$, $i_2 = 4$. If the function adheres to Condition 2, then

$$\begin{aligned} \int_0^1 f_{24}(\bar{x}_2, \bar{x}_4) d\bar{x}_2 &= 0 \qquad \text{and} \\ \int_0^1 f_{24}(\bar{x}_2, \bar{x}_4) d\bar{x}_4 &= 0. \end{aligned} \tag{4.2}$$

From these conditions, we can find f_0 explicitly, by

$$\begin{aligned} \int_0^1 \cdots \int_0^1 f(\bar{x}) d\bar{x} &= \int_0^1 \cdots \int_0^1 \left(f_0 + \sum_{s=1}^{n} \sum_{i_1 < \cdots < i_s} f_{i_1 \ldots i_s}(\bar{x}_{i_1}, \ldots, \bar{x}_{i_s}) \right) \prod_{k=1}^{n} d\bar{x}_k \\ &= f_0. \end{aligned} \tag{4.3}$$

We also have that any function $f_{i_1 \ldots i_s}(\bar{x}_{i_1}, \ldots, \bar{x}_{i_s})$ taken from any of the 'dimensions' is orthogonal to any other, which we can write as

$$\begin{aligned} &\int_0^1 \cdots \int_0^1 f_{i_1 \ldots i_s}(\bar{x}_{i_1}, \ldots, \bar{x}_{i_s}) f_{j_1 \ldots j_r}(\bar{x}_{j_1}, \ldots, \bar{x}_{j_r}) d\bar{x} \\ &\quad = \int_0^1 \cdots \int_0^1 f_{i_1 \ldots i_s}(\bar{x}_{i_1}, \ldots, \bar{x}_{i_s}) f_{j_1 \ldots j_r}(\bar{x}_{j_1}, \ldots, \bar{x}_{j_r}) \prod_{k=1}^{n} d\bar{x}_k \\ &\quad = 0 \end{aligned} \tag{4.4}$$

if $(i_1,\ldots,i_s) \neq (j_1,\ldots,j_r)$, by Condition 2. For example, if we look at the integral over the unit hypercube of the product $f_1(\bar{x}_1)\cdot f_{13}(\bar{x}_1,\bar{x}_3)$,

$$\begin{aligned}\int_0^1\cdots\int_0^1 f_1(\bar{x}_1)\cdot f_{13}(\bar{x}_1,\bar{x}_3)d\bar{x} &= \int_0^1\cdots\int_0^1 f_1(\bar{x}_1)\cdot f_{13}(\bar{x}_1,\bar{x}_3)\prod_{k=1}^{n} d\bar{x}_k \\ &= \int_0^1\int_0^1 f_1(\bar{x}_1)\cdot f_{13}(\bar{x}_1,\bar{x}_3)d\bar{x}_1 d\bar{x}_3 \\ &= 0\end{aligned} \tag{4.5}$$

where the final equivalence is found by performing the integral with respect to $\bar{x}_3$. In general, the final equivalence with zero may be found by integrating with respect to any $\bar{x}_k$ which appears as an independent variable in only one function in the integrand.

Sobol provides a proof that this expansion exists and is unique [70] which may be followed in Appendix E, from which we obtain definitions of the constant f_0 and the functions comprising $f(\bar{x})$,

$$\begin{aligned} f_0 &= \int_0^1\cdots\int_0^1 f(\bar{x})d\bar{x} \\ f_i(\bar{x}_i) &= \int_0^1\cdots\int_0^1 f(\bar{x})d\bar{x}/d\bar{x}_i - f_0\end{aligned} \tag{4.6}$$

where the notation $d\bar{x}/d\bar{x}_i = d\bar{x}_1\ldots d\bar{x}_{i-1}d\bar{x}_{i+1}\ldots d\bar{x}_n$ indicates integration with respect to all independent variables except $\bar{x}_i$.

4.1.2 Sobol variances and Sobol indices

We can now use this expansion to define Sobol indices, following Sobol's later paper [71], Saltelli et al.'s book Global Sensitivity Analysis: The Primer [72] and Saltelli et al.'s paper [73]. If we assume $f(\bar{x})$ is square-integrable, then all the functions $f_{i_1\ldots i_s}$

are also square integrable. Squaring Equation (4.1) and integrating over the unit hypercube, we have

$$\begin{aligned}\int_0^1 \cdots \int_0^1 (f(\bar{x}))^2 d\bar{x} \\ = \int_0^1 \cdots \int_0^1 \left[f_0^2 + \left(\sum_{s=1}^{n} \sum_{i_1 < \cdots < i_s} f_{i_1 \ldots i_s}(\bar{x}_{i_1}, \ldots, \bar{x}_{i_s}) \right)^2 \right] d\bar{x} \\ + 2 f_0 \int_0^1 \cdots \int_0^1 \sum_{s=1}^{n} \sum_{i_1 < \cdots < i_s} f_{i_1 \ldots i_s}(\bar{x}_{i_1}, \ldots, \bar{x}_{i_s}) d\bar{x}.\end{aligned} \tag{4.7}$$

Using Condition 2, we have that the final integral on the right-hand-side is zero. Now consider the squared summation term. The integral of any of the 'cross terms' (for which the sequence $i_1 < \cdots < i_s$ does not match) will be equal to zero by Equation (4.4), and we have

$$\begin{aligned}\int_0^1 \cdots \int_0^1 \left(\sum_{s=1}^{n} \sum_{i_1 < \cdots < i_s} f_{i_1 \ldots i_s}(\bar{x}_{i_1}, \ldots, \bar{x}_{i_s}) \right)^2 d\bar{x} \\ = \int_0^1 \cdots \int_0^1 \sum_{s=1}^{n} \sum_{i_1 < \cdots < i_s} (f_{i_1 \ldots i_s}(\bar{x}_{i_1}, \ldots, \bar{x}_{i_s}))^2 d\bar{x} \\ = \sum_{s=1}^{n} \sum_{i_1 < \cdots < i_s} \int_0^1 \cdots \int_0^1 (f_{i_1 \ldots i_s}(\bar{x}_{i_1}, \ldots, \bar{x}_{i_s}))^2 \, d\bar{x}.\end{aligned} \tag{4.8}$$

Thus we have simplified equation (4.7) to

$$\int_0^1 \cdots \int_0^1 (f(\bar{x}))^2 d\bar{x} = f_0^2 + \sum_{s=1}^{n} \sum_{i_1 < \cdots < i_s} \int_0^1 \cdots \int_0^1 (f_{i_1 \ldots i_s}(\bar{x}_{i_1}, \ldots, \bar{x}_{i_s}))^2 \, d\bar{x}. \tag{4.9}$$

We now define

$$\begin{aligned} D &= \int_0^1 \cdots \int_0^1 (f(\bar{x}))^2 d\bar{x} - f_0^2 \\ D_{i_1 \ldots i_s} &= \int_0^1 \cdots \int_0^1 (f_{i_1 \ldots i_s}(\bar{x}_{i_1}, \ldots, \bar{x}_{i_s}))^2 \, d\bar{x} \end{aligned} \tag{4.10}$$

such that

$$D = \sum_{s=1}^{n} \sum_{i_1 < \cdots < i_s} D_{i_1 \ldots i_s}. \tag{4.11}$$

In the introduction to this chapter, we stated that we would look at a mathematical model $u = f(\{\bar{x}_i\}_{i=1}^n)$ with random inputs $\{\bar{x}_i\}_{i=1}^n$. Thus we begin to look at the $\bar{x}_1, \ldots, \bar{x}_n$ in our analysis thus far as continuous, independent, random, uniformly-distributed variables $\bar{X}_1, \ldots, \bar{X}_n$ on the interval $[0,1]$. The probability distribution function for each variable is therefore

$$f_{PDF}(\bar{x}_k) = \begin{cases} 1 & \text{if} \quad \bar{x}_k \in [0,1] \\ 0 & \text{otherwise} \end{cases} \tag{4.12}$$

for $k = 1, \ldots, n$. We label $F_{PDF}(\bar{x}) = \prod_{k=1}^n f_{PDF}(\bar{x}_k)$. The output of the mathematical model $U = f(\bar{X})$ is itself a continuous random variable for which we can calculate the expectation and variance. The expectation of U is

$$\mathbb{E}[U] = \mathbb{E}[f(\bar{X})] = \int_{-\infty}^{\infty} \cdots \int_{-\infty}^{\infty} f(\bar{x}) F_{PDF}(\bar{x}) d\bar{x} = \int_0^1 \cdots \int_0^1 f(\bar{x}) d\bar{x} = f_0 \tag{4.13}$$

by the definition of f_0 in equation (4.6). There is also a meaning in this sense of the 'first dimension' functions $f_i(\bar{x}_i)$, whose definition was given in equation (4.6). Looking at the expectation of U given the i^{th} random variable $\bar{X}_i$,

$$\begin{aligned} \mathbb{E}_{\bar{X}_{\sim i}}[U|\bar{X}_i] = \mathbb{E}_{\bar{X}_{\sim i}}[f(\bar{X})|\bar{X}_i] &= \int_{-\infty}^{\infty} \cdots \int_{-\infty}^{\infty} f(\bar{x}) \frac{F_{PDF}(\bar{x})}{f_{PDF}(\bar{x}_i)} d\bar{x} / d\bar{x}_i \\ &= \int_0^1 \cdots \int_0^1 f(\bar{x}) d\bar{x} / d\bar{x}_i \\ &= f_i(\bar{x}_i) + f_0, \end{aligned} \tag{4.14}$$

where the subscript on the expectation operator indicates that the mean of U is taken over all possible values of every random variable $\{\bar{X}_j\}_{j=1}^n$ except $\bar{X}_i$. We rearrange to give

$$f_i(\bar{x}_i) = \mathbb{E}_{\bar{X}_{\sim i}}[U|\bar{X}_i] - f_0. \tag{4.15}$$

Using the expectation value $\mathbb{E}[U]$ and the definition of f_0, we can also find the variance of the random variable U,

$$\begin{aligned}
\text{Var}[U] &= \mathbb{E}[(U-\mathbb{E}[U])^2] = \mathbb{E}[(U-f_0)^2] = \mathbb{E}[(f(\bar{X})-f_0)^2] \\
&= \int_{-\infty}^{\infty}\cdots\int_{-\infty}^{\infty}(f(\bar{x})-f_0)^2 F_{PDF}(\bar{x})d\bar{x} \\
&= \int_0^1\cdots\int_0^1(f(\bar{x})-f_0)^2 d\bar{x} \\
&= \int_0^1\cdots\int_0^1(f(\bar{x}))^2 d\bar{x} + f_0^2 - 2f_0\int_0^1\cdots\int_0^1 f(\bar{x})d\bar{x} \\
&= \int_0^1\cdots\int_0^1(f(\bar{x}))^2 d\bar{x} - f_0^2 \\
&= D.
\end{aligned} \tag{4.16}$$

and so D, as defined in equation (4.10), is the variance of U.

Similarly, we can look at each of the functions $f_{i_1\ldots i_s}(\bar{X}_{i_1},\ldots,\bar{X}_{i_s})$ as continuous random variables. This time we redefine $F_{PDF}(\bar{x}_{i_1},\ldots,\bar{x}_{i_s}) = \prod_{k=i_1,\ldots,i_s} f_{PDF}(\bar{x}_k)$ to contain only the probability distribution functions of the variables $\bar{X}_{i_1},\ldots,\bar{X}_{i_s}$, and we have

$$\begin{aligned}
\mathbb{E}[f_{i_1\ldots i_s}(\bar{X}_{i_1},\ldots,\bar{X}_{i_s})] &= \int_{-\infty}^{\infty}\cdots\int_{-\infty}^{\infty} f_{i_1\ldots i_s}(\bar{x}_{i_1},\ldots,\bar{x}_{i_s})F_{PDF}(\bar{x}_{i_1},\ldots,\bar{x}_{i_s})d\bar{x}_{i_1}\ldots d\bar{x}_{i_s} \\
&= \int_0^1\cdots\int_0^1 f_{i_1\ldots i_s}(\bar{x}_{i_1},\ldots,\bar{x}_{i_s})d\bar{x}_{i_1}\ldots d\bar{x}_{i_s} \\
&= 0
\end{aligned} \tag{4.17}$$

where the final equality is by Condition 2. Having a zero expectation value simplifies the calculation of the variance of $f_{i_1\ldots i_s}(\bar{x}_{i_1},\ldots,\bar{x}_{i_s})$ significantly and

$$\begin{aligned}
\text{Var}[f_{i_1\ldots i_s}(\bar{X}_{i_1},\ldots,\bar{X}_{i_s})] &= \mathbb{E}[(f_{i_1\ldots i_s}(\bar{X}_{i_1},\ldots,\bar{X}_{i_s}) - \mathbb{E}[f_{i_1\ldots i_s}(\bar{X}_{i_1},\ldots,\bar{X}_{i_s})])^2] \\
&= \mathbb{E}[(f_{i_1\ldots i_s}(\bar{X}_{i_1},\ldots,\bar{X}_{i_s}))^2] \\
&= \int_{-\infty}^{\infty}\cdots\int_{-\infty}^{\infty}(f_{i_1\ldots i_s}(\bar{x}_{i_1},\ldots,\bar{x}_{i_s}))^2 F_{PDF}(\bar{x}_{i_1},\ldots,\bar{x}_{i_s})d\bar{x}_{i_1}\ldots d\bar{x}_{i_s} \\
&= \int_0^1\cdots\int_0^1(f_{i_1\ldots i_s}(\bar{x}_{i_1},\ldots,\bar{x}_{i_s}))^2 d\bar{x}_{i_1}\ldots d\bar{x}_{i_s} \\
&= D_{i_1\ldots i_s}
\end{aligned} \tag{4.18}$$

by the definition of $D_{i_1\ldots i_s}$ in equation (4.10). To be in-keeping with the notation for $f_i(\bar{x}_i)$, it should be noted that the expectation and variance values that make up $D_{i_1\ldots i_s}$ are technically taken over all the variables $\bar{X}_{i_1},\ldots,\bar{X}_{i_s}$, and should properly be written with their subscripts as $\mathrm{Var}_{\bar{X}_{i_1},\ldots,\bar{X}_{i_s}}[f_{i_1\ldots i_s}(\bar{X}_{i_1},\ldots,\bar{X}_{i_s})]$, $\mathbb{E}_{\bar{X}_{i_1},\ldots,\bar{X}_{i_s}}[(f_{i_1\ldots i_s}(\bar{X}_{i_1},\ldots,\bar{X}_{i_s})]$ and $\mathbb{E}_{\bar{X}_{i_1},\ldots,\bar{X}_{i_s}}[(f_{i_1\ldots i_s}(\bar{X}_{i_1},\ldots,\bar{X}_{i_s})^2]$. The subscripts were suppressed in the above equations for ease of reading.

To recap, if $\bar{x}_1,\ldots,\bar{x}_n$ are continuous, independent, random, uniformly-distributed variables $\bar{X}_1,\ldots,\bar{X}_n$, then the output of our mathematical model, $U = f(\bar{X})$ is itself a random variable and we have the properties [72]

$$\begin{aligned} f_0 &= \int_0^1 \cdots \int_0^1 f(\bar{x})d\bar{x} = \mathbb{E}[U] = \mathbb{E}[f(\bar{X})] \\ f_i(\bar{x}_i) &= \int_0^1 \cdots \int_0^1 f(\bar{x})d\bar{x}/d\bar{x}_i - f_0 = \mathbb{E}_{\bar{X}_{\sim i}}[U|\bar{X}_i] - \mathbb{E}[U] \\ &= \mathbb{E}_{\bar{X}_{\sim i}}[f(\bar{X})|\bar{X}_i] - \mathbb{E}[f(\bar{X})] \\ D &= \mathrm{Var}[U] = \mathrm{Var}[f(\bar{X})] \\ D_{i_1\ldots i_s} &= \mathrm{Var}_{\bar{X}_{i_1},\ldots,\bar{X}_{i_s}}[f_{i_1\ldots i_s}(\bar{X}_{i_1},\ldots,\bar{X}_{i_s})]. \end{aligned} \tag{4.19}$$

Using these variance measures, we define sensitivity indices [73]

$$S_{i_1\ldots i_s} = \frac{D_{i_1\ldots i_s}}{D} \tag{4.20}$$

which have properties [70]

- $\sum_{s=1}^{n}\sum_{i_1<\cdots<i_s} S_{i_1\ldots i_s} = 1$ and
- $u = f(\bar{x})$ is independent of the input $\bar{x}_i$ if and only if $S_{i_1\ldots i_s} = 0$ for all cases where $i \in \{i_1,\ldots,i_s\}$.

For example, a first-order index S_i is

$$S_i = \frac{D_i}{D} = \frac{\mathrm{Var}_{\bar{X}_i}[f_i(\bar{X}_i)]}{\mathrm{Var}[U]} = \frac{\mathrm{Var}_{\bar{X}_i}[\mathbb{E}_{\bar{X}_{\sim i}}[U|\bar{X}_i] - f_0]}{\mathrm{Var}[U]}, \tag{4.21}$$

by the definitions listed in equation (4.19). By properties of the variance, and since f_0 is a constant,

$$S_i = \frac{\mathrm{Var}_{\bar{X}_i}[\mathbb{E}_{\bar{X}_{\sim i}}[U|\bar{X}_i]]}{\mathrm{Var}[U]}, \tag{4.22}$$

which is the expected reduction in variance that would be obtained if $\bar{X}_i$ were fixed as a proportion of the total variance of U [73]. In effect, this is the proportion of the variance of the model output U that comes from the randomness of $\bar{X}_i$. The first-order indices describe how influential each input is on the output individually. It can be shown that the first-order Sobol indices lie in the range $[0,1]$ using the identity [74]

$$\mathrm{Var}_{\bar{X}_i}[\mathbb{E}_{\bar{X}_{\sim i}}[U|\bar{X}_i]] + \mathrm{Var}_{\bar{X}_{\sim i}}[\mathbb{E}_{\bar{X}_i}[U|\bar{X}_i]] = \mathrm{Var}[U], \tag{4.23}$$

so $\mathrm{Var}_{\bar{X}_i}[\mathbb{E}_{\bar{X}_{\sim i}}[U|\bar{X}_i]]$ is in the interval $[0, \mathrm{Var}[Y]]$. Similar identities can be used to show the same for higher order Sobol indices.

In some cases, the output behaviour cannot be fully described by the influence of individual input parameters, and higher order indices become important. These higher order indices capture the more complex dependence of the output on groups of inputs.

A third group of indices is formed from combinations of first-order and interaction indices - total effect indices. Total effect indices S_{T_i} are obtained by adding together every Sobol index which contains the suffix i, from every order

$$S_i^T = \sum_{s=1}^{n} \sum_{i \in \{i_1 < \cdots < i_s\}} S_{i_1 \ldots i_s} \tag{4.24}$$

and describe the total effect an input has on the output, including its interaction effects.

Finally in this section, we state that the use of random variables $\bar{X}_1, \ldots \bar{X}_n$ uniformly distributed on the range $[0,1]$ was without loss of generality since any space of input variables can be transformed onto the uniformly distributed unit hypercube [75].

4.2 Practical calculation of Sobol indices

Two methods to calculate Sobol indices have been used in this project; traditional Monte-Carlo method and polynomial chaos expansion (PCE). An explanation of each method will be discussed here. The Dakota software package was used to perform the analyses.

4.2.1 Monte Carlo Sobol indices

The Monte Carlo approximation of Sobol indices is the more computationally expensive of the two methods. It bypasses the ANOVA representation and approximates the

variances (4.19) directly. To estimate a first-order index, S_i, for example, we would need to estimate $\mathrm{Var}_{\bar{X}_i}[\mathbb{E}_{\bar{X}_{\sim i}}[U|\bar{X}_i]]$. Intuitively, we could first estimate the expectation $\mathbb{E}_{\bar{X}_{\sim i}}[U|\bar{X}_i]$ by taking the mean of N instances of the model U evaluated for a vector of n parameters $\bar{\mathbf{X}}$ which are all randomly chosen, except for $\bar{X}_i$ which is fixed. Then we would estimate $\mathrm{Var}_{\bar{X}_i}[\mathbb{E}_{\bar{X}_{\sim i}}[U|\bar{X}_i]]$ by repeating this process for M values of $\bar{X}_i$ and calculating the variance. This requires $N \times M$ model evaluations to calculate a single variance which can be very computationally expensive if a high accuracy is desired and the model itself is expensive to run.

A technique described by Saltelli et al. [72] to find $\mathrm{Var}_{\bar{X}_i}[\mathbb{E}_{\bar{X}_{\sim i}}[U|\bar{X}_i]]$ reduces this computational cost. For a system with n input parameters, we form two matrices, A and B from N randomly-generated parameter vectors,

$$A = \begin{pmatrix} \bar{x}_1^{(1)} & \bar{x}_2^{(1)} & \dots & \bar{x}_n^{(1)} \\ \bar{x}_1^{(2)} & \bar{x}_2^{(2)} & \dots & \bar{x}_n^{(2)} \\ \dots & \dots & \dots & \dots \\ \bar{x}_1^{(N)} & \bar{x}_2^{(N)} & \dots & \bar{x}_n^{(N)} \end{pmatrix} \quad \text{and} \quad B = \begin{pmatrix} \bar{x}_{n+1}^{(1)} & \bar{x}_{n+2}^{(1)} & \dots & \bar{x}_{2n}^{(1)} \\ \bar{x}_{n+1}^{(2)} & \bar{x}_{n+2}^{(2)} & \dots & \bar{x}_{2n}^{(2)} \\ \dots & \dots & \dots & \dots \\ \bar{x}_{n+1}^{(N)} & \bar{x}_{n+2}^{(N)} & \dots & \bar{x}_{2n}^{(N)} \end{pmatrix}. \tag{4.25}$$

In effect, two sets of samples have been taken and split across the two matrices. We also define a set of matrices C_i, where every entry is pointwise equal to the corresponding entry in B apart from the i^{th} column, which is replaced by the i^{th} column of A,

$$C_i = \begin{pmatrix} \bar{x}_{n+1}^{(1)} & \bar{x}_{n+2}^{(1)} & \dots & \bar{x}_i^{(1)} & \dots & \bar{x}_{2n}^{(1)} \\ \bar{x}_{n+1}^{(2)} & \bar{x}_{n+2}^{(2)} & \dots & \bar{x}_i^{(2)} & \dots & \bar{x}_{2n}^{(2)} \\ \dots & \dots & \dots & \dots & \dots & \dots \\ \bar{x}_{n+1}^{(N)} & \bar{x}_{n+2}^{(N)} & \dots & \bar{x}_i^{(N)} & \dots & \bar{x}_{2n}^{(N)} \end{pmatrix}. \tag{4.26}$$

By using each row of A, B and each C_i as its own set of input parameters to the model, we obtain vectors of length N of model solutions

$$\mathbf{u}_A = f(A), \quad \mathbf{u}_B = f(B), \quad \mathbf{u}_{C_i} = f(C_i). \tag{4.27}$$

We have $i \in \{1,2,\dots,n\}$, so this is $2+n$ vectors in total. To calculate each vector requires N model evaluations, so this is $(2+n)N$ evaluations in total. Compare this with the $N \times M$ model evaluations required by the intuitive method to find $\mathrm{Var}_{\bar{X}_i}[\mathbb{E}_{\bar{X}_{\sim i}}[U|\bar{X}_i]]$ described in the introduction to this section. To obtain a good approximation of each mean, $\mathbb{E}_{\bar{X}_{\sim i}}[U|\bar{X}_i]$, a large value of N must be used. Then for a good approximation of the variance $\mathrm{Var}_{\bar{X}_i}[\mathbb{E}_{\bar{X}_{\sim i}}[U|\bar{X}_i]]$, a large value of M must be used. In general, M will be

much larger than the number of parameters n in the model, meaning that this method is cheaper.

Now we show how these vectors can be used to calculate the Sobol indices. For a randomly-distributed variable Y, that has been sampled N times with samples labelled $\{y_j\}_{j=1}^N$, where the mean of these samples is $\mu = \frac{1}{N}\sum_{j=1}^N y_i$, the variance is

$$\begin{aligned}\mathrm{Var}[Y] &\approx \frac{\sum_{j=1}^N (y_i-\mu)^2}{N} \\ &= \frac{\sum_{j=1}^N y_i^2}{N} - 2\frac{\sum_{j=1}^N \mu y_i}{N} + \frac{\sum_{j=1}^N \mu^2}{N} \\ &= \frac{\sum_{j=1}^N y_i^2}{N} - 2\mu^2 + \mu^2 \\ &= \frac{\sum_{j=1}^N y_i^2}{N} - \mu^2\end{aligned} \tag{4.28}$$

The dot product $\mathbf{u}_A \cdot \mathbf{u}_A = \sum_{j=1}^N u_{A_j}^2$ is the sum of N squared samples of the randomly-distributed model solution U. Using the approximation in equation (4.28), we write that

$$\mathrm{Var}[U] \approx \frac{1}{N}\mathbf{u}_A \cdot \mathbf{u}_A - f_0^2 \tag{4.29}$$

where $f_0 = \frac{1}{N}\sum_{j=1}^N u_{A_j}$, an approximation of the expected value of U. By arguments that can be found in [72], we also approximate

$$\mathrm{Var}_{\bar{X}_i}[\mathbb{E}_{\bar{X}_{\sim i}}[U|\bar{X}_i]] \approx \frac{1}{N}\mathbf{u}_A \cdot \mathbf{u}_{C_i} - f_0^2. \tag{4.30}$$

We can be satisfied that this is reasonable by examining $\mathbf{u}_A$ and $\mathbf{u}_{C_i}$ [72]. The j^{th} entry of $\mathbf{u}_A$ and the j^{th} entry of $\mathbf{u}_{C_i}$ represent two model evaluations which differ in the values of every input parameter except for $\bar{x}_i$. If the model is weakly influenced by the parameter $\bar{x}_i$, then the j^{th} entries of $\mathbf{u}_A$ and $\mathbf{u}_{C_i}$ will be uncorrelated. If the model is strongly influenced by the parameter $\bar{x}_i$, then the j^{th} entries of $\mathbf{u}_A$ and $\mathbf{u}_{C_i}$ will be strongly correlated. This means that a large value in the j^{th} entry of $\mathbf{u}_A$ corresponds to a large value in the j^{th} entry of $\mathbf{u}_{C_i}$, and thus a larger value of the scalar product $\mathbf{u}_A \cdot \mathbf{u}_{C_i}$ is calculated.

Now we have the first-order Sobol indices,

$$S_i = \frac{\mathrm{Var}_{\bar{X}_i}[f_i(\bar{X}_i)]}{\mathrm{Var}[U]} = \frac{\mathrm{Var}_{\bar{X}_i}[\mathbb{E}_{\bar{X}_{\sim i}}[U|\bar{X}_i]]}{\mathrm{Var}[U]} \approx \frac{\frac{1}{N}\mathbf{u}_A \cdot \mathbf{u}_{C_i} - f_0^2}{\frac{1}{N}\mathbf{u}_A \cdot \mathbf{u}_A - f_0^2}. \tag{4.31}$$

There are n first-order Sobol indices corresponding to each of the n model input parameters. A similar method can be used to generate second-order indices, and so on. In the case of second-order indices S_{mn}, we have matrices C_{mn} which are equal to B but have both columns m and n exchanged for the corresponding columns in A.

To obtain the total index S_i^T, we need to find the sum of all Sobol indices of every order which have a suffix i. Alternatively, we can take the sum of all Sobol indices (this is equal to 1, as stated in the properties of Sobol indices) and minus the sum of all Sobol indices of every order which *do not* contain the suffix i [73],

$$S_i^T = 1 - \frac{\mathrm{Var}_{\bar{X}_{\sim i}}[\mathbb{E}_{\bar{X}_i}[U|\bar{X}_{\sim i}]]}{\mathrm{Var}[U]} = 1 - \frac{\frac{1}{N}\mathbf{u}_B \cdot \mathbf{u}_{C_i} - f_0^2}{\frac{1}{N}\mathbf{u}_A \cdot \mathbf{u}_A - f_0^2}. \tag{4.32}$$

The vectors $\mathbf{u}_B$ and $\mathbf{u}_{C_i}$ differ only in their values of the $\bar{x}_i$ input parameter – all other parameters are the same. By the same reasoning as before, their dot product $\mathbf{u}_B \cdot \mathbf{u}_{C_i}$ will therefore be large if $\bar{x}_i$ is *not* strongly influential.

This is the method used by Dakota to calculate Sobol indices through Monte Carlo estimates.

4.2.2 Polynomial chaos expansion

The aim of polynomial chaos expansion (PCE) is to attempt to calculate the probability density function (PDF) of the solution U to a mathematical model $U = f(\bar{X}) = f(\bar{x}_1, \ldots, \bar{x}_n)$ with stochastic model inputs $\{\bar{x}_j\}_{j=1}^n$. The PDF of U will depend on the PDFs of the random inputs. PCE is often described as a stochastic analogy of the finite element method (FEM). This is because it makes use of a function basis in much the same way as test functions from FEM.

The explanation of PCE given here follows that by Sudret [76] and the original work by Ghanem and Spanos [77]. As first shown by Weiner in 1938 [78], any second-order random variable Z has a polynomial chaos decomposition

$$Z = \sum_{j=0}^{\infty} Z_j \Psi_j(\{\xi_i\}_{i=1}^{\infty}) \tag{4.33}$$

where $\{Z_j\}_{j=0}^{\infty}$ are coefficients to be found, $\{\Psi_j\}_{j=0}^{\infty}$ are the set of multivariate Hermite polynomials and $\{\xi_i\}_{i=1}^{\infty}$ are independent mean-zero Gaussian random variables with variance 1. This expression is the basis of polynomial chaos expansions.

We consider again the mathematical model

$$U = f(\bar{X}) = f(\bar{x}_1, \ldots, \bar{x}_n) \tag{4.34}$$

with random input variables and seek to find its polynomial chaos decomposition

$$U = \sum_{j=0}^{\infty} U_j \phi_j(\bar{x}_1, \ldots, \bar{x}_n). \tag{4.35}$$

Similarly to Equation (4.33), $\{U_j\}_{j=0}^{\infty}$ are constant coefficients and the set $\{\phi_j\}_{j=0}^{\infty}$ are multivariate polynomials. These multivariate polynomials are formed by taking products of univariate polynomials $\{\psi_j(\bar{x}_i)\}_{j=0}^{\infty}$ with different arguments. The functions $\{\psi_j(\bar{x}_i)\}_{j=0}^{\infty}$ must form an orthogonal basis of all univariate polynomials. The basis chosen depends on the joint PDF of the input variables and is chosen by the Weiner-Askey scheme [79]. For example, if the random variables are normally distributed, the chosen polynomial basis $\{\psi_j(\bar{x}_i)\}_{j=0}^{\infty}$ is the Hermite polynomials and for uniform variables, we choose the Legendre polynomials. If the joint PDF of the set $\{\bar{x}_i\}_{i=1}^{n}$ is non-standard, it can be (approximately or exactly) transformed onto the joint standard normal PDF using the inverse CDF method [76] or the Nataf transform [80]. If the variables $\{\bar{x}_i\}_{i=1}^{n}$ are independent, different types of polynomials may be used for each [81].

Once we have a chosen basis of univariate polynomials $\{\psi_j(\bar{x}_i)\}_{j=0}^{\infty}$, we must be able to describe how to build the multivariate polynomials $\{\phi_j\}_{j=0}^{\infty}$. Instead of being described by the index j, these multivariate polynomials can be described by the index ζ: $\phi_\zeta \equiv \phi_j$. To be clear, these are the same functions with a different labelling scheme. This index $\zeta = \{\zeta_i\}_{i=1}^{M}$ represents a sequence of M non-negative integers which encode the building of each ϕ_ζ. The integer ζ_i selects a polynomial from the basis to operate on $\bar{x}_i$. For example, if $\zeta = (1,0,5)$, then the multivariate polynomial $\phi_\zeta(\bar{x}_1, \bar{x}_2, \bar{x}_3) = \psi_1(\bar{x}_1) \times \psi_0(\bar{x}_2) \times \psi_5(\bar{x}_3)$. For the bases chosen by the Weiner-Askey scheme, $\psi_i(\bar{X})$ is a polynomial with degree i. Specifically $\psi_0(\bar{X}) = \psi_0$ is a constant. The sequences, ζ will be used again when deriving the Sobol indices from the PCE.

To make it possible to calculate the coefficients, the sum in Equation (4.35) is truncated such that we only consider multivariate polynomials with degree p or less. This gives the truncated PCE of U

$$U = \sum_{j=0}^{P-1} U_j \phi_j(\bar{x}_1, \ldots, \bar{x}_n) \tag{4.36}$$

where $P = \frac{(n+p)!}{n!p!}$ the number of functions needed to make an n-dimensional basis of multivariate polynomials selected by the Weiner-Askey scheme [77]. When we describe 'multivariate polynomials with degree p or less', we mean that there are no terms which involve the product of more than p independent variables. This means the example given previously $\phi_\zeta(\bar{x}_1, \bar{x}_2, \bar{x}_3)$ with $\zeta = (1,0,5)$ is of degree 6. To obtain a degree of p or less, we must have

$$\sum_{i=1}^{M} \zeta_i \leq p \tag{4.37}$$

for any $\phi_j = \phi_\zeta$ in the truncated expression.

To calculate the expansion coefficients $\{U_j\}_{j=0}^{P-1}$ in Equation (4.36), Dakota's projection method capabilities have been used [81]. The method for calculating the coefficients in this way is described here.

We multiply Equation (4.35) by $\phi_i(\bar{x}_1, \ldots, \bar{x}_n)$ and take the expectation of both sides (repressing the dependence on $(\bar{x}_1, \ldots, \bar{x}_n)$ for brevity)

$$\mathbb{E}[U\phi_i] = \mathbb{E}\left[\left(\sum_{j=0}^{\infty} U_j \phi_j\right)\phi_i\right] = \mathbb{E}\left[U_i \phi_i^2\right]. \tag{4.38}$$

Orthogonality of the function basis has been employed - Weiner-Askey selected polynomials of different order or of different arguments are all orthogonal to one another [77]. The coefficient U_i can be written outside of the expectation since it is not random. We have

$$U_j = \frac{\mathbb{E}[U\phi_j]}{\mathbb{E}[\phi_j^2]} = \frac{\int U(\bar{X})\phi_j(\bar{X})\chi_n(\bar{X})d\bar{x}}{\int \phi_j^2(\bar{X})\chi_n(\bar{X})d\bar{x}} \tag{4.39}$$

where $\chi_n(\bar{X})$ is the joint PDF of the input parameters.

The denominator may be calculated analytically [76], and the integration to calculate the numerator is performed numerically, in this case by Gaussian quadrature. Through this we obtain the P coefficients U_j. We use Dakota's tensor product Gaussian quadrature capabilities [81] to integrate the numerator of Equation (4.39) in multiple dimensions. The type of quadrature is matched to the polynomials used in the expansion, for example, Gauss-Legendre quadrature for Legendre polynomials. If we have m_i quadrature points in each dimension, where i denotes the dimension, then we can integrate any polynomial of order $2m_i - 1$ exactly. This requires $\prod_{i=1}^{n} m_i$ evaluations

of the function U overall. If the quadrature order is equal for each dimension (for each input parameter) $m_i = m$, then we require m^n function evaluations.

In the integrand, we have $\phi_j(\bar{X})$ of order p and U truncated to order p in each dimension: we need at least a quadrature order of $p+1$ for accurate coefficients [82]. By calculating U_j for every term in the truncated expression, Equation (4.36), we now have the approximate polynomial chaos decomposition of U.

Finally, we need to find the Sobol indices. To relate the truncated PCE shown in Equation (4.36) to the ANOVA expansion in Equation (4.1), we define $\mathcal{J}_{k_1,\ldots,k_s}$. This is the set of all sequences $\{\zeta_i\}_{i=1}^M$ for which only the terms with $i \in \{k_1,\ldots,k_s\}$ are non-zero:

$$\mathcal{J}_{k_1,\ldots,k_s} = \left\{ \zeta : \begin{array}{ll} \zeta_i > 0 & \text{if } i \in \{k_1,\ldots,k_s\}, \\ \zeta_i = 0 & \text{if } i \notin \{k_1,\ldots,k_s\} \end{array} \right\}. \tag{4.40}$$

The choices of zeta which make up the set $\mathcal{J}_{k_1,\ldots,k_s}$ correspond to those multivariate polynomials ϕ_ζ which have arguments $\bar{X}_{k_1},\ldots\bar{X}_{k_s}$.

We now re-order the terms in Equation (4.36) according to their arguments:

$$\begin{aligned} U &= \sum_{j=0}^{P-1} U_j \phi_j(\bar{x}_1,\ldots,\bar{x}_n) \\ &= U_0 + \sum_{i=1}^{n} \sum_{\zeta\in\mathcal{J}_i} U_\zeta \phi_\zeta(\bar{x}_i) + \sum_{i_2=1}^{n} \sum_{i_1=1}^{i_2} \sum_{\zeta\in\mathcal{J}_{i_1,i_2}} U_\zeta \phi_\zeta(\bar{X}_{i_1},\bar{X}_{i_2}) \\ &\quad + \cdots + \sum_{1\le i_1<\cdots<i_s\le n} \sum_{\zeta\in\mathcal{J}_{i_1,\ldots,i_s}} U_\zeta \phi_\zeta(\bar{X}_{i_1},\ldots\bar{X}_{i_s}) \\ &\quad + \cdots + \sum_{\zeta\in\mathcal{J}_{1,2,\ldots,n}} U_\zeta \phi_\zeta(\bar{x}_1,\ldots,\bar{x}_n) \end{aligned} \tag{4.41}$$

Again we emphasise that the functions ϕ_ζ are the same as the functions ϕ_j from Equation (4.36) with a different labelling. Therefore the coefficients U_ζ are the same as U_j also. Each term $\sum_{\zeta\in\mathcal{J}_{i_1,\ldots,i_s}} U_\zeta \phi_\zeta(\bar{X}_{i_1},\ldots\bar{X}_{i_s})$ in Equation (4.41) depends on only the variables $\bar{X}_{i_1},\ldots\bar{X}_{i_s}$. Since this is the same construction as the terms in the ANOVA representation, and the ANOVA expansion is unique (see Appendix E), we have that Equation (4.41) *is* the ANOVA representation, where

$$f_{i_1\ldots i_s}(\bar{X}_{i_1},\ldots\bar{X}_{i_s}) = \sum_{\zeta\in\mathcal{J}_{i_1,\ldots,i_s}} U_\zeta \phi_\zeta(\bar{X}_{i_1},\ldots\bar{X}_{i_s}). \tag{4.42}$$

From this point, we can go back and calculate the Sobol indices as per Section 4.1.2. Since we have the ANOVA decomposition, the Sobol indices can be calculated analytically at a low additional computational cost as shown by Sudret in 2008 [76].

4.2.3 Comparison of Monte Carlo and polynomial chaos expansion methods

The most obvious difference between Monte Carlo and PCE methods for calculating Sobol indices is computing time. In a finite element code where it is relatively costly to find a model solution, the sensitivity analysis cost is dominated by the number of function evaluations. The Monte Carlo method described in Section 4.2.1 requires $(2+n)N$ model evaluations where n is the number of input parameters and N is the number of samples taken to approximate the mean $\mathbb{E}[U|\bar{X}_i]$. The PCE method described in Section 4.2.2 requires m^n function calls where m is the quadrature order used to calculate $\mathbb{E}[U\phi_j]$ and again n is the number of input parameters. Cost will clearly depend on the values of N and m chosen, but as a rule of thumb, PCE will have the upper hand for fewer than around 10 input parameters.

PCE has been shown to be accurate in a range of different applications [76].

Chapter 5

One-dimensional modelling results

In this chapter, uranium hydriding is modelled on a one-dimensional domain. The schematic in Figure 2.1 showed the hydriding process on a cross-section taken perpendicular to the metal surface. Figure 5.1 depicts the one-dimensional modelling domain with respect to that slice. The domain represents a line perpendicular to the metal surface, from the metal-atmosphere interface into the bulk of the metal.

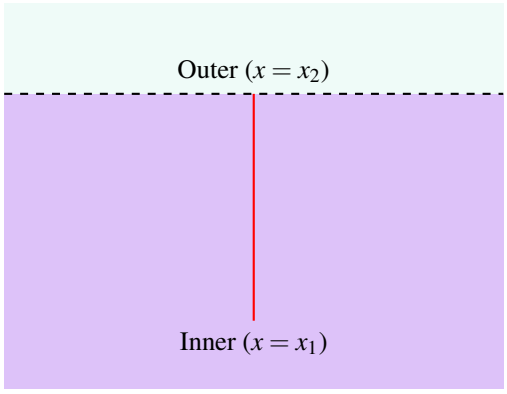

Figure 5.1: Representation of the one-dimensional solution domain in red. Purple indicates uranium metal and blue indicates the atmosphere.

Since the domain is one-dimensional, it will obviously not be possible to see the formation of hydride shapes. However, one-dimensional modelling is computationally cheap, and can be used to signpost important modelling parameters and effects which may carry through to higher-dimensional models. Also in one dimension, the inert surface passivation layer (SPL) will only affect the system by adding a time-delay to hydrogen reaching the uranium metal surface, thus increasing the time for hydride to begin to form. It will not be possible to see the effect of lateral stresses in the SPL caused by non-homogeneous expansion. For this reason, and to reduce complexity, the

1D system has been modelled without the presence of an SPL.

Figure 5.2 shows an example of how the results are graphically represented in this chapter. The figure shows a bar — the one-dimensional domain has been extruded horizontally to make the results easier to visualise. Each bar is a snapshot in time, and its colouring represents the value of a particular independent variable at each point in the domain, at that time. At the top of the figure is the domain boundary incident on the atmosphere and at the bottom is the boundary in the uranium metal bulk. Material lines which serve to show the system undergoing expansion or compression are shown by the horizontal lines spaced throughout the domain.

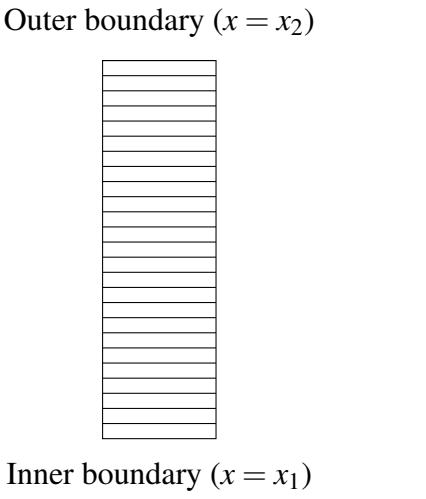

Figure 5.2: Bar representation of the one-dimensional solution domain.

Sometimes it will be advantageous to view all timesteps on one graph. In this case a space-time plot is created. The top and bottom of the image still represent the outer and inner boundaries respectively, and time is shown on the horizontal axis.

The governing differential equations used throughout this chapter are the one-dimensional equivalent of those derived in Chapter 2. In some cases, simplified versions of those equations are used. References or calculations for all physical parameters are given in Appendix F.

This chapter presents one-dimensional models of uranium hydriding, their simulated solutions, and in some cases, sensitivity analyses of the dependence of the solutions on input parameters. The sensitivity analyses are used to highlight important aspects of each model and inform successive models.

5.1 Instantaneous reaction kinetics models

The first three models presented in this chapter describe systems where the hydriding reaction is instantaneous. If the concentration of hydrogen is higher than the solubility limit, hydride is present with no time delay. The amount of hydride is calculated by the lever rule presented by Jernkvist and Massih [61], given in equation (2.46). Having an instantaneous reaction is equivalent to having an infinite rate k in the reaction rate equation (2.46), giving the equation for the hydride volume fraction, f as

$$f = f_e = \begin{cases} 0 & \text{if } C_{TOT} \leq C_{TSS} \\ \dfrac{C_{TOT} - C_{TSS}}{C_{UB} - C_{TSS}} & \text{if } C_{TSS} < C_{TOT} < C_{UB} \\ 1 & \text{if } C_{TOT} \geq C_{UB} \end{cases} \tag{5.1}$$

where the definition of f_e was given in equation (2.45). Since the reaction is assumed to be instantaneous, terms involving $\frac{\partial f}{\partial t}$ in mass and energy conservation (equations (2.48) and (2.28)) are not included. The differential equations governing the other dependent variables are different for each of the models presented in this section, and are thus defined ad hoc.

5.1.1 Model 1: Reaction-diffusion only model

The first set of equations solved on this one-dimensional domain form a simple reaction-diffusion system, where we solve for C, the hydrogen concentration and f, the volume fraction of hydride. The effects of temperature, stress and deformation are ignored. For a reaction-diffusion only model in one dimension, equation (2.21) for the hydrogen flux becomes

$$J = -D_U \frac{\partial C}{\partial x}. \tag{5.2}$$

Using this flux, equation (2.15) for hydrogen diffusion in one dimension therefore becomes the one-dimensional heat equation

$$\frac{\partial C}{\partial t} = -\frac{\partial J}{\partial x} = D_U \frac{\partial^2 C}{\partial x^2} \tag{5.3}$$

with D_U is a constant, the diffusivity of hydrogen in uranium metal. The boundary conditions applied on C are chosen such that there is no flux of hydrogen across the

inner boundary,

$$J|_{inner} = 0. \tag{5.4}$$

This boundary could represent two possible physical scenarios — the bottom of a uranium coupon is sitting on some solid apparatus (such that no hydrogen diffuses out across this boundary), or the centre of a symmetric uranium coupon (such that the concentration of hydrogen on each side of the boundary is equal, so flux is zero). The in-flux of hydrogen across the outer boundary is set to be proportional to the difference between the atmospheric concentration and the concentration in the metal, in the style of a Newton cooling condition:

$$J|_{outer} = -\lambda_C \left(C_{atm} - C\right), \tag{5.5}$$

with $\lambda_C = \frac{0.1}{a}$ where $a = 0.01$m is the domain length. The atmospheric concentration C_{atm} was chosen to be some value larger than the solubility limit to ensure hydride will be formed. The value is set at $C_{atm} = 1000 C_{TSS} = 1.047 \times 10^4 \text{mol m}^{-3}$. Initially, there is no hydride in the system, and there is a small concentration of hydrogen everywhere in the metal

$$\begin{gathered} f(t=0) = 0 \\ C(t=0) = C_{init} = C_{atm} \times 10^{-4} = 1.047 \text{mol m}^{-3}. \end{gathered} \tag{5.6}$$

This initial condition on C is set to remain in-keeping with the initial conditions for subsequent multi-physics models. The reason for choosing this value will be explained when those models are considered.

It takes a long time to see the effect of diffusion of hydrogen through the 0.01m domain since the diffusivity is so small ($D_U = 2.738 \times 10^{-13} \text{m}^2\text{s}^{-1}$ at 80°C [42]), so the timestep size is set at 1×10^6 seconds. Results from the FEM simulation of this model are shown in Figure 5.3. Each pair of bars represents the system at one timestep. The position, x, on the vertical axis has been nondimensionalised with respect to the domain length (0.01m). The colour of the left bar shows f and the right bar shows concentration that has been nondimensionalised with respect to C_{atm}. The nondimensional solubility limit $c_{TSS} = \frac{C_{TSS}}{C_{atm}} = 1 \times 10^{-3}$. By 2.1×10^7 seconds, the hydrogen concentration has surpassed this limit and a small amount of hydride is present. Later, at 8.1×10^7 seconds, $f = 1$ in a region local to the outer boundary, so this region is purely UH_3. In the final snapshot, taken at 1.41×10^8 seconds, some hydride has precipitated everywhere in the domain.

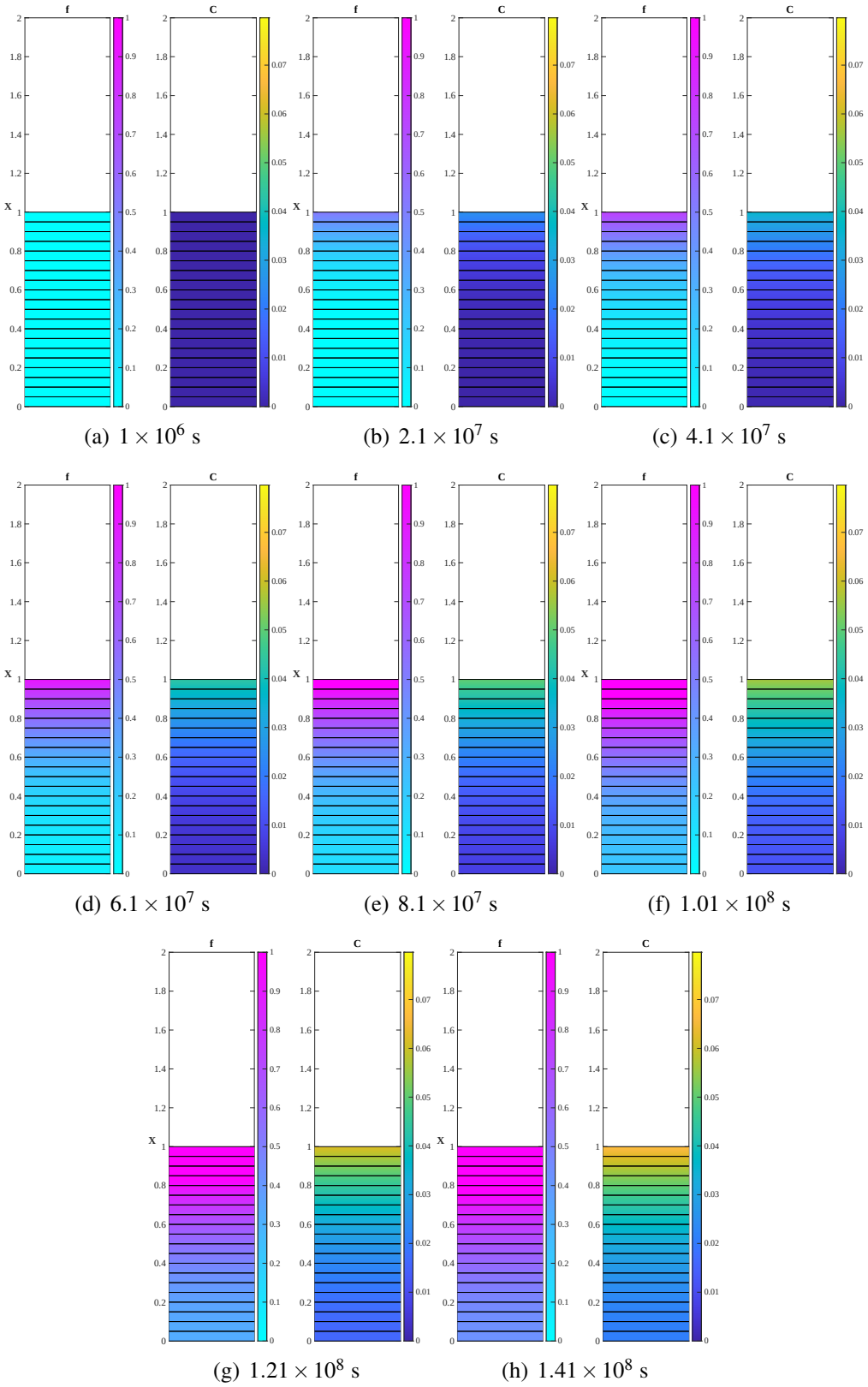

(a) 1×10^6 s (b) 2.1×10^7 s (c) 4.1×10^7 s

(d) 6.1×10^7 s (e) 8.1×10^7 s (f) 1.01×10^8 s

(g) 1.21×10^8 s (h) 1.41×10^8 s

Figure 5.3: Hydride volume fraction and nondimensionalised hydrogen concentration for a one-dimensional reaction-diffusion only model with instantaneous reaction kinetics (Model 1) from 1×10^6 seconds to 1.41×10^8 seconds.

5.1.2 Model 2: Multi-physics model

The second model discussed in this chapter includes equations for the conservation of energy and momentum and a constitutive law to form a multi-physics model for instantaneous reaction kinetics. These are the one-dimensional versions of equations (2.28), (2.31) and (2.44), respectively. This set of equations written here in full, alongside the governing equations for hydrogen concentration (5.3) and hydride volume fraction (5.1) as

$$\begin{aligned} \frac{\partial C}{\partial t} &= -\frac{\partial J}{\partial x} \\ \rho c_p \frac{\partial T}{\partial t} &= \kappa \frac{\partial^2 T}{\partial x^2} - J\frac{\partial \mu}{\partial x} \\ \frac{\partial \sigma}{\partial x} &= 0 \\ \sigma &= E\left(\frac{\partial u}{\partial x} - \varepsilon^{Th} - \varepsilon^{H}\right) \\ f &= f_e. \end{aligned} \tag{5.7}$$

In one dimension, the fourth order elasticity tensor C^{ijkl} reduces to the Young's modulus E. The equilibrium hydride volume fraction f_e is again defined by equation (2.45). The mass and energy conservation equations use the full temperature- and stress-dependent hydrogen flux J and chemical potential μ, given by

$$\begin{aligned} J &= -\frac{D_U C}{RT}\left(\frac{RT}{C}\frac{\partial C}{\partial x} + \frac{Q}{T}\frac{\partial T}{\partial x} - \frac{\bar{V}_H}{3}\frac{\partial \sigma}{\partial x}\right) \text{ and} \\ \mu &= \mu_0 + RT\ln(C) - \frac{\bar{V}_H}{3}\sigma\,. \end{aligned} \tag{5.8}$$

in one dimension. We note that the one-dimensional conservation of momentum equation means that the stress gradient is zero, so the stress gradient terms in J and $\frac{\partial \mu}{\partial x}$ are also zero.

The boundary conditions on concentration flux are unchanged from the last section and are given in equations (5.4) and (5.5). There is zero temperature flux across the inner boundary and a Newton cooling condition is used for the temperature on the outer boundary

$$\begin{aligned} \left.\frac{\partial T}{\partial x}\right|_{inner} &= 0 \\ \left.\frac{\partial T}{\partial x}\right|_{outer} &= \lambda_T\left(T^{atm} - T\right) \end{aligned} \tag{5.9}$$

where the proportionality constant is set to $\lambda_T = \frac{1}{a}$ where $a = 0.01$m is the domain length. One more boundary condition on the displacement u is required to complete the system. We impose that the inner boundary is stationary

$$u\big|_{inner} = 0. \tag{5.10}$$

Since only one condition has been applied on the u, and the set of governing differential equations contain second spatial derivatives of u, the natural (zero traction) boundary condition applies on the other boundaries.

Initial conditions on hydrogen concentration and hydride volume fraction temperature are unchanged from Model 1 and are given in equation (5.6). From the differential equations (5.7) and definitions of J and μ in equations (5.8), we see why a small initial concentration C is required. The concentration C appears in the denominator of some terms, so if we set the initial concentration to zero, we would have division by zero. The metal is initially is unstressed, undeformed and at the atmospheric temperature ($80°\text{C} = 353.15\text{K}$). These initial conditions can be written in full as

$$\begin{aligned} C(t=0) = C_{init} = C_{atm} \times 10^{-4} &= 1.047\text{mol m}^{-3} \\ T(t=0) &= 353.15\text{K} \\ u(t=0) &= 0 \\ \sigma(t=0) &= 0 \\ f(t=0) &= 0 \end{aligned} \tag{5.11}$$

The timestep size (1×10^6 s) and length of domain (0.01m) remain the same.

Results for the hydrogen concentration and hydride volume fraction from the multi-physics model are shown in Figure 5.4. Again, we see some hydride has been produced by 2.1×10^7 seconds, and by 1.41×10^8 seconds, the material is pure hydride up to a depth of 0.34cm from the boundary. Expansion can now be seen, and the outer boundary has been displaced upward by 0.41cm. Since there are natural zero traction conditions on the boundaries, and the material is allowed to expand freely, there is no mechanism by which non-zero stresses can occur. This is reflected in the results — stress is zero everywhere at all timesteps.

The equation for rate of change of temperature is the second of equations (5.7). The final term on the right hand side is prefixed by $D_U = 2.738 \times 10^{-13}\text{m}^2\text{s}^{-1}$, making it negligible compared to the other terms. This leaves us with the heat equation

and a Newton cooling boundary condition controlling the temperature. Since the initial temperature of the system is the same as the atmospheric temperature, we expect to observe no noticeable change throughout the simulation. Indeed the temperature differs negligibly from the initial condition throughout the simulation. Looking at the constitutive law, with $T = T_0$ and $\sigma = 0$, we see therefore that the only expansion experienced by the system is equal to that caused by the presence of diffusing hydrogen and reaction to form hydride.

5.1.2.1 Sensitivity analysis of Model 2

Sensitivity analysis was performed on the model discussed in section 5.1.2. In discussions with industrial collaborators, it was decided that the most important parameters to include in an initial sensitivity analysis were the diffusivity D_U, the atmospheric concentration of hydrogen C_{atm} and the proportionality constant λ_C which is used to calculate the concentration flux on the outer boundary.

In practice, the value of the atmospheric hydrogen concentration differs depending on the laboratory experiment or storage conditions of uranium. Thus for modelling purposes, it was not matched to a particular experiment but was set to $C_{atm} = 1000 \times C_{TSS}$. This led to choosing the sensitivity analysis parameter to be the ratio C_{atm}/C_{TSS}. Following the arguments in chapter 4, we have our three model inputs $\bar{x}_1 = D_U$, $\bar{x}_2 = C_{atm}/C_{TSS}$ and $\bar{x}_3 = \lambda_C$. We also must choose the output to our model, which we label as $\bar{u} = f(\bar{x}_1, \bar{x}_2, \bar{x}_3)$. Because stress and temperature did not change appreciably from their initial conditions, C, f and u were chosen to be the output parameters.

Since the chosen output parameters are time- and position-dependent variables, it remains to choose a single scalar value to represent each. To do this, we chose to monitor their value at an 'interesting' time and position during hydriding. This was chosen to be a point in the element adjacent to the outer boundary at the 200^{th} timestep (after 2×10^8 seconds).

Dakota software [81] was used to calculate first-order Sobol indices. The user must specify the distribution of the input parameters, the number of samples, and the correlation matrix between the input parameters. The inputs were chosen to be uniformly distributed around a mean value which has been found from experiment, or was nominally chosen. The mean value of the diffusivity distribution is given by $2.73 \times 10^{-13}\text{m}^2\text{s}^{-1}$ at 80°C [42]. The mean of the ratio C_{atm}/C_{TSS} was chosen to be 100 and of λ_C was chosen to be $\frac{1}{a}$, where $a = 0.01$m is the domain length. The bounds of the uniform distributions were chosen to be $\pm 10\%$ of this mean value in each case.

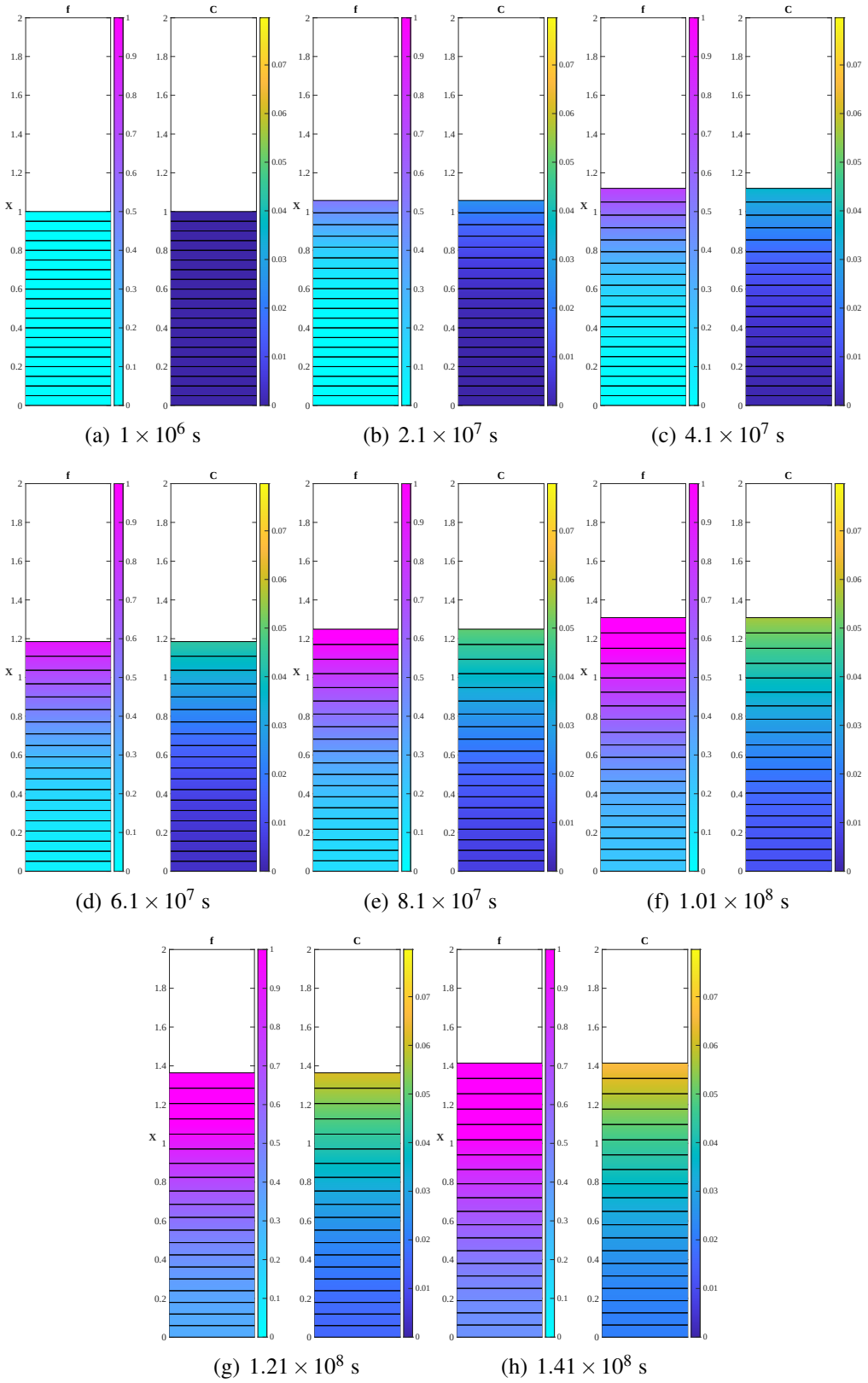

(a) 1×10^6 s (b) 2.1×10^7 s (c) 4.1×10^7 s

(d) 6.1×10^7 s (e) 8.1×10^7 s (f) 1.01×10^8 s

(g) 1.21×10^8 s (h) 1.41×10^8 s

Figure 5.4: Hydride volume fraction and nondimensionalised hydrogen concentration for a one-dimensional multi-physics model with instantaneous reaction kinetics (Model 2) from 1×10^6 seconds to 1.41×10^8 seconds.

The first-order Sobol indices with respect to these parameters were calculated by Monte Carlo and polynomial chaos expansion (PCE) methods and are shown in Tables 5.1 and 5.2 respectively. The Monte Carlo method used 10000 samples, and PCE was performed with order six quadrature.

Sobol indices are by definition in the range $[0,1]$, and an influential parameter is determined to have a Sobol index of the order 10^{-1}. Sobol indices of around 10^{-2} or smaller indicate less important parameters. We see that all three input parameters strongly influence the model outputs. It is noted that f and C exhibit very similar dependence on the input parameters in all cases. In this model, reaction rate is not dependent on stress or temperature. It depends solely on C, so it is no surprise that f and C should be highly correlated.

Section G.3 in Appendix G provides more detail and a graphical depiction of examples of 'influential' and 'non-influential' input parameters.

Table 5.1: First-order Sobol indices for Model 2 calculated by the Monte Carlo method with 10000 samples.

	Concentration (C)	Expansion (u)	UH_3 vol. frac. (f)
D_U	1.553×10^{-1}	3.266×10^{-1}	1.553×10^{-1}
$\frac{C_{atm}}{C_{TSS}}$	4.545×10^{-1}	3.570×10^{-1}	4.545×10^{-1}
λ_C	3.912×10^{-1}	3.131×10^{-1}	3.912×10^{-1}

Table 5.2: First-order Sobol indices for Model 2 calculated by the PCE method with quadrature order six.

	Concentration (C)	Expansion (u)	UH_3 vol. frac. (f)
D_U	1.588×10^{-1}	3.321×10^{-1}	1.588×10^{-1}
$\frac{C_{atm}}{C_{TSS}}$	4.469×10^{-1}	3.511×10^{-1}	4.469×10^{-1}
λ_C	3.920×10^{-1}	3.137×10^{-1}	3.920×10^{-1}

5.1.2.2 Validity of sensitivity analysis of Model 2

Initially, the number of samples for the Monte Carlo method was originally chosen to be 100 - a relatively small number for this type of approximation. When the number of samples was increased to 200, and then to 500, the Sobol indices were altered considerably, indicating that the sample size was insufficient. The indices were also

calculated by PCE for quadrature orders 3, 4 and 5. The supplementary tables of Sobol indices for all these cases are located in Appendix G.

We investigate how the value of the Sobol index depends on the number of Monte Carlo samples or PCE quadrature order. Figure 5.5 shows the indices with C as the output parameter and each of the three input parameters, for differing numbers of Monte Carlo samples and PCE quadrature order. We see that with increasing quadrature order, there is almost no change in the Sobol indices. Changing the number of Monte Carlo samples has a much more noticeable effect. Graphs for f and u are not included, since they show similar qualitative information.

A PCE of quadrature order $m = 3$ with $n = 3$ input parameters requires $m^n = 27$ calls to the model. For a Monte Carlo method with $n = 3$ input parameters and $N = 100$ to $N = 10000$ samples, the model is called $(2+n)N = 500$ to 50000 times. If it is accurate, the PCE method is clearly preferable in terms of computational cost. Whilst there are not enough data points to say definitively whether the Monte Carlo indices will converge close to the PCE indices, at least two of the plots (Figures 5.5(a) and 5.5(c)) show possible evidence of convergence. We also look for convergence with increasing quadrature order for the PCE method, but Figures 5.5(a) and 5.5(c) indicate that the Sobol indices have already converged on an accurate solution. With this evidence, we can say with confidence that the Sobol indices calculated by the PCE method with order three quadrature are accurate.

5.1.3 Discussion of Models 1 and 2

The results described thus far in this chapter are characterised by a slow diffusion process and hydriding over a long period of time. The final timestep shown for Models 1 and 2 is at 1.41×10^8 seconds after the start of the simulation. This is not the timescale usually observed for hydride production in experiments — Harker [7] reports that the first hydride sites nucleate almost immediately when there is no surface passivation layer (SPL). Brill et al. [83] also observe hydride nucleation on polished uranium metal almost immediately, with the surface almost covered with hydride after 80 seconds.

Also, we observe a shallow gradient of hydride formed through the domain — the profile of hydride volume fraction for Model 2 is shown in Figure 5.6 at three different timesteps. Note that the profiles end at differing values of x because the domain is undergoing expansion over time. After 2.1×10^7 seconds, there is some hydride present ($f > 0$) in more than half of the domain length. By the time there is

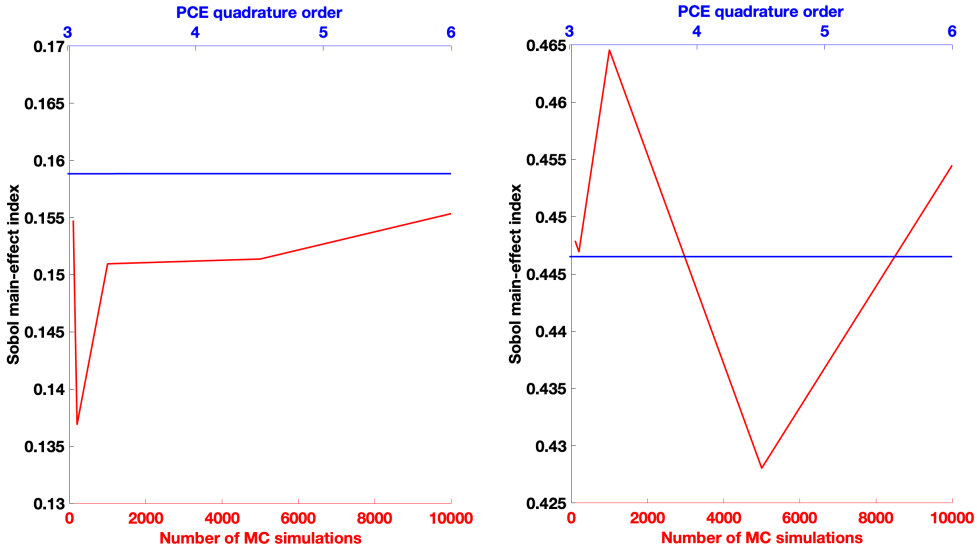

(a) C - D indices

(b) C - C_{atm}/C_{TSS} indices

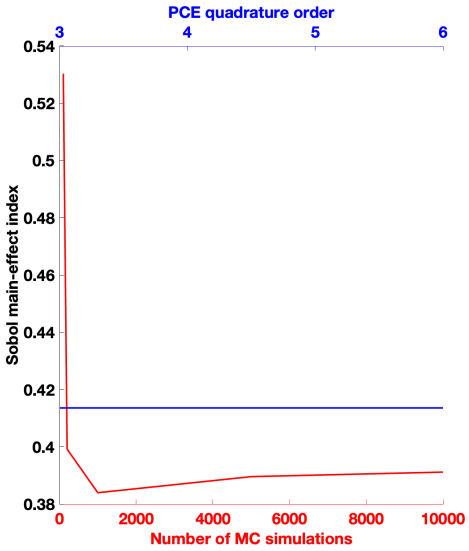

(c) C - λ_C indices

Figure 5.5: Graphs to show dependence of hydrogen concentration Sobol indices for Model 2 on PCE quadrature order and number of Monte Carlo Samples.

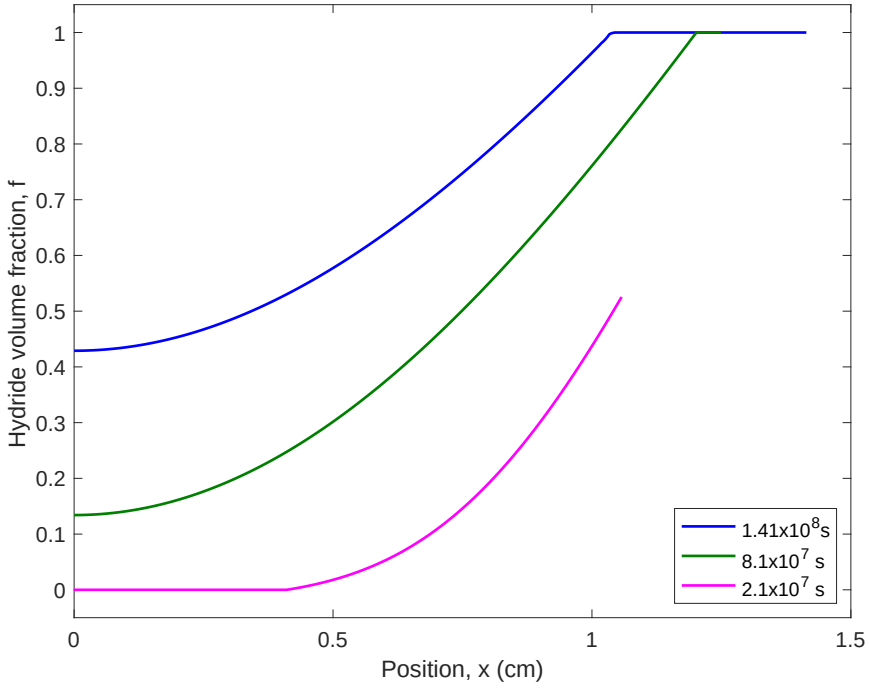

Figure 5.6: Hydride volume fraction profiles at three timesteps for Model 2.

a region of pure hydride close to the outer boundary (at 8.1×10^7 seconds), there is some hydride present everywhere in the domain. This gradual hydride volume fraction gradient is not consistent with the idea of modelling hydride blisters — whilst in a continuum model we don't define a definitive boundary between metal and hydride, we would expect to see a steeper transition between the two.

These effects could be explained by the reaction not proceeding fast enough, leaving the hydrogen with time to permeate deep into the metal. However, in these models, the reaction proceeds instantaneously, so there is no mechanism to reduce the reaction timescale.

If we look at the reaction equation in the range where hydriding proceeds ($C_{TSS} < C < C_{UB}$), then

$$f = f_e = \frac{C_{TOT} - C_{TSS}}{C_{UB} - C_{TSS}}. \tag{5.12}$$

The volume fraction of hydride depends on the solubility limit, C_{TSS}. Since $C_{UB} >> C_{TSS}$, the most significant effect on f_e relates to the difference $C_{TOT} - C_{TSS}$. The maximum value C_{TOT} can reach depends on the atmospheric concentration C_{atm}. This is all to say that the amount of hydride formed depends on the atmospheric concentration and the solubility limit. This is reflected in the sensitivity analysis — the first-order

Sobol indices indicate that their ratio C_{atm}/C_{TSS} strongly influences f.

As well as the ratio C_{atm}/C_{TSS}, the sensitivity analysis on Model 2 highlights the significant influence of the parameter λ_C. Since λ_C and C_{atm} are both parameters involved in the calculation of the outer boundary condition on C, we can conclude that this condition is highly influential on the results of the model and that choosing a physically accurate boundary condition is therefore highly important when looking for a physically accurate solution.

It would be possible to set an accurate value of C_{atm} to compare with particular experiments, but λ_C is not a parameter which has been measured experimentally in the literature. As a consequence of these findings and discussions with my industrial supervisor, a Sieverts' law condition will be imposed on the outer boundary to replace the flux condition. Sieverts' law has been described in section 2.9 and removes the need for a modelling parameter at the boundary like λ_C.

5.1.4 Model 3: Multi-physics model with Sieverts' Law boundary condition

A Sieverts' Law boundary condition (details of which can be seen in section 2.9) is imposed on the outer boundary,

$$C_S = \frac{K(T)\sqrt{P_{atm}}}{\bar{V}_U}. \tag{5.13}$$

such that we have the Dirichlet condition $C|_{outer} = C_S$. We must specify an ambient (partial) hydrogen pressure, P_{atm} and ambient temperature which is used to define $K(T)$. We chose to take experimental conditions from work done by A. Chohollo in her industrial placement project with AWE [66]. The hydrogen was at $80°C$ and a pressure of $10mbar$. Using the equations given in section 2.9, this gives the Sieverts boundary condition $C|_{outer} = C_S = K(T)\sqrt{P_{atm}} = 0.534molm^{-3}$.

The combination of an initial condition $C(t=0) = C_{init}$ and a Dirichlet condition on the outer boundary presents a problem — hydrogen concentration is being set to two different values on the outer boundary at $t = 0$. To solve this, the Sieverts' condition is 'switched on' using an exponential in time;

$$C|_{outer} = C_S - (C_S - C_{init})e^{-vt} \tag{5.14}$$

where v is chosen such that $e^{-vt} < 0.1$ after the first five seconds.

Previously, the value $C_{TSS} = 10.47 molm^{-3}$ has been used as a best guess for the terminal solid solubility. This value refers to hydrogen solubility in zirconium as measured by Une and Ishimoto [39] (see Appendix F, section F.1). An unpublished Arrhenius relation received through discussions with my industrial supervisor for the solubility limit of hydrogen in uranium is

$$C_{TSS} = 0.2446 e^{\frac{-52000}{RT}} \text{gcm}^{-3}. \tag{5.15}$$

which gives 4.981×10^{-3}mol m^{-}3 at 80°C. Note that this smaller value of C_{TSS} will lead to hydride formation at a lower hydrogen concentration. Using a physically accurate value of C_{TSS} is important since the ratio C_{atm}/C_{TSS} was determined to be an influential parameter in the sensitivity analysis of the previous model.

Finally, the size of the domain was also reduced in order to be on the same order of magnitude as a small uranium blister, from 0.01m to 1μm.

Apart from these changes to the solubility limit, domain length and concentration condition on the outer boundary, the model remains the same as Model 2. Thus the governing differential equations are equations (5.7), with boundary and initial conditions given by equations (5.4), (5.9), (5.10), (5.11) and as before there is no traction on the outer boundary.

Shorter timesteps are required to see change on the shorter length scale, so each timestep is now 1×10^{-2} seconds. Results for the hydrogen concentration (which is now nondimensionalised by C_S rather than C_{atm}) and hydride volume fraction are shown in Figure 5.7. Position is nondimensionalised by the new domain length 1μm. Similarly to the previous models, we observe hydrogen diffusion and hydride formation over time. After running the system for a long time, a steady state is reached where hydrogen concentration everywhere in the metal is equal to its maximum value, C_S. Figure 5.7(i) shows the steady state after 25 seconds. Hydride volume fraction everywhere is 1.1×10^{-3} and the outer boundary is displaced 6.2×10^{-10}m upwards from its original position. This displacement is too small to be appreciable on the figures. Once again, the temperature is not shown since it differs negligibly from the initial condition throughout the simulation.

5.1.4.1 Sensitivity analysis of Model 3

A sensitivity analysis was performed on Model 3. In section 5.1.2.2 Monte Carlo and PCE methods were compared. It was shown that the PCE method showed evidence

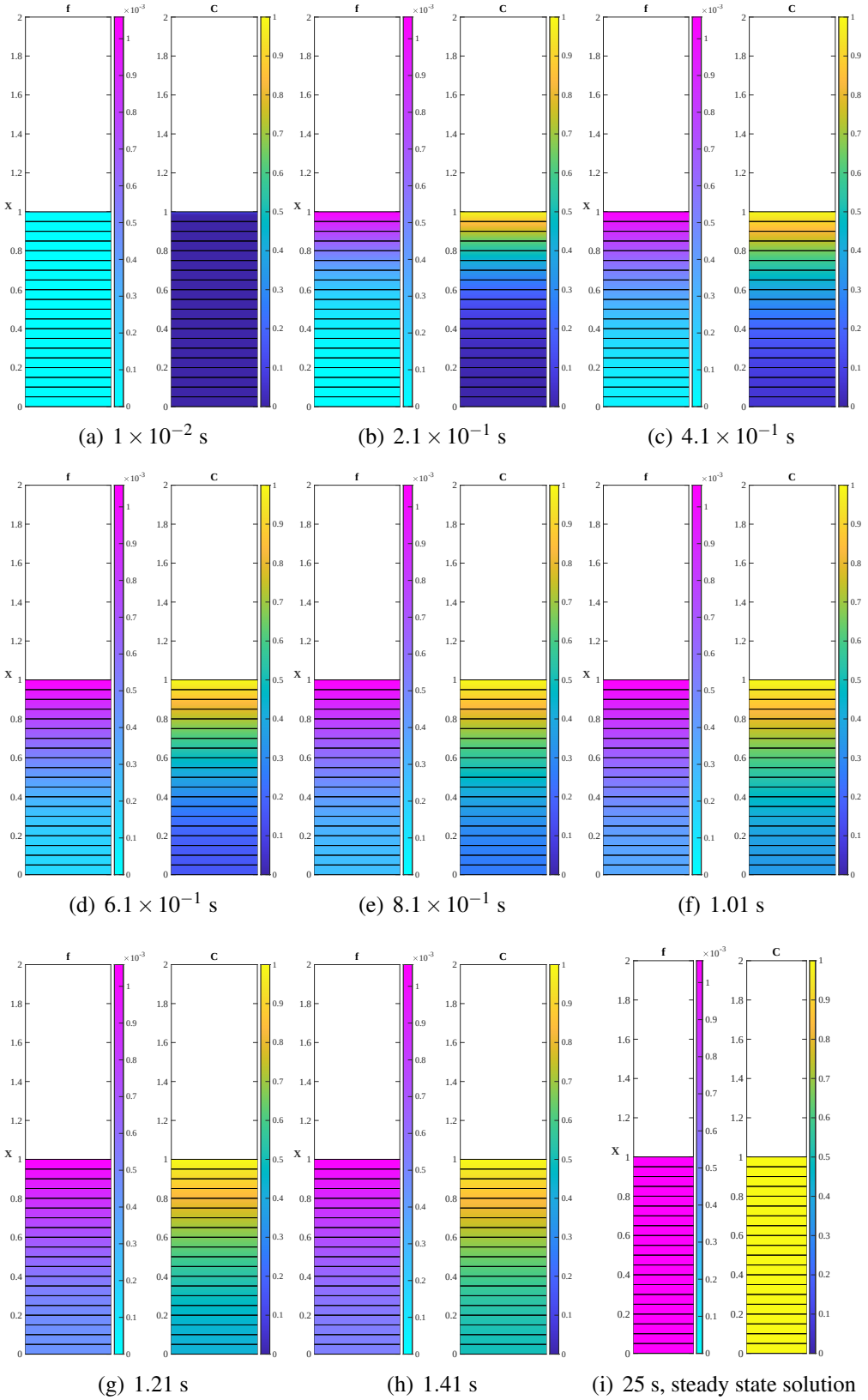

(a) 1×10^{-2} s (b) 2.1×10^{-1} s (c) 4.1×10^{-1} s

(d) 6.1×10^{-1} s (e) 8.1×10^{-1} s (f) 1.01 s

(g) 1.21 s (h) 1.41 s (i) 25 s, steady state solution

Figure 5.7: Hydride volume fraction and nondimensionalised hydrogen concentration for a one-dimensional multi-physics model with instantaneous reaction kinetics and Sieverts' law boundary condition (Model 3) from 1×10^{-2} seconds to 25 seconds.

of converging Sobol indices after relatively few model evaluations, while no such convergence could be seen from the Monte Carlo method. The Monte Carlo method also required many more evaluations of the model. For these reasons, this time only the PCE method was employed.

Table 5.3 contains the first-order Sobol indices for the dependence of u and f on six input parameters: D_U, C_{TSS}, P_{atm}, $\bar{V}_U$, $\bar{V}_H$, $\bar{V}_{Hr}$ and C_{UB}. The mean values of each input parameter are given in the table of physical parameters (Appendix F). They are again uniformly distributed with bounds of $\pm 10\%$ of the mean. The calculated Sobol indices are given in Table 5.3, and are plotted on the graphs in Figure 5.8.

Table 5.3: First-order Sobol indices for Model 3 calculated by the PCE method with quadrature order 3.

	Expansion (u)	UH_3 vol. frac. (f)
D_U	3.872×10^{-2}	4.105×10^{-5}
C_{TSS}	2.685×10^{-5}	6.899×10^{-5}
P_{atm}	4.600×10^{-2}	1.990×10^{-1}
$\bar{V}_U$	7.323×10^{-1}	8.003×10^{-1}
$\bar{V}_H$	7.179×10^{-9}	1.181×10^{-30}
$\bar{V}_{Hr}$	1.790×10^{-1}	7.583×10^{-32}
C_{UB}	1.049×10^{-29}	9.694×10^{-29}

Appendix G contains supplementary data regarding testing whether the bounds of the uniform distribution affect the conclusions of the sensitivity analysis. Sobol indices are shown for uniform distributions where the bounds are $\pm 5\%$ and $\pm 1\%$ of the mean. The same parameters are determined to dominate the model behaviour in each case.

The input parameters P_{atm} and $\bar{V}_U$ are shown to be highly influential parameters for calculating both f and u. These quantities both affect the size of the Sieverts' condition on C, which indicates once again that this boundary condition is instrumental in determining the amount of hydride precipitated. We also have that the deformation is strongly influenced by the boundary condition.

Recall that C_{UB} is defined in section 2.8.1 as the upper limit of C for which some uranium metal has not reacted to form hydride. A value for C_{UB} has not been found in the literature. In modelling, it has been set to a value slightly larger than the concentration of hydrogen in hydride, C_b, since by definition, $C_{UB} > C_b$. A value for the partial molar volume of hydrogen in uranium, $\bar{V}_H$ was also not found in the literature, so the value of the partial molar volume of hydrogen in zirconium was used in its place. Appendix F gives further details. The Sobol index data indicates that the values of C_{UB}

and $\bar{V}_H$ do not strongly affect f or u. As stated in the introduction to chapter 4, one application of sensitivity analysis is to indicate whether it is important to ensure that parameter has a precise and accurate measurement. This analysis shows that it is not important to have accurate data for C_{UB} and $\bar{V}_H$. However, this also implies that to obtain accurate data on deformation, $\bar{V}_{Hr}$, the partial molar volume of hydride in uranium metal, does need to be measured accurately.

The terminal solid solubility limit C_{TSS} is not an influential modelling parameter for either f or u. We reason that this is because its value is small when compared with the boundary condition on C, so the solubility limit is reached and hydride precipitates almost immediately when the simulation starts.

Finally, we note that the diffusivity D_U is not a particularly influential parameter for f, but it is more so for u. This indicates that u depends on D_U through a mechanism other than expansion due to hydride. By examining the governing equations, we see this must be through expansion due to solute hydrogen present in the metal.

5.1.4.2 Discussion of Model 3

The changes made when building Model 3 aimed to bring the model closer to a physically accurate model of hydriding. While a thorough quantitative comparison between A. Chohollo's experimental work [66] and this model has not been completed, we now observe hydride precipitation on the timescale of seconds, as seen experimentally, rather than 10^6 seconds.

However, we note there are still discrepancies. Firstly, we look at the long-term behaviour of the solution. A steady state is reached where the concentration and volume fraction are uniform on the domain, as is shown in Figure 5.7(i). Concentration is uniformly equal to C_{atm} and f is uniformly equal to 1.1×10^{-3}. Physically, we would expect the hydriding reaction to continue since $C > C_{TSS}$ and there is still uranium present, but the reaction does not proceed any further because f is equal to its equilibrium value f_e. This illustrates a significant problem with using a lever rule to measure the extent of reaction as in the model developed by Jernkvist and Massih [61].

We have assumed that the reaction is instantaneous in comparison with the extremely slow timescale of hydrogen diffusion through uranium metal. This assumption was originally made when looking at a 0.01m domain in Models 1 and 2. A timescale for diffusion across the length of this domain is $\gamma = \frac{a^2}{D} = \frac{(0.01m)^2}{2.738\times10^{-13}m^2s^{-1}} = 3.6 \times 10^8$s. In Model 3, the domain is 1μm long. The shortened domain gives way to a shortened timescale for diffusion to act across the domain: $\gamma = \frac{a^2}{D} = \frac{(1\mu m)^2}{2.738\times10^{-13}m^2s^{-1}} = 3.65$s.

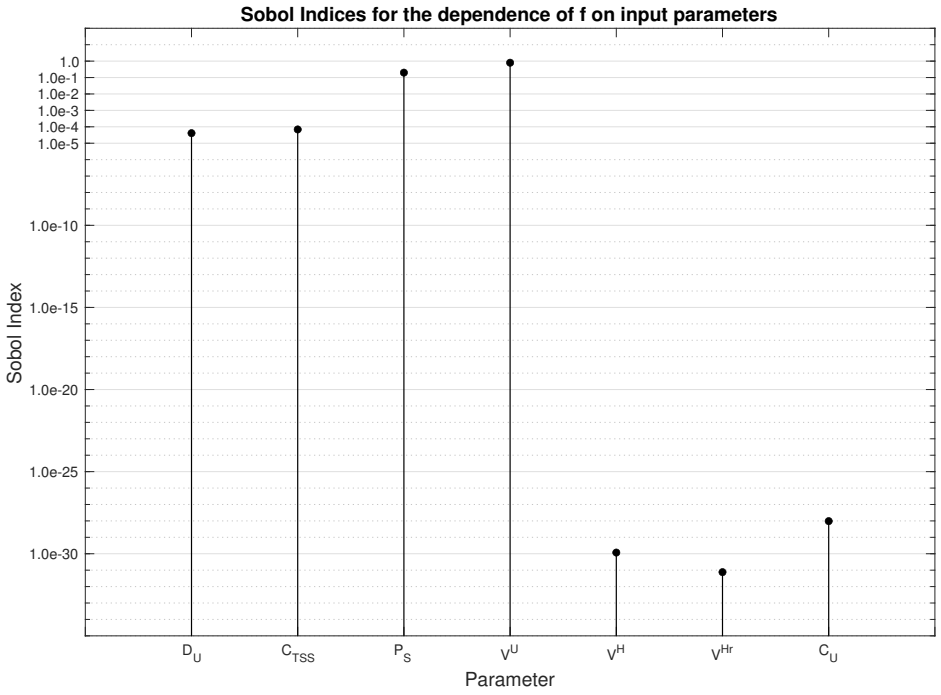

(a) Sobol indices with output parameter f

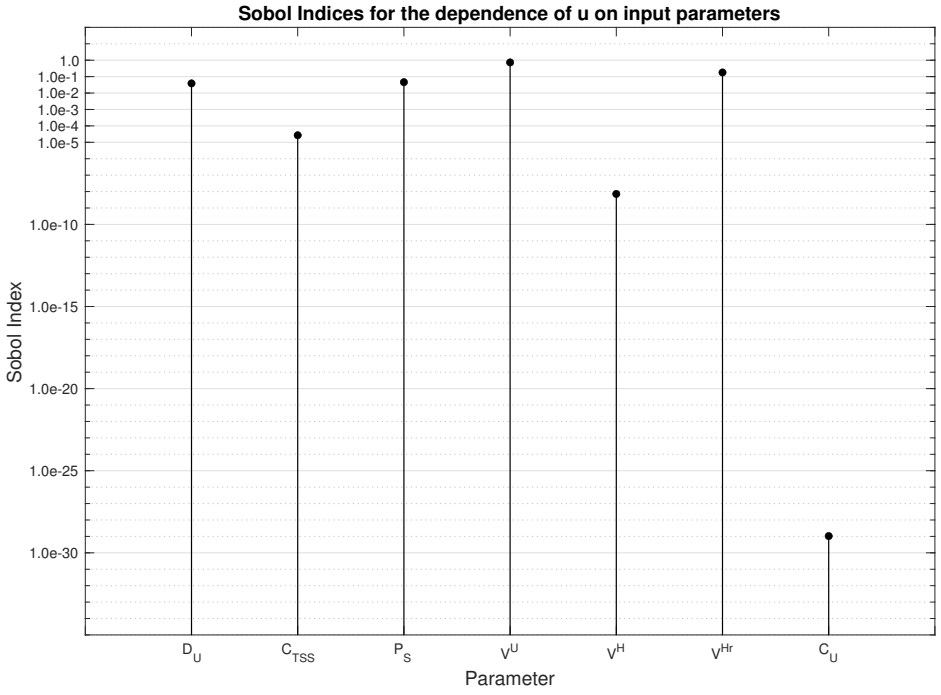

(b) Sobol indices with output parameter u

Figure 5.8: Graphs to show the first-order Sobol indices calculated by PCE with quadrature order 3 for sensitivity analysis of Model 3.

In this case, it may be more appropriate to look at the reaction occurring on a finite timescale.

When the reaction is assumed to be instantaneous, another problem is encountered – the $\frac{\partial f}{\partial t}$ terms are absent from the governing equations. This means that there is no sink term whereby hydride precipitation causes the depletion of diffusing hydrogen, and in the multi-physics models, there is no term to include changes in temperature due to exothermic reaction. This can be seen by comparison between the governing equations (5.7) used in this chapter, with the original equations (2.15) and (2.28) developed in chapter 2 for hydrogen diffusion and energy conservation respectively.

Even with the attempts made in Model 3 to make the boundary conditions more physically realistic, we still see the shallow gradient of f across the domain noted in Models 1 and 2. This could be a consequence of the absent hydrogen sink term. If hydrogen is depleted before it has chance to diffuse deeper into the metal, we may see hydride growth more localised near the outer boundary.

Because of these observations, some final changes are made to the model. The lever rule equation for reaction extent is replaced by a time-dependent equation based on the law of mass action and as a consequence, the $\frac{\partial f}{\partial t}$ terms are present in the differential equations.

5.2 Model 4: Time-dependent reaction kinetics model

Now, we describe and present results for a model with time-dependent reaction kinetics and investigate the effect of varying the reaction rate constant. The equation to model the extent of reaction is the rate law, equation (2.49). The differential equations describing conservation of mass, conservation of energy and the constitutive law are given by equations (2.53) and equation (2.55). The conservation of momentum equation is unchanged from the instantaneous reaction kinetics models. These governing

equations on a one-dimensional domain are listed together here for reference

$$\begin{aligned}
\frac{\partial C}{\partial t} &= -\frac{\partial J}{\partial x} + 3\frac{\partial U}{\partial t} \\
\frac{\partial U}{\partial t} &= \begin{cases} 0 & \text{if } C \leq C_{TSS} \\ -k_{Hr} C^3 U & \text{if } C > C_{TSS} \end{cases} \\
\rho c_p \frac{dT}{dt} - \Delta\bar{H}\frac{\partial U}{\partial t} &= \kappa\frac{\partial^2 T}{\partial x^2} - J\frac{\partial \mu}{\partial x} \\
\frac{\partial \sigma}{\partial x} &= 0 \\
\sigma &= E\left(\frac{\partial u}{\partial x} - \alpha(T - T_0) - \frac{1}{3}\left(C\bar{V}_H + \frac{(\bar{V}_{Hr})^2}{\bar{V}_U}\Delta U\right)\right)
\end{aligned} \tag{5.16}$$

where one-dimensional J and μ are defined by equations (5.8). The initial conditions remain the same as given in equations (5.11) for C, T, u and σ. The temperature at the inner and outer boundaries is again governed by zero flux and Newton cooling conditions respectively (given in equations (5.9)). Again, there is no traction on the outer boundary and the inner boundary is stationary and has zero hydrogen flux across it. To complete the system, we require another boundary condition on C and an initial condition on U. The initial concentration of U is given by

$$U(t = 0) = \frac{1}{\bar{V}_U} \tag{5.17}$$

since $\bar{V}_U$ is the volume occupied by one mole of uranium atoms, so its inverse is the molar uranium concentration. We refer to the nondimensional uranium concentration U^* regularly in this section, defined by $U^* = \bar{V}_U U$, so

$$U^*(t = 0) = 1. \tag{5.18}$$

To be clear, when $U^* = 1$, we have pure uranium metal. When $U^* = 0$, there is no pure uranium present, so we have pure UH_3.

The boundary condition on C is a Dirichlet condition with exponential 'switch-on' speed as in equation (5.14). In preliminary solves using the Sieverts' boundary condition, negligible change in U was observed over the simulation time. The Sieverts' concentration, C_S is the maximum value of C that can be attained anywhere in the domain. Since C_S ($= 0.534\text{molm}^{-3}$) is very small in comparison with the initial concentration of uranium $\frac{1}{\bar{V}_U}$ ($= 80000\text{molm}^{-3}$) the depletion of uranium will be extremely slow. We

revisit the description of Sieverts' law for further insight. Sieverts' law, as described in section 2.9, is an equation giving the number of moles of hydrogen dissolved per mole of uranium. This was converted to the number of moles of hydrogen dissolved per unit volume by dividing by $\bar{V}_U$. This is not a particularly convincing argument since the conversion does not take into account the surface area of the boundary. However, it is also not clear how one would measure the number of moles of uranium on a surface, nor how you would convert to obtain a concentration in mol m^{-3}. When confronted with this, and the comparison between hydrogen and uranium concentrations, it is not convincing that it is sensible to use this value of C_S directly as the boundary condition on C.

For now, we replace C_S by some other value $C_f = \dfrac{5}{\bar{V}_U}$. We choose this value since it sets C_f at five times the molar uranium concentration, in order to guarantee some hydride precipitation will be seen. The outer boundary condition on C is thus

$$C|_{outer} = C_f - (C_f - C_{init})e^{-vt} \tag{5.19}$$

with all quantities defined as before. We proceed with the investigation, and note that we cannot claim that the simulated results can be directly compared to any given experimental conditions.

To investigate different values of the rate constant k_{Hr}, we define the Damköhler number Da as the ratio between the rate of reaction and rate of diffusion

$$Da = \frac{k_{Hr}}{D_U}. \tag{5.20}$$

Since the reaction is order one and order three with respect to uranium and hydrogen concentrations respectively, k_{Hr} is in units of $\mathrm{mol}^{-3}\mathrm{m}^9\mathrm{s}^{-1}$. The diffusivity has units $\mathrm{m}^2\mathrm{s}^{-1}$, giving the units of Da as $\mathrm{mol}^{-3}\mathrm{m}^6$. Units of Da are suppressed for the remainder of the report. The domain length for Model 4 is 1×10^{-5}m.

The simulation on the above model has been run with values of Da ranging from 1×10^8 to 1×10^{12}. Results for nondimensionalised hydrogen and uranium concentrations with $Da = 1 \times 10^{12}$ from 0 seconds to 35 seconds are shown in Figure 5.9. Once again, temperature is not shown since it does not vary appreciably from the initial condition. To more easily visualise time-dependence of the results, we combine all timesteps onto a single plot, called a space-time plot. On these plots, x is plotted against time with the results for all timesteps shown together. These graphs are shown in Figure 5.10 for $Da = 1 \times 10^8$, $Da = 1 \times 10^9$ and $Da = 1 \times 10^{10}$, and 5.11 for

$Da = 1 \times 10^{11}$ and $Da = 1 \times 10^{12}$.

With the space-time plots, it is possible to clearly see time-dependence of the dependent variables. For each Da value, we see a gradual gradient of the hydrogen concentration and a steep gradient of uranium concentration developing across the domain over time. The region where the steep gradient in U^* is seen is labelled the transition region between uranium and hydride; above the transition region, we have pure UH_3 since $U^* = 0$, and below we have uranium metal with $U^* = 1$. As the simulations progress in time, the height of the domains increases showing expansion.

To more clearly see the transition region, Figure 5.12 shows the profile of U^* for each Da value after 35 seconds. The U^* gradient in the transition region is steeper for larger values of Da, but some hydride precipitates deeper in the domain (at smaller x values) for smaller Da. It is noted that the U^* profiles terminate at different x values because the final domain length differs.

5.2.1 Discussion of Model 4

From the space-time plots and U^* profiles, we know that steepness of the transition region and the depth of hydride precipitation depend on the Damköhler number, and as a result on the reaction rate k_{Hr}.

This project aims to model the formation of blisters — localised regions of pure hydride growing on the surface of uranium. In the continuum models which are the subject of this thesis, there is no interface between metal and hydride, but we are looking to simulate separate metal and hydride regions. The results of Model 4 demonstrate that in order to see pseudo-distinct regions of hydride and metal, we expect that the Da should take a value near the top end of the range 1×10^8 to 1×10^{12}.

By looking at the depth of hydride penetration over time, we see that the precipitation starts fast and slows down over the course of the simulation. This agrees qualitatively with hydride growth observed in experiment [16]. Expansion proceeds in a similar fashion, with the material growing quickly at the start of the simulation and slowing down. These effects exist for all values of Da but become more prominent with increasing Da.

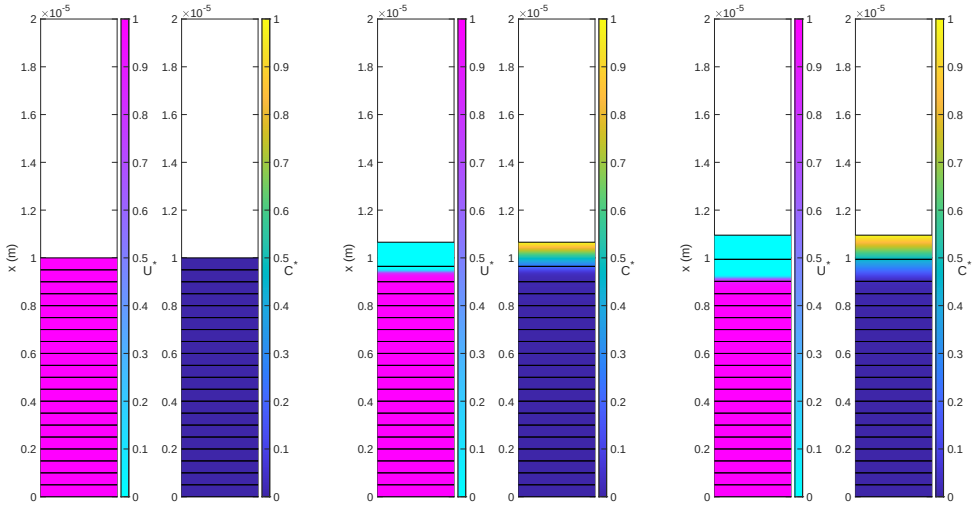

(a) 0 s (b) 5 s (c) 10 s

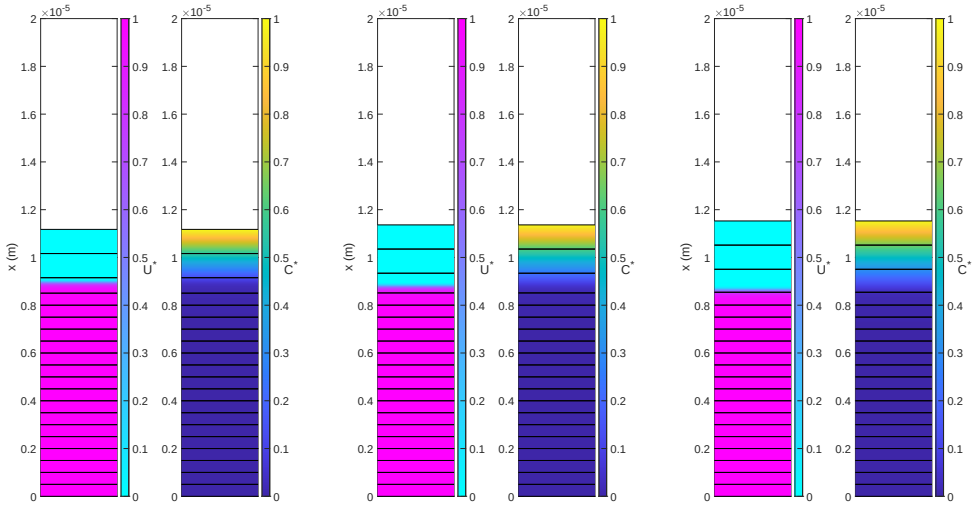

(d) 15 s (e) 20 s (f) 25 s

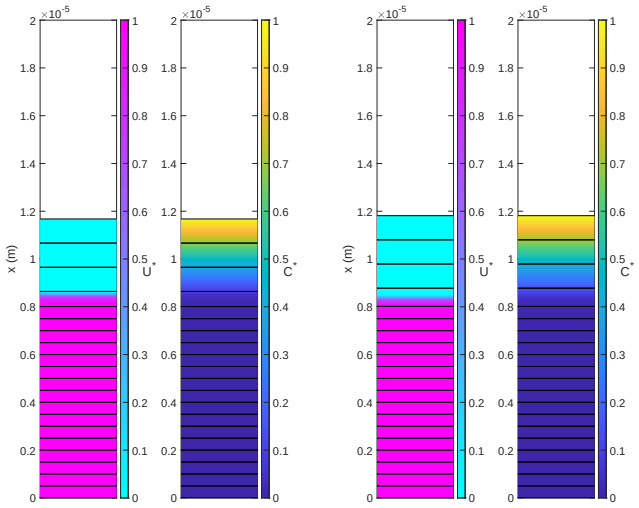

(g) 30 s (h) 35 s

Figure 5.9: Nondimensionalised uranium and hydrogen concentrations for a one-dimensional multi-physics model with time-dependent reaction kinetics (Model 4) and $Da = 1 \times 10^{12}$ from 0 seconds to 35 seconds.

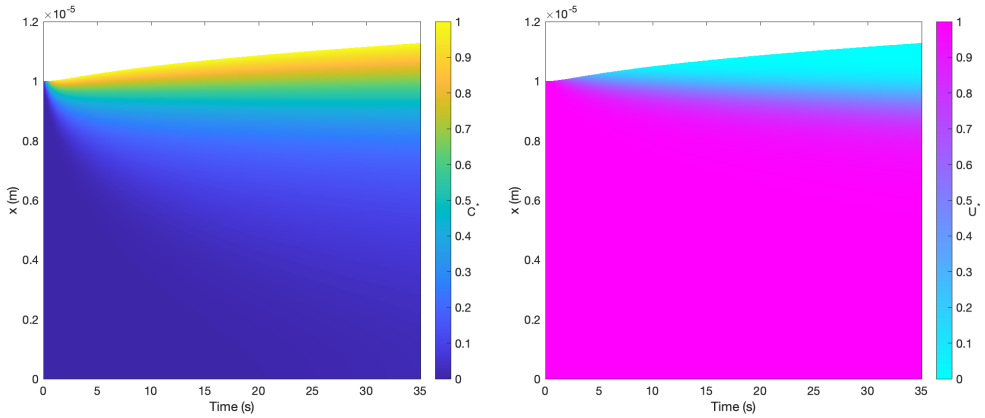

(a) C^*, $Da = 1 \times 10^8$ (b) U^*, $Da = 1 \times 10^8$

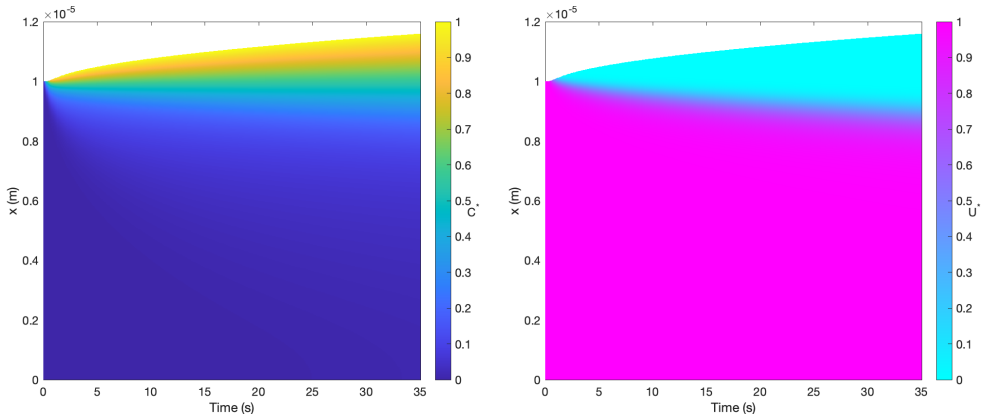

(c) C^*, $Da = 1 \times 10^9$ (d) U^*, $Da = 1 \times 10^9$

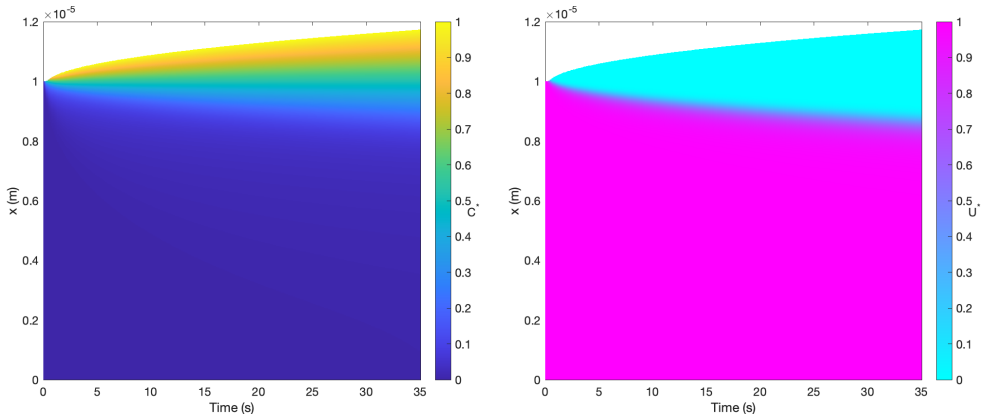

(e) C^*, $Da = 1 \times 10^{10}$ (f) U^*, $Da = 1 \times 10^{10}$

Figure 5.10: Space-time plots of nondimensionalised hydrogen C^* and uranium U^* concentrations for a one-dimensional multi-physics model with time-dependent reaction kinetics (Model 4) from 0 seconds to 35 seconds with Da values 1×10^8, 1×10^9 and 1×10^{10}.

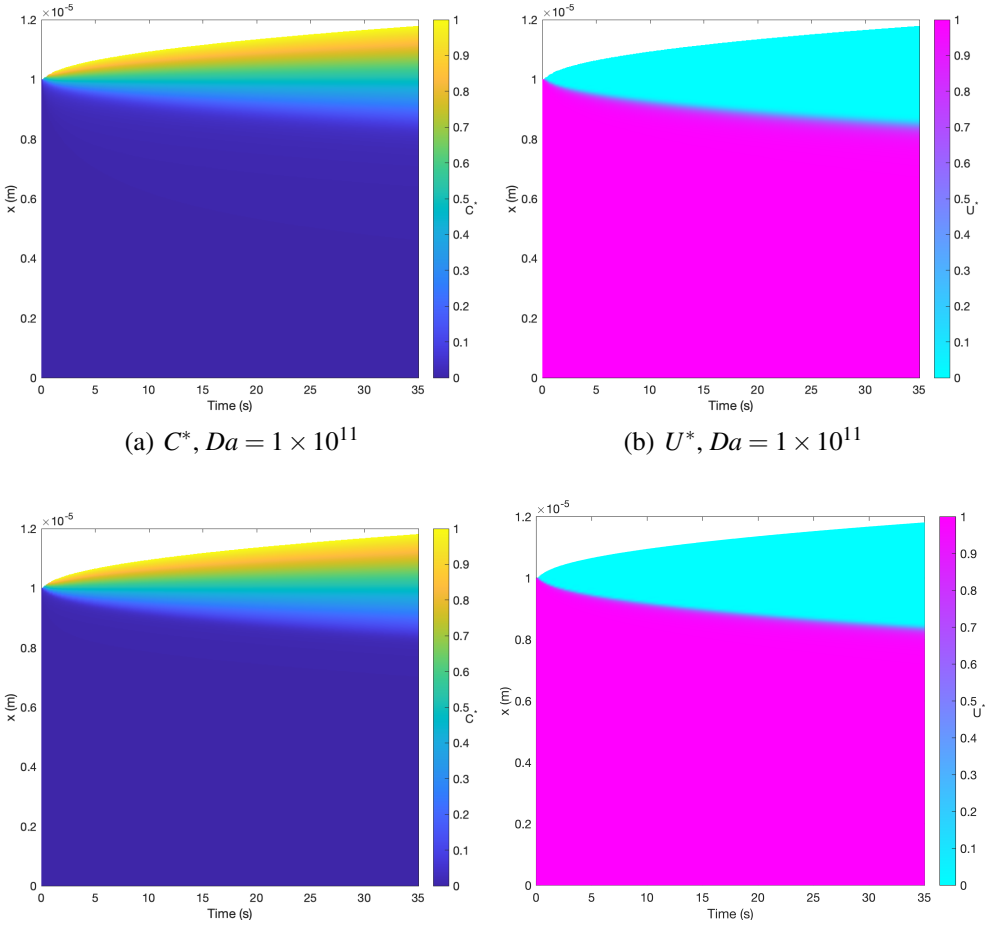

(a) C^*, $Da = 1 \times 10^{11}$

(b) U^*, $Da = 1 \times 10^{11}$

(c) C^*, $Da = 1 \times 10^{12}$

(d) U^*, $Da = 1 \times 10^{12}$

Figure 5.11: Space-time plots of nondimensionalised hydrogen C^* and uranium U^* concentrations for a one-dimensional multi-physics model with time-dependent reaction kinetics (Model 4) from 0 seconds to 35 seconds with Da values 1×10^{11} and 1×10^{12}.

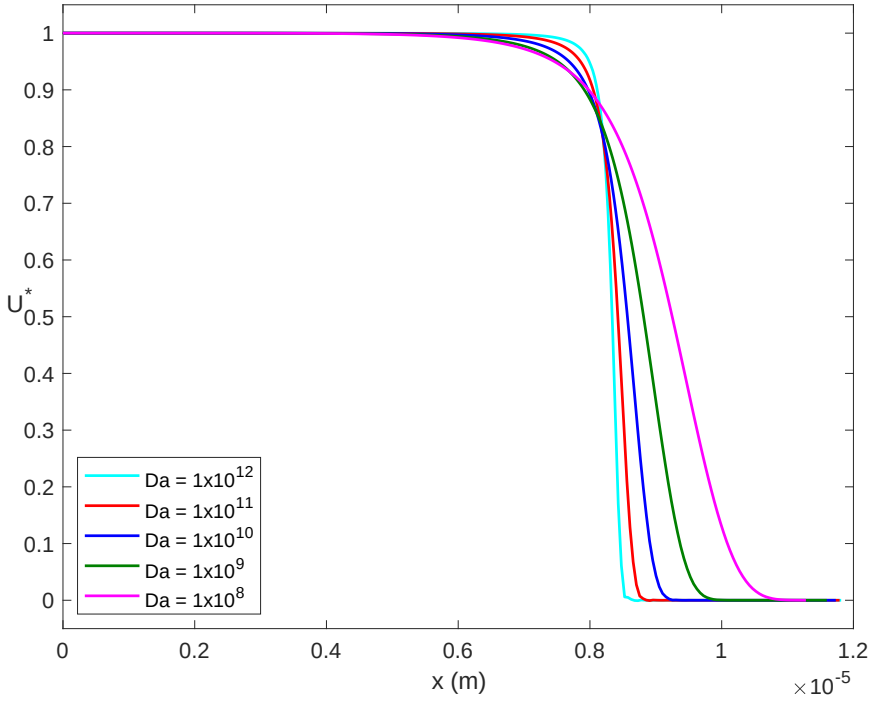

Figure 5.12: Profiles of nondimensionalised uranium concentration U^* for a one-dimensional multi-physics model with time-dependent reaction kinetics (Model 4) after 35 seconds with five different Da values.

5.3 Discussion and conclusions

In this chapter, four different models have been presented and solved using FEM. Results for the hydrogen concentration and extent of reaction have been presented and discussed. Sensitivity analysis has been performed to gain information on important parameters and aspects of the models. The models are presented in order of increasing fidelity to the full multi-physics model derived in Chapter 2, and findings from previous models are used to inform subsequent modelling procedures. The small discussion sections have already described important results that apply to individual models. Here, we discuss important results and aspects which apply to all the models in this chapter. Some will be used to inform modelling in two dimensions in Chapter 6.

One of the most important results is that the boundary condition describing hydrogen influx is highly influential on the results of the simulations. Therefore it will be of utmost importance to have a physically accurate boundary condition in order to see physically accurate solutions. For this model, we require that the boundary condition

will impose a Dirichlet condition on C, or a Neumann/ flux condition on $\frac{\partial C}{\partial x}$. Until this point, such a boundary condition has not been found in the literature.

From sensitivity analyses, we also found that while the diffusivity D_U has a greater effect on expansion, u, than on the concentration of hydrogen or extent of hydriding, it was consistently found to be less influential than the boundary condition parameters for both the flux and Sieverts' boundary conditions.

In the model derivation, we assumed that the system experiences only small deformations, as described in section 2.1. The one-dimensional final position of each material point in the plots for Models 2, 3 and 4 is calculated using $X = x + u$ in post-processing so the displacement can be visualised. We now examine whether this small deformation approximation is valid for the models presented here.

Results for Model 3 show a maximum displacement of 6.2×10^{-10}m, which is small when compared with a domain length of 1×10^{-6}m. However, in Model 2, the maximum displacement is 4.1×10^{-3}m. This is almost half the original domain length of 0.01m. Similarly, in Model 4, the maximum displacement is almost a fifth of the original domain length. While there is no limit placed on what is meant when we assume 'sufficiently small deformations', the assumption of clearly breaks down in these cases. In future work on multi-physics continuum models of uranium hydriding, if large displacements are seen, the small deformation approximation should be rescinded in favour of equations derived from large/finite deformation theory.

The large deformations seen in Model 4 are a consequence of the extremely high concentration of hydrogen imposed on the boundary. We set the boundary condition with equation (5.19), and $C_f = \dfrac{5}{\bar{V}_U}$. This means that the final concentration of hydrogen in the metal at the outer boundary is five times higher than the concentration of uranium, or $C_f = 4 \times 10^5$mol m^{-3}. Using the ideal gas law on the hydrogen used in A. Chohollo's experimental set-up (pressurised to 10mbar at 353.15K) gives that the concentration of hydrogen in the atmosphere is 0.34mol m^{-3}. As explained previously, the equation to calculate the boundary condition on C in the metal given the concentration of hydrogen in the atmosphere is still unknown, though it seems implausible that there is an absorption mechanism by which the concentration will be this much higher than the atmospheric concentration. Without a well-defined equation to model absorption, it is not possible to say from a modelling perspective whether the small deformation approximation will hold when using parameters with a high fidelity to experimentally measured parameters.

From an experimental perspective, however, we can say that we would expect hydrides on the micron scale [9, 18] and we have that, if unrestricted by stress, the volume ratio of hydride to uranium metal is $\frac{\bar{V}_{Hr}}{\bar{V}_U} = 1.75$. The size of deformation seen in experiment depends on how much the stress restricts this deformation.

Chapter 6

Two-dimensional modelling results

In this chapter, hydriding is modelled in two-dimensions. Figure 2.1 showed a cross-section of the uranium-surface passivation layer (SPL)-hydrogen system, taken perpendicular to the material surface with the atmosphere at the top. The red rectangles in Figure 6.1 depict the boundaries of the two-dimensional Cartesian modelling domain as part of that cross-section. Figures 6.1(a) and 6.1(b) show the domain for uranium with an SPL, and without an SPL respectively. The domain is bounded by four straight lines called the inner ($y = y_1$), outer ($y = y_2$), left ($x = x_1$), and right ($x = x_2$) boundaries. The outer boundary is where the solid meets the atmosphere, across which hydrogen diffuses into the metal. The domain is a square of side length 1×10^{-5}m, so that

$$x_1 = y_1 = 0 \quad \text{and} \quad x_2 = y_2 = 1 \times 10^{-5}\text{m}. \tag{6.1}$$

The full multi-physics model is deconstructed into two constituent parts, the reaction-diffusion-only problem and the thermoelastic problem. In each case, the finite element method (FEM) is employed to calculate the dependent variables on the domain for all timesteps. Important results from these simulations are discussed. Afterwards, a discussion is presented which describes the difficulties encountered when combining the reaction-diffusion and thermoelastic models into one multi-physics model.

6.1 Reaction-diffusion-only models

Now, a reduced model is presented for a system where hydrogen absorbs onto the outer boundary, diffuses into the solid, and hydriding occurs. This is in the absence of temperature, stress and displacement effects, so it is similar to Model 1 presented in the

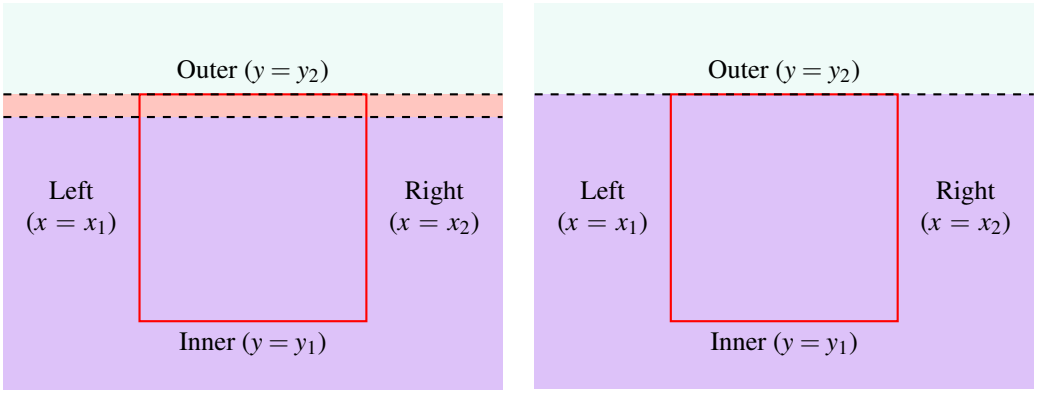

(a) With SPL (b) Without SPL

Figure 6.1: Representation of the two-dimensional solution domain. Purple indicates uranium metal, pink is the SPL, and the atmosphere is shown in blue.

one-dimensional case. Unlike Model 1, the reaction kinetics are time-dependent, and the uranium concentration U describes extent of reaction, following the discussions in Chapter 5. In the first instance, the material is purely uranium metal and the system is represented by the schematic in Figure 6.1(b). In the second instance, we add a surface passivation layer (SPL) as in Figure 6.1(a).

The differential equations for the reaction-diffusion-only model on a two-dimensional Cartesian domain are:

$$\begin{aligned} \frac{\partial C}{\partial t} &= D\left(\frac{\partial^2 C}{\partial x^2} + \frac{\partial^2 C}{\partial y^2}\right) + 3\frac{\partial U}{\partial t} \\ \frac{\partial U}{\partial t} &= \begin{cases} 0 & \text{if } C \leq C_{TSS} \\ -k_{Hr} C^3 U & \text{if } C > C_{TSS} \end{cases} \end{aligned} \tag{6.2}$$

where all quantities are defined as in the one-dimensional results chapter and again, the reaction rate k_{Hr} is defined relative to the diffusivity $k_{Hr} = Da\ D_U$. Note that in the conservation of mass equation, the diffusivity is D, not D_U, since diffusivity of hydrogen in the SPL is different to that in uranium metal.

Initially, the system once again has a relatively small quantity of hydrogen

$$C(x, y, t = 0) = C_{init} = \frac{C_{TSS}}{10}. \tag{6.3}$$

The boundary conditions on hydrogen concentration are zero flux across the inner, left

and right boundaries

$$\left.\frac{\partial C}{\partial y}\right|_{inner} = \left.\frac{\partial C}{\partial x}\right|_{left} = \left.\frac{\partial C}{\partial x}\right|_{right} = 0 \tag{6.4}$$

and a Dirichlet condition on the outer boundary which is 'switched on' exponentially in time

$$C|_{outer} = C_f - (C_f - C_{init})e^{-vt} \tag{6.5}$$

The final concentration on the outer boundary is set to $C_f = 5.0\text{mol m}^{-3}$, and the switch-on speed $v = 4.61\text{s}^{-1}$. With this switch-on speed, the exponential factor e^{-vt} has decreased from 1 to approximately 0.01 after 1 second.

6.1.1 Uranium metal model

Firstly, we investigate a purely uranium metal model, as shown in the schematic 6.1(b). The governing differential equations (6.2) with $D = D_U$ are used alongside boundary and initial conditions on concentration, equations (6.3), (6.5) and (6.4). To complete the system, an initial condition on the uranium concentration U is required. Since we are modelling pure uranium metal, the initial condition for uranium concentration is the same as in the one-dimensional Model 4:

$$U(x,y,t=0) = \frac{1}{\bar{V}_U}. \tag{6.6}$$

Again, U is nondimensionalised to $U^* = \bar{V}_U \times U$, and so $U^*(x,y,t=0) = 1$.

This system can now be solved using FEM on the two-dimensional domain. After some initial solving attempts, it was clear that a mesh with small elements would be required to resolve steep gradients in C and U^* in the y-direction. These steep gradients were seen only near the outer boundary, so to save computation time, a mesh was created with more, smaller elements close to the outer boundary and fewer, larger elements deeper into the metal bulk. We refer to the schematic of the two-dimensional Cartesian mesh in Figure 3.1(b). In the schematic, the elements are of equal width and height. Now, we need elements whose height depends on their y-coordinate.

Specifically, the y-coordinate of the bottom and top nodes of each element are

scaled by the y-dependent functions $G_b(y)$ and $G_t(y)$ respectively

$$\begin{aligned} G_b(y) &= L_y \left(\frac{e_y}{N_y} \right)^{0.05} \\ G_t(y) &= L_y \left(\frac{e_y + 1}{N_y} \right)^{0.05} \end{aligned} \tag{6.7}$$

where $L_y = 1 \times 10^{-5}$m is the total domain length in the y-direction, $N_y = 5000$ is the total number of elements in the y-direction and e_y is element number in the y-direction counted from 0 to $N_y - 1$. The problem was solved with quadratic interpolation, so there are nine nodes in each element, in a three-by-three grid. In a given element, the y-coordinate of the bottom and top rows of nodes is set by $G_b(y)$ and $G_t(y)$ respectively, and the y-coordinate of the middle row was placed at the midpoint, $\frac{1}{2}(G_t(y) + G_b(y))$.

Since the steep gradients are only in the y-direction, in the x-direction, the element widths remain uniform. The problem has no x-dependence so there is no need for a large number of elements in the x-direction. This would only be detrimental to the speed of computation and generate unnecessarily large data files. The number of elements in the x-direction, $N_x = 10$.

Though there is no x-dependence in this problem, there is still merit in solving on a two-dimensional domain. It provides an opportunity to make sure the system and the non-uniform mesh behave as expected before moving on to more complex conditions. The timestep size is chosen to be 0.01 seconds and each simulation runs for 20000 timesteps giving a total simulation length of 200 seconds.

Figure 6.2 shows an example of a simulated result after 200 seconds with $Da = 1 \times 10^{12}$. The concentrations of hydrogen and uranium are uniform in the x-direction, as expected for a problem with no x-dependence. Hydrogen has diffused into the metal uniformly in the x-direction and displays a shallow gradient in the y-direction. Hydride forms as a layer at the top of the metal. We see that the transition region between metal (shown in pink) and hydride (blue) is narrow, as we would expect following the findings of one-dimensional simulations. The hydriding reaction has proceeded to a depth of between $3 - 4 \times 10^{-8}$m into the metal.

To visualise the progress of the reaction in time, a slice is taken through the domain at $x = 5 \times 10^{-6}$ m, and space-time plots are made of C and U^* along this line to see how they depend on y and t over the first 200 seconds. Space-time plots for four different values of Da are shown in Figures 6.3 and 6.4. The figures do not show smooth C and U^* data, because plots were made at intervals of 10 seconds.

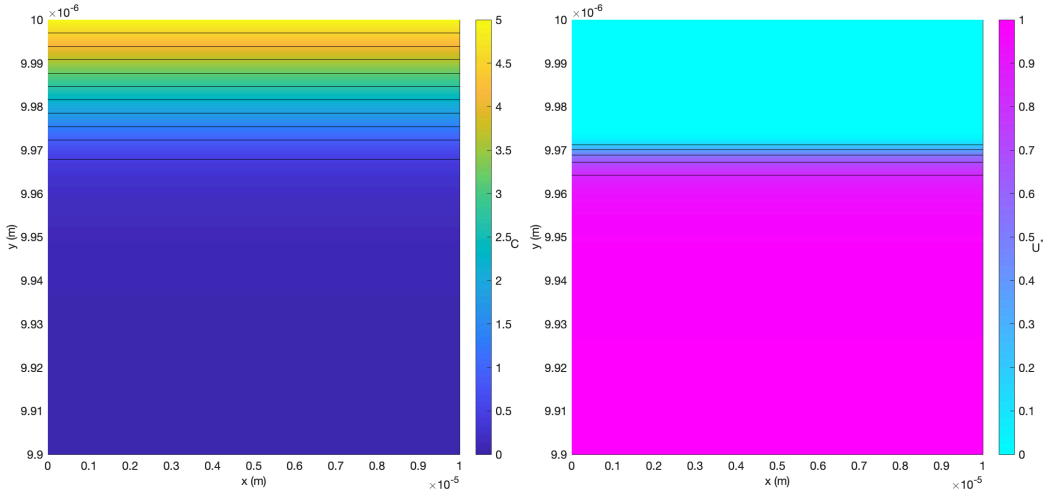

(a) Hydrogen concentration C

(b) Nondimensionalised uranium concentration U^*

Figure 6.2: Hydrogen concentration in mol m^{-3} and nondimensionalised uranium concentration for a two-dimensional reaction-diffusion model with no SPL at 200 seconds, from $y = 9.9 \times 10^{-6}$m to $y = 1 \times 10^{-5}$m. $Da = 1 \times 10^{12}$. Contours of C are drawn at every 0.5mol m^{-3} and contours of U^* are drawn at every 0.2.

For each value of Da from 1×10^9 to 1×10^{12}, hydriding is observed, though for $Da = 1 \times 10^9$, there is no region where $U^* = 0$, so no pure UH_3 is seen. As observed in the one-dimensional case, systems with a larger Da value exhibit steeper transition regions between metal and hydride.

After some time, for each Da value, the hydride thickness appears constant in time, so a steady state seems to have evolved. The time to reach this apparent 'steady state' and the thickness of the hydride layer both exhibit positive correlation with increasing Da. The 'steady state' profiles of $C(y)$ and $U^*(y)$ along $x = 0.5$ after 200 seconds are shown in Figure 6.5. Here, those trends are clearly exhibited. For Da values of 1×10^8 and 1×10^9 no layer of pure UH3 is produced. Above $Da = 1 \times 10^{10}$ however, an increase in Da produces a thicker hydride layer, and has a steeper hydrogen concentration gradient near the boundary.

The details of this 'steady state', however, are less interesting than the potential implications of the fact it exists at all. From the differential equations (6.2) and the outer boundary condition on hydrogen concentration (6.5), we see that the interplay between the timescales of reaction and diffusion and the boundary condition on C must be key to this effect. Since the initial concentration of hydrogen C_{init} is much smaller than the final outer boundary condition C_f and diffusion is so slow, a steep concentration gradient is induced close to the boundary. A hydride growth period follows where the metal

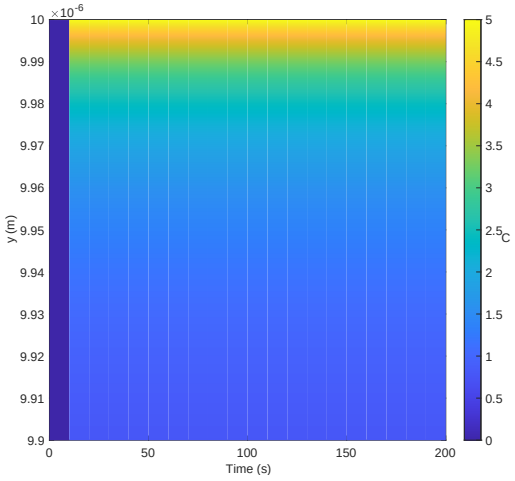

(a) C, $Da = 1 \times 10^9$

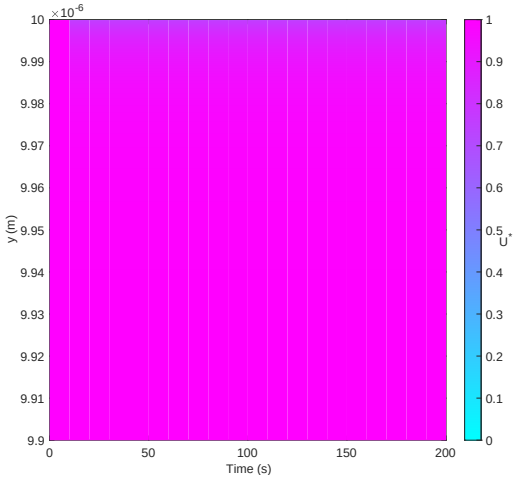

(c) U^*, $Da = 1 \times 10^9$

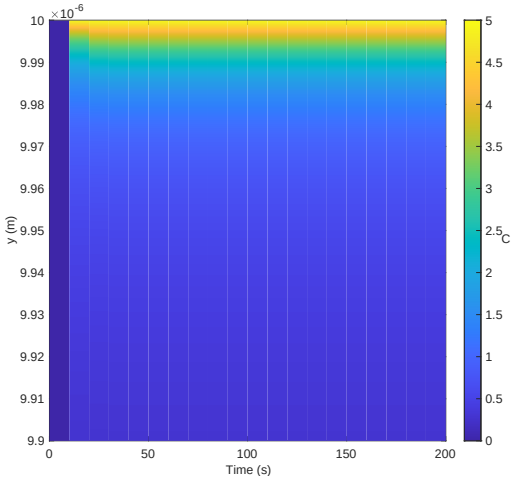

(b) C, $Da = 1 \times 10^{10}$

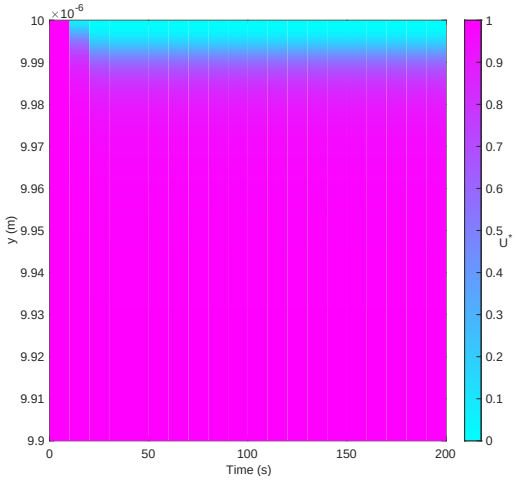

(d) U^*, $Da = 1 \times 10^{10}$

Figure 6.3: Space-time plots along the line $x = 5 \times 10^{-6}$m of hydrogen concentration in mol m^{-3} and nondimensionalised uranium concentration for a two-dimensional reaction-diffusion model with no SPL, with $Da = 1 \times 10^9$ and $Da = 1 \times 10^{10}$ from 0 seconds to 200 seconds, from $y = 9.9 \times 10^{-6}$ to $y = 1 \times 10^{-5}$. Data is plotted every 10 seconds.

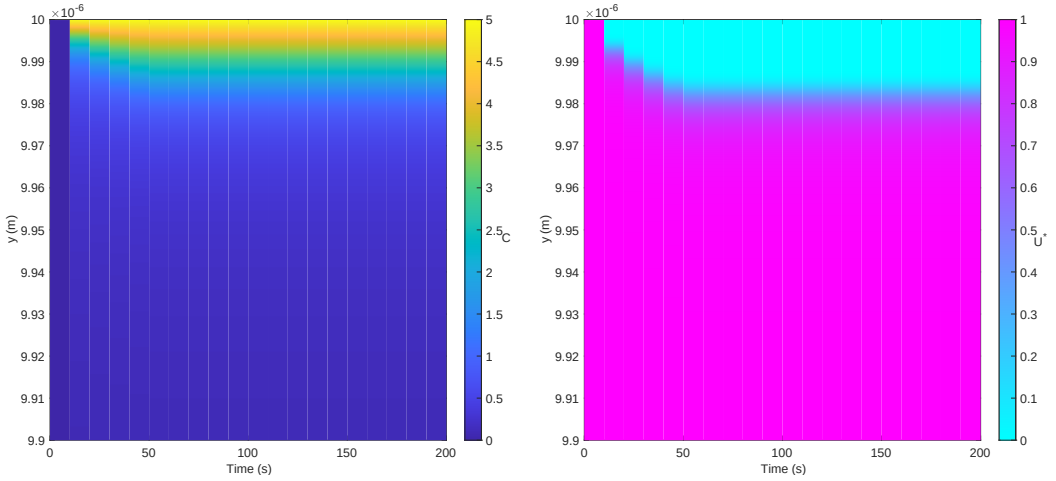

(a) C, $Da = 1 \times 10^{11}$

(c) U^*, $Da = 1 \times 10^{11}$

(b) C, $Da = 1 \times 10^{12}$

(d) U^*, $Da = 1 \times 10^{11}$

Figure 6.4: Space-time plots along the line $x = 5 \times 10^{-6}$m of hydrogen concentration in mol m^{-3} and nondimensionalised uranium concentration for a two-dimensional reaction-diffusion model with no SPL, with $Da = 1 \times 10^{11}$ and $Da = 1 \times 10^{12}$ from 0 seconds to 200 seconds, from $y = 9.9 \times 10^{-6}$ to $y = 1 \times 10^{-5}$. Data is plotted every 10 seconds.

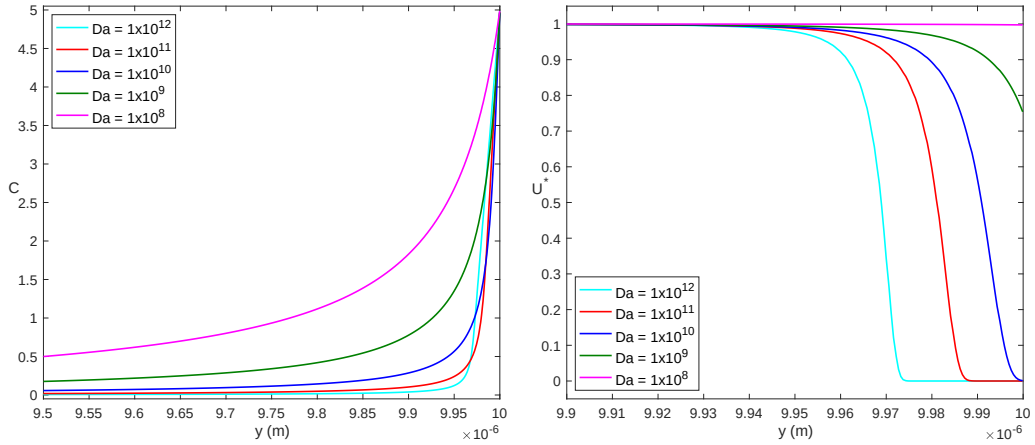

(a) Hydrogen concentration C

(b) Nondimensionalised uranium concentration $U*$

Figure 6.5: Concentration profiles along the line $x = 5 \times 10^{-6}$ for a two-dimensional reaction-diffusion model with no SPL at 200 seconds for five Da values. Hydrogen concentration profile shown for y in the interval $[9.5 \times 10^{-6}, 1 \times 10^{-5}]$ and nondimensionalised uranium profile shown for y in the interval $[9.9 \times 10^{-6}, 1 \times 10^{-5}]$.

and hydrogen react to form a surface hydride layer. The duration of this phase and thickness of hydride layer are governed by the relative reaction rate, Da. Larger Da values mean that reaction proceeds and depletes the diffused hydrogen faster, before it can penetrate deeper. This causes the hydrogen profile to remain steeper and closer to the boundary.

Once this initial fast period is over, there is a hydride layer with $U* = 0$, a transition region with depleted uranium concentration, and the uranium metal phase with $U* = 1$. The hydrogen concentration in the latter two phases is small compared to the hydride layer. Referring to the governing equations (6.2), we see this causes the reaction to proceed at a reduced rate and the remaining significant terms describe pure diffusion. The system has therefore not transitioned to a true steady state, but rather to a quasi-steady state which evolves in time with a rate controlled by the diffusivity D_U.

A quasi-steady state was not seen in the one-dimensional modelling. It can be seen in Figures 5.10 and 5.11, however, that the hydriding reaction is slowing over time. The boundary condition for atmospheric hydrogen used in the one-dimensional model is much larger than in this case. Further investigations would need to be performed to determine whether this effect exists for any size of boundary condition, given a

sufficient amount of time, and whether it persists in multi-physics models.

6.1.2 Uranium metal with surface passivation layer model

Next, we investigate hydriding of uranium metal with a pre-existing surface passivation layer (SPL) as shown in Figure 6.1(a). This SPL will have non-uniform physical parameters in an attempt to replicate the preferential hydrogen diffusion paths seen in experiments, such as grain boundaries and non-uniform SPL thickness. We model a system with an SPL that makes up 1% of the depth of the whole domain, 1×10^{-7}m.

The SPL affects the initial condition on uranium concentration. Physically, we should see two distinct regions represented; one which is entirely uranium metal, with $U^*(t=0)=1$, and the other which is entirely uranium compounds in the SPL, with $U^*(t=0)=0$. We label the position where the metal meets SPL as $y = Y^{SPL} = 9.9 \times 10^{-6}$m. The SPL thickness 1×10^{-7}m $= 1000$Å was chosen as it is within the range (500Å to 2000Å) of those in experiments by R.M. Harker on the effect of SPL thickness on the uranium-hydrogen reaction [7]. The initial uranium profile in the y-direction is the step function shown in Figure 6.6(a). From the inner boundary to Y^{SPL}, the material is completely uranium, and from Y^{SPL} to the outer boundary, there is no uranium — this is the SPL.

However, as described in Chapter 3, in FEM, dependent variables are continuous across element boundaries by definition, and inside elements, they are approximated by finitely-many polynomial shape functions. This means that dependent variables cannot be truly discontinuous in FEM. To resolve this problem, we approximate the step-function between uranium and SPL by a scaled tanh function. This function is defined by

$$F(y) = 1 - \frac{\frac{1}{1+e^{\lambda(\mu-y)}} - A}{B-A} \tag{6.8}$$

where $A = \frac{1}{1+e^{\lambda\Sigma}}$, $B = \frac{1}{1+e^{-\lambda\Sigma}}$, $\mu = Y^{SPL}$, $\lambda = 2000\text{m}^{-1}$ and $\Sigma = 2.5 \times 10^{-8}$m. The quantity Σ controls the width of the function. The quantities λ and Σ are not experimentally determined – they have been chosen to give a tanh function that is relatively steep to model the step-function. The nondimensional initial concentration of uranium follows this tanh function inside a transition region between metal and SPL of width

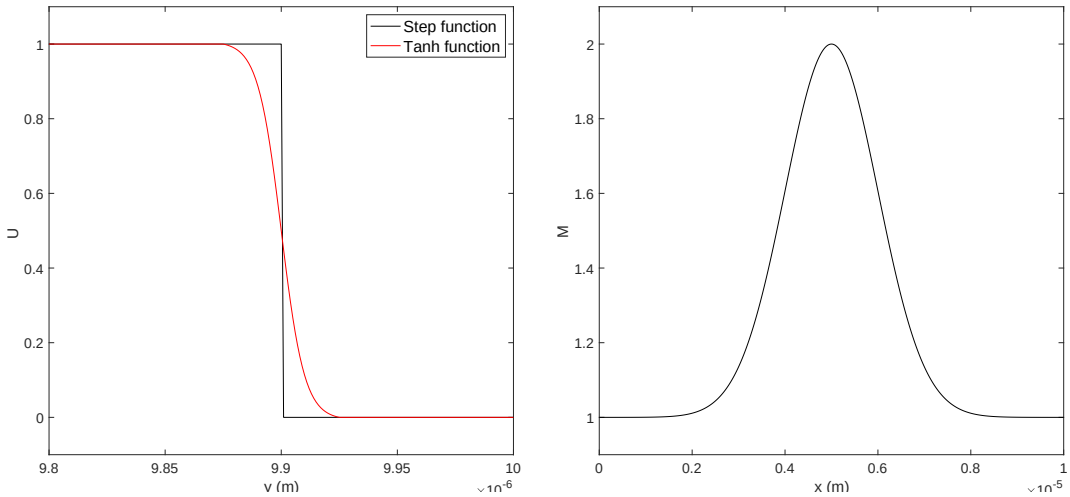

(a) Initial uranium concentration, U^* (b) Gaussian function, $M(x)$

Figure 6.6: Graphs to show the step function and tanh function describing the initial nondimensionalised uranium concentration and the scaled translated Gaussian function, $M(x)$, with the peak at $x = 5 \times 10^{-6}$m and squared standard deviation is 1×10^{-12}m^2 used to introduce non-uniformity in the diffusivity.

2Σ, and is defined on the whole domain by

$$U^*(x,y,t=0) = \begin{cases} 1 & \text{if } y > Y^{SPL} + \Sigma \\ F(y) & \text{if } Y^{SPL} - \Sigma \leq y \leq Y^{SPL} + \Sigma \\ 0 & \text{if } y < Y^{SPL} - \Sigma. \end{cases} \tag{6.9}$$

The smooth initial uranium concentration is labelled as the tanh curve in Figure 6.6(a). Since $U^* = 0$ in the SPL, the reaction term in the rate law is equal to zero. In the transition region, $U^* > 0$ initially, so reaction can proceed in the transition layer.

The governing differential equations are the same as those defined for the pure uranium model, with the notable exception that the diffusivity of hydrogen in the SPL, D_{SPL} is different to that in pure uranium metal, D_U. Since the main component of the SPL is uranium dioxide, we set D_{SPL} equal to the diffusivity of hydrogen in uranium dioxide, UO_2. In the transition region between pure metal and pure SPL, the diffusivity $D_T(y)$ follows the same tanh function shape as the uranium concentration

$$D_T(y) = D_{SPL} + (D_U - D_{SPL})F(y). \tag{6.10}$$

As it is described up to this point, the model describes a homogenous metal with a homogeneous SPL on its surface. However, as discussed in chapter 1, UH_3 is observed to form in localised pits below the SPL, which can be due to preferential hydrogen diffusion in that region [37, 38]. Currently, the model has no mechanism for localised hydride growth, so we introduce an SPL with a non-uniform diffusivity. Since this preferential diffusion has not yet been quantified in the literature, we impose that the SPL diffusivity has a Gaussian x-dependence by multiplying $D_T(y)$ by some Gaussian $M(x)$. The translated, scaled Gaussian function $M(x)$ used is shown in Figure 6.6(b). The peak of $M(x)$ is in the centre of the domain, at $x = 5 \times 10^{-6}$m, the squared standard deviation is $1 \times 10^{-12}\text{m}^2$ and it is translated and scaled such that it has a maximum value of 2, and tends to 1 far from $x = 5 \times 10^{-6}$m. We now have that the diffusivity is x-dependent in the SPL and transition regions and is equal to $M(x)D_{SPL}$ and $M(x)D_T(y)$ respectively.

The governing ODEs are therefore given by equations (6.2) with

$$D = \begin{cases} M(x)D_{SPL} & \text{if } y > Y^{SPL} + \Sigma \\ M(x)D_T(y) & \text{if } Y^{SPL} - \Sigma \leq y \leq Y^{SPL} + \Sigma \\ D_U & \text{if } y < Y^{SPL} - \Sigma \end{cases} \tag{6.11}$$

and $k_{Hr} = Da \times D_U$ with $Da = 1 \times 10^{14}$. The boundary and initial conditions on C remain the same as for the pure metal problem, and are given by equations (6.3), (6.4) and (6.5). Notably, the condition on the outer boundary now applies to the interface between the atmosphere and SPL. The initial condition for U^* is equation (6.9).

An FEM simulation with timesteps of length 0.1 seconds was run to find C and U^*. So that the hydride is distinguishable from the SPL in the results (both have $U^* = 0$), $1 - F(y)$ is added onto U^* in post-processing, and we re-label this quantity as U^* for the remainder of this results section. The results for U^* are shown in Figures 6.7(a), 6.7(b) and 6.7(c) at 100, 500 and 1000 seconds respectively. Contours of U^* are drawn at intervals of 0.05. Some hydride has precipitated by 100 seconds, and by 1000 seconds there is a region where U^* has depleted from 1 to 0.754. There is a layer across the width of the domain with a small amount of hydride, and a central region where more hydride has precipitated.

Since the minimum U^* value seen is 0.754 so far, another simulation was run for much longer in the hopes of seeing the long-term solution. The Damköhler number was reduced to 1×10^{11} so that longer timesteps (1 second) could be taken without

giving a non-converging Newton method. Figure 6.8(a) shows the values of U^* after 1000 seconds. This snapshot was taken at the same time as the final timestep for the $Da = 1 \times 10^{14}$ simulation that was shown in Figure 6.7(c) though less hydride has precipitated: the minimum value of U^* is 0.964. Figures 6.8(b), 6.8(c) and 6.8(d) show the simulation when left to run for 25000, 50000 and 75000 seconds, respectively. Note that the minimum y value has been changed from 9.8×10^{-6}m in Figure 6.7 to 9.5×10^{-6}m in Figure 6.8, since hydride precipitates deeper in the domain in these large-time solutions. The colour range of U^* has also changed to reflect the greater range of values seen in these results. Contours of U^* are drawn at intervals of 0.05 from 0.05 to 0.95. After 25000 seconds, the minimum value of U^* is 0.223. After 50000 seconds, the central region has $U^* = 0$, so pure hydride is seen. By 75000 seconds, the pure hydride region has grown in the x- and y-directions.

6.1.3 Discussion of reaction-diffusion-only models

We now discuss the results of the pure metal initial condition and the metal-SPL initial condition for reaction-diffusion-only models.

Firstly, we note that in the metal-SPL model, the diffusivity of hydrogen in uranium is different to the diffusivity of hydrogen in the SPL. The values, as given in the table of parameters in Appendix F, show that D_U is more than 50 times larger than D_{SPL}. This means that hydrogen diffuses faster once it reaches the metal than it does through the SPL. This could mean that hydride would not form at the SPL-metal interface because it doesn't have the chance to build up. But since C_{TSS} is so small, the reaction proceeds readily with a small amount of hydrogen and we see hydride formed at this interface.

In the pure metal model, we observed that if the Da value is small (see Figures 6.3(a) and 6.3(c) for $Da = 1 \times 10^9$), the hydriding reaction proceeds more slowly, and hydrogen has time to diffuse deeper into the metal. This leads to a shallower concentration profile and less hydride. The outer boundary condition on C will also have an effect on this — if the concentration is large enough, we will see more hydride precipitated regardless. Evidence of this is shown in Figures 5.10(c) and 5.10(d) from the one-dimensional Model 4 where we have $Da = 1 \times 10^9$ with a much larger boundary condition.

A similar situation arises in the uranium-SPL system, though there is an added level of complexity. The SPL is inert in the presence of hydrogen, so hydrogen just diffuses through it. The hydrogen concentration at Y^{SPL} depends on the hydrogen concentration imposed on the outer boundary and the (potentially x-dependent) diffusivity in the SPL.

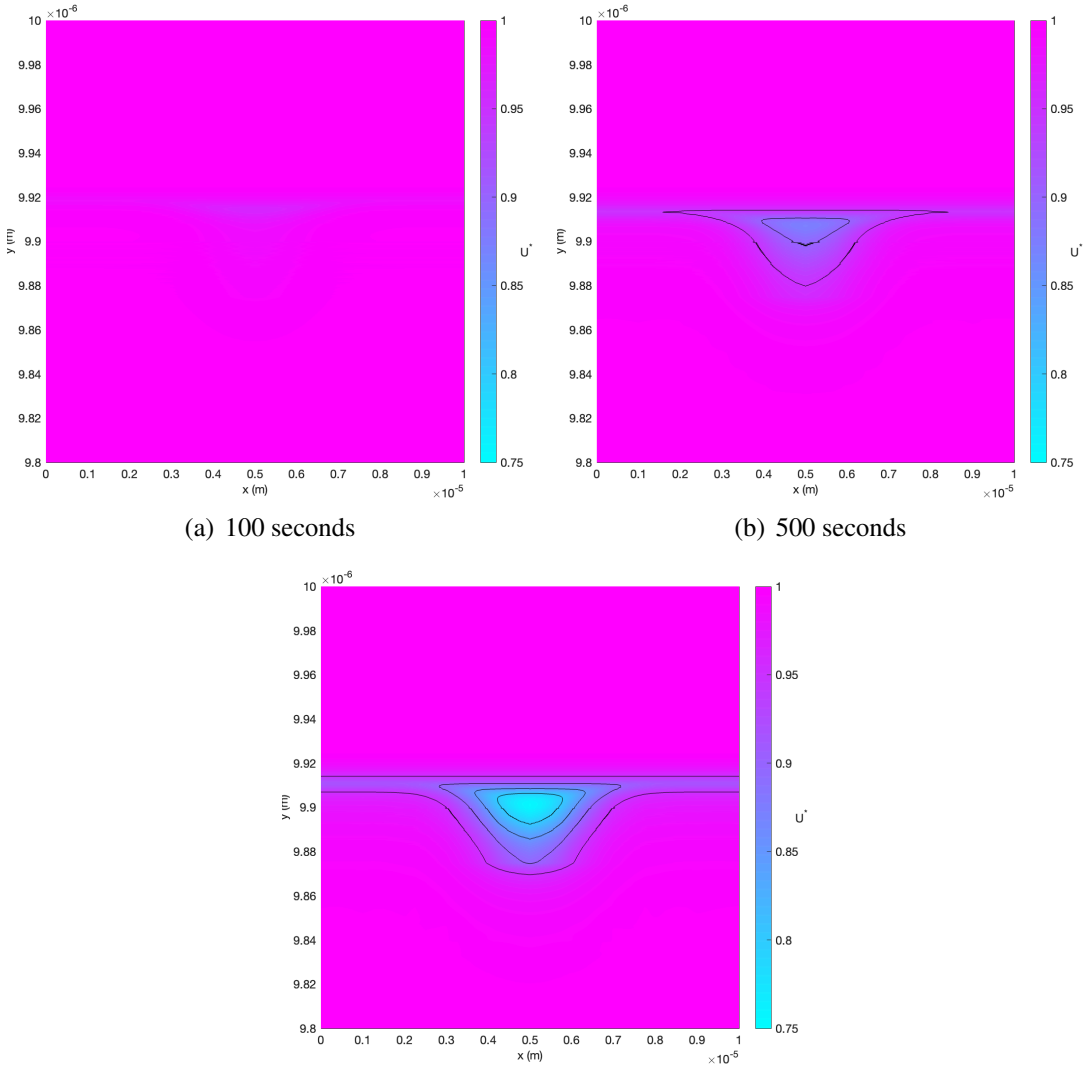

(a) 100 seconds

(b) 500 seconds

(c) 1000 seconds

Figure 6.7: U^* for a two-dimensional reaction-diffusion model with SPL, with $Da = 1 \times 10^{14}$, from 100 seconds to 1000 seconds, from $y = 9.8 \times 10^{-6}$ to $y = 1 \times 10^{-5}$. Contours are drawn at intervals of 0.05 from 0.75 to 0.95. The x-dependent diffusivity is controlled by the Gaussian function $M(x)$.

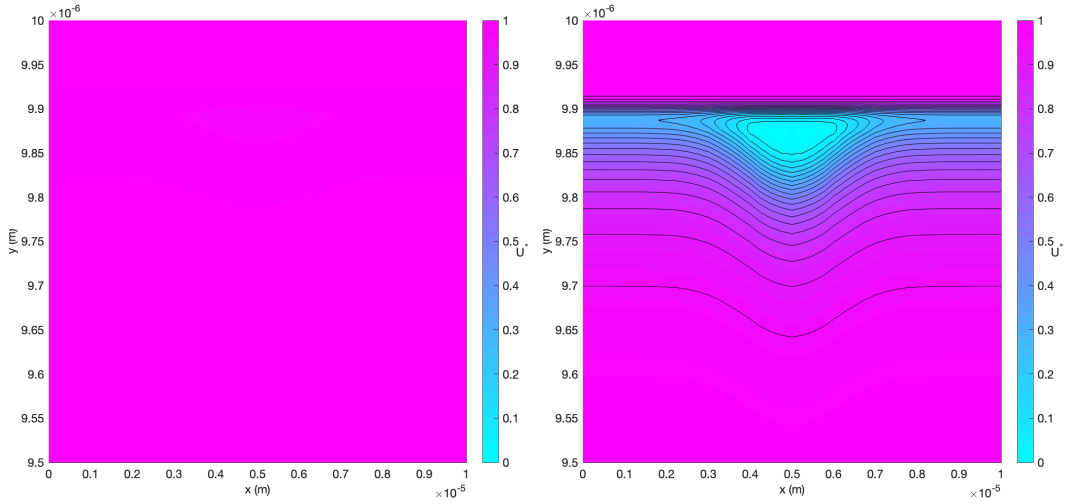

(a) 1000 seconds

(c) 50000 seconds

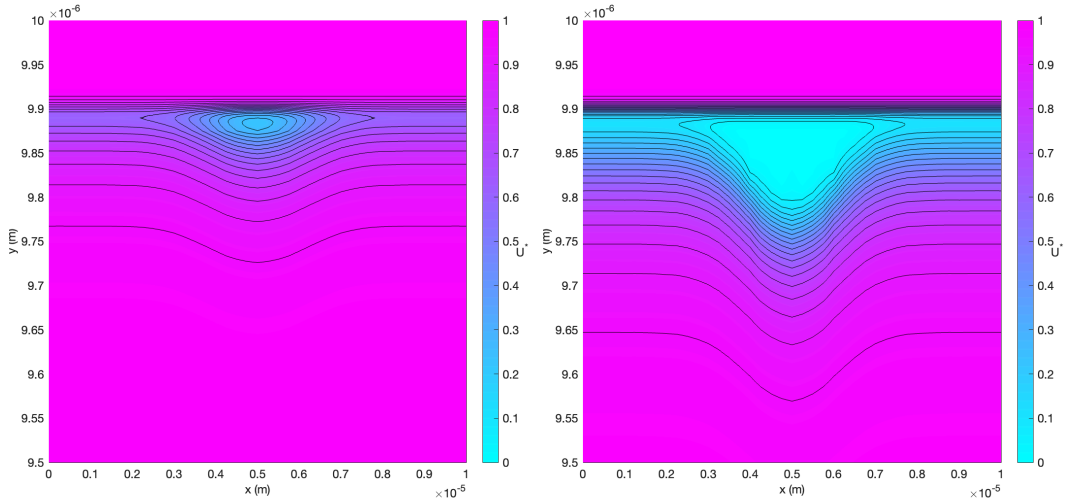

(b) 25000 seconds

(d) 75000 seconds

Figure 6.8: U^* for a two-dimensional reaction-diffusion model with SPL, with $Da = 1 \times 10^{11}$, from 1000 seconds to 75000 seconds, from $y = 9.5 \times 10^{-6}$ to $y = 1 \times 10^{-5}$. Contours are drawn at intervals of 0.05 from 0.05 to 0.95. The x-dependent diffusivity is controlled by the Gaussian function $M(x)$.

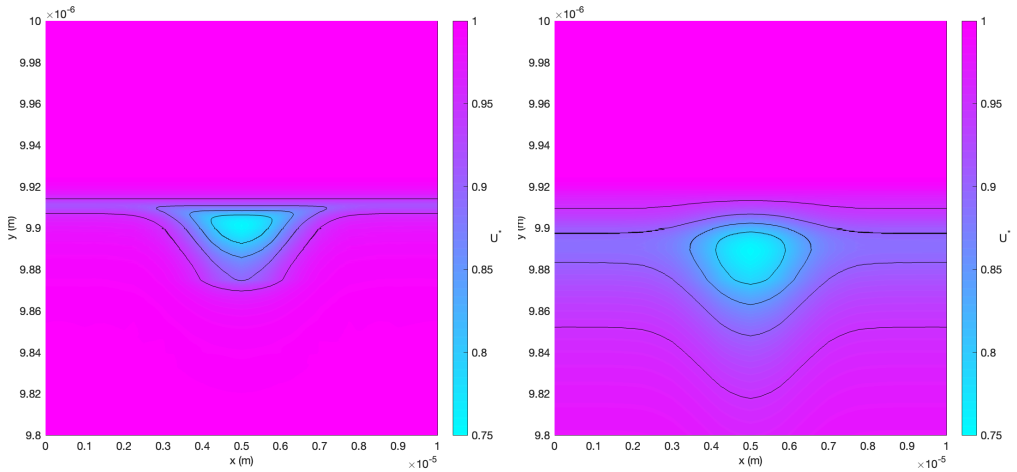

(a) $Da = 1 \times 10^{14}$, $t = 100s$ (b) $Da = 1 \times 10^{11}$, $t = 6800s$

Figure 6.9: Comparison of U^* for $Da = 1 \times 10^{14}$ and $Da = 1 \times 10^{11}$ for timesteps at which they have approximately the same minimum value of $U^* = 0.75$ from $y = 9.8 \times 10^{-6}$m to $y = 1 \times 10^{-5}$m.

This concentration $C(Y^{SPL})$ now acts like a boundary condition for the metal. $C(Y^{SPL})$ starts small and grows slowly, leading to a gradual U^* profile when combined with a smaller Da. This can be seen in Figure 6.9. The figure shows U^* for $Da = 1 \times 10^{14}$ after 100 seconds and $Da = 1 \times 10^{11}$ after 6800 seconds, after which their minimum U^* value is approximately the same (0.75). The hydriding has a significantly shallower gradient for the lesser value of Da.

In their empirical work on hydride nucleation and growth, Arkush et al. [9] observe that hydride blisters grown under an SPL have a 'final' size that depends on the oxide thickness. Recall that uranium hydride, if its growth is unrestricted, will take up a greater volume than the uranium it is formed from; the partial molar volume of uranium hydride is greater than the partial molar volume of uranium. If this growth is restricted, pressure is generated. Arkush et al. state that this pressure, exerted by the SPL on the hydride blister, is causing the cessation of growth. However, in section 6.1.1, we observed that a quasi-steady state could potentially exist without the consideration of stress and deformation. This type of analysis, where it is possible to analyse parts of a system in isolation is one if the benefits of mathematical modelling.

In this model, once a hydride layer is grown on the surface of the metal, it functions in the same way an inert SPL would. It provides a barrier, through which hydrogen must diffuse if it is to reach the metal and cause more hydride to precipitate. The thickness of the hydride grown on the pure metal model turns out to be of the same

order as the thickness of the pre-existing SPL. We anticipated that this might mean we would observe a quasi-steady state with an SPL. However, even after 75000 seconds, the hydrogen concentration did not reach a quasi-steady state, and therefore neither did the extent of hydriding. This is not evidence enough to say a quasi-steady state does not exist. More investigations would have to be completed over a range of Da, C_f and functions $M(x)$ with long simulation times to see if quasi-steady states can be seen with an SPL. If the quasi-steady state does exist, we can expect it will evolve at a time that depends on these parameters. Alternatively, more work could be done to find physically accurate values in the literature and see if a quasi-steady state can be seen when the conditions are close to physically accurate values.

In the work by Harker [7], the amount of hydrogen that has diffused into the metal/SPL block is calculated from the measured drop in pressure in the atmosphere. It is not clear how to use this value to obtain a boundary condition that could be used in this model. Therefore this work cannot be directly compared with our work. However, we do see that pure UH_3 is precipitated almost immediately (in the first 10 seconds) for a system with no SPL, as was concluded by Harker. This can be seen in Figures 6.3 and 6.4: there is some pure hydride from the first plotted timestep at 10 seconds.

In the SPL model, pure hydride is seen at some time between 25000 seconds and 50000 seconds with a 1000Å-thick SPL and $Da = 1 \times 10^{12}$. In Harker's work, the time observed was on the scale of 2000 to 5000 seconds. We conclude that to see more realistic initiation times, we would have to change the function controlling the non-uniformity of the diffusivity in the SPL, $M(x)$ to have a larger maximum value.

From the sensitivity analysis in the one-dimensional results chapter, it was learned that parameters controlling the boundary condition on C are highly influential on model results. If this conclusion holds also for the models presented here, finding a physically accurate way to model this boundary condition will be crucial to compare simulated results to experiments.

Finally, an attempt was made to solve the reaction-diffusion-only system with an x-dependent SPL thickness to replicate a scratch in the SPL but a solution to the model could not be found. This is briefly discussed in Appendix H.

6.2 Thermoelastic models

Next, we look at the linear thermoelastic problem on the two-dimensional Cartesian domain. We use the momentum equilibrium equation and linear thermoelastic constitutive law with the small-deformation approximation as derived in chapter 2

$$\begin{aligned} \frac{\partial \sigma_{ij}}{\partial x_j} &= 0 \\ \varepsilon_{ij} = \frac{1}{2}\left(\frac{\partial u_i}{\partial x_j} + \frac{\partial u_j}{\partial x_i}\right) &= \frac{1+\nu}{E}\sigma_{ij} - \frac{\nu}{E}\sigma_{kk}\delta_{ij} + \alpha\Delta T\delta_{ij} \end{aligned} \tag{6.12}$$

for different temperature profiles on the domain by solving the static heat equation

$$\frac{\partial^2 T}{\partial x_i \partial x_i} = 0. \tag{6.13}$$

In this reduced model, the domain has length 1m in both x- and y-directions. The initial conditions are that the material is unstressed, undeformed and the temperature is uniformly $T_0 = 353.15K$ ($80^\circ C$).

Framing the linear thermoelasticity problem in the terms of the two-dimensional Cartesian weak form equation (3.42), and writing $(x_1, x_2) = (x, y)$ gives the six residual equations

$$\begin{aligned} &\int_{x_1}^{x_2}\int_{y_1}^{y_2}\left\{\sigma_{xx}\frac{\partial\phi(x,y)}{\partial x} + \sigma_{xy}\frac{\partial\phi(x,y)}{\partial y}\right\}dxdy = \int_{\partial\Omega}\phi(x,y)\begin{pmatrix}\sigma_{xx}\\ \sigma_{xy}\end{pmatrix}\cdot\mathbf{n}dS \\ &\int_{x_1}^{x_2}\int_{y_1}^{y_2}\left\{\sigma_{xy}\frac{\partial\phi(x,y)}{\partial x} + \sigma_{yy}\frac{\partial\phi(x,y)}{\partial y}\right\}dxdy = \int_{\partial\Omega}\phi(x,y)\begin{pmatrix}\sigma_{xy}\\ \sigma_{yy}\end{pmatrix}\cdot\mathbf{n}dS \\ &\int_{x_1}^{x_2}\int_{y_1}^{y_2}\left(\frac{\partial u_x}{\partial x} - \frac{1+\nu}{E}\sigma_{xx} + \frac{\nu}{E}(\sigma_{xx}+\sigma_{yy}) - \alpha\Delta T\right)\phi(x,y)dxdy = 0 \\ &\int_{x_1}^{x_2}\int_{y_1}^{y_2}\left(\frac{\partial u_y}{\partial y} - \frac{1+\nu}{E}\sigma_{yy} + \frac{\nu}{E}(\sigma_{xx}+\sigma_{yy}) - \alpha\Delta T\right)\phi(x,y)dxdy = 0 \\ &\int_{x_1}^{x_2}\int_{y_1}^{y_2}\left(\frac{1}{2}\left(\frac{\partial u_x}{\partial y} + \frac{\partial u_y}{\partial x}\right) - \frac{1+\nu}{E}\sigma_{xy}\right)\phi(x,y)dxdy = 0 \\ &\int_{x_1}^{x_2}\int_{y_1}^{y_2}\left\{\frac{\partial T}{\partial x}\frac{\partial\phi(x,y)}{\partial x} + \frac{\partial T}{\partial y}\frac{\partial\phi(x,y)}{\partial y}\right\}dxdy = \int_{\partial\Omega}\phi(x,y)\begin{pmatrix}\frac{\partial T}{\partial x}\\ \frac{\partial T}{\partial y}\end{pmatrix}\cdot\mathbf{n}dS \end{aligned} \tag{6.14}$$

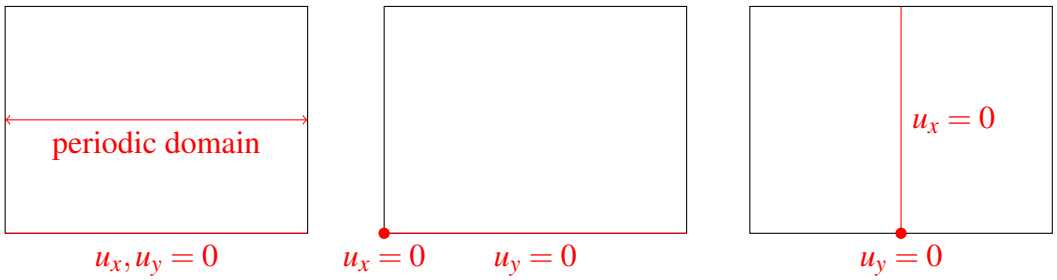

(a) Conditions I (b) Conditions II (c) Conditions III

Figure 6.10: Three different sets of displacement boundary conditions.

to be solved for the six variables u_x, u_y σ_{xx}, σ_{yy}, σ_{xy} and T respectively. By 'respectively', it is meant that the ordering of the equations in the finite element Jacobian relative to the order of the variables must be as shown here. As discussed in section 2.10, each of the equations of thermoelasticity is derived from the variation of a certain variable. That variable is the unknown associated with that equation. For example, the third equation of (6.14) is derived from the variation $\delta\sigma_{xx}$, so is associated with the variable σ_{xx}. In the description of the finite element method in chapter 3, it was stated that applying a Dirichlet boundary condition to a variable u_l means that, at nodes on that boundary, u_l is pinned. The residual equation on those nodes is automatically satisfied and the associated entries are not added into the Jacobian matrix. If a different respective ordering is used, the equations are associated with the wrong variables and the wrong equation is removed from the Jacobian. In this case, a solution to the problem cannot be found. This problem was encountered in the development of this two-dimensional model — the order of equations as shown above was used, but the stress components were listed before the displacements. A finite element solution could not be found until this problem was identified and rectified.

The term on the right-hand-side of each of the first two equations of (6.14) refers to traction $\sigma \cdot \mathbf{n}$ on $\partial\Omega$. The boundary $\partial\Omega$ is split into two parts; $\partial\Omega_u$ and $\partial\Omega_\sigma$ on which displacement and traction boundary conditions are applied respectively. If the condition on $\partial\Omega_\sigma$ is described as 'traction-free', there is zero traction on the boundary, so $\sigma \cdot \mathbf{n} = 0$ on that boundary and the term on the right-hand-side of each of the Cauchy momentum equations is zero. On the part of the boundary where we impose the displacement, $\partial\Omega_u$, the displacement is pinned.

Two different sets of Dirichlet boundary conditions were imposed on T. The first was to increase the temperature on the top and bottom boundaries by 10% over a number of timesteps. Since the static heat equation governs temperature, the temperature

increases uniformly. The second was to increase the top boundary temperature by 5%, while keeping the temperature on the bottom boundary equal to T_0 to observe a uniform temperature gradient. The temperature boundary conditions were both imposed by changing them from T_0 over a number of timesteps to make sure they were compatible with the initial condition. The term on the right-hand-side of the final equation of (6.14) allows for a condition on the temperature flux across $\partial\Omega$. The two types of boundary conditions imposed on the temperature here are Dirichlet conditions (where the temperature is pinned on part of the boundary) or where there is zero temperature flux so the term on the right-hand-side is zero.

We also look at three different ways to constrain deformation, via three different sets of boundary conditions on the displacement, $\mathbf{u}$. These are labelled Conditions I, Conditions II and Conditions III in Figure 6.10. Conditions I impose periodic conditions in the x-direction and no displacement of the bottom boundary in either direction. Conditions II impose that the bottom boundary cannot move in the y-direction and the bottom left corner cannot move in the x-direction. This means that the bottom-left corner is pinned in place and the bottom boundary may stretch to the right but may not deform upwards or downwards. Conditions III impose that the centre of the bottom domain is pinned in the y-direction and the centre-line of the domain ($x = 0.5$) cannot move in the x-direction. This means that the point at the centre of the bottom boundary is pinned in place and the centre-line may not deform to the left or right. In all three cases, traction free boundary conditions are imposed on boundaries where there is no displacement boundary condition. In Conditions II and Conditions III, there is zero temperature flux imposed across the left and right boundaries. Zero temperature flux across left and right boundaries is naturally imposed in Conditions I since the domain is periodic in the x-direction.

In this section, we increase the temperature in two different ways and impose three kinds of boundary conditions. We will discuss the results and the relevance of these problems in the context of uranium hydriding.

6.2.1 Uniform temperature

First we look at the case where the temperature of the system is raised uniformly by 10% and impose Conditions I on the displacement. When attempting to solve the system, the Newton method did not converge and no solution was found. To try to find a solution, the domain mesh was refined and smaller timesteps were taken. When this did not lead to a convergent Newton method, an adaptive timestepping algorithm

was employed. This is where the duration of timestep is selected based on the size of error of the solution compared to a cheaply computed estimate. The size of timestep chosen by the algorithm was very small, and the solver would stop solving after a few timesteps. This was due to the timestep size being too small to be allowed by the software's default tolerance measures.

Next, we impose Conditions II on the system. These new conditions resulted in a solution being found for the uniform temperature case with a quadratically convergent Newton method. Figures 6.11(a), 6.11(b) and 6.11(c) show the simulated u_x, u_y and σ_{xx} values. We see that u_x appears constant in the y-direction and linear in the x-direction, and vice versa for u_y. We generate displacement profiles in the x- and y-directions along the right and bottom boundaries, shown in 6.11(f) and 6.11(g) respectively and see that this linear displacement is indeed the case. The stress σ_{xx} in Figure 6.11(c) is very small everywhere in the domain. The other two calculated stress components σ_{xy} and σ_{yy} are not shown as they also take very small values everywhere. It is assumed that stress is zero to a machine precision value which has been multiplied by constants in the calculation.

If a square domain undergoing uniform temperature increase is allowed to deform freely, it will expand uniformly, or in other words, its displacement will be linear. This is what is shown in Figure 6.11. The deformation is not restricted by Conditions II, and therefore there is zero stress.

In uniform expansion, the x-displacement u_x will be negative on the left boundary and positive on the right boundary. Conditions I imposes that all independent variables will take an equal value on the left and right boundaries with periodic boundary conditions, and thus imposing Conditions I did not allow uniform expansion.

6.2.2 Uniform temperature gradient

Next, we look at the case where the temperature of the top boundary is raised by 5% and impose Conditions I on the displacement. Again, a solution to the system could not be found because the Newton method did not converge.

Conditions II were applied instead, and a solution to this system was found, though the Newton method converged slower than quadratically. The temperature gradient is shown in Figure 6.13(a) and Figures 6.12(a) and 6.12(b) show the displacement in the x- and y-directions respectively. Figures 6.12(c), 6.12(d) and 6.12(e) show the three distinct stress components σ_{xx}, σ_{yy} and σ_{xy}. Figure 6.12(f) shows the trace of the stress tensor $Tr(\sigma) = \sigma_{xx} + \sigma_{yy}$.

From Figures 6.12(a) and 6.12(b), we see that deformation is qualitatively different from the uniform heating case — particularly that there is no x-displacement near the bottom boundary and the y-displacement is non-linear. Figures 6.13(c) and 6.13(e) show the displacement along the right boundary and top boundary respectively. We see that the top boundary experiences linear displacement in the x-direction and non-linear displacement in the y-direction. The top boundary is a convex curve shape. On the right boundary, we see that the system exhibits some compression since $\frac{\partial u_y}{\partial y} < 0$.

The regions where compression is seen corresponds to regions of compressive stress (the negative values of $\mathrm{Tr}(\sigma)$ in Figure 6.12(f)). From $\mathrm{Tr}(\sigma)$ it is also possible to deduce that there are tensile stresses in the vicinity of the central bottom boundary, indicating that the material is pulling away from the boundary. This stress is large; its maximal value is around 2.9×10^7Pa.

With a uniform temperature gradient in 2D, an unrestricted domain will change shape as is illustrated in the schematic, Figure 6.14. The zero y-displacement condition on the bottom boundary in Conditions II means the domain cannot deform in this way, hence stresses are induced.

Finally, imposing Conditions III lifts these restrictions and allows the domain to deform freely under an imposed uniform temperature gradient. The domain is now set to have zero x-displacement on the vertical centre-line at $x = 0.5$ and zero y-displacement at the point where this line meets the bottom boundary, as illustrated in Figure 6.10(c). The results of the simulation are shown in Figures 6.15 and 6.16. We see the deformation is qualitatively similar to the schematic in Figure 6.14 — the top boundary is a convex curve and the bottom boundary is concave as shown in Figures 6.16(d) and 6.16(h). The x-displacement on the bottom boundary is zero since $T = T_0$, and is linear on the top boundary where $T = 1.05 \times T_0$. The x-displacement on the left and right boundaries is linear. Figures 6.15(d) and 6.15(e) show the stress component σ_{xx} and $Tr(\sigma)$. They are everywhere small enough to be considered machine precision, as are the components σ_{xy} and σ_{yy} which are not shown. This is as expected for this unrestricted expansion.

6.2.3 Discussion of thermoelastic models

The simulated results for a uniform temperature gradient with Conditions II differ from the two experiments where the domain is allowed to deform freely because stresses are induced. The maximal value of $Tr(\sigma)$ is approximately 2.9×10^7Pa, even though the deformation is small relative to the size of the domain — the maximum y-displacement

is less than 1mm, compared to the 1m domain length. It was noted that the Newton method converged slower than quadratically. Imposing Conditions I meant that solutions could not be found in either the case of uniform temperature increase, or uniform temperature gradient.

Because the Young's modulus is so large for metals (for uranium, $E = 2.08 \times 10^{11}$ [84]), if the boundary conditions sufficiently restrict deformation, the stresses induced can be large. If the the value of an independent variable at a given node changes by a sufficient amount between two timesteps, the solution from the previous timestep becomes a poor initial guess for the advanced timestep. This can lead to Newton methods which converge at a slower-than-quadratic rate or do not converge at all. We have encountered that issue in this section when the domain is experiencing large changes in the stress values between timesteps.

To combat this problem, it is possible to nondimensionalise the stress variables, and calculate $\frac{\sigma_{xx}}{E}$, $\frac{\sigma_{xy}}{E}$ and $\frac{\sigma_{yy}}{E}$. When the simulation ran in this case, the Newton method converged quadratically on the solution for all timesteps. This happens because the Young's modulus E will no longer appear in the governing differential equations (6.12), and so there are smaller changes in the independent variables between timesteps.

However, when we move to a multi-physics model, nondimensionalising does not resolve the issue. Since stress appears in the hydrogen flux $\mathbf{J}$ and the chemical potential, μ, it therefore appears in the conservation of mass and energy equations — see equations (2.21), (2.24), (2.15) and (2.28) respectively. In fact, there are terms in the energy conservation equation which have squared stress terms. Nondimensionalisation of the stress will mean the Young's modulus is introduced into these equations instead.

In one-dimensional modelling, the stress was calculated as zero everywhere because the growth of the domain was not restricted. However, when attempting to model hydriding in two dimensions, the non-uniform expansion and temperature changes associated with localised hydride formation will cause stresses in the system.

Though it is possible to solve the continuum multi-physics model with FEM for hydriding on a two-dimensional domain, there are many factors which make it difficult. They are listed here:

- The metal-hydride transition region requires many small elements to resolve the steep gradient in U^*. These small elements mean that small timesteps must be taken.

- Small elements are required to resolve steep stress gradients.

- Fast-changing stress values require small timesteps to be taken so that the previous solution is still a good initial guess for the next timestep.

- There are three timescales in the problem: diffusion of hydrogen controlled by D, reaction to form hydride controlled by k_{Hr} and the switch-on speed of the outer boundary condition on C controlled by v. All three of these timescales must be considered when choosing a timestep size.

By choosing extremely small timesteps and elements, the problems of resolving steep gradients and fast-changing dependent variables are solved. However, the simulation will need to run for a large number of timesteps to see change on the diffusion timescale. We then encounter the problem of the code being computationally expensive and generating large amounts of data.

To solve this, the first step in future work would be to solve the system on a fully adaptable mesh with an adaptive timestepping regime. This will ensure that small elements and timesteps are used only where they are needed. The problem will still be computationally expensive because adaptivity requires calculation, but hopefully less so than indiscriminately decreasing the element size and timestep length.

Referring to the problem of Condition II with a uniform temperature gradient, we also note that the calculated stress is large, even though the deformation is small relative to the size of the domain — the maximum y-displacement is less than $\frac{1}{1000}$ of the domain length. In one-dimensional modelling, we saw deformations up to $\frac{1}{5}$ of the domain size. Thus, with a full working multi-physics model for hydriding, we could potentially expect very large stress values.

Finally, in the sensitivity analysis of Model 3 in one-dimensional modelling, we concluded that $\bar{V}_{Hr}$, the partial molar volume of hydride in uranium metal is highly influential on the expansion. This value is expected to be very important when calculating large stresses that depend on deformation.

6.3 Discussion and conclusions

The quasi-steady states seen in the pure metal model could be evidence of a mechanism for cessation of hydride growth existing in a system which solely models reaction and diffusion. Alternatively it could contribute to the slowing of growth alongside stresses generated by the SPL. Developing mathematical models allows us to explore these mechanisms in isolation.

A multi-physics model could be used to calculate stress, and therefore predict whether the ultimate tensile strength of a given material has been reached. This could be used to predict the occurrence of hydride blisters breaching the SPL. Sensitivity analysis of such models could be used to determine parameters that influence the time or blister size when the SPL is breached.

As discussed in the last section, running simulations on these two-dimensional models is computationally expensive. Running sensitivity analysis experiments on these two-dimensional models would take a vast amount of computing time since a whole simulation must be run to obtain a single data point. However, it lends itself to easy parallelisation since each data point can be obtained individually and compared at the end. It would be important to parallelise any parameter experiments on two-dimensional models.

In future work on these models, it should be noted that the physical parameters of uranium hydride used here do not differ from those for uranium metal. To have a model with high fidelity to experiment, a full set of physical parameters should be used. It is not always possible to find existing parameters in the literature.

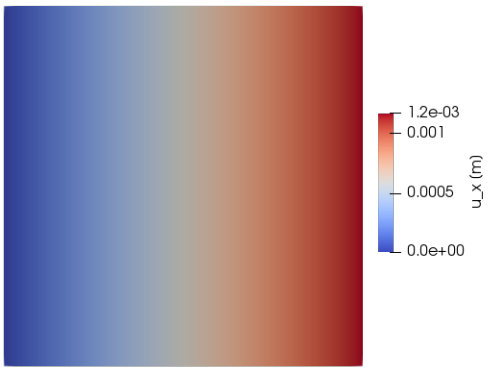

(a) u_x

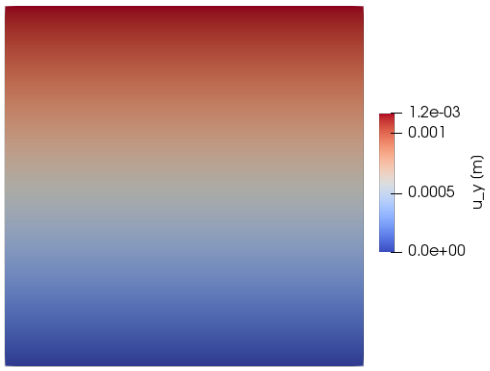

(b) u_y

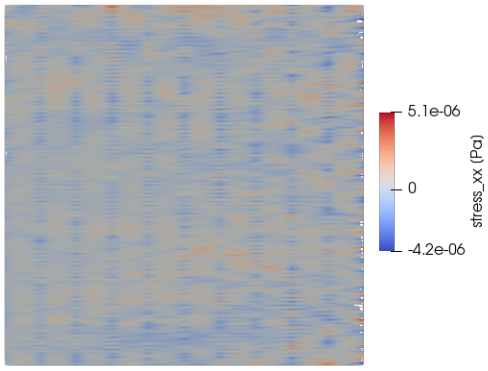

(c) σ_{xx}

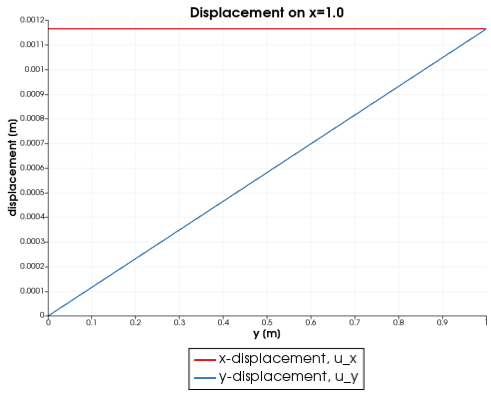

(f) Displacement on right boundary

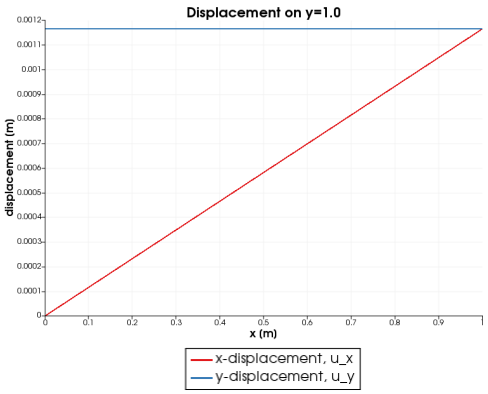

(g) Displacement on top boundary

Figure 6.11: Graphs to show deformation and stress due to uniform temperature increase with Conditions II.

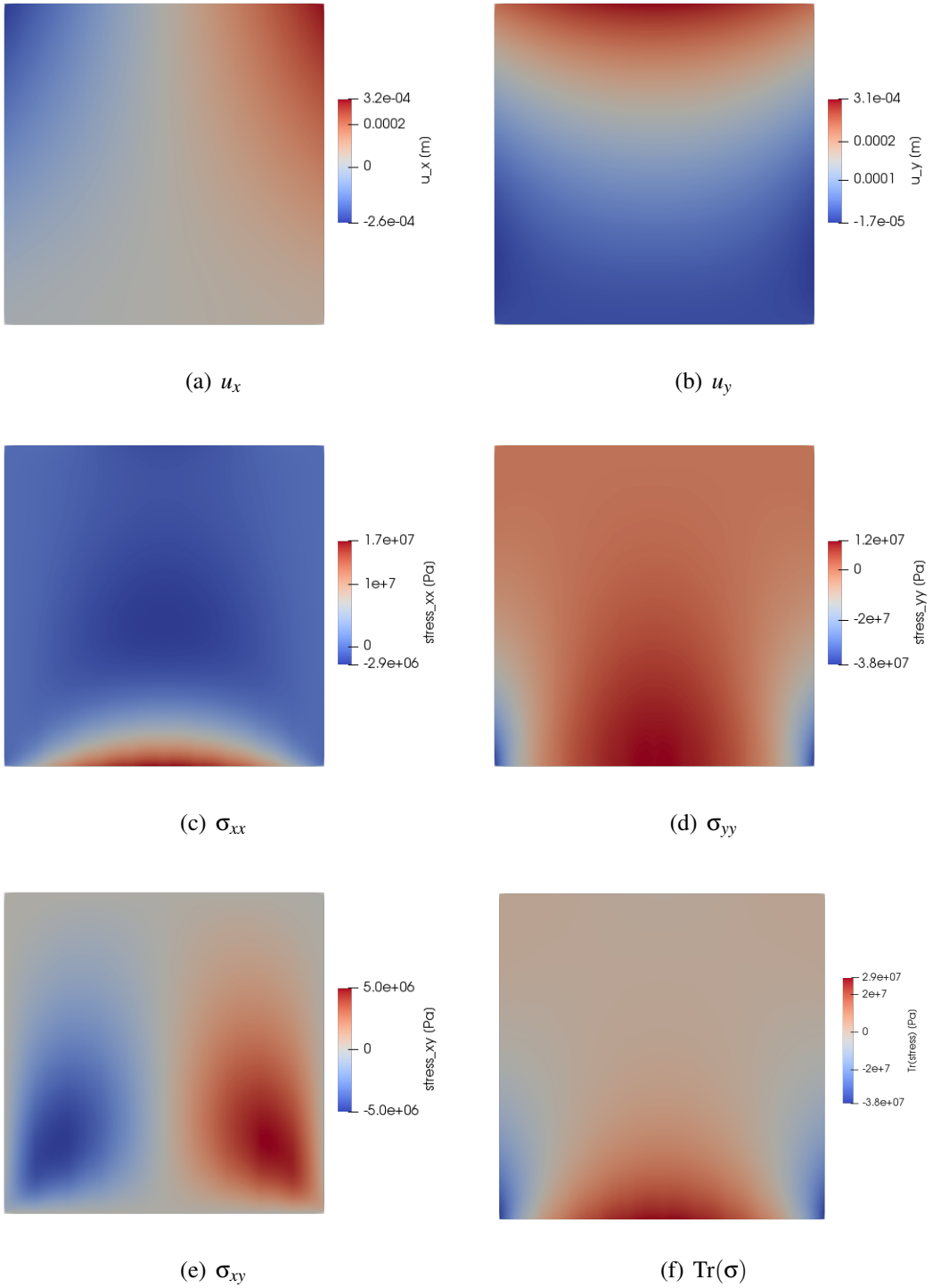

(a) u_x (b) u_y

(c) σ_{xx} (d) σ_{yy}

(e) σ_{xy} (f) $\mathrm{Tr}(\sigma)$

Figure 6.12: Graphs to show displacement and stress in a uniform temperature gradient with Conditions II.

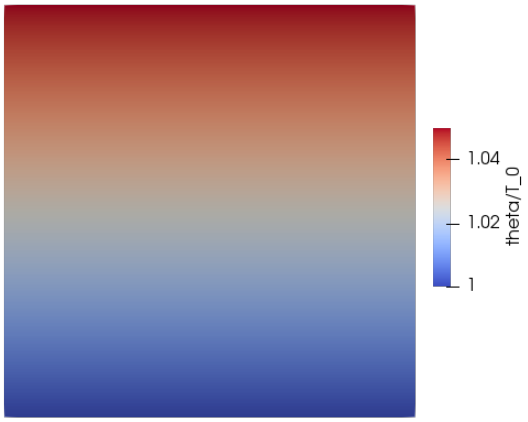

(a) T/T_0

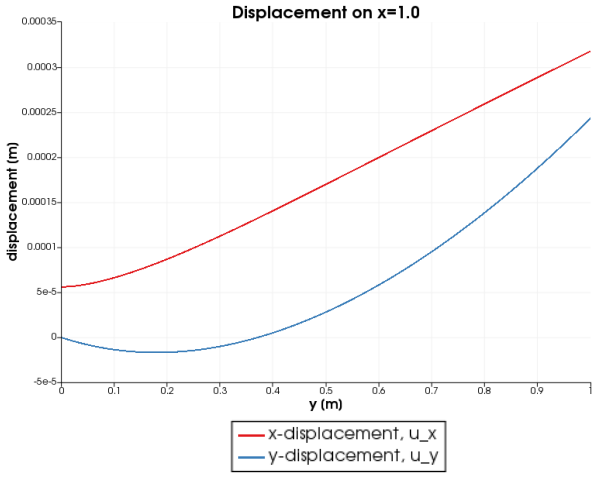

(c) Displacement on right boundary

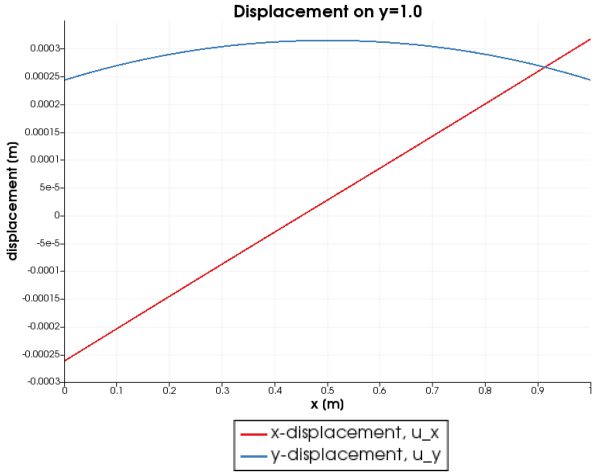

(e) Displacement on top boundary

Figure 6.13: Graphs to show temperature, and displacement on the right and top boundaries in a uniform temperature gradient with Conditions II.

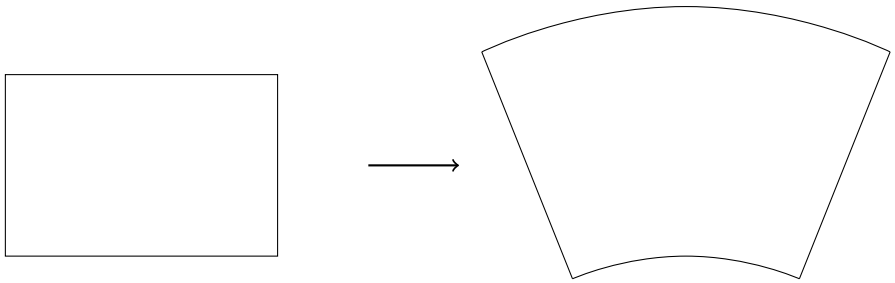

Figure 6.14: Schematic to show unrestricted deformation of a two-dimensional domain in a uniform temperature gradient, with the temperature at the top boundary higher than that at the bottom.

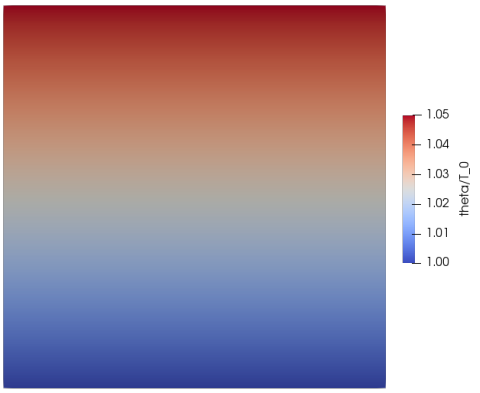

(a) T/T_0

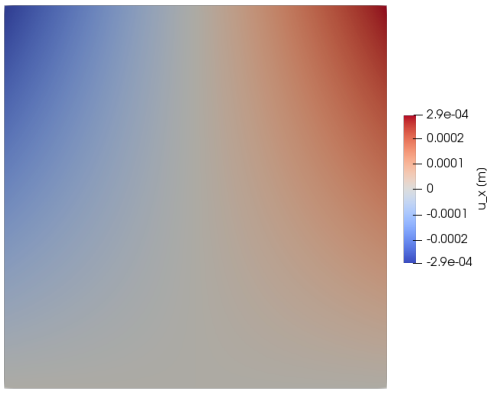

(b) u_x

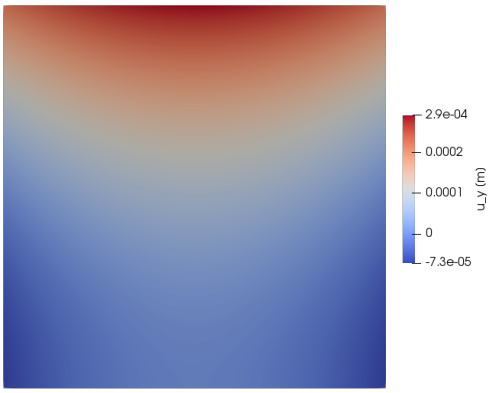

(c) u_y

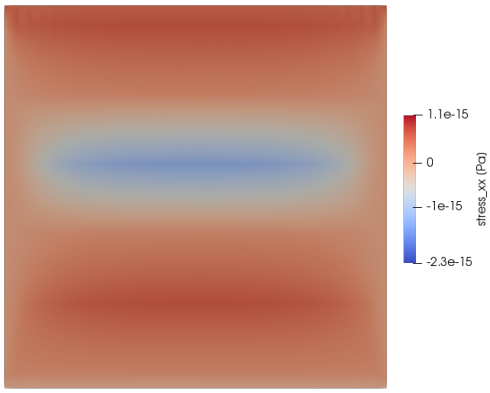

(d) σ_{xx}

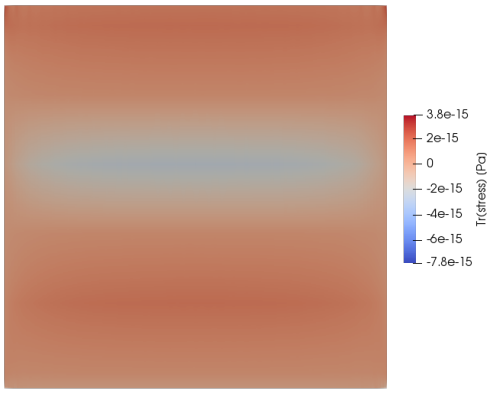

(e) $\mathrm{Tr}(\sigma)$

Figure 6.15: Graphs to show temperature, displacement and stress in a uniform temperature gradient with Conditions III.

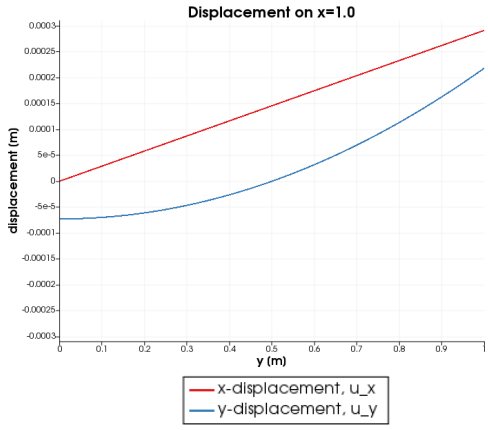

(c) u_x and u_y on right boundary

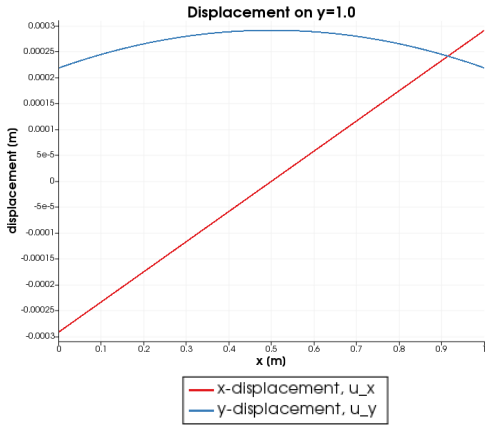

(d) u_x and u_y on top boundary

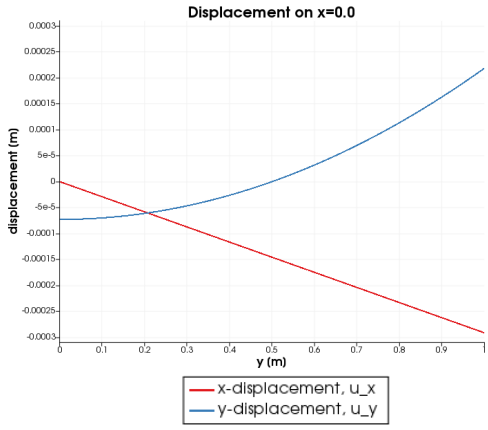

(g) u_x and u_y on left boundary

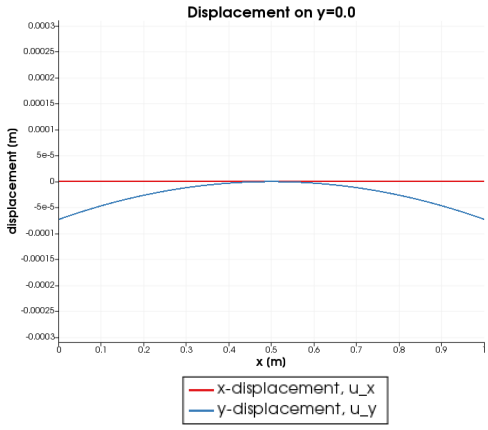

(h) u_x and u_y on bottom boundary

Figure 6.16: Graphs to show displacement on the boundaries in a uniform temperature gradient with Conditions III.

Chapter 7

Future work

Some important areas of future work are apparent from the discussions of one- and two-dimensional modelling results. Firstly, it is important to obtain a boundary condition on C of the correct form that is physically consistent, or use some other method to model hydrogen in-flux into the system. This could be achieved by finding a method to properly convert the Sieverts' law given by Powell [63, 64].

Secondly, it is clear that a mesh and timestepping method which can sufficiently resolve the solutions for the two-dimensional multi-physics model must be found. This will open up the potential to study the effects of both hydride-induced stress and pre-existing stress. It would be possible to investigate whether tensile stress produces preferential hydriding regions as seen experimentally in zirconium [35] and niobium [32]. It would also be interesting to attempt to replicate the experimental findings of Appel et al. in their pre-stressed uranium bars [27]. Alongside the introduction of stress in the diffusion equation via the chemical potential, μ, a stress-dependent solid solubility limit could be introduced, following the lead of previous modelling by Puls [33] and Varias [34]. It would be possible to compare the effects of stress-dependent C_{TSS} and μ as reasons for preferential hydriding. It would also be interesting to see the effect of multiple blisters in one domain and explore how their stress fields interact.

On the theme of stress and deformation, a more complicated nonlinear elasticity model could be employed. Since UH_3 is highly brittle, it is not physically accurate to model it as a linearly elastic material. Appel et al. also found that plastic deformation is important to SPL cracking [27].

Interesting work has been done by S. Blaxland in their 2015 thesis [85], and by Greenbaum et al. [86, 87], to determine which hydride shapes are energetically preferable based on the strain energy calculated by FEM. With the full version of the model

in this work (that includes reaction-diffusion and thermoelastic effects), hydride is produced when it is energetically preferable based on the stress field, but also on the temperature and local concentration of hydrogen. After more development to the two-dimensional model in this work, it would be possible to investigate whether the same shapes are energetically preferable in the short- and long-term after the inclusion of these effects.

Another obvious next step is to complete a thorough investigation over a range of boundary conditions and preferential diffusion functions to see if the observed quasi-steady state exists in two-dimensional models with an SPL.

By proceeding with sensitivity analysis on the two-dimensional (and potentially higher-dimensional) multi-physics models, it will be possible to investigate the dependence of the model results on physical parameters such as the external pressure of hydrogen, size of pre-existing stress and initial temperature. Sensitivity analysis could be used to highlight important areas of future experimental investigation. As discussed previously, running sensitivity analyses on two-dimensional FEM models is computationally costly. One way to reduce computational cost may be to approximate the temperature by a constant value. In the one-dimensional multi-physics models, temperature did not change appreciably from its initial value in any of the models. Unless it becomes clear that this is different in two dimensions, it is proposed that temperature is set to a constant value to remove one of the equations.

In the longer term, models on an axisymmetric cylindrical domain and in three dimensions could be solved. This could be used to explore intrinsically higher-dimensional effects, such as three-dimensional stress effects and the morphology of hydrides in three-dimensions.

Finally, in terms of the model derivation, it would be mathematically elegant to obtain a variational formulation for the whole system, as was done for linear thermoelasticity in section 2.10, if the relevant invariants can be found or derived.

Bibliography

[1] J.P. Blackledge. "- An Introduction to the Nature and Technology of Hydrides". In: *Metal Hydrides*. Ed. by W.M. Mueller, J.P. Blackledge, and G.G. Libowitz. New York: Academic Press, 1968. Chap. 1, pp. 51 –89.

[2] G.L Powell. "Uranium Corrosion Near Ambient Temperature". In: *Uranium Processing and Properties*. Ed. by Jonathan S. Morrell and Mark J. Jackson. New York: Springer, 2013. Chap. 7, pp. 189–206.

[3] T. C. Totemeier. "Characterization of uranium corrosion products involved in a uranium hydride pyrophoric event". In: *Journal of Nuclear Materials* 278.2 (2000), pp. 301 –311.

[4] F. Le Guyadec et al. "Pyrophoric behaviour of uranium hydride and uranium powders". In: *Journal of Nuclear Materials* 396.2-3 (2010), pp. 294–302.

[5] J. Glascott. "A model for the initiation of reaction sites during the uranium-hydrogen reaction assuming enhanced hydrogen transport through thin areas of surface oxide". In: *Philosophical Magazine* 94.3 (2014), pp. 221–241.

[6] D.F. Teter, R.J. Hanrahan, and C.J. Wetteland. *Uranium Hydride Nucleation Kinetics: Effects of Oxide Thickness and Vacuum Outgassing*. Tech. rep. Los Alamos National Laboratory, New Mexico, 2001.

[7] Robert M. Harker. "The influence of oxide thickness on the early stages of the massive uranium-hydrogen reaction". In: *Journal of Alloys and Compounds* 426.1-2 (2006), pp. 106–117.

[8] A. Banos, N. J. Harker, and T. B. Scott. "A review of uranium corrosion by hydrogen and the formation of uranium hydride". In: *Corrosion Science* 136 (2018), pp. 129–147.

[9] R. Arkush et al. "Site related nucleation and growth of hydrides on uranium surfaces". In: *Journal of Alloys and Compounds* 244.1-2 (1996), pp. 197–205.

[10] J. Bloch and M.H. Mintz. “Kinetics and mechanisms of metal hydrides formation - a review”. In: *Journal of Alloys and Compounds* 253-254 (1997), pp. 529–541.

[11] G. C. Allen and P. M. Tucker. “Surface oxidation of uranium metal as studied by X-ray photoelectron spectroscopy”. In: *J. Chem. Soc., Dalton Trans.* (5 1973), pp. 470–474.

[12] G.C. Allen and J.C.H. Stevens. “The Behaviour of Uranium Metal in Hydrogen Atmospheres”. In: 84.1 (1988), pp. 165–174.

[13] S. G. Bazley, J. R. Petherbridge, and J. Glascott. “The influence of hydrogen pressure and reaction temperature on the initiation of uranium hydride sites”. In: *Solid State Ionics* 211 (2012), pp. 1–4.

[14] L.W. Owen and R.A. Scudamore. “A microscope study of the initiation of the hydrogen-uranium reaction”. In: *Corrosion Science* 6.11 (1966), pp. 461–468.

[15] J. Bloch et al. “The initial kinetics of uranium hydride formation studied by a hot-stage microscope technique”. In: *Journal of The Less-Common Metals* 103.1 (1984), pp. 163–171.

[16] J. Bloch and M.H. Mintz. “Kinetics and mechanism of the U-H reaction”. In: *Journal of The Less-Common Metals* 81.2 (1981), pp. 301–320.

[17] J.B. Condon. “Calculated Vs. Experimental Hydrogen Reaction Rates With Uranium”. In: *Journal of Physical Chemistry* 79.4 (1975), pp. 392–397.

[18] A. Banos, C. A. Stitt, and T. B. Scott. “The effect of sample preparation on uranium hydriding”. In: *Corrosion Science* 113 (2016), pp. 91 –103.

[19] J. Glascott and I.M. Findlay. “The oxidation of uranium hydride during its instantaneous or gradual exposure to oxygen”. In: *Journal of Alloys and Compounds* 649 (2015), pp. 426–439.

[20] N. Patel et al. “Influence of Uranium Hydride Oxidation of Uranium Metal Behaviour”. In: *Conference Paper: Global* (2013).

[21] J.M. Haschke, T.H. Allen, and L.A. Morales. “Reactions of plutonium dioxide with water and hydrogen-oxygen mixtures: Mechanisms for corrosion of uranium and plutonium”. In: *Journal of Alloys and Compounds* 314.1 (2001), pp. 78 –91.

[22] M.H. Mintz and Y. Zeiri. “Hydriding kinetics of powders”. In: *Journal of Alloys and Compounds* 216.2 (1995), pp. 159 –175.

[23] F.W. Young, J.V. Cathcart, and A.T. Gwathmey. “The rates of oxidation of several faces of a single crystal as determined with elliptically polarized light”. In: *Acta Metallurgica* 4 (1956), pp. 145–152.

[24] J V Cathcart, G F Petersen, and C J Sparks. “The Structure of Thin Oxide Films Formed on Nickel Crystals The Structure of Thin Oxide Films Formed on Nickel Crystals”. In: *Journal of the Electrochemical Society* 116.5 (1969), pp. 664–668.

[25] D Moreno et al. “Physical discontinuities in the surface microstructure of uranium alloys as preferred sites for hydrogen attack”. In: 230 (1996), pp. 181–186.

[26] T. L. Martin et al. “Atomic-scale Studies of Uranium Oxidation and Corrosion by Water Vapour”. In: *Scientific Reports* 6.25618 (2016).

[27] O. Appel et al. “The influence of external stress/strain on the uranium-hydrogen reaction”. In: *Journal of Nuclear Materials* 510 (2018), pp. 123–130.

[28] R. E. Rundle. “The Structure of Uranium Hydride and Deuteride”. In: *Journal of the American Chemical Society* 69.7 (1947), pp. 1719–1723.

[29] J. Bloch and M.H. Mintz. “Types of hydride phase development in bulk uranium and holmium”. In: *Journal of Nuclear Materials* 110 (1982), pp. 251–255.

[30] C.D. Cann and E.E. Sexton. “An electron optical study of hydride precipitation and growth at crack tips in zirconium”. In: *Acta Metallurgica* 28.9 (1980), pp. 1215–1221.

[31] M.P. Puls. “Elastic and plastic accommodation effects on metal-hydride solubility”. In: *Acta Metallurgica* 32.8 (1984), pp. 1259–1269.

[32] J. Lufrano, P. Sofronis, and H. K. Birnbaum. “Modelling of hydrogen transport and elastically accommodated hydride formation near a crack tip”. In: *Journal of the Mechanics and Physics of Solids* 44.2 (1996), pp. 179–205.

[33] M.P. Puls. “The effects of misfit and external stresses on terminal solid solubility in hydride-forming metals”. In: *Acta Metallurgica* 29.12 (1981), pp. 1961–1968.

[34] A.G. Varias. “Mathematical Model for Hydrogen Diffusion, Energy Flow and Hydride Formation in Zirconium under Stress”. In: *Solid Mechanics Research Office Report BR-04-10-98* (1998).

[35] J. Bair, M. Asle Zaeem, and M. Tonks. “A review on hydride precipitation in zirconium alloys”. In: *Journal of Nuclear Materials* 466 (2015), pp. 12–20.

[36] Y.S Kim, S.J. Kim, and K.S. Im. “Delayed hydride cracking in Zr-2.5Nb tube with the cooling rate and the notch tip shape”. In: *Journal of Nuclear Materials* 335.3 (2004), pp. 387–396.

[37] R. Dutton and M.P. Puls. *Effect of Hydrogen on Behavior of Materials*. New York: TMS-AIME, 1976, pp. 512–525.

[38] G. A. McRae, C. E. Coleman, and B. W. Leitch. “The first step for delayed hydride cracking in zirconium alloys”. In: *Journal of Nuclear Materials* 396.1 (2010), pp. 130–143.

[39] K. Une and S. Ishimoto. “Terminal Solid Solubility of Hydrogen in Unalloyed Zirconium by Differential Scanning Calorimetry”. In: *Journal of Nuclear Science and Technology* 41.9 (2004), pp. 949–952.

[40] A. McMinn, E.C. Darby, and J.S. Schofield. “The Terminal Solid Solubility of Hydrogen in Zirconium Alloys”. In: *Zirconium in the Nuclear Industry: Twelfth International Symposium* (2000).

[41] J.P. Giroldi, P. Vizcano, and A.D. Banchik. “Terminal solid solubility of hydrogen in titanium”. In: *AATN 2003: 30th Annual meeting of the Argentine Association of Nuclear Technology* (2003).

[42] M.J. Mallett and M.W. Trzeciak. “Hydrogen-Uranium Relationships”. In: *Transactions of the American Society of Metals* 50 (1958), pp. 981–993.

[43] A.G. Varias and A.R. Massih. “Hydride-induced embrittlement and fracture in metals - effect of stress and temperature distribution”. In: *Journal of the Mechanics and Physics of Solids* 50 (2002), pp. 1469–1510.

[44] M. Quecedo and C. Muños-Reja. “A Model for the Thermally Assisted Diffusion of Hydrogen in Zirconium Alloys and its FEM Solution”. In: *ENUSA Industrias Avanzadas Report* (2015).

[45] M. A. Hill et al. “Filiform-mode hydride corrosion of uranium surfaces”. In: *Journal of Nuclear Materials* 442.1-3 (2013), pp. 106–115.

[46] J.A. Tanski, R.J. Hanrahan, and M.E. Hawley. “A Model for the Initiation and Growth of Metal Hydride Corrosion”. In: *Sandia National Laboratory Report* 836 (2000).

[47] J. R. Kirkpatrick and J. B. Condon. “The linear solution for hydriding of uranium”. In: *Journal of The Less-Common Metals* 172-174 (1991), pp. 124–135.

[48] N.P. Galkin et al. In: *Mosk. Khim-Tekhnol Inst.* 43.67 (1963).

[49] R. Speiser. “The Thermodynamics of Metal Hydrogen Systems”. In: *Metal Hydrides*. Ed. by William M. Mueller, James P. Blackledge, and George G. Libowitz. New York: Academic Press, 1968. Chap. 3, pp. 51 –89.

[50] P.G. Shewmon. *Diffusion in Solids*. New York: McGraw-Hill Book Company, 1963.

[51] M Martin et al. “Absorption and desorption kinetics of hydrogen storage alloys”. In: *Journal of Alloys and Compounds* 238 (1996), pp. 193–201.

[52] A.G. Varias. “On the Diffusion in Solids under Finite Deformation”. In: *The Open Mechanics Journal* 1 (2007), pp. 26–28.

[53] N. Eliaz and L. Banks-Sills. “Chemical Potential, Diffusion and Stress - Common Confusions in Nonmenclature and Units”. In: *Corrosion Reviews* 26.2-3 (2008), pp. 87–103.

[54] F.M. Raoult. “General law of vapour pressures of solvents”. In: *Comptes Rendus* 104 (1887), pp. 1430–1433.

[55] J.C.M. Li, R.A. Orani, and L.S. Darken. “The Thermodynamics of Stressed Solids”. In: *Zeitschrift für Physikalische Chemie* 49 (1966), pp. 271–290.

[56] A.G. Varias. “On the Coupling of Mass Diffusion and Non-Mechanical Energy Flow in Metals under Finite Deformation”. In: *The Open Mechanics Journal* 2 (2008), pp. 57–61.

[57] S. Prussin. “Generation and distribution of dislocations by solute diffusion”. In: *Journal of Applied Physics* 32.10 (1961), pp. 1876–1881.

[58] F. Yang. “Interaction between diffusion and chemical stresses”. In: *Materials Science and Engineering A* 409.1-2 (2005), pp. 153–159.

[59] H. Peisl. “Lattice strains due to hydrogen in metals”. In: *Hydrogen in Metals I. Basic Properties*. Ed. by G. Alefield and J. Volkl. New York: Springer, 1978, pp. 53–74.

[60] B.A. Boley and J.H. Weiner. *Theory of Thermal Stresses*. New York: John Wiley & Sons, 1960.

[61] L. O. Jernkvist and A R Massih. “Multi-field modelling of hydride forming metals Part I: Model Formulation and Validation”. In: *Computational Materials Science* 85 (2014), pp. 383–401.

[62] A. Sieverts. “The Absorption of Gases by Metals”. In: *Zeitschrift für Metallkunde* 21 (1929), pp. 37–46.

[63] G.L. Powell. “The Uranium-Hydrogen Binary System”. In: *Uranium Processing and Properties*. Ed. by J. S. Morrell and M.J. Jackson. New York: Springer, 2013. Chap. 6, pp. 1–34.

[64] G. L. Powell. “Solubility of hydrogen and deuterium in body-centered-cubic uranium alloys”. In: *Journal of Physical Chemistry* 83.5 (1979), pp. 605–613.

[65] N. R. Gubel et al. “Introduction to Uranium”. In: *Uranium Processing and Properties*. Ed. by J. S. Morrell and M.J. Jackson. New York: Springer, 2013. Chap. 1, pp. 1–34.

[66] A.Chohollo. “A literature review and statistical investigation of early hydride nucleation sites on depleted uranium”. PhD thesis. University of Manchester, 2011.

[67] M.A. Biot. “Thermoelasticity and Irreversible Thermodynamics”. In: *Journal of Applied Physics* 27.3 (1956), pp. 240–253.

[68] M.H. Sadd. “Strain Energy and Related Principles”. In: *Elasticity: Theory, Applications, and Numerics*. Elsevier Science & Technology, 2009. Chap. 6, pp. 113 –133.

[69] oomph-lib. *Main Page*. oomph-lib.maths.man.ac.uk/doc/html/index.html. Online; accessed 22 May 2018. 2017.

[70] I M Sobol. “Sensitivity analysis for nonlinear mathematical models”. In: *Mathematical Modelling Computational Experiments* 1.4 (1993), pp. 407–414.

[71] I. M. Sobol. “Global sensitivity indices for nonlinear mathematical models and their Monte Carlo estimates”. In: *Mathematics and Computers in Simulation* 55 (2001), pp. 271–280.

[72] A. Saltelli et al. “Variance-based Methods”. In: *Global Sensitivity Analysis: The Primer*. Chichester, England: John Wiley & Sons, 2008. Chap. 4, pp. 155 –182.

[73] Andrea Saltelli et al. “Variance based sensitivity analysis of model output. Design and estimator for the total sensitivity index”. In: *Computer Physics Communications* 181.2 (2010), pp. 259–270.

[74] A.M. Mood, F.A. Graybill, and D.C. Boes. *Introduction to the Theory of Statistics*. McGraw-Hill, 1974.

[75] Richard P. Dwight, Stijn G.L. Desmedt, and Pejman Shoeibi Omrani. “Sobol Indices for Dimension Adaptivity in Sparse Grids”. In: *Simulation-Driven Modeling and Optimization*. Ed. by Slawomir Koziel, Leifur Leifsson, and Xin-She Yang. Cham, Switzerland: Springer, 2016. Chap. 15, pp. 371–395.

[76] Bruno Sudret. “Global sensitivity analysis using polynomial chaos expansions”. In: *Reliability Engineering and System Safety* 93.7 (2008), pp. 964–979.

[77] Roger G. Ghanem and Pol D. Spanos. *Stochastic Finite Elements: A Spectral Approach*. Berlin, Heidelberg: Springer-Verlag, 1991.

[78] Norbert Wiener. “The Homogeneous Chaos”. In: *American Journal of Mathematics* 60.4 (1938), pp. 897–936.

[79] Dongbin Xiu and George Em Karniadakis. “The Weiner-Askey Polynomial Chaos for Stochastic Differential Equations”. In: *SIAM Journal on Scientific Computing* 24.2 (2002), pp. 619–644.

[80] A. Nataf. “Détermination des Distribution dont les marges sont Données”. In: *Comptes Rendus de l’Academie des Sciences* 225 (1962), pp. 42–43.

[81] Brian M. Adams et al. “Dakota, A Multilevel Parallel Object-Oriented Framework for Design Optimization, Parameter Estimation, Uncertainty Quantification, and Sensitivity Analysis. Version 6.8”. In: *Sandia National Laboratories* (2018).

[82] Brian M. Adams et al. “Dakota, A Multilevel Parallel Object-Oriented Framework for Design Optimization, Parameter Estimation, Uncertainty Quantification, and Sensitivity Analysis: Theory Manual. Version 6.8”. In: *Sandia National Laboratories* (2018).

[83] M Brill, J Bloch, and M H Mintz. “Experimental verification of the formal nucleation and growth rate equations – initial UH3 development on uranium surface”. In: 266 (1998), pp. 180–185.

[84] PeriodicTable.com. *Technical data for Uranium*. periodictable.com/Elements/092/data.html. Online; accessed 25 Jun 2020. 2015.

[85] S. Blaxland. "The involvement of stress in uranium corrosion phenomena". PhD thesis. University of Manchester, 2015.

[86] Yair Greenbaum et al. "The strain energy and shape evolution of hydrides precipitated at free surfaces of metals". In: *Journal of Alloys and Compounds* 452 (Mar. 2008), pp. 325–335.

[87] Yair Greenbaum et al. "Elastic fields generated by a semi-spherical hydride particle on a free surface of a metal and their effect on its growth". In: *Journal of Alloys and Compounds* 509 (Mar. 2011), pp. 4025–4034.

[88] E. S. Fisher. "Temperature dependence of the elastic moduli in alpha uranium single crystals, Part IV (298K to 923K)". In: *Journal of Nuclear Materials* 18.1 (1966), pp. 39–54.

[89] AZOM.com. *Uranium*. www.azom.com/properties.aspx?ArticleID=604. Online; accessed 25 Jun 2020. 2015.

[90] B. M. Abraham and E. Flotow. "The Heats of Formation of Uranium Hydride, Uranium Deuteride and Uranium Tritide at 25". In: *Journal of the American Chemical Society* 77.6 (1955), pp. 1446–1448.

[91] Lars Onsager. "Reciprocal Relations in Irreversible Processes. I." In: *Phys. Rev.* 37 (4 1931), pp. 405–426.

[92] K.G. Denbigh. *Thermodynamics of the Steady State*. London: Methuen, 1951.

[93] E. Hopf. "The partial differential equation $u_t + uu_x = \mu u_{xx}$". In: *Communications on Pure and Applied Mathematics* 3.3 (1950), pp. 201–230.

[94] MATLAB. *version 9.0.0 (R2016a)*. Natick, Massachusetts: The MathWorks Inc., 2016.

[95] Zhiyong Ren et al. "Thermodynamic properties of α-uranium". In: *Journal of Nuclear Materials* 480 (2016), pp. 80–87.

[96] J. B. Condon. "Standard Gibbs energy and standard enthalpy of formation of UH3 from 450 to 750 K". In: *Journal of Chemical Thermodynamics* 12.11 (1980), pp. 1069–1078.

[97] J.H. Gittus. *Uranium - Metallurgy of the Rarer Metals*. 1963.

[98] The engineering toolbox. *Specific Heats for Metals*. engineeringtoolbox.com/specific-heat-metals-d_152.html. Online; accessed 27 Nov 2018. 2018.

[99] IAEA : International Atomic Energy Agency. *Thermophysical Properties of Materials for Nuclear Engineering: A Tutorial and Collection of Data*. Tech. rep. Vienna, 2008.

[100] IAEA : International Atomic Energy Agency. *Thermophysical Properties of Materials for Water Cooled Reactors IAEA-TECDOC 949*. Tech. rep. Vienna, 1997.

[101] B.F. Kammenzind et al. "Hydrogen Pickup and Redistribution in Alpha Annealed Zircaloy-4". In: *Proceedings of Zirconium in the Nuclear Industry: Eleventh International Symposium*. Ed. by G.P. Sabol E.R. Bradley. American Society for Testing and Materials, 1996, 338370.

[102] A. Sawatzky. "The diffusion and solubility of hydrogen in the alpha phase of zircaloy-2". In: *Journal of Nuclear Materials* 2.1 (1960), pp. 62–68.

[103] V.J. Wheeler. "The diffusion and solubility of hydrogen in uranium dioxide single crystals". In: *Journal of Nuclear Materials* 40 (1971), pp. 189–194.

Appendix A

Chemical potential of a stressed solid

The chemical potential of some chemical species in a system is defined as the derivative of internal energy of the system with respect to the change of number of particles of that species. The chemical potential of a dilute solute in an unstressed solid is given by Raoult's law for an ideal solution,

$$\mu = \mu_0 + RT\ln(C) \tag{A.1}$$

where μ_0 is the chemical potential with zero solute concentration [54]. The chemical potential for a stressed solid is found by a thermodynamics argument by Li et al. [55], the details of which are sketched below.

Consider isothermal processes on a two-component system with a mobile component, labelled M, and an immobile component, I. In the system we are considering, M is the diffusing hydrogen and I is the uranium metal. The system is considered to be a unit cube, each face of which is in contact with a body of fluid, F. M is mobile within F, and the walls of the system are penetrable only by M. The setup is shown in Figure A.1, which is taken from the paper by Li et al..

The fluid in contact with the faces of the system whose normal is parallel to the x-direction is under pressure P_x and M has chemical potential μ_M^x in this fluid. The same is true for P_y and μ_M^y, and P_z and μ_M^z in the fluid in contact with the faces of the system whose normal is parallel to the y- and z-directions respectively. Consider two of the fluid blocks connected by a tube filled with the same fluid F as shown in Figure A.1. The ends of the tube are such that M may flow through but F may not. Consider the case where $\mu_M^x \neq \mu_M^y$. A chemical potential gradient exists along the tube, which will cause M to flow down it. However, this process is an isothermal conversion of heat to

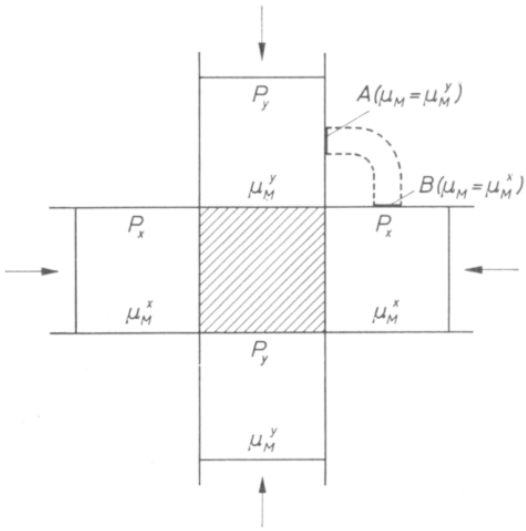

Figure A.1: Diagram of a unit cube of immobile material, I, with pressure exerted on each face by a fluid, F. Image taken from Li et al. 1966 [55]. The striped region in the centre is the block of I, and the four white squares are the blocks of fluid, F. The labels P_x and P_y give the pressure of F in each fluid-filled block (P_z is the pressure of F in contact with the two faces of I whose normal is parallel to the z-direction that cannot be seen in this two-dimensional sketch). The labels μ_M^x and μ_M^y are the chemical potential of the mobile component, M, in that fluid block (again, μ_M^z is the chemical potential of M in the fluid blocks in contact with the two faces of I whose normal is parallel to the z-direction). The dashed line indicates the tube connecting the points A (where $\mu_M = \mu_M^y$) and B (where $\mu_M = \mu_M^x$).

work, which violates the second law of thermodynamics, so we must have $\mu_M^x = \mu_M^y$. By similar arguments, we can say that $\mu_M^x = \mu_M^y = \mu_M^z$.

Next, we consider removing a section of the stressed solid such that the cuts made are always perpendicular to the principal stress axes. The stresses which acted on this section while it was part of the whole may be reapplied by fluid blocks as in the case of the whole above. The thought experiment may then be repeated for this set-up and we find again that the chemical potential is equal in each fluid block. This implies that the chemical potential of the mobile component M is equal throughout the system for any elastically-supported stresses.

To find this uniform quantity, μ_M, we consider reversible, isothermal processes on a closed system. The first law of thermodynamics states that the internal energy of the system is conserved. We have

$$dU = đQ + đW \tag{A.2}$$

where U is the internal energy, $đQ$ is the heat going into the system and $đW$ is work

done on the system. A statement of the second law of thermodynamics for reversible processes is

$$đQ = TdS \tag{A.3}$$

where T is the temperature and S is the entropy. Putting this into the first law statement and integrating along a cycle gives

$$\oint dU = T \oint dS + \oint đW \tag{A.4}$$

for an isothermal process. The system is closed so the first term is zero and the process is reversible so the second term is zero, Thus the work done is also zero. This means that work done on a closed isothermal system is path-independent for reversible processes. This path independence may be exploited to find the chemical potential μ_M.

We look at the transfer of δn_M moles of M from the surface of the stressed solid I into F. This process may be performed in two ways. The first is by moving M whilst I is in the current stressed state.

The work required to add one mole of M to the stressed solid is W_M and to F is W_M^F. This gives the work done on the solid for the first path is

$$W_1 = \delta n_M \left(W_M^F - W_M \right). \tag{A.5}$$

The second path is by relaxing all stresses on the body, transferring one mole of M from I to F, and then reapplying the stresses. To relax the stresses, the work done on the body is $-w$. The work done to transfer M is the sum of the work done for the transfer itself, $(\mu_M - \mu_M^0)\delta n_M$, and the work done in the fluid expansion, $W_M^F \delta n_M$. Then the work done to reapply the stress on I will be $w - \frac{\partial w}{\partial n_M}\delta n_M$. This is the negative of the amount of work done to relieve the stress initially, decremented by an amount proportional to the amount of M lost. The total work done on the solid for the second path is

$$W_2 = (\mu_M - \mu_{M0} - \frac{\partial w}{\partial n_M} + W_M^F)\delta n_M. \tag{A.6}$$

All the processes described are reversible, so the work done is path independent. This means we can equate $W_1 = W_2$ and obtain

$$\mu_M = \mu_{M0} + \frac{\partial w_M}{\partial n_M} - W_M, \tag{A.7}$$

which is our expression for the chemical potential of M stressed solid, I. The first term

on the right hand side is the chemical potential for the unstressed solid. The second term is the partial molal strain energy. The final term is the work done by the applied stresses when a mole of M is added to the body, also called the work of addition.

The chemical potential for the unstressed body is taken from Raoult's law, Equation (A.1), and we have

$$\mu_M = \mu_0 + RT\ln(C) + \frac{\partial w_M}{\partial n_M} - W_M \tag{A.8}$$

Using the 1998 paper by Varias [34] on the hydrogen-zirconium system, we derive expressions for the partial molal strain energy and the work of addition. The applied stress is σ, and the strain is ε, so we have the strain energy for a material particle with volume V is given by

$$w_M = \int_0^{\varepsilon_{mn}} V\sigma_{ij}d\varepsilon^{ij} = \int_0^{\sigma_{mn}} V\sigma_{ij}C^{ijkl}d\sigma_{kl} \tag{A.9}$$

where C is the compliance tensor. Taking the derivative with respect to the number of moles of M, we obtain

$$\begin{aligned}\frac{\partial w_M}{\partial n_M} &= \frac{\partial}{\partial n_M}\left(\int_0^{\sigma_{mn}} V\sigma_{ij}C^{ijkl}d\sigma_{kl}\right) \\ &= \int_0^{\sigma_{mn}}\left(\frac{\partial V}{\partial n_M}C^{ijkl}\sigma_{ij} + \frac{\partial C^{ijkl}}{\partial n_M}V\sigma_{ij}\right)d\sigma_{kl}.\end{aligned} \tag{A.10}$$

If we further make the assumption that the compliance does not depend on the number of moles of hydrogen, we have $\frac{\partial C^{ijkl}}{\partial n_M} = 0$. Now we finally have

$$\frac{\partial w}{\partial n_M} = \frac{1}{2}\bar{V}^H C^{ijkl}\sigma_{ij}\sigma_{kl} \tag{A.11}$$

where $\frac{\partial V}{\partial n_M} = \bar{V}^H$ is the partial molar volume of hydrogen.

Now, also need an expression for the work of addition W_M. This is the work done by σ on the volume V for each mole of hydrogen added [55],

$$W_M = V\sigma_{ij}\frac{\partial \varepsilon^{ij}}{\partial n_M}. \tag{A.12}$$

We assume the metal is isotropic and thus the deformation will be a volumetric expansion. This means the shear strain elements will be zero and $\varepsilon^{ij} = \phi\delta^{ij}$ where ϕ is the normal strain in each direction. Now we look at the ratio of the change in volume of an element $\Delta\Omega$ to its original volume Ω during volumetric expansion. The normal

strain in each direction measures the change in length L of a material line element relative to the original length of the element – $\frac{\Delta L}{L}$. Considering a cube of volume V and side-length L, we have

$$\frac{\Delta\Omega}{\Omega} = \frac{3\,\Delta L}{L} = \varepsilon^{(ii)} \tag{A.13}$$

in each direction, where the superscript (ii) indicates no summation over i. Relating this to our problem, the change in volume per mole of hydrogen addition is $\bar{V}^H$, the original volume is V, and $\frac{\partial\varepsilon^{ij}}{\partial n_M}$ is the strain per mole of hydrogen addition. This gives

$$\frac{\bar{V}^H}{V}\delta^{ij} = 3\frac{\partial\varepsilon^{ij}}{\partial n_M}. \tag{A.14}$$

Substituting the strain per mole of added hydrogen into equation (A.12) gives the work of addition

$$W_M = V\sigma_{ij}\frac{\partial\varepsilon^{ij}}{\partial n_M} = V\sigma_{ij}\frac{\bar{V}^H}{3V}\delta^{ij} = \frac{\sigma_k^k}{3}\bar{V}^H. \tag{A.15}$$

Equations (A.11) and (A.15) are substituted into (A.8) to give

$$\mu_M = \mu_0 + RT\ln(C) + \frac{1}{2}\bar{V}^H C^{ijkl}\sigma_{ij}\sigma_{kl} - \frac{\sigma_k^k}{3}\bar{V}^H. \tag{A.16}$$

Looking at the molal strain energy and work of addition terms, we see that $\frac{\partial w_M}{\partial n_M} \propto E^{-1}\sigma^2$ and $W_M \propto \sigma$ where E is the Young's modulus of the metal. The Young's modulus of uranium is approximately $2\times10^{11}Pa$ [88][84]. The ultimate tensile and compressive strengths of uranium (the largest stress values we could reasonably expect to measure) are on the order of 10^8Pa [89] and therefore $\frac{\partial w_M}{\partial n_M}$ is negligible compared with W_M, so we neglect this term.

The final equation for chemical potential of hydrogen diffusing in a block of stressed uranium is thus

$$\mu_M = \mu_0 + RT\ln(C) - \frac{\sigma_k^k}{3}\bar{V}^H. \tag{A.17}$$

Appendix B

Conservation of energy

To derive the equation we use for the non-mechanical energy in the model, an argument is used which is similar to that of Varias' 2008 paper [56]. We look at the equation of energy per unit mass, Φ, for a deforming solid,

$$\rho \frac{D\Phi}{Dt} = \sigma : \frac{D\varepsilon}{Dt} - \nabla_{\mathbf{X}} \cdot \mathbf{J}^E \tag{B.1}$$

where σ is the Cauchy stress, ε is the strain tensor and the derivatives $\frac{D}{Dt}$ are material derivatives, so for some ϕ, $\frac{D\phi}{Dt} = \frac{\partial \phi}{\partial t} + \mathbf{V} \cdot \nabla_{\mathbf{X}} \phi$, where $\mathbf{V}$ is the Eulerian velocity of a material point and $\nabla_{\mathbf{X}}$ takes the derivative with respect to the Eulerian coordinate system. Every derivative in this section is taken with respect to the Eulerian coordinates, so for brevity, $\nabla = \nabla_{\mathbf{X}}$.The first term on the right-hand-side of equation (B.1) is the mechanical energy (since the derivative of the strain energy = stress power) and the second term is the Eulerian flux of the so-called non-mechanical energy, $\mathbf{J}^E$.

We look at this in the context of a solid material with a gas diffusing through it. In general, the energy depends on the number of molecules of the diffusing substance per unit mass of the system η, the entropy per unit mass of the system S, and the strain tensor ε:

$$\Phi = \Phi(\eta, S, \varepsilon_{ij}). \tag{B.2}$$

Thus we may write the material derivative of Φ as

$$\frac{D\Phi}{Dt} = \frac{D\eta}{Dt} \frac{\partial \Phi}{\partial \eta}\bigg|_{S,\varepsilon_{ij}} + \frac{DS}{Dt} \frac{\partial \Phi}{\partial S}\bigg|_{\eta,\varepsilon_{ij}} + \sum_{i,j} \frac{D\varepsilon_{ij}}{Dt} \frac{\partial \Phi}{\partial \varepsilon_{ij}}\bigg|_{\eta,S} \tag{B.3}$$

and use this to define certain thermodynamic quantities. We say that the state variables ε_{ij} are thermodynamically conjugate to the thermodynamic tensions, the stress σ_{ij}.

This means we write $\frac{\sigma_{ij}}{\rho} = \frac{\partial \Phi}{\partial \varepsilon_{ij}}|_{\eta,S}$, where the factor of $\frac{1}{\rho}$ is because Φ is energy per unit mass. Chemical potential, μ is the change in internal energy due to the addition or removal of diffuser to the system, so we have $\mu = \frac{\partial \Phi}{\partial \eta}|_{S,\varepsilon_{ij}}$. We also use the relation between entropy, energy and temperature, $\frac{\partial \Phi}{\partial S}|_{\eta,\varepsilon_{ij}} = T$. The first term on the right-hand-side governs energy change due to sources or sinks of particles, the second is related to heat and the third results from solid deformations.

Similarly, we look at the entropy per unit mass of the system. As a function of state, S may be uniquely determined as a function of T, η and σ_{ij}

$$S = S(T, \eta, \sigma_{ij}). \tag{B.4}$$

Therefore, we may also write the material derivative of the entropy,

$$\frac{DS}{Dt} = \frac{DT}{Dt}\frac{\partial S}{\partial T}\bigg|_{\eta,\sigma_{ij}} + \frac{D\eta}{Dt}\frac{\partial S}{\partial \eta}\bigg|_{T,\sigma_{ij}} + \sum_{i,j}\frac{D\sigma_{ij}}{Dt}\frac{\partial S}{\partial \sigma_{ij}}\bigg|_{T,\eta}. \tag{B.5}$$

The partial derivative of the entropy per unit mass with respect to temperature,

$$\frac{\partial S}{\partial T}\bigg|_{\eta,\sigma_{ij}} = \frac{c_s}{T} = \frac{c_p}{T} \tag{B.6}$$

where c_s, the specific heat capacity at constant stress, is assumed to be equal to the specific heat at constant pressure, c_p. Since η is the number of molecules of the diffusing substance per unit mass of the solid, we can write that $\eta = \frac{C}{\rho}$, the concentration of the substance divided by the density of the solid, so

$$\frac{D\eta}{Dt} = \frac{1}{\rho}\frac{DC}{Dt} - \frac{C}{\rho^2}\frac{D\rho}{Dt}. \tag{B.7}$$

We use the conservation of mass in density terms,

$$\frac{D\rho}{Dt} = \frac{\partial \rho}{\partial t} + \mathbf{V}\cdot\nabla\rho = -\rho\nabla\cdot\mathbf{V} \tag{B.8}$$

to write this as

$$\frac{D\eta}{Dt} = \frac{1}{\rho}\left(\frac{DC}{Dt} + C\nabla\cdot\mathbf{V}\right). \tag{B.9}$$

Then, we use Fick's law in the Eulerian frame (this is the same as equation (2.7))

$$\frac{\partial C}{\partial t} + \nabla \cdot (C\mathbf{V} + \mathbf{J}) = \frac{DC}{Dt} + C\nabla \cdot \mathbf{V} + \nabla \cdot \mathbf{J} = 0 \tag{B.10}$$

to give that

$$\frac{D\eta}{Dt} = -\frac{1}{\rho}\nabla \cdot \mathbf{J}. \tag{B.11}$$

We also have that the derivative of entropy with respect to η is the heat of transport of the diffusing substance divided by the temperature, $\frac{\partial S}{\partial \eta} = \frac{Q}{\rho T}$ [56], with a factor of $\frac{1}{\rho}$ since the entropy is per unit volume.

Replacing the derivatives $\frac{\partial \Phi}{\partial \varepsilon_{ij}}$, $\frac{\partial \Phi}{\partial \eta}$, $\frac{\partial \Phi}{\partial S}$, $\frac{D\eta}{Dt}$ and $\frac{\partial S}{\partial \eta}$ in equations (B.3) and (B.5), we now have

$$\rho \frac{D\Phi}{Dt} = -\mu \nabla \cdot \mathbf{J} + \rho T \frac{DS}{Dt} + \sigma : \frac{D\varepsilon}{Dt} \tag{B.12}$$

and

$$\rho \frac{DS}{Dt} = \frac{\rho c_p}{T}\frac{DT}{Dt} - \frac{Q}{T}\nabla \cdot \mathbf{J} + \frac{D\sigma}{Dt} : \left.\frac{\partial S}{\partial \sigma}\right|_{T,\eta}. \tag{B.13}$$

σ and ε are a work conjugate pair: $\sigma : \frac{D\varepsilon}{Dt}$ is equal to rate of work per unit undeformed volume of the body.

We now use the 1998 paper by Varias [34] on hydrogen diffusion in Zirconium (a similar problem to the one presented here) to adapt equations (B.12) and (B.13) to the hydriding problem. We assume that the deformation is purely elastic. Elastic deformation is a reversible process, so must generate zero entropy. This means that the final term on the right-hand-side of (B.13) is zero. We also introduce a new term into equation (B.13) which describes change in entropy due to the reaction to form hydride. This reaction, $U + 3H \rightarrow UH_3$ removes one mole of uranium atoms and three moles of hydrogen atoms from the system for every one mole of hydride created. Thus, the rate of change in concentration of each of the three species due to the reaction alone is related by

$$\frac{DC_{Hr}}{Dt} = -\frac{DU}{Dt} = -3\frac{DC}{Dt} \tag{B.14}$$

where C_{Hr} is the hydride concentration and U is the uranium concentration. The material derivative of the entropy due to the reaction alone is therefore

$$\frac{\partial S}{\partial C_{Hr}}\frac{DC_{Hr}}{Dt} + \frac{\partial S}{\partial U}\frac{DU}{Dt} + \frac{\partial S}{\partial C}\frac{DC}{Dt} = \left(\frac{\partial S}{\partial C_{Hr}} - \frac{\partial S}{\partial U} - 3\frac{\partial S}{\partial C}\right)\frac{DC_{Hr}}{Dt}. \tag{B.15}$$

In general, the entropy is not measured in chemical reactions, but rather the enthalpy, H. The entropy change associated with a given reaction is calculated from the change in enthalpy divided by the temperature. For the uranium hydriding reaction, we have the molar enthalpy of formation of UH_3, $\Delta\bar{H}$ as measured by Abraham and Flotow [90]. To convert this to entropy change per unit volume, we divide by ρT. Thus the term in brackets, describing the change in entropy due to the formation of one mole of UH_3 is replaced by $\frac{\Delta\bar{H}}{\rho T}$. We also use that by definition, the volume fraction of hydride, f, is equal to the hydride concentration multiplied by the partial molar volume of hydride, $f = \bar{V}_{Hr}C_{Hr}$, so that $\frac{DC_{Hr}}{Dt} = \frac{1}{\bar{V}_{Hr}}\frac{Df}{Dt}$. This means that equation (B.13) for the hydriding problem is

$$\rho\frac{DS}{Dt} = \frac{c_p}{T}\frac{DT}{Dt} - \frac{Q}{T}\nabla\cdot\mathbf{J} + \frac{\Delta\bar{H}}{\bar{V}_{Hr}T}\frac{Df}{Dt} \tag{B.16}$$

To replace the $\frac{DS}{Dt}$ term, we begin by equating (B.1) and (B.12) , which are both equations for $\rho\frac{D\Phi}{Dt}$. We rearrange for $\rho\frac{DS}{Dt}$, to give

$$\begin{aligned}\rho\frac{DS}{Dt} =& \frac{\mu}{T}\nabla\cdot\mathbf{J} - \frac{1}{T}\nabla\cdot\mathbf{J}^E \\ =& -\nabla\cdot\left(\frac{\mathbf{J}^E}{T} - \frac{\mu}{T}\mathbf{J}\right) - \frac{\mathbf{J}^E}{T^2}\nabla T - \mathbf{J}\cdot\nabla\left(\frac{\mu}{T}\right) \\ =& -\nabla\cdot\left(\frac{\mathbf{J}^E}{T} - \frac{\mu}{T}\mathbf{J}\right) - \frac{1}{T}\left(\frac{\mathbf{J}^E}{T}\nabla T + T\mathbf{J}\cdot\nabla\left(\frac{\mu}{T}\right)\right)\end{aligned} \tag{B.17}$$

The next part of the derivation is concerned with calculating the fluxes of energy $\mathbf{J}^E$ and diffusing substance $\mathbf{J}$. We label the two terms on the right-hand-side of (B.17), and it becomes

$$\rho\frac{DS}{Dt} = -\nabla\cdot\mathbf{S} + \Psi, \tag{B.18}$$

where

$$\Psi = -\frac{1}{T}\left(\frac{\mathbf{J}^E}{T}\nabla T + T\mathbf{J}\cdot\nabla\left(\frac{\mu}{T}\right)\right) \tag{B.19}$$

and

$$\mathbf{S} = \frac{\mathbf{J}^E - \mu^M\mathbf{J}}{T}. \tag{B.20}$$

Now. by integrating over the material volume Ω and using the divergence theorem, we obtain

$$\frac{d}{dt}\int_\Omega \rho S dV = \int_\Omega \Psi dV - \int_{\partial\Omega}\mathbf{S}\cdot\mathbf{n}dA. \tag{B.21}$$

This states that the rate of change of entropy within a volume Ω is equal to the difference between rate of entropy generated within the volume and the rate at which it

flows out of the volume across its surface $\partial\Omega$.

Finally, we must replace the flux of non-mechanical energy, $\mathbf{J}^E$. To this end, we employ the Onsager reciprocity relation from thermodynamics [91]. The laws of Fourier and Fick relate the heat and mass fluxes to their so-called thermodynamic forces, temperature gradient and chemical potential, respectively. When both gradients are present in a system, the two processes are coupled. This coupling is accounted for by assuming that both fluxes $\mathbf{J}$ and $\mathbf{J}^E$ depend linearly on the two vector thermodynamic forces, Δ^E which drives non-mechanical energy flow, and Δ^M which drives mass flow.

We write the equations to describe this as

$$\begin{aligned} \mathbf{J}^E &= L^E\Delta^E + L^{EM}\Delta^M \\ \mathbf{J} &= L^{ME}\Delta^E + L^M\Delta^M \end{aligned} \tag{B.22}$$

where L^E, L^M, L^{EM} and $L^{ME}$are coefficients. The Onsager reciprocity relation states that the coefficients L^{EM} and L^{ME} are equal [34, 91].

Now, the two thermodynamic forces and three coefficients must be found. We have a relation due to Denbigh [92] relating mass and non-mechanical energy flux with the rate of generation of internal entropy per unit volume arising from mass and heat flow,

$$\Psi = \frac{1}{T}\left(\mathbf{J}^E\cdot\Delta^E + \mathbf{J}^M\cdot\Delta^M\right). \tag{B.23}$$

This is the same quantity as the Ψ defined in (B.19) to be the specific rate of generation of internal entropy, so we equate the two and obtain

$$-\frac{\mathbf{J}^E}{T}\cdot\nabla T - T\mathbf{J}\cdot\nabla\left(\frac{\mu}{T}\right) = \mathbf{J}\cdot\Delta^E + \mathbf{J}\cdot\Delta^M \tag{B.24}$$

From this, we have equations for the thermodynamic forces

$$\Delta^E = -\frac{1}{T}\nabla T \qquad \Delta^M = -T\nabla\left(\frac{\mu}{T}\right), \tag{B.25}$$

so our fluxes become

$$\begin{aligned} \mathbf{J}^E &= -\frac{L^E}{T}\nabla T - TL^{EM}\nabla\left(\frac{\mu}{T}\right) \\ \mathbf{J} &= -\frac{L^{ME}}{T}\nabla T - TL^M\nabla\left(\frac{\mu}{T}\right) \end{aligned} \tag{B.26}$$

To be able to have a full equation for the non-mechanical energy flux, we also need the

coefficients L^M, L^E and $L^{EM} = L^{ME}$.

Firstly, we consider the equation (2.21) derived in chapter 2 for the flux of diffusing substance, which is given again here,

$$\mathbf{J} = -\frac{D_U C}{RT}\left(\nabla\mu + \frac{Q}{T}\nabla T\right). \tag{B.27}$$

We equate this with our definition of $\mathbf{J}$ in terms of the thermodynamic forces,

$$-\frac{D_U C}{RT}\left(\nabla\mu + \frac{Q}{T}\nabla T\right) = -\frac{L^{ME}}{T}\nabla T - L^M T\nabla\left(\frac{\mu}{T}\right). \tag{B.28}$$

Expanding the gradient of $\frac{\mu}{T}$ and equating coefficients in $\nabla\mu$ and ∇T gives the coefficients

$$L^M = \frac{D_U C}{RT} \qquad \text{and} \qquad L^{ME} = L^{EM} = \frac{D_U C(\mu+Q)}{RT}. \tag{B.29}$$

Now, to obtain the final coefficient L^E, we consider a situation in the absence of mass flux. We have $\mathbf{J} = \mathbf{0}$, so from the definition of mass flux (B.27),

$$\nabla\mu = -\frac{Q}{T}\nabla T. \tag{B.30}$$

Using this relation to replace $\nabla\mu$ in the expansion of $\nabla\left(\frac{\mu}{T}\right)$, we may write

$$\nabla\left(\frac{\mu}{T}\right) = \frac{Q+\mu}{T^2}\nabla T. \tag{B.31}$$

Fourier's Law for the flux of thermal energy, $\mathbf{J}^E = -\kappa\nabla T$, where κ is the thermal conductivity, holds in the absence of mass flux. We use this to replace $\mathbf{J}^E$ and (B.31) to replace $\nabla\left(\frac{\mu}{T}\right)$ and rearrange to finally obtain

$$L^E = \kappa T + \frac{D_U C(\mu+Q)^2}{RT}, \tag{B.32}$$

the final coefficient to be calculated. We have the Eulerian flux of non-mechanical energy is

$$\begin{aligned}\mathbf{J}^E =& -\left(\kappa + \frac{D_U C(\mu+Q)^2}{RT^2}\right)\nabla T - \frac{DC(\mu+Q)}{R}\nabla\left(\frac{\mu}{T}\right)\\ =&(\mu+Q)\mathbf{J} - \kappa\nabla T\end{aligned} \tag{B.33}$$

This flux is now substituted into the first line of equation (B.17), which gives

$$\rho T \frac{DS}{Dt} = \nabla \cdot (\kappa \nabla T) - Q \nabla \cdot \mathbf{J} - \mathbf{J} \cdot \nabla \mu. \tag{B.34}$$

Finally, we substitute this into equation (B.16) to give

$$\rho c_p \frac{DT}{Dt} + \frac{\Delta \bar{H}}{\bar{V}_{Hr}} \frac{Df}{Dt} = \nabla_{\mathbf{X}} \cdot (\kappa \nabla_{\mathbf{X}} T) - \mathbf{J} \cdot \nabla_{\mathbf{X}} \mu \tag{B.35}$$

where we also return to the explicit derivatives with respect to the Eulerian coordinates.

Appendix C

Weak form in cylindrical co-ordinates

In this chapter, we present a derivation of the weak form equations for thermoelasticity in a cylindrical domain. The implementation is described so that it can be implemented in an axisymmetric model of uranium hydriding. Modelling on axisymmetric cylindrical domains provides a way to look at solutions for a quasi-three-dimensional system, without the computational complexity of a true three-dimensional domain.

In deriving the weak form equations for one- and two-dimensional Cartesian domains in section 3.3, the divergence theorem was employed to transfer a spatial derivative from all second-spatial-derivative and F-type terms, and the boundary terms are obtained as a result. We present a neat way to transfer the spatial derivative in general orthogonal co-ordinate systems.

We define a domain Ω, the cylinder which occupies the region $r \in [0, \tilde{R}]$, $\theta \in [0, 2\pi)$, $Z \in [a, b]$, and $\partial\Omega$ is the cylinder boundary. The coordinate system (r,θ,Z) is shown in Figure C.1.

The weak form is found for the equations of linear thermoelasticity, to show the method. The weak form of the other equations can be found similarly. The equations for linear thermoelasticity, derived in Chapter 2 are given here for reference:

$$\begin{aligned} \varepsilon_{ij} = \left(\frac{1+\nu}{E}\right)\sigma_{ij} - \frac{\nu}{E}\sigma_{kk} + \alpha\Delta T\,\delta_{ij} = 0 \\ \nabla\cdot\sigma = 0 \end{aligned} \tag{C.1}$$

In a general co-ordinate system, the strain tensor is defined by

$$\varepsilon = \frac{1}{2}\left((\nabla\otimes\mathbf{u}) + (\nabla\otimes\mathbf{u})^{\mathsf{T}}\right) \tag{C.2}$$

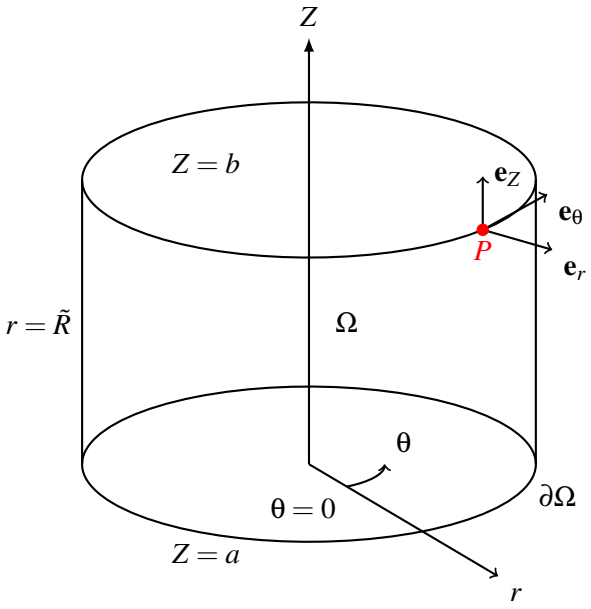

Figure C.1: Cylindrical coordinate system.

where $\otimes$ is the tensor product, defined by $(\mathbf{a}\otimes\mathbf{b})_{ij} = (\mathbf{e}_j\cdot\mathbf{a})(\mathbf{e}_i\cdot\mathbf{b})$. Taking the tensor product $\boldsymbol{\nabla}\otimes\mathbf{u}$ in cylindrical coordinates, we obtain

$$\boldsymbol{\nabla}\otimes\mathbf{u} = \left(\mathbf{e}_r\frac{\partial}{\partial r} + \mathbf{e}_\theta\frac{1}{r}\frac{\partial}{\partial\theta} + \mathbf{e}_Z\frac{\partial}{\partial Z}\right)\otimes\left(u_r\mathbf{e}_r + u_\theta\mathbf{e}_\theta + u_Z\mathbf{e}_Z\right). \tag{C.3}$$

This results in the strain tensor

$$\begin{aligned}\varepsilon &= \frac{1}{2}\left((\boldsymbol{\nabla}\otimes\mathbf{u}) + (\boldsymbol{\nabla}\otimes\mathbf{u})^\intercal\right)\\ &= \frac{1}{2}\begin{pmatrix} 2\frac{\partial u_r}{\partial r} & \frac{1}{r}\frac{\partial u_r}{\partial\theta} - \frac{u_\theta}{r} + \frac{\partial u_\theta}{\partial r} & \frac{\partial u_Z}{\partial r} + \frac{\partial u_r}{\partial Z}\\ \frac{1}{r}\frac{\partial u_r}{\partial\theta} - \frac{u_\theta}{r} + \frac{\partial u_\theta}{\partial r} & 2\left(\frac{u_r}{r} + \frac{1}{r}\frac{\partial u_\theta}{\partial\theta}\right) & \frac{1}{r}\frac{\partial u_Z}{\partial\theta} + \frac{\partial u_\theta}{\partial Z}\\ \frac{\partial u_Z}{\partial r} + \frac{\partial u_r}{\partial Z} & \frac{1}{r}\frac{\partial u_Z}{\partial\theta} + \frac{\partial u_\theta}{\partial Z} & 2\frac{\partial u_Z}{\partial Z}\end{pmatrix}.\end{aligned} \tag{C.4}$$

Then the three components of the linear thermoelastic constitutive relation that correspond to the diagonal elements of the strain tensor are

$$\begin{aligned}\frac{\partial u_r}{\partial r} &= \frac{1}{E}\sigma_{rr} - \frac{\nu}{E}(\sigma_{\theta\theta}+\sigma_{ZZ}) + \alpha\Delta T\\ \frac{u_r}{r} + \frac{1}{r}\frac{\partial u_\theta}{\partial\theta} &= \frac{1}{E}\sigma_{\theta\theta} - \frac{\nu}{E}(\sigma_{rr}+\sigma_{ZZ}) + \alpha\Delta T\\ \frac{\partial u_Z}{\partial Z} &= \frac{1}{E}\sigma_{ZZ} - \frac{\nu}{E}(\sigma_{rr}+\sigma_{\theta\theta}) + \alpha\Delta T,\end{aligned} \tag{C.5}$$

and the three distinct components corresponding to the off-diagonal elements of the strain tensor are

$$\begin{aligned}\frac{1}{2}\left(\frac{1}{r}\frac{\partial u_r}{\partial \theta}-\frac{u_\theta}{r}+\frac{\partial u_\theta}{\partial r}\right)&=\frac{1+\nu}{E}\sigma_{r\theta}\\ \frac{1}{2}\left(\frac{\partial u_Z}{\partial r}+\frac{\partial u_r}{\partial Z}\right)&=\frac{1+\nu}{E}\sigma_{rZ}\\ \frac{1}{2}\left(\frac{1}{r}\frac{\partial u_Z}{\partial \theta}+\frac{\partial u_\theta}{\partial Z}\right)&=\frac{1+\nu}{E}\sigma_{\theta Z}.\end{aligned} \tag{C.6}$$

There are no second spatial derivatives in the constitutive relation. With reference to the weak form of reaction diffusion equations, equation (3.7), this means all terms in the constitutive relation are of the R term type. Therefore to obtain the weak form of these equations, we do not require the spatial derivative of the shape functions. However, this is not the case for Cauchy's momentum equation. In the weak form of Cauchy's momentum equation, the stress is a type F term. In the two-dimensional Cartesian weak form, given in the first two of equations (6.14), we see that by having stress as an F type term, we obtain the traction boundary terms.

To calculate the weak form of Cauchy's momentum equation, we define three vector test functions, which are equivalent to the value of the scalar test function $\psi(\mathbf{x})=\psi(r,\theta,Z)$ in the direction of each of the three unit vectors

$$\begin{aligned}\boldsymbol{\Psi}_1(r,\theta,Z)&=\psi(r,\theta,Z)\mathbf{e}_r,\\ \boldsymbol{\Psi}_2(r,\theta,Z)&=\psi(r,\theta,Z)\mathbf{e}_\theta \quad \text{and}\\ \boldsymbol{\Psi}_3(r,\theta,Z)&=\psi(r,\theta,Z)\mathbf{e}_Z.\end{aligned} \tag{C.7}$$

We write the integral form of the momentum equations as the three equations, for $i=1,2,3$,

$$\begin{aligned}\int_\Omega(\boldsymbol{\nabla}\cdot\boldsymbol{\sigma})\cdot\boldsymbol{\Psi}_i(r,\theta,Z)dV&=\int_{\partial\Omega}(\boldsymbol{\sigma}\cdot\boldsymbol{\Psi}_i)\cdot\mathbf{n}dS-\int_\Omega\boldsymbol{\sigma}\colon(\boldsymbol{\nabla}\otimes\boldsymbol{\Psi}_i)\,dV\\ &=\int_{Z=a}^{b}\int_{\theta=0}^{2\pi}(\boldsymbol{\sigma}\cdot\boldsymbol{\Psi}_i)\cdot\mathbf{e}_r\Big|_{r=\tilde{R}}\tilde{R}d\theta dZ+\int_{\theta=0}^{2\pi}\int_{r=0}^{\tilde{R}}(\boldsymbol{\sigma}\cdot\boldsymbol{\Psi}_i)\cdot\mathbf{e}_Z\Big|_{Z=b}rdrd\theta\\ &\quad-\int_{\theta=0}^{2\pi}\int_{r=0}^{\tilde{R}}(\boldsymbol{\sigma}\cdot\boldsymbol{\Psi}_i)\cdot\mathbf{e}_Z\Big|_{Z=a}rdrd\theta-\int_{Z=a}^{b}\int_{\theta=0}^{2\pi}\int_{r=0}^{\tilde{R}}\boldsymbol{\sigma}\colon(\boldsymbol{\nabla}\otimes\boldsymbol{\Psi}_i)\,rdrd\theta dZ\\ &=0\end{aligned} \tag{C.8}$$

where the divergence theorem has been used to transfer the spatial derivative onto $\boldsymbol{\Psi}$. Now, we must evaluate $\boldsymbol{\sigma}\colon \boldsymbol{\nabla} \otimes \boldsymbol{\Psi}_i$ and $\boldsymbol{\sigma} \cdot \boldsymbol{\Psi}_i$ for $i = 1,2,3$. We have

$$\boldsymbol{\nabla} \otimes \boldsymbol{\Psi}_i = \left(\mathbf{e}_r \frac{\partial}{\partial r} + \mathbf{e}_\theta \frac{1}{r} \frac{\partial}{\partial \theta} + \mathbf{e}_Z \frac{\partial}{\partial Z} \right) \otimes \left((\Psi_i)_r \mathbf{e}_r + (\Psi_i)_\theta \mathbf{e}_\theta + (\Psi_i)_Z \mathbf{e}_Z \right) \tag{C.9}$$

which, for each vector test function, is

$$\begin{aligned} \boldsymbol{\nabla} \otimes \boldsymbol{\Psi}_1 = \begin{pmatrix} \frac{\partial \psi}{\partial r} & \frac{1}{r}\frac{\partial \psi}{\partial \theta} & \frac{\partial \psi}{\partial Z} \\ 0 & \frac{\psi}{r} & 0 \\ 0 & 0 & 0 \end{pmatrix}, \boldsymbol{\nabla} \otimes \boldsymbol{\Psi}_2 = \begin{pmatrix} 0 & -\frac{\psi}{r} & 0 \\ \frac{\partial \psi}{\partial r} & \frac{1}{r}\frac{\partial \psi}{\partial \theta} & \frac{\partial \psi}{\partial Z} \\ 0 & 0 & 0 \end{pmatrix}, \\ \boldsymbol{\nabla} \otimes \boldsymbol{\Psi}_3 = \begin{pmatrix} 0 & 0 & 0 \\ 0 & 0 & 0 \\ \frac{\partial \psi}{\partial r} & \frac{1}{r}\frac{\partial \psi}{\partial \theta} & \frac{\partial \psi}{\partial Z} \end{pmatrix}. \end{aligned} \tag{C.10}$$

We take the contraction of the stress tensor with each of these to give

$$\begin{aligned} \boldsymbol{\sigma}\colon (\boldsymbol{\nabla} \otimes \boldsymbol{\Psi}_1) &= \frac{\partial \psi}{\partial r}\sigma_{rr} + \frac{1}{r}\frac{\partial \psi}{\partial \theta}\sigma_{r\theta} + \frac{\partial \psi}{\partial Z}\sigma_{ZZ} + \frac{\psi}{r}\sigma_{\theta\theta}, \\ \boldsymbol{\sigma}\colon (\boldsymbol{\nabla} \otimes \boldsymbol{\Psi}_2) &= -\frac{\psi}{r}\sigma_{r\theta} + \frac{\partial \psi}{\partial r}\sigma_{\theta r} + \frac{1}{r}\frac{\partial \psi}{\partial \theta}\sigma_{\theta\theta} + \frac{\partial \psi}{\partial Z}\sigma_{\theta Z} \quad \text{and} \\ \boldsymbol{\sigma}\colon (\boldsymbol{\nabla} \otimes \boldsymbol{\Psi}_3) &= \frac{\partial \psi}{\partial r}\sigma_{Zr} + \frac{1}{r}\frac{\partial \psi}{\partial \theta}\sigma_{Z\theta} + \frac{\partial \psi}{\partial Z}\sigma_{ZZ}. \end{aligned} \tag{C.11}$$

For the boundary terms,

$$\begin{aligned} \boldsymbol{\sigma} \cdot \boldsymbol{\Psi}_1 &= \psi(\sigma_{rr}\mathbf{e}_r + \sigma_{r\theta}\mathbf{e}_\theta + \sigma_{rZ}\mathbf{e}_z), \\ \boldsymbol{\sigma} \cdot \boldsymbol{\Psi}_2 &= \psi(\sigma_{\theta r}\mathbf{e}_r + \sigma_{\theta\theta}\mathbf{e}_\theta + \sigma_{\theta Z}\mathbf{e}_z) \quad \text{and} \\ \boldsymbol{\sigma} \cdot \boldsymbol{\Psi}_3 &= \psi(\sigma_{Zr}\mathbf{e}_r + \sigma_{Z\theta}\mathbf{e}_\theta + \sigma_{ZZ}\mathbf{e}_z). \end{aligned} \tag{C.12}$$

Therefore, the weak form equations of the three Cauchy equation components are

$$\int_{Z=a}^{b}\int_{\theta=0}^{2\pi}\int_{r=0}^{\tilde{R}}\left[\frac{\partial\psi}{\partial r}\sigma_{rr}+\frac{1}{r}\frac{\partial\psi}{\partial\theta}\sigma_{r\theta}+\frac{\partial\psi}{\partial Z}\sigma_{ZZ}+\frac{\psi}{r}\sigma_{\theta\theta}\right]rdrd\theta dZ=$$
$$\int_{Z=a}^{b}\int_{\theta=0}^{2\pi}\psi\sigma_{rr}\Big|_{r=\tilde{R}}\tilde{R}d\theta dZ+\int_{\theta=0}^{2\pi}\int_{r=0}^{\tilde{R}}\psi\sigma_{rZ}\Big|_{Z=b}rdrd\theta-\int_{\theta=0}^{2\pi}\int_{r=0}^{\tilde{R}}\psi\sigma_{rZ}\Big|_{Z=a}rdrd\theta$$
$$\int_{Z=a}^{b}\int_{\theta=0}^{2\pi}\int_{r=0}^{\tilde{R}}\left[-\frac{\psi}{r}\sigma_{r\theta}+\frac{\partial\psi}{\partial r}\sigma_{\theta r}+\frac{1}{r}\frac{\partial\psi}{\partial\theta}\sigma_{\theta\theta}+\frac{\partial\psi}{\partial Z}\sigma_{\theta Z}\right]rdrd\theta dZ=$$
$$\int_{Z=a}^{b}\int_{\theta=0}^{2\pi}\psi\sigma_{\theta r}\Big|_{r=\tilde{R}}\tilde{R}d\theta dZ+\int_{\theta=0}^{2\pi}\int_{r=0}^{\tilde{R}}\psi\sigma_{\theta Z}\Big|_{Z=b}rdrd\theta-\int_{\theta=0}^{2\pi}\int_{r=0}^{\tilde{R}}\psi\sigma_{\theta Z}\Big|_{Z=a}rdrd\theta$$
$$\int_{Z=a}^{b}\int_{\theta=0}^{2\pi}\int_{r=0}^{\tilde{R}}\left[\frac{\partial\psi}{\partial r}\sigma_{Zr}+\frac{1}{r}\frac{\partial\psi}{\partial\theta}\sigma_{Z\theta}+\frac{\partial\psi}{\partial Z}\sigma_{ZZ}\right]rdrd\theta dZ=$$
$$\int_{Z=a}^{b}\int_{\theta=0}^{2\pi}\psi\sigma_{Zr}\Big|_{r=\tilde{R}}\tilde{R}d\theta dZ+\int_{\theta=0}^{2\pi}\int_{r=0}^{\tilde{R}}\psi\sigma_{ZZ}\Big|_{Z=b}rdrd\theta-\int_{\theta=0}^{2\pi}\int_{r=0}^{\tilde{R}}\psi\sigma_{ZZ}\Big|_{Z=a}rdrd\theta. \tag{C.13}$$

The six constitutive relations in their weak form are

$$\int_{Z=a}^{b}\int_{\theta=0}^{2\pi}\int_{r=0}^{\tilde{R}}\left\{\frac{\partial u_r}{\partial r}-\frac{1}{E}\sigma_{rr}+\frac{\nu}{E}(\sigma_{\theta\theta}+\sigma_{ZZ})-\alpha\Delta T\right\}\psi rdrd\theta dZ=0$$
$$\int_{Z=a}^{b}\int_{\theta=0}^{2\pi}\int_{r=0}^{\tilde{R}}\left\{\frac{u_r}{r}+\frac{1}{r}\frac{\partial u_\theta}{\partial\theta}-\frac{1}{E}\sigma_{\theta\theta}+\frac{\nu}{E}(\sigma_{rr}+\sigma_{ZZ})-\alpha\Delta T\right\}\psi rdrd\theta dZ=0$$
$$\int_{Z=a}^{b}\int_{\theta=0}^{2\pi}\int_{r=0}^{\tilde{R}}\left\{\frac{\partial u_Z}{\partial Z}-\frac{1}{E}\sigma_{ZZ}+\frac{\nu}{E}(\sigma_{rr}+\sigma_{\theta\theta})-\alpha\Delta T\right\}\psi rdrd\theta dZ=0$$
$$\int_{Z=a}^{b}\int_{\theta=0}^{2\pi}\int_{r=0}^{\tilde{R}}\left\{\frac{1}{2}\left(\frac{1}{r}\frac{\partial u_r}{\partial\theta}-\frac{u_\theta}{r}+\frac{\partial u_\theta}{\partial r}\right)-\frac{1+\nu}{E}\sigma_{r\theta}\right\}\psi rdrd\theta dZ=0$$
$$\int_{Z=a}^{b}\int_{\theta=0}^{2\pi}\int_{r=0}^{\tilde{R}}\left\{\frac{1}{2}\left(\frac{\partial u_Z}{\partial r}+\frac{\partial u_r}{\partial Z}\right)-\frac{1+\nu}{E}\sigma_{rZ}\right\}\psi rdrd\theta dZ=0$$
$$\int_{Z=a}^{b}\int_{\theta=0}^{2\pi}\int_{r=0}^{\tilde{R}}\left\{\frac{1}{2}\left(\frac{1}{r}\frac{\partial u_Z}{\partial\theta}+\frac{\partial u_\theta}{\partial Z}\right)-\frac{1+\nu}{E}\sigma_{\theta Z}\right\}\psi rdrd\theta dZ=0. \tag{C.14}$$

These equations can then be used as the weak form of a thermoelastic problem on a three-dimensional cylindrical domain, or used on an axisymmetric cylindrical domain by neglecting θ dependence. The integrals over θ will be replaced with multiplication by 2π.

Appendix D

Code validation

The test case of the Viscous Burgers' Equation (VBE) was selected to validate the model implementation. This equation has semi-analytic solutions which may be compared with the oomph-lib solution. It also provides the means to test the implementation of both the R- and F-type terms described in section 3.3.

The VBE may be written in two different forms

$$\frac{\partial y}{\partial t} + y\frac{\partial y}{\partial x} = \zeta\frac{\partial^2 y}{\partial x^2} \tag{D.1}$$

or

$$\frac{\partial y}{\partial t} + \frac{\partial}{\partial x}\left(\frac{1}{2}y^2\right) = \zeta\frac{\partial^2 y}{\partial x^2}. \tag{D.2}$$

where ζ is a constant. These can be described in the framework of advection-reaction-diffusion equations. The first formulation has the term $y\frac{\partial y}{\partial x}$, which would be a type $R\left(y, \frac{\partial y}{\partial x}\right)$ term. This term is exchanged in the second formulation for a type $F\left(y, \frac{\partial y}{\partial x}\right)$ term: $\frac{\partial}{\partial x}\left(\frac{1}{2}y^2\right)$.

D.1 Cole-Hopf transformation

The Cole-Hopf transformation [93] is used to solve the VBE. The substitution is

$$y = -2\zeta\frac{\partial}{\partial x}(\ln\phi) = -2\zeta\frac{\phi_x}{\phi}, \tag{D.3}$$

whose inverse is

$$\phi = \exp\left(-\frac{1}{2\zeta}\int y dx\right). \tag{D.4}$$

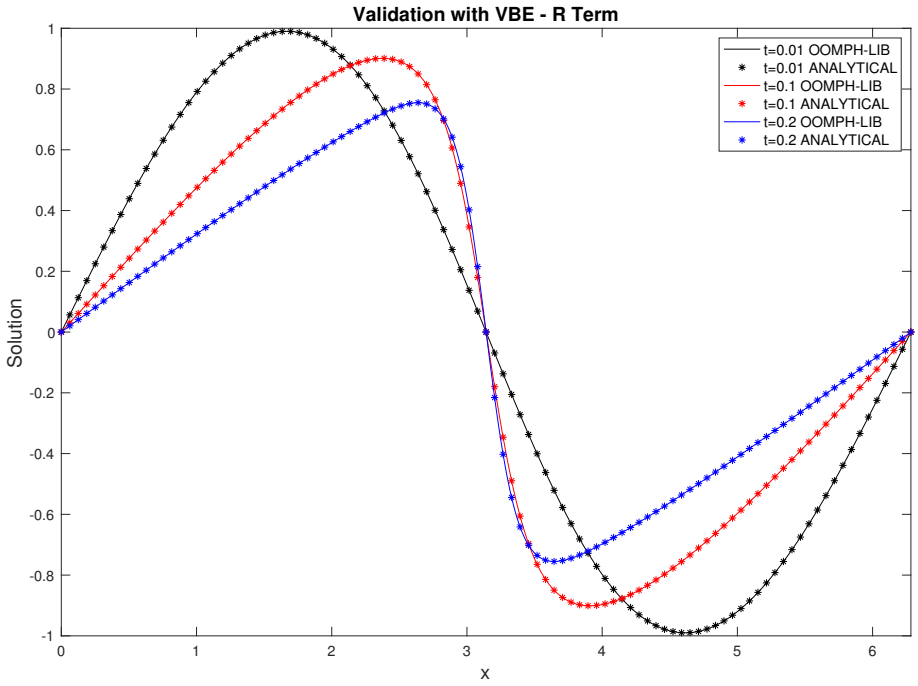

Figure D.1: Graph to show the comparison between the oomph-lib and reference solutions for the R-type term at three different times.

Use of equation (D.3) on the VBE gives

$$\frac{\partial}{\partial x}\left(\frac{1}{\phi}\frac{\partial \phi}{\partial t}\right) = \zeta \frac{\partial}{\partial x}\left(\frac{1}{\phi}\frac{\partial^2 \phi}{\partial x^2}\right). \tag{D.5}$$

Integrating the above equation with respect to x once and redefining ϕ as $\phi \times \exp\left(-\int C(t)dt\right)$ to get rid of the function $C(t)$ which arises from the integration, we obtain

$$\frac{\partial \phi}{\partial t} = \zeta \frac{\partial^2 \phi}{\partial x^2}, \tag{D.6}$$

the heat equation. When zero Dirichlet boundary conditions are imposed, we have the solution to the heat equation

$$\phi(x,t) = (4\pi\zeta t)^{1/2} \int_{-\infty}^{\infty} \exp\left(-\frac{(x-x')^2}{4\zeta t} - \frac{1}{2\zeta}\int_0^{x'} f(x'')dx''\right) dx' \tag{D.7}$$

where $f(x'')$ is the initial condition. The use of Equation (D.4) results in an analytic solution $y(x,t)$ for the VBE.

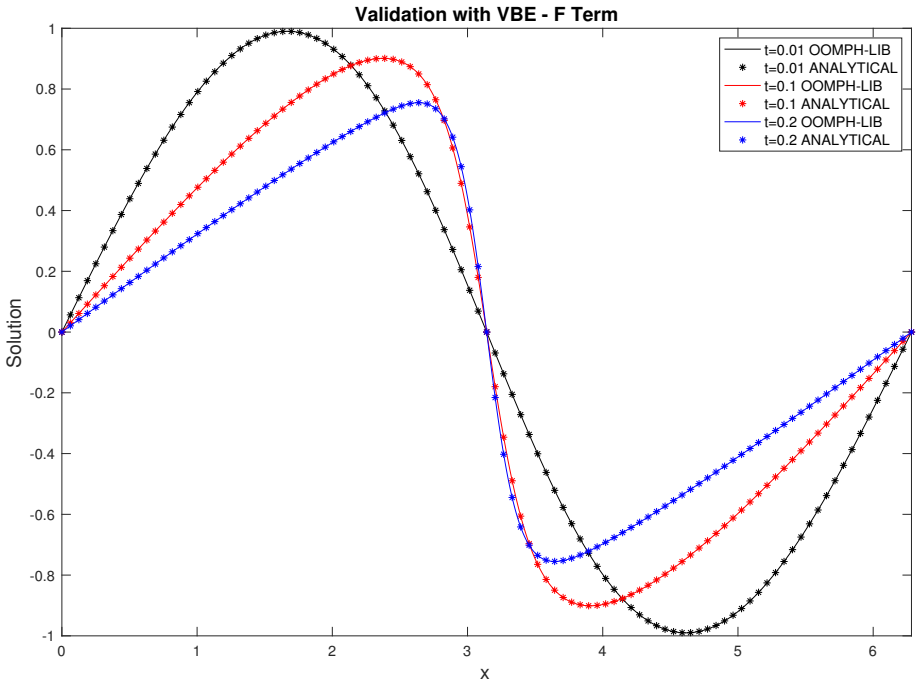

Figure D.2: Graph to show the comparison between the oomph-lib and reference solutions for the F-type term at three different times.

D.2 Solutions of the viscous Burgers' equation

Numeric integration was used to obtain semi-analytic solutions which could then be compared to results from oomph-lib. MATLAB [94] was used to find the semi-analytic reference solutions because it is easy to integrate between infinite limits using its in-built functions. Figure D.1 shows the comparison for the R-type term and similarly Figure D.2 for the F-type term. We see that the oomph-lib solutions and reference solutions exhibit the same behaviour.

D.3 Convergence study

Convergence studies were performed to check the rate of convergence of the oomph-lib solution to the semi-analytical solution found in MATLAB. The solutions were compared over the whole domain $x \in [0, 2\pi]$ at $t = 1.0$. oomph-lib computes the error between its solution and the reference solution on a one-dimensional domain by

calculating

$$\text{relative error} = \sqrt{\frac{\int_\zeta \left| u_{oomph-lib} - u_{ref} \right|^2 dx}{\int_\zeta \left| u_{ref} \right|^2 dx}}. \tag{D.8}$$

The integrals are evaluated numerically with Gauss quadrature. The number of elements of the oomph-lib solution will change in each simulation of the refinement study, which also changes the locations of the Gauss nodes. The value of the reference solution is then required at each Gauss node to calculate the error. However, evaluating this solution is extremely time-consuming - it would be preferable to only do it once. To facilitate this, the reference solution was evaluated on the domain discretised by $600,000$ elements and to obtain the value at an intermediate point, linear interpolation is implemented. The large number of elements compared with that of the oomph-lib solution ensures that the interpolation will closely approximate the actual solution.

The relative error was calculated for nine different lengths of timestep and seven different element lengths. The results of the convergence study are shown in Figures D.3 and D.4.

From Figure D.3, we see that generally the relative error decreases with increasing number of elements. However, for each size of timestep used (even when $\Delta t = 0.00001$), the error value reaches a plateau. This is because the error due to the spatial refinement becomes negligible compared to that due to the temporal refinement. The steepest gradient of the relative error decrease for $\Delta t = 0.00001$ before the plateau is approximately -2.90 on the log-log scale. Using the element size $h = \frac{\text{length of domain}}{N}$ gives us an equation for the relationship between h and relative error

$$\text{relative error} = C_1 h^{2.90} \tag{D.9}$$

with some proportionality constant C_1. It is expected that the error is proportional to h^{p+1} where p is the degree of the polynomial which describes the shape functions on the elements. Since quadratic elements are used here, we would expect a relation whereby the relative error is $O(h^3)$, so we have very good agreement with this.

The gradient of the relative error graphs increase with increasing N before the plateau is reached. This is because the first data points on the graph are for a very small number of elements. A mesh this coarse will not properly capture the shape of the solution at all, so we may expect that the line would steepen.

Figure D.4 shows the same data points but plotted with error against the inverse of the timestep size. Here, we see the error becoming saturated by low spatial refinement,

except for the error data for 1000 elements. The gradient of the line representing the relative error calculated for 1000 elements is approximately -1.01 on the log-log scale. This gives the expression

$$\text{relative error} = C_2 \Delta t^{1.01} \tag{D.10}$$

where C_2 is again some constant of proportionality.

The timestepper used was BDF2, a second-order scheme, which is expected to exhibit relative error of $O(\Delta t^2)$ for every timestep taken. If N_T timesteps are taken, the error is $O(N_T \Delta t^2)$. Using that the total time, T, is a constant, and $\Delta t = \frac{T}{N_T}$, we have that the error after N_T timesteps is $O(\Delta t)$. Clearly, we see excellent agreement with this in the convergence study. We can say that the solution is converging with reduction in timestep size as expected.

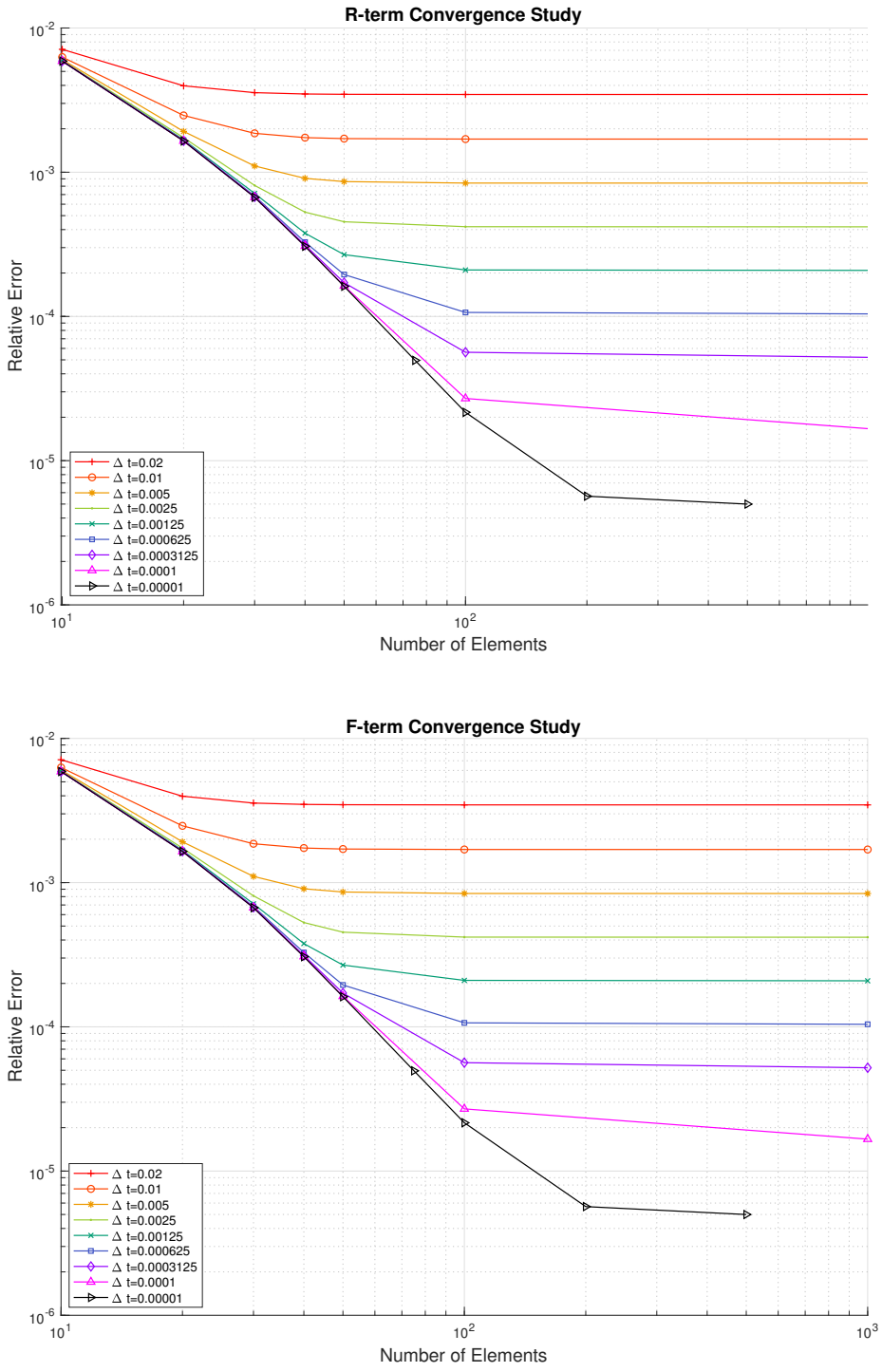

Figure D.3: Graphs to show the convergence of the oomph-lib solutions to the reference solution with increasing N for nine different sizes of timestep.

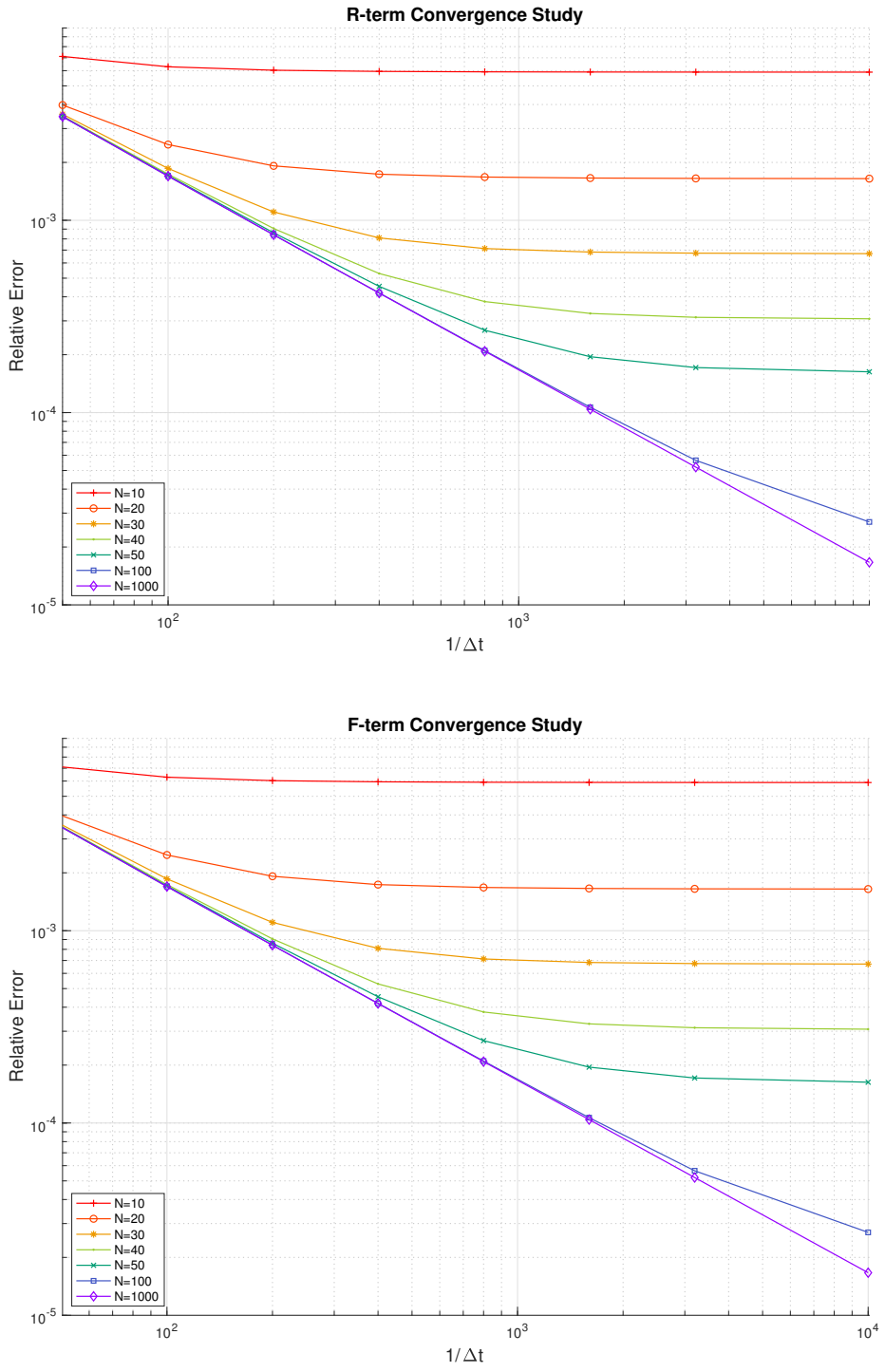

Figure D.4: Graphs to show the convergence of the oomph-lib solutions to the reference solution with decreasing timestep size for seven different N values.

Appendix E

Sobol theorem

This proof is by I.M. Sobol [70] and refers to Chapter 4. We will show that the expansion into 'summands of different dimensions' exists and is unique. To achieve this, we obtain definitions for each function $f_{i_1\ldots i_s}(\bar{x}_{i_1}\ldots\bar{x}_{i_s})$ in the expansion

$$\begin{aligned} f(\bar{x}) &= f_0 + \sum_{i=1}^{n} f_i(\bar{x}_i) + \sum_{i=1}^{n}\sum_{i<j} f_{ij}(\bar{x}_i,\bar{x}_j) + \cdots + f_{12\ldots n}(\bar{x}_1,\ldots,\bar{x}_n) \\ &= f_0 + \sum_{s=1}^{n}\sum_{i_1<\cdots<i_s} f_{i_1\ldots i_s}(\bar{x}_{i_1}\ldots\bar{x}_{i_s}) \\ &= f_0 + F(\bar{x}_{i_1}\ldots\bar{x}_{i_s}). \end{aligned} \tag{E.1}$$

We will use the notation $d\bar{x}/d\bar{x}_i = d\bar{x}_1\ldots d\bar{x}_{i-1}d\bar{x}_{i+1}\ldots d\bar{x}_n$ to indicate integration with respect to all independent variables except $\bar{x}_i$.

We define the constant f_0 by integrating $f(\bar{x})$ with respect to all the independent variables

$$\int_0^1\cdots\int_0^1 f(\bar{x})d\bar{x} = \int_0^1\cdots\int_0^1 f(\bar{x})\prod_{k=1}^{n} d\bar{x}_k = f_0. \tag{E.2}$$

Next we define the 'first dimension' functions. Consider

$$\begin{aligned} g_i(\bar{x}_i) &= \int_0^1\cdots\int_0^1 f(\bar{x})d\bar{x}/d\bar{x}_i \\ &= \int_0^1\cdots\int_0^1 \left(f_0 + F(\bar{x}_{i_1}\ldots\bar{x}_{i_s})\right)d\bar{x}/d\bar{x}_i \\ &= f_0 + f_i(\bar{x}_i) \end{aligned} \tag{E.3}$$

so we may define

$$f_i(\bar{x}_i) \coloneqq g_i(\bar{x}_i) - f_0 = \int_0^1 \cdots \int_0^1 f(\bar{x}) d\bar{x}/d\bar{x}_i - f_0. \tag{E.4}$$

Next we define the 'second dimension' functions by considering the function

$$\begin{aligned} g_{ij}(\bar{x}_i,\bar{x}_j) &= \int_0^1 \cdots \int_0^1 f(\bar{x}) d\bar{x}/d\bar{x}_i d\bar{x}_j \\ &= \int_0^1 \cdots \int_0^1 \left(f_0 + F(\bar{x}_{i_1} \ldots \bar{x}_{i_s})\right) d\bar{x}/d\bar{x}_i d\bar{x}_j \\ &= f_0 + f_i(\bar{x}_i) + f_j(\bar{x}_j) + f_{ij}(\bar{x}_i,\bar{x}_j) \end{aligned} \tag{E.5}$$

so we may define

$$f_{ij}(\bar{x}_i,\bar{x}_j) \coloneqq g_{ij}(\bar{x}_i,\bar{x}_j) - \left(f_0 + f_i(\bar{x}_i) + f_j(\bar{x}_j)\right) \tag{E.6}$$

and the 'higher dimension' functions are defined similarly.

In Chapter 4, there were two conditions

- f_0 is constant (Condition 1), and
- $\int_0^1 f_{i_1 \ldots i_s}(\bar{x}_{i_1}, \ldots, \bar{x}_{i_s}) d\bar{x}_k = 0$ for $i_1 \leq k \leq i_s$ (Condition 2)

which we will now see may be obtained from the definitions of the functions $f_{i_1 \ldots i_s}(\bar{x}_{i_1} \ldots \bar{x}_{i_s})$ given above. Condition 1 is immediate from he definition of f_0. Integrating Equation (E.3) with respect to $\bar{x}_i$ gives

$$\begin{aligned} \int_0^1 g_i(\bar{x}_i) d\bar{x}_i &= \int_0^1 \left(\int_0^1 \cdots \int_0^1 f(\bar{x}) d\bar{x}/d\bar{x}_i \right) d\bar{x}_i = \int_0^1 \cdots \int_0^1 f(\bar{x}) d\bar{x} \\ &= \int_0^1 \left(f_0 + f_i(\bar{x}_i)\right) d\bar{x}_i \\ &= f_0 + \int_0^1 f_i(\bar{x}_i) d\bar{x}_i. \end{aligned} \tag{E.7}$$

By comparing the final term on the first line with the final line, and using the definition of f_0, we have that $\int_0^1 f_i(\bar{x}_i) d\bar{x}_i = 0$. Now, integrating Equation (E.5) with respect to

$\bar{x}_j$, we obtain

$$\begin{aligned}\int_0^1 g_{ij}(\bar{x}_i,\bar{x}_j)d\bar{x}_j &= \int_0^1 \left(\int_0^1 \cdots \int_0^1 f(\bar{x})d\bar{x}/d\bar{x}_i d\bar{x}_j\right) d\bar{x}_j \\ &= \int_0^1 \cdots \int_0^1 f(\bar{x})d\bar{x}/d\bar{x}_i = f_0 + f_i(\bar{x}_i) \\ &= \int_0^1 \left(f_0 + f_i(\bar{x}_i) + f_j(\bar{x}_j) + f_{ij}(\bar{x}_i,\bar{x}_j)\right) d\bar{x}_j.\end{aligned} \tag{E.8}$$

Utilising the previous result that $\int_0^1 f_i(\bar{x}_i)d\bar{x}_i = 0$, we have

$$\begin{aligned}\int_0^1 g_{ij}(\bar{x}_i,\bar{x}_j)d\bar{x}_j &= f_0 + f_i(\bar{x}_i) \\ &= f_0 + f_i(\bar{x}_i) + \int_0^1 f_{ij}(\bar{x}_i,\bar{x}_j)d\bar{x}_j\end{aligned} \tag{E.9}$$

and so $\int_0^1 f_{ij}(\bar{x}_i,\bar{x}_j)d\bar{x}_j = 0$. The same method may be used for all 'higher dimension' functions such that we have $\int_0^1 f_{i_1\ldots i_s}(\bar{x}_{i_1},\ldots,\bar{x}_{i_s})d\bar{x}_k = 0$ for $i_1 \leq k \leq i_s$, which is Condition 2.

Appendix F

Table of physical parameters

A list of values for the physical parameters used in this report are shown here alongside sources and notes where necessary. Some of the values could not be found in the literature for U and are instead given for another metal-hydrogen system.

Symbol	Meaning	Value	Source	Notes
E	Young's Modulus (U)	$208 \times 10^9 Pa$	Online - Technical Data for Uranium: periodictable.com [84]	
ν	Poisson's ration (U)	0.23	Online - Technical Data for Uranium: periodictable.com [84]	
λ	Lamé's first parameter (U)	$7.20 \times 10^{10} Pa$		Calculated from $\lambda = \frac{E\nu}{(1+\nu)(1-2\nu)}$
μ	Shear Modulus (U)	$8.46 \times 10^{10} Pa$		Calculated from $\mu = \frac{E}{2(1+\nu)}$
α	Coefficient of thermal expansion	$3.3 \times 10^5 K^{-1}$	Estimated from graph in [95]	
$\bar{V}_H$	Partial molar volume of hydrogen in metal	$7 \times 10^{-7} m^3 mol^{-1}$	Found in Varias and Massih (2002) [43] (citing Dutton et.al. (1977))	No value found in the literature - value is for H in Zr
$\bar{V}_{Hr}$	Partial molar volume of hydride in metal	$2.19 \times 10^{-5} m^3 mol^{-1}$	Condon (1980) [96]	

Symbol	Meaning	Value	Source	Notes
$\bar{V}_U$	Partial molar volume of uranium	$1.25 \times 10^{-5} m^3 mol^{-1}$	Condon (1980) [96]	
C_{TSS}	Terminal solid solubility limit for H in metal	$10.47 molm^{-3}$	Une and Ishimoto (2004) [39]	No value for U found in the literature - value is for Zr. Value quoted is $0.55 wppm$: calculation in Section F.1
		$4.981 \times 10^{-3} molm^{-3}$	Discussions with industrial supervisor	This value is at $353.15K$/ $80°C$. he Arrhenius equation is $0.2446e^{\frac{-52000}{RT}} gcm^{-3}$
C_b	Bound concentration of H in UH3	$137000 m^3 mol^{-1}$		Calculated using $\frac{3}{\bar{V}_{Hr}}$
C_{UB}	Minimum total concentration of H in the system for pure UH3	$137500 m^3 mol^{-1}$		No value found in the literature - set to some value greater than C_b.
D_U	Diffusivity of H in U	$2.738 \times 10^{-13} m^2 s^{-1}$	Mallett and Trzeciak (1958) [42]	Calculated using $10^{(-2420/T)-1.71} cm^2 s^{-1}$ at $353.15K$/ $80°C$

Symbol	Meaning	Value	Source	Notes
ρ	Density of α-uranium	$19070 kgm^{-3}$	Found in Banos, Harker and Scott (2018) [8] (Citing Gittus (1963)[97])	
$\Delta\bar{H}$	Molar enthalpy of formation of UH3 from U and H	$-126993 Jmol^{-1}$	Abraham and Flotow (1955) [90]	
c_p	Specific heat capacity of U at constant temperature	$120 Jkg^{-1}K^{-1}$	Online - Specific Heats for Metals: engineeringtoolbox.com [98]	
κ	Heat conductivity (U)	$22.6 Wm^{-1}K^{-1}$	Found in IAEA document (2008) [99] (Citing IAEA document (1997) [100])	Given for $300K$/ $26.85°C$
Q	Heat of transport of H in metal/ Activation energy for H diffusion in metal	$25000 Jmol^{-1}$	Found in Jernkvist and Massih (2014) [61] (Citing [101] and [102])	No value for U found in the literature - value is for Zircaloy

Symbol	Meaning	Value	Source	Notes
D_{SPL}	Diffusivity of hydrogen in UO_2	$5.137 \times 10^{-15} m^2 s^{-1}$	Wheeler (1971) [103]	Calculated from a regression on the graph in Wheeler's 1971 paper, using $T = 353.15K / 80°C$
a	Length of domain			
γ	Characteristic timescale of diffusion			Calculated using a^2/D
λ_C	Proportionality constant for concentration flux boundary condition			Calculated using $\frac{0.1}{a}$
λ_T	Proportionality constant for temperature flux boundary condition			Calculated using $\frac{1}{a}$
P_{atm}	Partial pressure of hydrogen in the atmosphere	$10mbar$		Set to this value to match experimental value from A. Chohollo for comparison to data [66]

Symbol	Meaning	Value	Source	Notes
T_{atm}	Atmospheric temperature	$353.15K / 80°C$		Set to this value to match experimental value from A. Chohollo for comparison to data [66]
$K(T)$	Temperature-dependent constant for Sieverts' law		Powell (1979) [64]	Calculated by equation (2.57)
C_S	Concentration of hydrogen in uranium due to Sieverts' law			Calculated by $\frac{K(T)\sqrt{P_{atm}}}{V_U}$.
C_f	Final value of concentration Dirichlet boundary condition			Set to a value so that hydride formation is seen
R	The ideal gas constant	$8.31 JK^{-1}mol^{-1}$		
μ_0	The chemical potential of hydrogen in unstressed uranium at zero hydrogen concentration			The value of μ_0 is arbitrary and does not affect any calculations

F.1 Terminal solid solubility limit calculation

The value for C_{TSS} quoted from Une and Ishimoto (2004) [39] is

$$C_{TSS} = 3.39 \times 10^4 \times \exp(-27291/RT)\text{wppm} . \tag{F.1}$$

For $298K$, this value is $C_{TSS} = 0.55$wppm, thus for every 1kg of U, the solubility limit is 0.55×10^{-6}kg of H.

The molar weight of uranium is $238u \times N_A = 0.238\text{kg mol}^{-1}$. The number of moles in 1kg of uranium is therefore $\frac{1\text{kg}}{0.238\text{kg mol}^{-1}} = 4.20\text{mol}$.

The partial molar volume of uranium is $1.25 \times 10^{-5}\text{m}^3\text{mol}^{-1}$. The volume taken up by 4.20mol of uranium is therefore $4.20\text{mol} \times (1.25 \times 10^{-5})\text{m}^3\text{mol}^{-1} = 5.25 \times 10^{-5}\text{m}^3$.

Molar weight of hydrogen is $1u \times N_A = 9.99 \times 10^{-4}\text{kg mol}^{-1}$. The number of moles in 0.55×10^{-6}kg of hydrogen is therefore $\frac{0.55\times10^{-6}\text{kg}}{9.99\times10^{-4}\text{kg mol}^{-1}} = 5.50 \times 10^{-}4\text{mol}$.

At the solubility limit, the number of moles of hydrogen in the volume taken up by 1kg of uranium is $\frac{5.50\times10^{-4}\text{mol}}{5.25\times10^{-5}\text{m}^3} = 10.47\text{mol m}^{-3}$. This is the concentration (in mol m^{-3}) of hydrogen in uranium at the solubility limit.

Appendix G

Sensitivity analysis additional data

G.1 Additional sensitivity analysis data for Model 2 calculated by the Monte Carlo method

Table G.1: First-order Sobol indices for Model 2 calculated by the Monte Carlo method with 100 samples.

	Concentration (C)	Expansion (u)	UH_3 vol. frac. (f)
D_U	1.547×10^{-1}	3.047×10^{-1}	1.547×10^{-1}
$\frac{C_{atm}}{C_{TSS}}$	4.479×10^{-1}	3.516×10^{-1}	4.479×10^{-1}
λ_C	5.304×10^{-1}	4.233×10^{-1}	5.303×10^{-1}

Table G.2: First-order Sobol indices for Model 2 by the Monte Carlo method with 200 samples.

	Concentration (C)	Expansion (u)	UH_3 vol. frac. (f)
D_U	1.369×10^{-1}	3.140×10^{-1}	1.369×10^{-1}
$\frac{C_{atm}}{C_{TSS}}$	4.469×10^{-1}	3.620×10^{-1}	4.469×10^{-1}
λ_C	3.992×10^{-1}	3.266×10^{-1}	3.992×10^{-1}

Table G.3: First-order Sobol indices for Model 2 calculated by the Monte Carlo method with 1000 samples.

	Concentration (C)	Expansion (u)	UH_3 vol. frac. (f)
D_U	1.510×10^{-1}	3.129×10^{-1}	1.510×10^{-1}
$\frac{C_{atm}}{C_{TSS}}$	4.646×10^{-1}	3.594×10^{-1}	4.646×10^{-1}
λ_C	3.840×10^{-1}	3.072×10^{-1}	3.840×10^{-1}

Table G.4: First-order Sobol indices for Model 2 calculated by the Monte Carlo method with 5000 samples.

	Concentration (C)	Expansion (u)	UH_3 vol. frac. (f)
D_U	1.514×10^{-1}	3.204×10^{-1}	1.514×10^{-1}
$\frac{C_{atm}}{C_{TSS}}$	4.281×10^{-1}	3.320×10^{-1}	4.281×10^{-1}
λ_C	3.896×10^{-1}	3.415×10^{-1}	3.905×10^{-1}

G.2 Additional sensitivity analysis data for Model 2 by the PCE method

Table G.5: First-order Sobol indices for Model 2 calculated by the PCE method with quadrature order 3.

	Concentration (C)	Expansion (u)	UH_3 vol. frac. (f)
D_U	1.588×10^{-1}	3.321×10^{-1}	1.588×10^{-1}
$\frac{C_{atm}}{C_{TSS}}$	4.469×10^{-1}	3.511×10^{-1}	4.469×10^{-1}
λ_C	3.920×10^{-1}	3.137×10^{-1}	3.920×10^{-1}

Table G.6: First-order Sobol indices for Model 2 calculated by the PCE method with quadrature order 4.

	Concentration (C)	Expansion (u)	UH_3 vol. frac. (f)
D_U	1.588×10^{-1}	3.321×10^{-1}	1.588×10^{-1}
$\frac{C_{atm}}{C_{TSS}}$	4.469×10^{-1}	3.511×10^{-1}	4.469×10^{-1}
λ_C	3.920×10^{-1}	3.137×10^{-1}	3.920×10^{-1}

Table G.7: First-order Sobol indices for Model 2 calculated by the PCE method with quadrature order 5.

	Concentration (C)	Expansion (u)	UH_3 vol. frac. (f)
D_U	1.588×10^{-1}	3.321×10^{-1}	1.588×10^{-1}
$\frac{C_{atm}}{C_{TSS}}$	4.469×10^{-1}	3.511×10^{-1}	4.469×10^{-1}
λ_C	3.920×10^{-1}	3.137×10^{-1}	3.920×10^{-1}

G.3 Influential and non-influential input parameters

Figure G.1 shows the dependence of the output parameter f on input parameters D^U and $\bar{V}_{Hr}$ in Model 3. In each case, the value of f is taken at the node on the outer boundary after 200 timesteps. When varying D_U, $\bar{V}_{Hr}$ is held at its mean value and vice versa. The change in f when $\bar{V}_{Hr}$ is varied by $\pm 10\%$ from its mean value is negligible compared to the change in f when D^U is varied by $\pm 10\%$. We conclude that D^U and strongly influences f and $\bar{V}_{Hr}$ weakly influences f. This illustrates what is meant by 'influential' and 'non-influential' parameters.

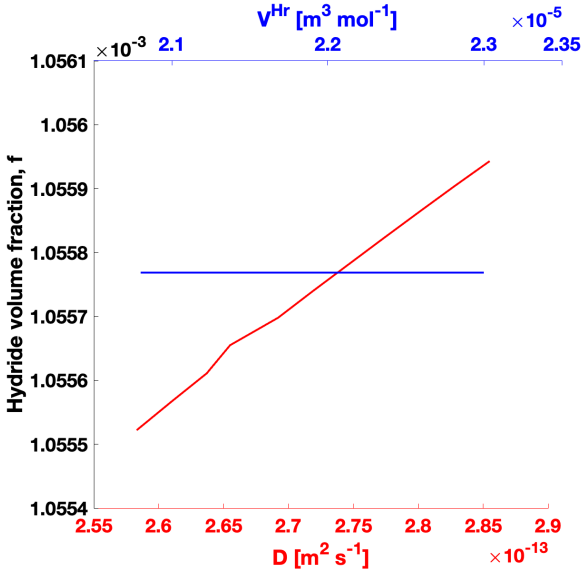

Figure G.1: Graphs to show dependence of f on D_U and $\bar{V}_{Hr}$ in one-dimensional Model 3. The value of f is taken after 200 timesteps at the node on the outer boundary.

G.4 Additional sensitivity analysis data for Model 3 by the PCE method

Table G.8: First-order Sobol indices for Model 3 calculated by the PCE method with quadrature order 3 and limits of the uniform distribution $\pm 1\%$ of the mean value.

	Expansion (u)	UH_3 vol. frac. (f)
D_U	3.889×10^{-2}	3.861×10^{-5}
C_{TSS}	2.746×10^{-5}	6.928×10^{-5}
P_{atm}	4.642×10^{-2}	2.000×10^{-1}
$\bar{V}_U$	7.335×10^{-1}	7.999×10^{-1}
$\bar{V}_H$	7.589×10^{-9}	3.358×10^{-28}
$\bar{V}_{Hr}$	1.811×10^{-1}	2.763×10^{-28}
C_{UB}	4.004×10^{-28}	3.316×10^{-26}

Table G.9: First-order Sobol indices for Model 3 calculated by the PCE method with quadrature order 3 and limits of the uniform distribution $\pm 5\%$ of the mean value.

	Expansion (u)	UH_3 vol. frac. (f)
D_U	3.883×10^{-2}	3.925×10^{-5}
C_{TSS}	2.726×10^{-5}	6.958×10^{-5}
P_{atm}	4.626×10^{-2}	1.999×10^{-1}
$\bar{V}_U$	7.319×10^{-1}	7.999×10^{-1}
$\bar{V}_H$	7.387×10^{-9}	2.274×10^{-29}
$\bar{V}_{Hr}$	1.820×10^{-1}	1.873×10^{-29}
C_{UB}	6.734×10^{-29}	7.282×10^{-28}

Appendix H

Surface passivation layer with x-dependent thickness

To model a scratch in the SPL, the y-position of each node was multiplied by the x-dependent function

$$P(x) = 1 \times 10^{-}5 - \frac{1000\text{Å}}{2} e^{-\frac{(x-\mu)^2}{2\sigma^2}} \tag{H.1}$$

where $\mu = 5 \times 10^{-6}$m and $\sigma^2 = 1 \times 10^{-15}$m^2. This would give a minimum SPL thickness of 500Å and a maximum thickness of 1000Å. A close zoom on the scratch is shown in the left frame of figure H.1. Moving downwards from the top of the image, the grey coloured region is the atmosphere, the blue region is SPL, the white blurred region is the transition between SPL and metal (centred on $y = 9.9 \times 10^{-}6$m) and the red region is pure metal. The gridlines are plotted every $10^{-}7$m in the x- and y-directions.

The line $y = 9.93 \times 10^{-6}$m lies in the SPL region, and therefore we should expect that $U^* = 0$. The Newton method is solved on the initial condition, and the resultant profile of U^* along the white line $y = 9.93 \times 10^{-6}$m is shown in the right frame of Figure H.1. The Newton method has converged on a clearly incorrect solution. More work is needed to develop a working model with an x-dependent SPL thickness.

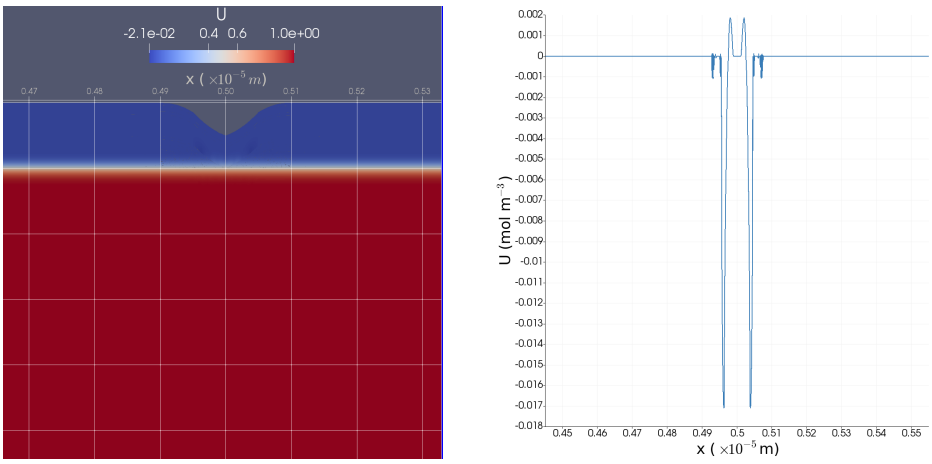

Figure H.1: Close-up image of the thin SPL region and uranium concentration initial condition along the line $y = 9.93 \times 10^{-6}$m.